UNIVERSITY OF SOUTHAMPTON

FACULTY OF ENGINEERING AND PHYSICAL SCIENCES

School of Engineering

Development and Integration of Full-Field Imaging Techniques for Assessment of Composite Structures

by

Irene Jiménez-Fortunato

ORCID ID 0000-0002-7050-3303

Thesis for the degree of Doctor of Philosophy

April 2021

UNIVERSITY OF SOUTHAMPTON

ABSTRACT

FACULTY OF ENGINEERING AND PHYSICAL SCIENCES

School of Engineering

Thesis for the degree of Doctor of Philosophy

Development and Integration of Full-Field Imaging Techniques for Assessment of Composite Structures

Irene Jiménez-Fortunato

A new versatile approach is proposed to assess the mechanical performance of composite structures. The focus of the PhD is on the development and integration of Thermoelastic Stress Analysis (TSA) and Digital Image Correlation (DIC) that are both surface based imaging techniques. The overarching goal is to create a Non-Destructive Evaluation (NDE) system for assessing the mechanical response of large composite structures using both TSA and DIC, and to use these techniques to detect defects and damage within these structures.

One of the greatest challenges with inspecting large composite structures is the need for a multi-camera setup to offer full coverage of the structure. For this to be financially viable, lower cost cameras are required. Part of this study investigates the feasibility of replacing expensive infra-red (IR) cameras based on photon detectors with low-cost microbolometers to conduct TSA, and utilising standard high-resolution white light cameras instead of expensive high-speed cameras to facilitate DIC on structures under cyclic loading.

In TSA, the dynamic behaviour of cyclic loading has led to the use of the photon detector based IR cameras that have an instantaneous response over a controllable integration time. In contrast, microbolometer based IR cameras are much cheaper, however, their performance is intrinsic to the sensor material and is governed by a fixed thermal time constant that drives the response time. To assess the suitability of different microbolometer cameras, alongside the different image processing algorithms for TSA, a means of simulating the camera response has been devised. The response from two microbolometer cameras is simulated: a standard microbolometer (<£10k) and a very low cost (<£500) microbolometer based thermal core. The thermoelastic response is simulated for the case of a Brazilian disc specimen, which provides a complex 2D stress field, and in-plane elasticity has a known analytical solution. The results from camera simulations are compared with the experimental data, and the limitations of the use of microbolometer based cameras for TSA are highlighted. Additionally, three image processing algorithms for TSA, i.e. least-squares fitting, lock-in and Fast-Fourier Transform (FFT), are compared. The study showed that the least-squares fitting is the most appropriate as the lock-in and FFT approaches are affected by spectral leakage. Most importantly, the results obtained with the thermal core are promising, strongly indicating that multiple camera TSA is a realistic possibility with an outlook to having cameras permanently installed on structures. However, at present, it is clear that the thermal core can only be used in a qualitative sense, as it has a very low response alongside significant attenuation caused by the low-pass filtering effect.

An in-depth study of the variables affecting the microbolometer based TSA is performed by means of simulations and experiments. To define the microbolometer performance, a Simulink model is developed to study the influence of the fixed time constant, inbuilt 'noise reduction' filters, signal noise, and different waveform inputs. The study shows that for transient temperature signals, such as those necessary for TSA, microbolometers behave as low-pass filters, hence, the thermoelastic response is attenuated as the loading frequency increases beyond a cut-off frequency. A parametric study considering different test specimen materials, noise reduction features, camera frame rates, loading frequencies and loading amplitudes has been performed experimentally to confirm the findings of the model. This allowed a new calibration approach based on the loading frequency to be devised, which provides faster post-processing. The procedure is developed and validated using a CFRP sample with an internal defect by comparing the thermoelastic response obtained with the photon detector and microbolometer. Additionally, Brazilian disc experimental data collected with the noise reduction on and off enables the validation of the calibration technique with the analytical solution.

Previous work on orthotropic composite laminates has indicated that the thermoelastic response might be driven by the temperature change in the resin-rich surface layer or the fibre reinforced substrate layers. It is clear that the response is dependent on the loading frequency used in the experiments and that heat transfer plays an important role. The 'source' of the thermoelastic response is studied in detail, in well-characterised glass and carbon reinforced composite laminates with different stacking sequences. Classical Laminate Theory (CLT) is used to determine the theoretical thermoelastic response from the resin-rich layer, the surface ply and homogenised through the entire laminate. Experiments are conducted where the thermoelastic response is obtained alongside strain measurements obtained simultaneously using DIC and strain gauges. To conduct the DIC during a cyclic test a new approach based on the least-squares algorithm developed for TSA is applied and named as 'Least-Squares DIC' (LSDIC). The measurement of the strain fields enables an independent 'measure' of the thermoelastic response to be derived without any influence of heat transfer. The approach enables the source of the thermoelastic response to be established categorically and highlights how differences in fibre volume fraction, surface resin layer and paint thickness must be accounted for if any form of quantitative study is to take place using TSA.

Combining the stress metric from TSA and the strain measurement from LSDIC enables the extraction of a parameter related to the overall structural stiffness. To investigate a full-field 'damage parameter' based on integrating the thermoelastic response and the LSDIC strains, an experimental campaign was conducted on GFRP coupons with different stacking sequences. Specimens were loaded at different stress levels to create damage, and inspected with TSA and LSDIC at lower load levels, as well as with X-ray Computed Tomography (CT) scans between loadings to verify the presence of any damage. The approach suggested that there is degradation of the matrix coefficient of thermal expansion due to microcracking.

Finally, microbolometer-based TSA and LSDIC are applied simultaneously in a structural composite component (T-joint of a wind turbine blade spar). The integration of TSA and LSDIC was facilitated by implementing an interpolation approach so that both data sets are constructed on the same image plane at the same spatial resolution to provide a demonstration of how the integrated approach could be applied at a structural scale.

Table of Contents

List of Tables

List of Figures

Research Thesis: Declaration of Authorship

Print name: Irene Jiménez-Fortunato

Title of thesis: Development and Integration of Full-Field Imaging Techniques for Assessment of Composite Structures

I declare that this thesis and the work presented in it are my own and has been generated by me as the result of my own original research.

I confirm that:

1. This work was done wholly or mainly while in candidature for a research degree at this University;

2. Where any part of this thesis has previously been submitted for a degree or any other qualification at this University or any other institution, this has been clearly stated;

3. Where I have consulted the published work of others, this is always clearly attributed;

4. Where I have quoted from the work of others, the source is always given. With the exception of such quotations, this thesis is entirely my own work;

5. I have acknowledged all main sources of help;

6. Where the thesis is based on work done by myself jointly with others, I have made clear exactly what was done by others and what I have contributed myself;

7. Parts of this work have been published as indicated in section 8.2.

Signature: …… Date: …….

Acknowledgements

I would like to express my sincere gratitude for the support and guidance received from my PhD supervisors Professor Janice Barton, Dr Daniel Bull and Professor Ole Thomsen. I would like to thank Dr Cédric Devivier for the support received with the Matlab scripts, Dr Andy Robinson for the training and help in TSRL, and Dr Karthik 'Ram' Ramakrishnan for manufacturing the CFRP panels at the University of Bristol. I would like to acknowledge the financial support provided by the EPSRC Doctoral Training Grant (DTG). I am also grateful to the EPSRC Future Composites Manufacturing Research Hub (CIMComp) for their support, and the Researchers Network for the organisation of social events and for inviting me to be part of the Researchers Network committee.

The final stage of the PhD has taken place during the Covid-19 pandemic, but the numerous virtual chats, pubs and games have made it more enjoyable. I am thankful to my friends and colleagues for going through this experience together. Last but not least, my deepest gratitude goes to my family, friends and Sergi for their unconditional support throughout the PhD journey.

Acronyms

ADC	Analogue-to-Digital
AFP	Automated Fibre Placement
BST	Barium Strontium Titanate
BVID	Barely Visible Impact Damage
CCD	Charge Coupled Device
CFRP	Carbon Fibre Reinforced Polymer
CLT	Classical Laminate Theory
CoV	Coefficient of Variation
CT	Computed Tomography
DC	Direct Current
DIC	Digital Image Correlation
DL	Digital Level
DoF	Degrees of Freedom
DSTO	Defence Science and Technology Organisation
DVD	Digital Volume Correlation
EMD	Empirical Mode Decomposition
FEA	Finite Element Analysis
FFT	Fast Fourier Transform
FFTDIC	Fast Fourier Transform Digital Image Correlation
FOV	Field of View
FPA	Focal-Plane Array
FPF	First Ply Failure
FR	Frame Rate
FRP	Fibre Reinforced Polymer
GAM	Generalized Additive Model
GFRP	Glass Fibre Reinforced Polymer

GLARE	Glass Laminate Aluminium Reinforced Epoxy
GMR	Giant Magnetoresistance
IMF	Intrinsic Mode Function
IR	Infrared
IT	Integration time
LF	Loading Frequency
LIDIC	Lock-in Digital Image Correlation
LSDIC	Least-Squares Digital Image Correlation
LSTL	Large Structures Testing Laboratory
LT	Lock-n Thermography
LUT	Look-up Table
LWIR	Long-Wavelength IR
MB	Microbolometer
MiTE	Microbolometer Thermoelastic Evaluation
MWIR	Mid-Wavelength IR
NDE	Non-Destructive Evaluation
NETD	Noise Equivalent Temperature Difference
NIF	Number of Integrated Frames
NR	Noise Reduction
NUC	Non-Uniformity Correction
PD	Photon Detector
PET	Polyethylene Terephthalate
PGM	Probabilistic Graphical model
PPS	Polyphenylene Sulfide
PPT	Pulsed Phase Thermography
PT	Pulse Thermography
PVC	Polyvinyl Chloride
QWIP	Quantum Well Infrared Photodetector
RC	Resistor-Capacitor

RGB	Red Green Blue
ROC	Receiver Operating Characteristic
ROI	Region of Interest
RTM	Resin Transfer Moulding
SAN	Styrene Acrylonitrile
SENT	Single Edge Notched Tension
SG	Strain Gauge
SGRE	Siemens Gamesa Renewable Energy
SHM	Structural Health Monitoring
SIF	Stress Intensity Factor
SLS	Super Lattice Structure
SNR	Signal to Noise Ratio
SPATE	Stress Pattern Analysis by Thermal Emission
SVD	Singular-Value Decomposition
SWIR	Short-Wavelength IR
TDIC	Thermography and Digital Image Correlation
TSA	Thermoelastic Stress Analysis
UAV	Unmanned Aerial Vehicle
UD	Unidirectional
UHMWPE	Ultra-High-Molecular-Weight-Polyethylene
WNN	Wavelet Neural Network
ZNSSD	Zero Normalised Sum of Squared Difference

List of symbols

ROMAN SYMBOLS	
A^*	Normalised in-plane stiffness matrix of the laminate
$A^{\Delta T}$	Thermal expansion transformation coefficients
A_r	Amplitude of the reference signal
A_{th}	Absorbance
C_{p_r}	Specific heat capacity at constant pressure of the resin
C_p	Specific heat capacity at constant pressure
C_{th}	Thermal capacity
C_ε	Specific heat capacity at constant strain
E_r	Young's modulus of the resin
F_{amb}	Ambient flux count
F_{avg}	Average flux count
F_{nom}	Nominal flux count
F^p	Flux count of each pixel
G_r	Shear modulus of the resin
G_{th}	Thermal conductance
I_s	Current
L_0	Load amplitude
N_{PD}	Number of photons absorbed by a photon detector
N_b	Number of photons emitted
N_x	Load per unit width
P_C	Power flow through the heat capacity
P_G	Power flow through the thermal resistance
Q_h	Internal heat generation per unit volume
R_{th}	Thermal resistance
T_0	Mean temperature of the cycle

T_b	Base temperature
T_{bb}	Temperature of a blackbody
T_e	Transformation matrix
V_f	Fibre volume fraction
V_s	Voltage
V_t	Tangential Speed
f_c	Cut-off frequency
k_B	Boltzmann's constant $1.38065 \cdot 10^{-23} J/K$
$\bar{r}$	Mean of the reference signal
r_{norm}	Normalised reference signal
v_I	Input voltage
v_c	Voltage at the capacitor
h	Plank's constant $6.626 \cdot 10^{-34}$Js / composite laminate total thickness
A	Extensional stiffness / calibration constant / cross-sectional area / area
Amp	Amplitude
B	Bending-extension coupling stiffness
B	Stefan-Boltzmann's constant / Bending-extension coupling stiffness
C	Capacitor / constant
CP	Calibration Parameter
CoV	Coefficient of Variance
D	Bending stiffness
DL^p	Digital Level of each pixel
DL	Digital Level
E	Young's modulus
F	Load
$I(\lambda, T)$	Radiation
IT	Integration time
K	Thermoelastic constant
L	Load / Strain length of the sample

M	External moments applied
N	Total number of samples / points averaged / external loads applied
NL	Noise level
PC	Photon Counts impinging on a photon detector
Q	Stiffness
R	Radius / Radiance impinging a microbolometer / Resistor
S	Thermoelastic signal / Shear strength
SS	Subset size
ST	Step size
STD	Standard Deviation
SW	Strain Window
T	Temperature
V	displacement
VSG	Virtual Strain Gauge
X	Reference signal / Strength parallel to the fibres
Y	Reference signal quadrature / Strength transverse to the fibres
a	Responsivity / in-plane compliance matrix of the laminate
b	Coupling compliance matrix of the laminate
c	Noise amplification / speed of light / compression
d	Intrinsic noise / flexural compliance matrix of the laminate / fibre diameter
e	Emissivity
f	Fibre (subscript) / frequency
l	Displacement of sample
m	$\cos\theta$
n	$\sin\theta$
r	Resin / Reference signal
t	Time / thickness / tension
$u(x)$	Displacement
w	Width

GREEK SYMBOLS

Φ_b	Radiant emittance
Φ_s	Thermal radiation sensors transform radiant flux
$\mathcal{T}_{DIC}$	Global residual for DIC
$\Gamma^{\Delta T}$	stress coefficient vector
Φ_{MB}	Radiant emittance microbolometer
α_r	Coefficient of linear thermal expansion of the resin
γ_{12}	Shear strain
$\dot{\varepsilon}$	Strain rate
ε^0	Strain at midplane
ε^f	Flexural strain
ν_r	Poisson's ratio of the resin
ρ_r	Density of the resin
τ_{12}	Shear stress
τ_{th}	Thermal time constant
ϕ_{sd}	Scan delay in phase
ϕ_{tc}	Time constant delay in phase
ϕ_{td}	System transport delay in phase
Δ	Change, peak-to-peak
$\Delta\Phi_{Son}$	Activated incident radiant flux
α	Coefficient of linear thermal expansion
γ	Shear strain
ε	Strain
θ	Fibre angle with respect x
κ	Curvatures
λ	Wavelength
ν	Poisson's ratio
ρ	Density

σ	Stress
τ	Time constant
ω	Frequency (rad)
ϕ	Phase

Chapter 1. Introduction

1.1 Project Background and Motivation

Fibre reinforced polymer composite materials are widely used for aero, marine, transportation and energy structure applications [1-5]. They exhibit high stiffness and strength relative to their weight and excellent performance when subjected to fatigue loads. Several NDE (Non-Destructive Evaluation) methods have been investigated to improve the assessment of composite structures. The preferred NDE technique in the aerospace and wind turbine sectors is ultrasound, while in the marine sector are simple tap tests [1, 2, 6-8]. In both cases, the NDE methods used only describe the presence of damage or defects and are time-consuming and expensive to undertake, in particular for the purpose of tracking damage growth. Additionally, these methods do not take into account how damage interacts within a complex structure under load, as there is no information of stress and strain in the vicinity of a defect. Therefore, novel, more versatile and high-fidelity techniques must be developed to overcome these limitations. The PhD project investigates the two well-established full-field imaging techniques of Thermoelastic Stress Analysis (TSA) and Digital Image Correlation (DIC) for application to composite structure with a view to developing "strain-based NDE" methodologies.

Composite structures are manufactured from different fibres and matrix materials such as glass, carbon, epoxy, textile reinforcements, vinylester or in some cases even polyester resins [9, 10]. Additionally, the stacked sheets can be from unidirectional (UD) fibres or woven fibres tows [9]. For the case of sandwich structures for wind turbine blades the core materials used can be balsa, polyvinyl chloride (PVC) foam, styrene-acrylonitrile (SAN) foam or polyethylene terephthalate (PET) foam [10]. Aluminium alloy honeycombs are used in the manufacturing of satellites or aircraft structures [1, 8]. Additionally, Nomex honeycombs are used in aircraft structures [11] and chassis for motorsport cars [12]. The mixture of different composite materials, layup options, manufacturing processes, structural geometry and loading configurations leads to a highly complex structure.

The failure behaviour of composite structures strongly depends on local design features e.g. manufacturing defects, load environment and environmental conditions. Damage examples in composite laminates [10] can be broken down into lamina scale (matrix-cracking, fibre-matrix debonding, fibre-breakage), laminate scale (delamination) or structural scale (often extensive component damage that may be associated with buckling driven delamination). In addition, there can be subsurface damage induced by impact loads (intra-lamina and inter-lamina levels) without any visible surface damage, e.g. Barely Visible Impact Damage (BVID). Furthermore, defects caused by the manufacturing processes, such as wrinkles, misalignment, dry spots, disbonds and voids, are common in many types of structures, and can contribute towards complex failure processes and knock down in performance.

The detection of damage and defects is particularly important in load carrying and high-value structures. There have been several studies incorporating NDE methods on these structures. Yang et al. [7] studied different types of NDE techniques applied on wind turbine blades. The NDE methods included were ultrasonic NDE (ultrasound-echo, air-coupled ultrasonics, tap test and local resonance spectroscopy among others), optical NDE (DIC, shearography, etc.), electromagnetic NDE (eddy current, microwave among others), optical thermography (TSA, pulsed thermography, lock-in thermography, etc.), non-optical thermography and radiographic NDE. These techniques have demonstrated capability for defect and damage detection.

The strain-based NDE techniques studied by Yang et al. [7] were TSA and DIC. TSA consists of measuring changes of temperature with an infrared (IR) camera that occurs in an elastic solid due to change in stress or strain [13]. The temperature change obtained is related to the sum of the principal stresses. DIC consists of recording two or more images of a solid where the loading increases with time and extracting the displacement fields based on the tracking of the contrast of a speckle pattern applied on the surface of the specimen [14]. The displacements can be transformed into strains, so the strain field on the surface of the specimen is obtained. Regarding TSA, Bonnet and Dutton [15] found that TSA and Finite Element Analysis (FEA) agreed well for 4.5 m long wind turbine blade section, and that manufacturing defects could be detected at an early stage by using TSA measurements, which would be relevant to implement this technique in the wind energy sector. Additionally, Rajic and Galea [16] inspected an F/A-18 airframe structure subject to fatigue testing by a developed Structural Health Monitoring (SHM) based on TSA. The stress concentration around a 20 mm diameter hole was successfully detected. Due to the recent development in thermal detector technology, an in-situ SHM technique based on TSA was successfully applied, so that the tracking of the structure state could be performed between inspections while the structure is in service.

TSA is performed by using IR cameras that can be divided in two main groups: (1) photon detectors and (2) thermal detectors that include ferroelectric detectors (Barium Strontium Titanate - BST) and microbolometers (Vanadium Oxide - VOx - and Amorphous Silicon - a-Si) [17]. The photon detector is a high-sensitivity detector (20 mK [17]), more expensive, larger and heavier compared to the microbolometer (low-sensitivity, 40 mK [17]) due to the cryocooler or Stirling cooler, which is essential as photon detectors only operate at cryogenic temperatures [13]. Regarding the thermal detectors, microbolometers present higher sensitivity and smaller pixel size allowing higher spatial resolution than the ferroelectric detectors. The noise equivalent temperature difference (NETD), which is the minimum detectable temperature, is ~0.039 K for microbolometers compared to ~0.1 K for ferroelectric detectors [17]. However, the temperature sensitivity for TSA is achieved by capturing image series and applying lock-in processing that enables better signal-to-noise ratio (SNR) [18]. Temperature changes as small as 4 mK [19] can be extracted to provide ΔT, the small thermoelastic temperature change provided by the TSA image processing.

The TSA technique was developed using photon detector IR cameras for most of the experiments studied in the literature review, but Wong et al. [20] considered microbolometers to perform measurements in aircraft structures. The results from photon detectors and microbolometers in TSA were compared and they presented a good agreement, but several corrections were required on the microbolometer readings as highlighted by Rajic and Rowlands [21] due to a specific sensor property, i.e. the thermal time constant. They showed that the temperature reading performed with the microbolometer needed to be corrected in amplitude and in phase to obtain the expected results due to the low-pass filtering behaviour driven by the thermal time constant. A calibration factor was extracted from a model to correct the decay in amplitude of the temperature data at higher loading frequencies. Therefore, to use the TSA technique for large composite structure inspections, which would typically require more cameras to offer a larger coverage, low-cost microbolometers are studied, in this thesis, with a view to reduce the operational and acquisition costs by replacing expensive and heavy IR photon detector cameras.

A variation of the DIC technique is Lock-in DIC (LIDIC) [22] that consists of applying a lock-in processing (same as for TSA) to the full-field strain data acquired from the images taken with DIC on a component undergoing cyclic loading. The LIDIC method allows the mean and amplitude of strain, and its phase to be extracted. This approach facilitates the evaluation of the effect of any damage in the component on the strain field without interrupting (pausing) the fatigue test and without the need to synchronise image capture [22], e.g. triggering image capture at the peaks of the cyclic load. Additionally, a dynamic test, such as cyclic loading, would typically require a high-speed camera to obtain adequate sampling, which adds a cost expense to the test. The approach would be too costly to scale up with multiple high-speed cameras that will have a limited capture rate (typically < 50 frames per second), which can lead to an under-sampled dataset on a dynamic cyclic test. However, with careful selection of the camera frame rate and loading frequency, it has been demonstrated that LIDIC can obtain accurate measurements on under-sampled data, removing the need for expensive high-speed cameras [22]. Additionally, LIDIC reduces noise as the lock-in amplifier extracts the signal information from a noisy signal [22]. The integration of both DIC and TSA allows the extraction of strain and stress fields in the vicinity of the damage. As an example, Crammond et al. [23] applied DIC and TSA methods to a bonded double butt strap joint. The information on the stress and strain fields were obtained. The DIC results were transformed to obtain the sum of principal stresses, as in TSA, to compare and validate both techniques. An FEA model was developed and validated with the DIC and TSA results. In [24] it was shown that the DIC data could be used for motion compensation. Also, Bull et al. [25] applied TSA and LIDIC on a part of the corner of a Carbon Fibre Reinforce Polymer (CFRP) wing spar that presented a wrinkle defect along the centre inner corner. Subsurface wrinkles were detected with both techniques by obtaining stress and strain concentrations surrounding the wrinkle defect, as well as the presence of delaminations when the load increased.

The type of algorithm used to determine the mean, amplitude and phase of TSA and DIC data can influence the quality of the processed data. In the majority of previous studies, a lock-in algorithm has been used. However, there are other approaches such as least-squares and fast Fourier transforms. These alternative algorithms are explored in the thesis to better understand their influence on processed data, and if they offer any advantages over the traditional lock-in algorithm.

1.2 Aim and Objectives

The main aim of the PhD is to develop a low-cost approach for TSA to combine with DIC and create an alternative means of NDE for composite materials and complex structures in a structural testing environment where multiple cameras are required. The overarching goal is to provide the basis for inspection of large structures, and characterise any damage in terms of local stress and strain fields. Therefore, the approach would facilitate multiple cameras placed around the structure that would inspect several regions of interest simultaneously at minimal acquisition and operational costs. To reduce costs, TSA would be performed with low-cost microbolometer IR cameras instead of expensive IR photon detectors, and DIC would use low frame rate white light cameras instead of expensive high-speed cameras to provide direct and detailed strain and stress measures in the vicinity of evolving damaged zones. Development of such imaging methodology would enable the capture of damage initiation and propagation, and the local stress and strain state in the vicinity of the evolving damage, and provide a tool that could be deployed for monitoring large structural tests.

The objectives to fulfil the main aims are:

1. Critical assessment of the **current state of the art of NDE techniques** used to inspect composite materials and structures, and the most common **types of damage and defects in high-value complex composite structures**.
2. Develop **IR camera performance models** for application to TSA.
3. Evaluate and enhance **Digital Image Correlation** (DIC) and **Thermoelastic Stress Analysis** (TSA) for application in **cyclic loading testing**, including post-processing **algorithms**, and using **modelling approaches** for efficient implementation of the combined techniques.
4. Devising a **new means of calibrating the effect of low-pass filtering** in microbolometer based IR cameras for quantitative TSA.
5. Introduce the use of **IR thermal cores** of few millimetres in size for TSA, with a view to in-situ NDE as SHM and **real-time inspections**.
6. Devise a technique, based on DIC, that enables the **source of the thermoelastic response** of different **orthotropic laminated composites** to be identified.
7. **Integrate TSA and DIC** on the same image plane using interpolation procedures (pixel matching) and image registration.

8. Introduction of a **strain based NDE methodology** for damage analysis and assessment based on the stress and strain fields obtained with **TSA** and **DIC** to obtain a **constitutive parameter** that relates both fields.

The project aligns with and complements Jack S. Callaghan's PhD project sponsored by Siemens Gamesa Renewable Energy (SGRE) that focuses on developing and validating a new integrated methodology for 'high fidelity' testing and computational modelling of composite sub-structures and structures. The project intersects directly with the EPSRC funded strategic equipment grant Structures 2025: A high fidelity, data-rich, paradigm for structural testing (EP/R008787/1). The work described in the thesis provides the basis for the application of DIC and TSA to large structures. A structural demonstrator is being constructed with support from SGRE. The demonstration involves testing a part of a wind turbine blade structure and defining a substructural test that mimics the loading experienced in the actual blade. Jack S. Callaghan has designed the loading rig (see Figure 1.1) that will be constructed in the Large Structures Testing Laboratory (LSTL) of the University of Southampton. The imaging systems and data processing approaches devised in the present PhD will be deployed in the structural test and provide the main industrial demonstration of the Structures 2025 facility.

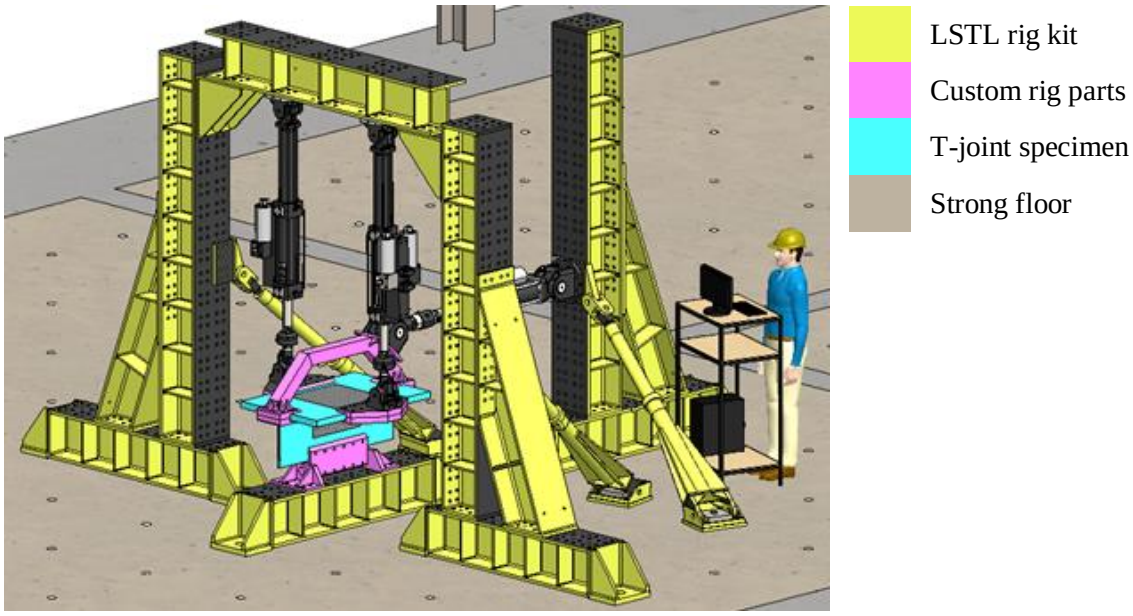

Figure 1.1 Substructural testing rig

1.3 Novelty

The key aspects of novelty in the PhD project can be summarised as follows:

1. Devising a means to assess the performance of different IR cameras for TSA based on camera simulations (related to objective 2).
2. Development of TSA with low-cost microbolometers, including initial assessment of miniaturised thermal core, to reduce acquisition and operational costs (related to objectives 4 and 5).

3. Establishing a new approach that utilises DIC to identify the 'source' of the thermoelastic response from laminated orthotropic composite materials with low and high conductivity, such as GFRP and CFRP respectively (related to objective 6).
4. Integration of TSA and DIC techniques to generate a performance parameter based on a combination of the data (related to objectives 3 and 7).
5. Application of the TSA and DIC approaches to large composite structures (related to objectives 7 and 8).

The TSA technique uses IR cameras, usually photon detectors, but they are expensive, therefore, low-cost IR cameras, i.e. microbolometers, are considered to reduce the cost. For the same cost of purchasing a photon detector, 10 microbolometers could be acquired so that a larger area of the structure would be covered. TSA has been applied with microbolometers in coupons and metallic airframe structures and has been proved to be successful in [20, 21, 26], where the need for calibration was highlighted alongside the need for increased inspection time (3 - 6 minutes) compared to photon detectors (few seconds) to obtain accurate results. The thermal time constant, which is fixed by the detector material, has a significant effect on the results, and here, it is shown that the effect of the response time results in a low-pass filtering of the TSA data. Moreover, the effect of an in built 'noise reduction' feature is identified, which causes significant attenuation of the recorded thermoelastic response. Rajic and Rowlands also [21] examined temperature variations of 0.5 K to 2 K (high SNR). However, for inspection purposes in a large structural test or in-situ monitoring the input load applied into the structure may be significantly lower. Hence, here the temperature change that is studied is reduced to the order of few mK (low SNR), to investigate the repeatability of Rajic and Rowlands [21] for small temperature changes. In the approach developed in Chapter 5, a calibration is performed after the TSA post-processing instead of at the temperature field of each frame, resulting in faster processing. Additionally, other variables can affect microbolometer based TSA post-processing, such as the frequency input into the script, noise reduction feature of the camera, and different waveforms. Hence, a new modelling approach is devised that simulates such effects and enables these to be considered in the context of a large structural test.

In the thesis, two IR cameras are considered for TSA: a thermal core microbolometer, and a standard microbolometer. A means of assessing and comparing their performance in TSA is devised. TSA has been commonly applied using the lock-in algorithm; however, due to the application of cyclic sinusoidal load signals, other algorithms such as the least-squares, and FFT can be used for post-processing. Pitarresi [27] showed the comparison among different algorithms on a single camera, and Rajic and Street [26] compared qualitatively different microbolometers with similar characteristics to a photon detector. Therefore, there is need to provide an assessment of combined IR cameras and different algorithms. The study includes the development of camera models to create simulated data, which includes all the IR sensors and camera characteristics, to compare with

experimental data. The demonstrator used is a Brazilian disc [28], as closed form analytical solution exists for the stress when considering plane elasticity.

There are different factors influencing heat transfer of laminated composites such as the resin-rich surface layer thickness, the loading frequency of the experiments and the temperature change in the substrate layers. From the work in [29] and [30], it is clear that in laminated orthotropic composite materials, the thermoelastic response could be a function of the stress in the surface ply, but also that the thickness of the surface resin layer plays a role. Therefore, the novelty is to study and understand the thermoelastic response by using DIC to assess the TSA results. Although there have been several studies that focus on the nature of the thermoelastic response from laminated orthotropic composites, here a novel approach is presented that removes several uncertainties in the measurements. DIC is used to provide an independent measure of the strain of the laminate that is constant throughout the thickness for undamaged specimens, and it is not influenced by heat transfer, as well as removing the uncertainties regarding the cyclic loading caused by test machine limitations. The thermoelastic response is calculated from the DIC measured strains using three different possibilities for the source of the thermoelastic response: isotropic resin-rich surface layer, orthotropic surface ply and global laminate. The three calculated thermoelastic responses from the DIC measured strains are compared with the measured TSA results. The study has considered GFRP and CFRP, as they present low and high conductivity respectively, two cross-ply laminates ($[0,90]_{3s}$ and $[90,0]_{3s}$), with the same stiffness behaviour but different thermoelastic response due to the difference in the surface ply, and a shear dominated laminate, $[\pm 45]_{3s}$.

Following the assessment of the thermoelastic response, a constitutive or damage parameter that would provide information of the structure state, i.e. stiffness, has been assessed. It consisted of taking the GFRP laminates described previously and applying damage by increasing the stress in successive stages. Between stress levels, the specimens are inspected using TSA and DIC at a low load that does not create damage, and X-ray Computed Tomography (CT) scans to understand how the damage initiates and progresses. The new experimental derived constitutive parameter is defined as the normalised thermoelastic response from TSA (indicative of stress) divided by the sum of the strains from DIC. It provides information on the stiffness state of the laminate but also on the degradation of the coefficients of thermal expansion as these reduce due to micro-cracking [31] and are present in TSA.

TSA and DIC techniques have been mainly applied at small-scale structures such as coupons, composite laminates, laminates with stress concentrations zones, etc [23]. The combination of DIC and TSA techniques enable obtaining strain and stress fields, respectively, to characterise the vicinity of the damage and the damage itself to assess the state of the structure. Hence, one aspect of novelty has been the integration and application of both techniques to larger multi-material structures subjected to complex loading configurations and the extraction of a parameter indicative of the state

of the structural stiffness. It requires both techniques being applied simultaneously and positioned on the same image plane with the same spatial resolution.

1.4 Report Structure

Chapter 2 starts with an overview of the mechanics of orthotropic laminated composites, summarising the basic Classical Laminate Theory (CLT) and its application to thermal properties to underpin the work presented in Chapter 6. The Chapter also contains an overview of the application of failure criteria as this is used to determine the loads applied in the experiments described in Chapter 6 and Chapter 7. A brief review of the type of damage that can occur in laminated composites and complex composite structures is also provided. A summary of common NDE techniques applied to composite structures is also presented, which includes ultrasound, tap test and resonance spectroscopy, shearography, thermography and X-ray CT-scan.

Chapter 3 describes full-field imaging methods i.e. TSA and DIC studied in the PhD. In the TSA section, a description of the TSA theory applied in composite materials, the experimental setup and post-processing are presented. It is followed by the definition of IR cameras, in particular, photon detectors and microbolometers. Due to the focus of this PhD in the development of microbolometers for TSA, a more detailed review is presented. The LIDIC approach is introduced in Chapter 3. It also includes a summary of the algorithms used for TSA, which can also be applied to DIC for cyclic tests, and an overview of integrating IR images with DIC.

Chapter 4 presents a performance comparison of the two microbolometer cameras using a new camera simulation model. The comparison of the cameras has been done by developing camera models to simulate experimental data with the same characteristics as the cameras. The camera simulations approach is presented, followed by the TSA simulated data and results comparing the simulations with the experimental data for each microbolometer using a Brazilian disc test specimen.

Chapter 5 presents a study of the microbolometer based TSA. Firstly, a detailed description of the working principles of microbolometers is presented followed by a system equivalence description linking the mechanical and thermal system to an electrical equivalence system. Importantly this captures the effect of the thermal time constant, which is fixed and dependent on the detector material, and causes the microbolometer to act as a low-pass filter. Simulations have been carried out using Matlab, and Simulink to analyse how different variables have an effect on the microbolometer based TSA. A detailed description of the development of the new calibration technique is provided, which includes assessing the effect of camera frame rate, noise reduction feature, loading frequency, loading amplitude and different materials. The technique is validated by using a damaged CFRP sample and an aluminium Brazilian disc.

Chapter 6 provides an assessment of the source of the thermoelastic response on GFRP and CFRP composite materials. It includes the description of the methodology, which includes experiments and

analytical calculations. Material properties were obtained by means of an extensive mechanical testing campaign, micrograph analysis, and a detailed survey of the literature. Finally, DIC was used to understand the 'source' of the thermoelastic response of different stacking sequences considering three possible scenarios: 1) resin-rich surface layer, 2) orthotropic surface layer, and 3) global laminate.

Chapter 7 includes the determination of a constitutive parameter that describes the material stiffness by combining TSA and DIC data. It is first assessed on GFRP coupons with different stacking sequences by designing experiments that increase the load progressively to increasing target load steps and undertaking an inspection with TSA and DIC simultaneously. The extraction of a constitutive parameter indicative of the strain was applied to a T-joint substructure, representative of a real world component containing a complex geometry, multiple materials and complex loading. TSA was performed with the microbolometer on wind turbine blade T-joint substructure to implement the calibration approach described in Chapter 5; the results were validated with results from a photon detector.

Finally, Chapter 8 provides a discussion of the outcomes of the previous chapters, summarises the conclusions and impact of the work described in the thesis, alongside the lessons learnt on using TSA and DIC simultaneously, and suggestions of areas for future work.

Chapter 2. A Review of Analysis Techniques and Damage Mechanisms in Composite Materials

2.1 Mechanics of Orthotropic Laminated Composite Materials

Laminated fibre-reinforced composite materials consist of two constituent materials that have different properties, these are fibres with high strength and stiffness, and the matrix that binds together the laminate (reinforcement) [32]. A ply is formed by unidirectional continuous or discontinuous fibres embedded into a matrix, while a laminate is a bonded stack of plies with fibres at different principal material orientations. Figure 2.1 shows the construction of a laminate formed by different plies.

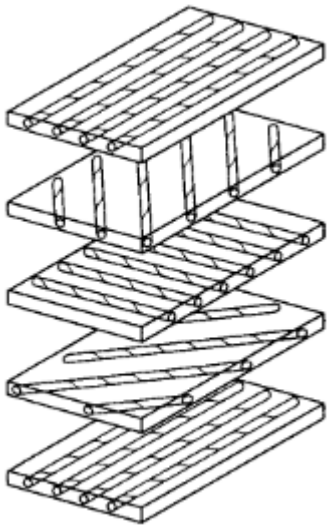

Figure 2.1 Exploded view of laminate construction [33]

A single ply is orthotropic as the body has three mutually perpendicular planes of material symmetry. However, a laminate can be isotropic, when the material properties are the same in every direction of the body, by bonding together plies of different fibre orientations.

For the work described in the thesis, the composite laminates were produced using pre-impregnated (pre-preg) material consolidated in an autoclave. The typical procedure was followed, which consisted of laying up the plies into a ‘stack’ with different stacking sequences and curing the laminate using an autoclave, where temperature and pressure are applied, as prescribed by the manufacturer's data sheet.

A key objective of the PhD is to better understand the nature of the thermoelastic response from laminated orthotropic composite materials, which depends on the coefficient of thermal expansion and the stress distribution. Therefore, it is necessary to present the basic mechanics. A summary of

Classical Laminate Theory (CLT) is described, which is valid for laminated orthotropic materials. It relates the stress to the strain by defining the material properties of a laminate based on the fibre direction of a single lamina in the laminate stack. The derivation presented in this subsection is based on that given in the books by Reddy [32], Jones [33], and Daniel and Ishai [34].

In Figure 2.2, the reference axes are shown, axes $1-2$ correspond to the axes of a single ply being 1 the direction of the fibres and 2 perpendicular to the fibre direction and axes $x-y$ represents an arbitrary coordinate system.

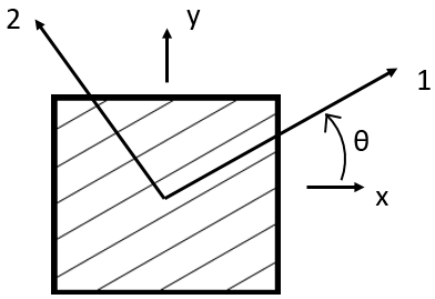

Figure 2.2 Generalised composite material coordinates in a ply

The generalised Hooke's law [33] relates the stresses and strains, for a contracted notation, it is

$$\sigma_i = Q_{ij}\varepsilon_j \quad \text{for } i,j = 1,\dots,6 \tag{2.1}$$

where σ_i are the stress components in an element as shown in Figure 2.3 in x, y and z coordinates, $Q_{i,j}$ is the stiffness matrix whose terms depends on material properties and ε_j are the strain components.

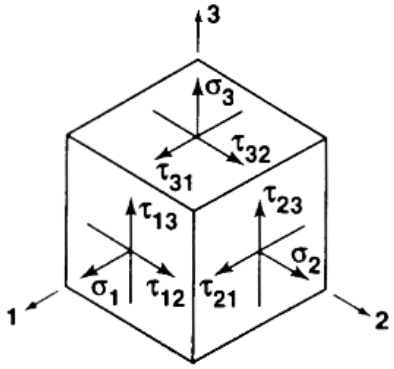

Figure 2.3 Stress on an element [33]

For an orthotropic material, there is no coupling between normal stresses and shear strains, therefore, there are null terms in the stiffness matrix as shown in the following expression:

$$\begin{bmatrix}\sigma_1\\ \sigma_2\\ \sigma_3\\ \sigma_{23}\\ \sigma_{31}\\ \sigma_{12}\end{bmatrix}=\begin{bmatrix}Q_{11} & Q_{12} & Q_{13} & 0 & 0 & 0\\ Q_{12} & Q_{22} & Q_{23} & 0 & 0 & 0\\ Q_{13} & Q_{23} & Q_{33} & 0 & 0 & 0\\ 0 & 0 & 0 & Q_{44} & 0 & 0\\ 0 & 0 & 0 & 0 & Q_{55} & 0\\ 0 & 0 & 0 & 0 & 0 & Q_{66}\end{bmatrix}\begin{bmatrix}\varepsilon_1\\ \varepsilon_2\\ \varepsilon_3\\ \varepsilon_{23}\\ \varepsilon_{31}\\ \varepsilon_{12}\end{bmatrix} \tag{2.2}$$

Considering a plane stress state, where σ_3, σ_{23} and σ_{31} are null, the previous relationship is simplified to

$$\begin{bmatrix}\sigma_1\\ \sigma_2\\ \sigma_6\end{bmatrix}=\begin{bmatrix}Q_{11} & Q_{12} & 0\\ Q_{12} & Q_{22} & 0\\ 0 & 0 & Q_{66}\end{bmatrix}\begin{bmatrix}\varepsilon_1\\ \varepsilon_2\\ \varepsilon_6\end{bmatrix} \tag{2.3}$$

where the subscript 6 indicates the in-plane shear stress and strain.

The reduced stiffness constants are defined from the material properties of Young's moduli in the fibre direction, E_1, and in the transverse direction, E_2, from the Poisson's ratios ν_{12} and ν_{21}, and the shear modulus, G_{12}, as follows:

$$\begin{aligned}Q_{11} &= \frac{E_1}{1-\nu_{12}\nu_{21}}\\ Q_{22} &= \frac{E_2}{1-\nu_{12}\nu_{21}}\\ Q_{12} &= \frac{\nu_{12}E_2}{1-\nu_{12}\nu_{21}}\\ Q_{66} &= G_{12}\end{aligned} \tag{2.4}$$

Equation (2.3) can be expressed in the coordinate system $x-y$ by using the following transformation matrices for the strains and the stresses:

$$[T_\varepsilon]=\begin{bmatrix}m^2 & n^2 & mn\\ n^2 & m^2 & -mn\\ -2mn & 2mn & m^2-n^2\end{bmatrix} \tag{2.5}$$

$$[T_\sigma]=\begin{bmatrix}m^2 & n^2 & -2mn\\ n^2 & m^2 & 2mn\\ mn & -mn & m^2-n^2\end{bmatrix} \tag{2.6}$$

where $m=\cos\theta$ and $n=\sin\theta$, and θ is the angle between the $x-y$ laminate axes and the $1-2$ principal material directions shown in Figure 2.2.

The transformation for the coefficient of thermal expansion ($[\alpha]$) is the same used to transform the coordinates of strain.

Therefore, the stress-strain relationship for a generally orthotropic lamina is

$$\begin{bmatrix}\sigma_x\\ \sigma_y\\ \sigma_{xy}\end{bmatrix}=\begin{bmatrix}\bar{Q}_{11} & \bar{Q}_{12} & \bar{Q}_{16}\\ \bar{Q}_{12} & \bar{Q}_{22} & \bar{Q}_{26}\\ \bar{Q}_{61} & \bar{Q}_{62} & \bar{Q}_{66}\end{bmatrix}\begin{bmatrix}\varepsilon_x\\ \varepsilon_y\\ \varepsilon_{xy}\end{bmatrix} \tag{2.7}$$

where the $\bar{Q}_{ij}$ terms can be obtained by

$$\begin{bmatrix}\bar{Q}_{11}\\ \bar{Q}_{22}\\ \bar{Q}_{66}\\ \bar{Q}_{12}\\ \bar{Q}_{16}\\ \bar{Q}_{26}\end{bmatrix}=\begin{bmatrix}m^4 & n^4 & 2m^2n^2 & 4m^2n^2\\ n^4 & m^4 & 2m^2n^2 & 4m^2n^2\\ m^2n^2 & m^2n^2 & -2m^2n^2 & (m^2-n^2)^2\\ m^2n^2 & m^2n^2 & m^4+n^4 & -4m^2n^2\\ m^3n & -mn^3 & mn^3-m^3n & 2(mn^3-m^3n)\\ mn^3 & -m^3n & m^3n-mn^3 & 2(m^3n-mn^3)\end{bmatrix}\begin{bmatrix}Q_{11}\\ Q_{22}\\ Q_{12}\\ Q_{66}\end{bmatrix} \tag{2.8}$$

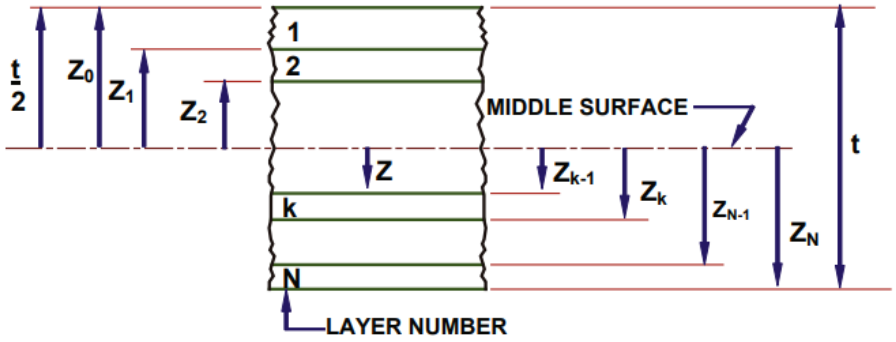

Figure 2.4 Geometry of an N-layered laminate [35]

Considering now a laminate formed of different plies, as shown in Figure 2.4, the resultant force and moment intensities of a laminate are defined as follows:

$$\begin{bmatrix}N_x\\ N_y\\ N_{xy}\end{bmatrix}=\begin{bmatrix}A_{11} & A_{12} & A_{16}\\ A_{12} & A_{22} & A_{26}\\ A_{13} & A_{26} & A_{66}\end{bmatrix}\begin{bmatrix}\varepsilon_x^0\\ \varepsilon_y^0\\ \varepsilon_{xy}^0\end{bmatrix}+\begin{bmatrix}B_{11} & B_{12} & B_{16}\\ B_{12} & B_{22} & B_{26}\\ B_{13} & B_{26} & B_{66}\end{bmatrix}\begin{bmatrix}\kappa_x\\ \kappa_y\\ \kappa_{xy}\end{bmatrix} \tag{2.9}$$

$$\begin{bmatrix}M_x\\ M_y\\ M_{xy}\end{bmatrix}=\begin{bmatrix}B_{11} & B_{12} & B_{16}\\ B_{12} & B_{22} & B_{26}\\ B_{13} & B_{26} & B_{66}\end{bmatrix}\begin{bmatrix}\varepsilon_x^0\\ \varepsilon_y^0\\ \varepsilon_{xy}^0\end{bmatrix}+\begin{bmatrix}D_{11} & D_{12} & D_{16}\\ D_{12} & D_{22} & D_{26}\\ D_{13} & D_{26} & D_{66}\end{bmatrix}\begin{bmatrix}\kappa_x\\ \kappa_y\\ \kappa_{xy}\end{bmatrix} \tag{2.10}$$

where $[N]_{x,y}$ are the resultant in-plane force intensity (N/m) in the x and y direction and shear force intensity in xy axis; $[M]_{x,y}$ are the resultant moment intensity (Nm/m) about the y and x axis and twisting moment intensity about the xy axis; $[\varepsilon^0]_{x,y}$ the strains at the midplane; $[\kappa]_{x,y}$ are the curvatures; and $[A]$, $[B]$ and $[D]$ are the matrix stiffness coefficients that are calculated as:

$$A_{ij}=\sum_{k=1}^{N}(z_k-z_{k-1})\left(\bar{Q}_{ij}\right)_k \tag{2.11}$$

$$B_{ij} = \sum_{k=1}^{N} \left(-\frac{1}{2}\right)\left(z_k^2 - z_{k-1}^2\right)\left(\bar{Q}_{ij}\right)_k \tag{2.12}$$

$$D_{ij} = \sum_{k=1}^{N} \frac{1}{3}\left(z_k^3 - z_{k-1}^3\right)\left(\bar{Q}_{ij}\right)_k \tag{2.13}$$

where A_{ij} are extensional stiffnesses, B_{ij} are the bending-extension coupling stiffnesses and D_{ij} are the bending stiffnesses. In particular, A_{13} and A_{23} are shear coupling stiffness, B_{ij} are the coupling between bending and extension, and D_{13} and D_{23} are the coupling between bending and twisting.

Equations (2.9) and (2.10) can be written in compact form:

$$\begin{bmatrix}[N]_{x,y} \\ [M]_{x,y}\end{bmatrix} = \begin{bmatrix}[A] & [B] \\ [B] & [D]\end{bmatrix}\begin{bmatrix}[\varepsilon^0]_{x,y} \\ [\kappa]_{x,y}\end{bmatrix} \tag{2.14}$$

When a laminate is symmetric, i.e. has the same ply distribution on top and bottom of the thickness centre line, bending-extension coupling does not occur, hence, $[B] = 0$ and the strain is constant throughout the laminate thickness.

The global laminate in-plane coefficients of thermal expansion are calculated as follows [36]:

$$[\alpha]_{x,y} = [a]\left[\sum_{k=1}^{N}(z_k - z_{k-1})\left([T_\varepsilon]^{-1}\begin{bmatrix}\frac{E_1}{1-\nu_{12}\nu_{21}} & \frac{\nu_{21}E_1}{1-\nu_{12}\nu_{21}} & 0 \\ \frac{\nu_{21}E_1}{1-\nu_{12}\nu_{21}} & \frac{E_2}{1-\nu_{12}\nu_{21}} & 0 \\ 0 & 0 & G_{12}\end{bmatrix}\begin{bmatrix}\alpha_1 \\ \alpha_2 \\ 0\end{bmatrix}\right)_k\right] \tag{2.15}$$

where k is the designated ply, z is the coordinate of ply k or $k-1$ [36], N is the total number of plies that form the laminate, and $[a]$ is the in-plane compliance matrix of the laminate [34] that is calculated from the elements in $[A]$ as follows:

$$\begin{aligned} a_{11} &= \frac{A_{22}A_{33} - A_{23}^2}{A} \\ a_{22} &= \frac{A_{11}A_{33} - A_{13}^2}{A} \\ a_{33} &= \frac{A_{11}A_{22} - A_{12}^2}{A} \\ a_{12} &= \frac{A_{13}A_{23} - A_{12}A_{33}}{A} \\ a_{13} &= \frac{A_{12}A_{23} - A_{22}A_{13}}{A} \end{aligned} \tag{2.16}$$

$$a_{23} = \frac{A_{12}A_{13} - A_{11}A_{23}}{A}$$

where A is

$$A = A_{11}A_{22}A_{33} + 2A_{12}A_{23}A_{13} - A_{22}A_{13}^2 - A_{33}A_{12}^2 - A_{11}A_{23}^2 \quad (2.17)$$

The equations presented in this subsection are used in Chapter 6 to calculate the thermoelastic response from measured DIC strains to understand the thermoelastic response in orthotropic composite materials considering three different approaches, i.e. isotropic resin-rich layer, orthotropic surface ply and global laminate.

The prediction of failure in laminated fibre-reinforced composite materials can be done following different failure criteria defined by functions. These failure criteria can be classified into three groups [36]:

1. Independent conditions (maximum strain and stress criteria)
    - Strain or stress components of the principal coordinate system do not interact in the failure mechanisms, hence, there are several functions to fulfil.
2. Quadratic criteria (Tsai-Wu, Hoffman and Tsai-Hill)
    - All strain or stress components interact in the failure mechanisms, hence, are combined into a single function.
3. Physically based criteria (Puck and LaRC03)
    - Distinguish between fibre failure and matrix failure, the criteria are calculated for two basic failure modes based on 2D plane stress, in fibre failure mode and inter-fibre failure mode [37, 38].

The different expressions of the mentioned failure criteria are described in the literature [34, 37, 38]. The failure criteria were calculated using ESAComp [39] to design the experiments in Chapter 6 and Chapter 7 to define the maximum load at which the specimen is considered to be damaged. The Puck and LaRC03 are chosen as the preferred failure criteria as they are based on realistic approaches, where the different fibre and matrix failures are taken into account.

2.2 Damage and Defects in Composite Structures

Composite materials present different characteristics in how they perform and fail compared to metals due to the heterogeneity of their microstructure. This section will revise the generic types of damage/defects in a composite material [40, 41]. For that, the following definitions are required:

- **Fracture** is understood as breakage of material showing formation of internal surfaces. Fibre breakage, cracks in matrix, fibre/matrix debonds and delamination (separation of bonded plies) are examples of fracture in composite materials.
- **Damage** denotes to all irreversible changes brought into the material due to energy dissipating physical or chemical processes, resulting from the application of thermomechanical loadings. It indicates distributed changes. Examples include:
  - Multiple fibre-bridged matrix cracking in an unidirectional (UD) composite
  - Multiple intralaminar cracking in a laminate
  - Local delamination distributed in an interlaminar plane
  - Fibre/matrix interfacial slip due to multiple matrix cracking
- **Failure** is defined as the incapacity of a given material system (structure) to perform its function. Fracture is an example of failure but a material could fracture locally and still perform its function. The failure event is due to the progression of various damage mechanisms.

The generic type of damage/defects [40, 41] in composite materials are:

- **Interfacial debonding**

Fibre-reinforced composite performance is widely influenced by the properties of the fibre and matrix resin interface. The adhesion bond at the interface affects the macroscopic mechanical properties of the composite, which has a significant role in stress transfer between fibre and matrix. For example, a matrix crack develops at a low stress level if the fibres are weakly held by the matrix. On the contrary, if the fibres are strongly bonded to the matrix, the matrix cracking is delayed and the composite fails catastrophically due to fibre fracture as the matrix cracks. Interfacial slipping, and fibre pull-out are also influenced by the constraint between the fibre and the matrix.

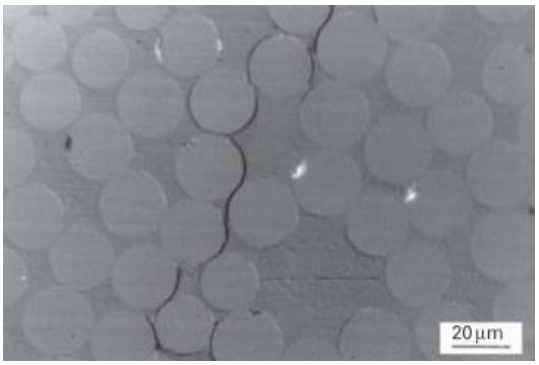

Figure 2.5 Debonds in a fibre-reinforced composite [40]

- **Matrix microcracking or intralaminar cracking**

This type of failure occurs within the ply of a laminated composite material. Fibre-reinforced composites have high strength and stiffness properties in the longitudinal direction. Nevertheless,

their properties are usually low in the transverse direction. Hence, they develop cracks along fibres, which are normally the first observed form of damage. In laminates with plies in different fibre directions, these cracks can be formed from a defect in a given ply and grow through the thickness of the ply and running parallel to the fibres in that ply. These cracks are caused by tensile loading, fatigue loading and changes in temperature. They can also originate from fibre/matrix debonds or manufacturing-induced defects such as voids and inclusions.

- **Delamination or interlaminar cracking**

The definition of interlaminar cracking is cracking in the interfacial plane between two adjoining plies in a laminate causing separation of the plies and is denoted as delamination. It can occur at free edges, i.e. at holes or at an exposed through thickness surface. The laminate develops through-thickness normal and shear stresses at the traction-free surface due to in-plane loading extending a short distance into the laminate plane. These stresses can cause local cracking in the interlaminar planes. Delaminations can also form due to low-velocity impact and can occur below the surface of the structure under relatively light impact (i.e. dropped tool) while the surface appears undamaged to visual inspection [2, 42].

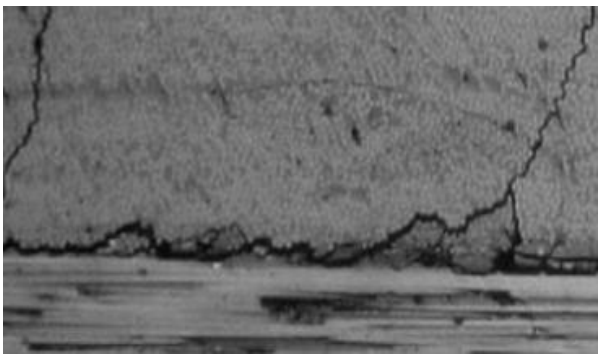

Figure 2.6 Interlaminar delamination crack formed due to joining of two matrix cracks [40]

- **Fibre breakage**

Breakage of fibres causes the ultimate failure of a fibre-reinforced composite. In a UD composite loaded in tension in the fibre direction, the individual fibres fail at their weak points and stress redistributes between fibres and matrix, affecting other fibres in the local vicinity of the broken fibres and possibly breaking some others. The interface between fibres and matrix transfers the stress from the broken fibre to the fibre at a certain distance, generating another fibre break if the stress is bigger than the fibre strength.

- **Manufacturing defects**

For polymer matrix composites, the defects caused during manufacturing can be in the fibre domain (fibre misalignment, irregular fibre distribution, broken fibres), in the matrix (voids) or at the fibre/matrix interface (disbonds, delaminations). Voids are one of the main defects found in all types

of composite materials. The formation of voids is controlled by manufacturing variables, such as vacuum pressure, cure temperature, cure pressure, and resin viscosity. The presence of voids has a significant degradation effect on the overall material behaviour, affecting the flexural, transverse and shear properties [41]. Wrinkle defect [43] are formed during manufacturing due to out-of-plane misalignment of the fibre paths (wrinkling) and it is common in thick components or curved sections. Wrinkle defect has a significant influence on mechanical performance. The detection of a crack particularly due to a wrinkle defect is studied in section 5.4.2.1.

2.2.1 Failure Modes in Complex Real World Structures

Failure modes of wind turbine blades, as an example of complex composite structure, are described below. The failure modes for wind turbine blades can be extrapolated to other complex composite structures such as aerostructures and automotive parts. The element used as a demonstrator is a 25 m blade of the V52 wind turbine blade of Vestas Wind Systems A/S. The terms taken into account for the description of the failure modes stated in Sørensen et al. [44] are shown in Figure 2.7 and Figure 2.8. The aerodynamic shell is formed of upwind and downwind skins adhesively bonded along the leading and trailing edges by adhesive films. Also, the flanges of the main spar are bonded to the skins by adhesive films.

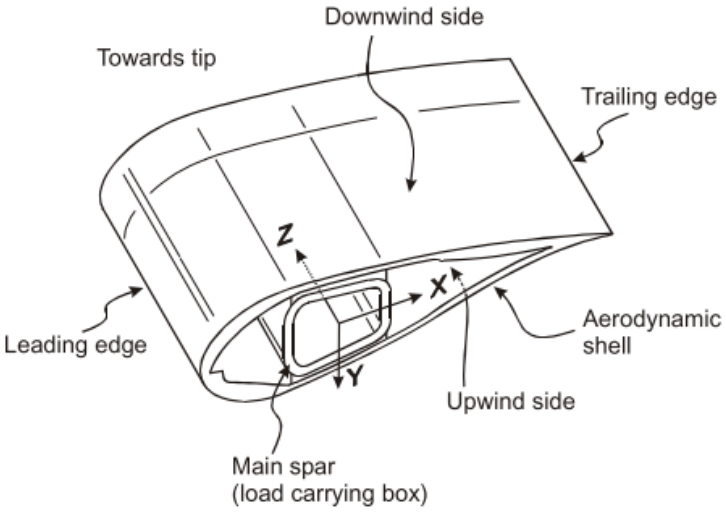

Figure 2.7 Main elements of a wing turbine blade [44]

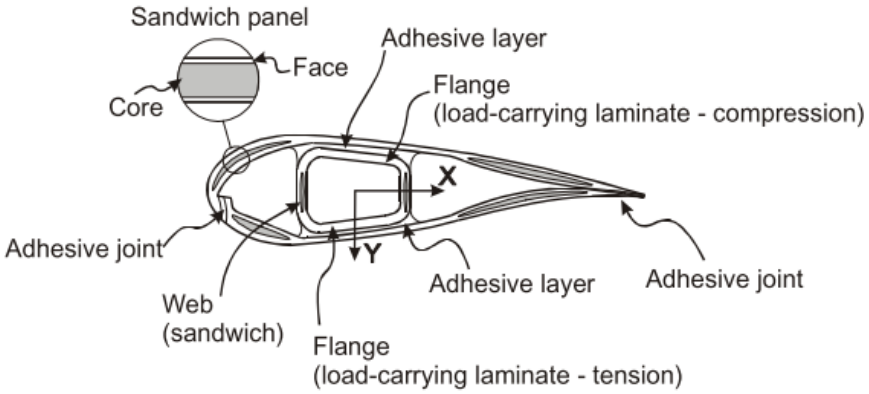

Figure 2.8 Blade construction elements nomenclature [44]

Sørensen et al. [44] studied 7 types of failure modes observed experimentally:

1) Damage creation and growth in the adhesive film assembling skin and main spar flanges.
2) Damage creation and growth on the adhesive film assembling the up- and downwind skins along leading and/or trailing edges.
3) Damage creation and growth at the boundary between face and core in sandwich panels used in skins and main spar web.
4) Internal damage creation and growth in laminates found in skin and/or main spar flanges, under a tensile or compression load.
5) Splitting and fracture of independent fibres in laminates found in skin and main spar.
6) Damage creation induced by buckling of the skin and growth in the bond between the skin and main spar under compressive load (a particular case of type 1).
7) Creation and growth of cracks in the gel-coat, debonding of the gel-coat from the skin.

In a complex structure, there are different defects/damage that can take place due to the different joints of simpler composite structures. Therefore, NDE techniques used to inspect large composite structures need to consider the possible defect/damage that can occur and that can successfully be identified.

2.3 Non-Destructive Evaluation Techniques

This section presents various NDE methods used for the inspection of composite materials in sectors such as aerospace, wind energy and marine. It describes the advantages and disadvantages of the common NDE methods in terms of damage detection and damage growth. The aim of the section is to identify how full-field techniques such as TSA and DIC, which are elaborated in Chapter 3, can enhance and inform NDE.

2.3.1 Ultrasound NDE method

The preferred method in the aerospace and wind turbine industries is usually ultrasound [6]. This NDE method can be divided into ultrasound-echo, air-coupled ultrasonics, laser ultrasonics, among others [7]. Ultrasound-echo technique [45] consists of immersing the structure in water to provide a

coupling between the actuator/sensor and the structure, then a short ultrasound pulse is transmitted, and the echo signal is detected by a transmitting-receiving transducer. There are two types of scan: 1) through transmission attenuation and 2) time-of-flight. The former is affected by cracks, so they attenuate the ultrasound signal that enables the detection of cracks, the latter uses the time delay of a reflected signal. The depth of the defect can be calculated based on the time taken for the signal to reflect back. The ultrasound-echo technique has been used to inspect wind turbine blades, in particular, to detect bonding regions [7]. It was noticed that a high voltage pulse was required due to the damping of GFRP to obtain high resolution and was able to detect defects in sandwich structures of 50 mm thickness [46]. On the other hand, this technique presents limitations in terms of sound attenuation and contact with the sample testing, as well as the water immersion introducing moisture in the structure. It was shown in [47] that the test on a real damaged wind turbine blade did not provide usable results due to tenuous coupling.

The air-coupled ultrasonic [7] differs from the ultrasound-echo as it uses air instead of water as the coupling medium. It does not cause ingress of moisture in the structure, but the signal is more attenuated than when using water as coupling medium. This technique can, therefore, be considered non-contact. As an example, it was used in [48] to inspect a glider structure, in particular, CFRP stringer reinforcement rods of 3 x 3 mm^2 sectional area and 320 mm long. The length of the delamination regions were 30 and 50 mm. It detected the delaminations and estimated the length of the zone with an uncertainty of several millimetres. Therefore, it can be said that air-coupled ultrasound works well for defects and damage larger than 10 mm.

Laser ultrasonic method [7] measures the ultrasonic response from multiple points by using a scanning sensing laser beam. It is non-contact and attractive due to its high spatial resolution. This technique has been applied in aerospace composite structures [49] made of CFRP, GFRP and metal-aluminium laminates such as GLARE©. A thermoplastic Cetex© Polyphenylene Sulfide (PPS) composite panel was inspected and the laser ultrasonic method detected the presence of a crack, delaminated areas and porosity in a thermoplastic CFRP composite laminae. Furthermore, this technique was used to inspect a 12 mm thick complex formed component, and it showed an advantage with respect to the ultrasound-echo technique by being independent of the contour shape. Abetew et al. [50] and Toyama et al. [51] have performed recent work on the laser ultrasonic technique to inspect thick (~10 mm) composite materials. A limitation of this technique is the elimination of a small part of the material at the point of contact with the sample by means of ablation or vaporisation due to high power of the laser. A high power of laser allows a thicker sample to be analysed, but the laser power should be limited to avoid surface damage. Additionally, the laser presents a hazard for the technician using this technique.

2.3.2 Tap Test and Resonance Spectroscopy

In the marine sector, the tap test and resonance spectroscopy are common NDE techniques. Simple tap tests consist of tapping each point of the structure with a hammer or coin and listening to the

sound radiated [52]. It can be done by the operator, which is a disadvantages as it relies on the human interpretation of the sound, or measurement instrumentation. Due to the thickness, material type, porosities, damage or defects, the sound radiated changes [7] detecting irregularities. This technique was applied in a ceramic and ultra-high-molecular-weight polyethylene (UHMWPE) thick-sectioned composite (22.35 mm thick) with an artificial delamination inserted (0.127 mm thick) [53]. It was shown that this method is limited by the frequency of excitation to stimulate the resonance to detect small defects, therefore, the defect detection was improved when the material membrane located above the defect is less stiff and the bandwidth of the excitation frequency is as broad as possible, making this technique suitable for thick components.

Local resonance spectroscopy [7] is an advanced tapping test where an impact is produced on the structure surface by an impulse hammer, vibration occurs in the structure generating a sound that is recorded by a microphone and is related to the contact stiffness of the surface. Additional information of the inner structure is extracted by the force recorded at the hammer tip. This method has been applied for detection of generated impact damage (delamination of about 35 x 35 mm) and real damage on wind turbine blades [47]. The limitations are that damage cannot be identified if the hammer does not impact exactly at the centre of the damaged spot, and that there is no standard system setup and software (low technological readiness level).

2.3.3 Shearography

Shearography [7] is an optical NDE technique that measures surface deformation, in particular, deformation derivatives (strains) from coherent laser illumination. A speckle pattern is generated by a laser light interference with the material surface. Two images of the speckle pattern are recorded by a charge coupled device (CCD) camera, the first one when the specimen is unloaded and the second one when stresses are applied. Hence, the structure must be loaded, either thermally or by application of pressure or vibration excitation. This requires extra equipment for the inspections. Shearography has been shown to be suitable for inspection of laminated structures (metal sheets, CFRP or GFRP laminates, etc), and can identify damage well in sandwich structures [54]. It has also been used to inspect a fairing assembly and the vertical stabilizer of a military aircraft [55], which showed it was able to detect the presence of disbonds.

2.3.4 Thermography

Thermography [7, 56] uses infrared (IR) radiation to perform the measurements with an IR camera. It can be divided into two types: active and passive. In active thermography, the sample surface is excited by using a flash, IR radiators, halogen lamps or hot/cold air, whereas the passive approach consists in monitoring the structure in its normal operating condition without any external additional source applied. The defect or damage depth is determined by considering the heat conduction from the surface to the inside of the structure.

Active thermography [7] is divided into three different methodologies: pulse thermography (PT), pulsed phase thermography (PPT) and lock-in thermography (LT). A short time energy pulse is applied in PT, it heats the surface of the material and an IR camera takes measurements of the progression of the surface temperature. PPT analyses the frequency domain of the PT by considering thermal wave conduction. LT applies periodic heat source excitation to evaluate information found on the phase and magnitude of the reflected thermal wave. PT was applied to 4 mm thickness GFRP plates bonded together with a total thickness of 13 mm to check the quality of the bonding [57]. The results obtained with PT showed good agreement with the results obtained with an ultrasound C-scan. The PPT technique was used to investigate the initiation and propagation of fatigue damage in lap joints with carbon fibre epoxy adherents [58]. It was shown that the PPT was able to detect the damage caused by fatigue by comparing the results performed before and after fatigue loading. Furthermore, it was shown in [47] that LT technique was capable of detecting hidden defects on a wind turbine blade such as near surface layers separation.

On-site thermography testing of a wind turbine was performed in [56] as an example of passive thermography. It detected potential defects and damage, but there were two features that needed detailed assessment as they can be confused with subsurface defects, when in fact there were surface inhomogeneities.

2.3.5 X-Ray CT-Scan

X-ray Computed Tomography (CT) [59] uses X-rays collected at different angles to generate a 3D volumetric reconstruction of the internal structure. The sample to be inspected is placed on a controlled turntable located between the X-ray source and an imaging system. The size of the sample is limited by the space available between the X-ray source and the imaging system. The setup is enclosed in a chamber that protects the user from the X-ray radiation. The technique allows damage or defects within the structure to be detected and measured. It can provide high fidelity information of the internal geometry and capture defects such as fibre waviness, voids, and damage, i.e. delaminations and matrix cracking. The technique is time extensive and depends on the level of resolution required to observe the features. As examples of CT-scanning, Ellison and Kim [59] successfully implemented a method to improve the post-processing of the CT-scan to separate internal damage into information about intra and interlaminar damage using impacted samples of UD carbon/epoxy panels. Also, Bull et al. [25] applied this technique to a wing spar section with curvature to detect a wrinkle defect to validate other experimental techniques, in particular, LIDIC and TSA. An adaptation of DIC known as Digital Volume Correlation (DVC) can be applied to X-ray CT-scan images [60, 61], which enables the extraction of strain data by tracking contrast to obtain displacement and, hence, obtain internal strains. However, to perform DVC, specimens need to be loaded mechanically within the X-ray system, which significantly limits the size of samples that can be inspected.

2.3.6 Advantages and Limitations of NDE techniques

Table 2.1 provides the advantages and limitations of the described NDE techniques discussed in the previous sections. This is augmented by the work of Yang et al. [7], where an overview of several NDE methods, in particular, those presented previously, have been used for inspection of large structures, such as wind turbine blades.

The ultrasound-echo technique has the advantage of being able to inspect thick samples (~50 mm) and is used mainly to identify manufacturing defects. However, it requires contact with the structure and needs water as coupling medium, which can add moisture to the inspected sample. Its application is generally limited to post manufacturing inspections and the size of the water bath restricts the specimen size. Air couple ultrasound has the advantage of not requiring contact with the structure and not adding moisture, but the signal suffers strong attenuation and is suitable for thin structures (up to 10 mm). The accessibility is better than for ultrasound-echo due to the removal of the water container, hence, complex structures can be inspected. While ultrasound-echo and air couple ultrasound inspect a single point on the structure, laser ultrasound can analyse several points, which provides more information of the defects and damage on the structure, but adds complexity. Additionally, samples with curvatures can be analysed in comparison with the ultrasound-echo technique. The ultrasound techniques are suitable for defect and damage detection, and can be used for a range of structure size and geometry. Moreover, it only shows the presence of the damage, and it assesses how damage evolves in e.g. a fatigue test, but the test must be paused for the application of ultrasound techniques. In addition, the mechanisms driving the damage evolution are not identified, simply its presence, location and size.

The tap test is easy to use, affordable and versatile, and can identify damage in thick (~ 20 mm) composite structures. However, it heavily relies on the technician skills as he/she is required to listen to the radiated sound, which is subjective. It also requires the previous knowledge of the location of a defect/damage. In contrast, local resonance spectroscopy is an automation of the tap test, where the sound is recorded by a microphone and analysed afterwards, which removes the need to rely on human interpretation. Nonetheless, to detect defects, the impact must occur on the defect/damage. Once again, these techniques do not provide the mechanisms driving the damage evolutions, i.e. the strain and stress local to the damage. To apply the techniques during a fatigue test, the test must be stopped.

In contrast with ultrasound, tap tests and spectroscopy techniques, shearography provides the measurement of surface deformations of a region. Hence, it could characterise damage in terms of the in-plane strains, but usually, the shearography image is used to identify the extent of the damage. Additionally, it could be used for in-service inspection or during a fatigue test, but the optics would need to be carefully isolated from any vibrations. The technique is only suitable for thin structures

(~ 4mm) i.e. flat laminated composites, and the cost of this technique is high because of the optical system required to perform the inspections.

Thermography techniques, in general, are limited by the thickness of the sample and the ability of the structure material to conduct heat to the surface to be analysed by an IR camera. In general, IR camera systems are usually more expensive than a standard CCD camera, but have the advantage of a simple set-up and do not require contact with the structure. Moreover, passive thermography can be used in-service without the need for any additional heating excitation. The active thermography techniques, PT, PPT and LT, require an external source to input the heat excitation and additional equipment to perform the experiments. However, they are relatively insensitive to vibrations and could be conducted during a test, without the need to pause the testing. As previously, these techniques provide only the location and the extent of the defect/damage, but do not characterise it in terms of local strains/stresses.

Finally, X-ray CT-scan provides a data-rich information of the internal structure of the sample, and hence, different defect/damage can be detected. Any type of structure in terms of geometry and thickness can be analysed, within the limitations of the size of the scanner and hutch available. Due to its complexity, it is a time consuming and expensive technique. When performing DVC in X-ray CT-scan images, it is possible to obtain deformations, and hence, strains, so that the defect/damage, and its vicinity can be characterised. However, the specimen must be loaded mechanically, which limits specimen size. Depending on the CT-scanner, it is possible to perform mechanical tests inside it while collecting X-ray images. Otherwise, the application of the load must be done outside the scanner, the test stopped and the sample taken to the X-ray hutch for the analysis. The procedure is very dependent on the ability to stop a test and maintain a load on the specimen to keep any cracks open to properly apply DVC. Hence, these type of investigations just examine the change in the extent of the damage rather than attempting to evaluate the strains. Moreover, pausing tests give stresses and strains an opportunity to relax and affect the progression of the damage.

To sum up, the NDE techniques presented in this section do not show how defects/damage interacts with mechanical loading of the structure, except for Shearography and DVC that can provide strain information. Therefore, TSA [62] and DIC [22] are considered, as they can produce data-rich information on the stress and strain, respectively, without causing further damage growth by loading the sample during short times and at low load. Additionally, multiple cameras can be placed around a large structure to inspect different regions simultaneously. The data obtained can be used to detect damage, understand damage growth, and validate FEA models. A detailed description of TSA and DIC techniques is presented in Chapter 3.

Table 2.1 NDE techniques comparison

NDE Technique	Advantages	Limitations	Usefulness of the output	References
Ultrasound-echo	Depth, high resolution	Contact, moisture content, sound attenuation	Voltage electrical pulse and travel time, it is possible to know where the damage is through thickness	[7, 46, 47, 55, 57]
Air Couple Ultrasound	No contact, complex shapes, no moisture	Strong attenuation, close to the sample	Voltage electrical pulse, from time is possible to know the position of the damage from the surface, the medium in this case is air, which is a drawback as it presents higher attenuation than water	[7, 48]
Laser Ultrasound	No contact	Sensitivity, efficiency, complex	Voltage of the pulse from several points	[7, 49-51]
Tap Test	Ease of operation, affordability, versatility	Contact, technician skills	Sound pressure of a point, the data of undamaged is needed to be compared and observed if the sound pressure has reduced showing the presence of damage	[7, 53]
Local Resonance Spectroscopy	Large areas	Contact, accuracy	Sound pressure (information of the contact stiffness) and excitation force of the hammer (extract additional internal structure information) of a point	[7, 47]
Shearography	No contact, fast, sensitivity	Thickness, cost, unique set-up	Displacement of the structure (strains) where the laser speckle pattern is applied, any change in stiffness is detected	[7, 55, 63]
Passive Thermography	No contact, fast	Accuracy, dependent on material emissivity	Surface temperature of a region of the structure during the normal working process of this one	[7, 56]
Pulsed Thermography	No contact, fast, resolution, sensitivity	Dependent on material emissivity, thickness	Surface temperature progression of a region of the structure right after the excitation of this one considering thermal wave conduction	[7, 56]
Pulsed Phase Thermography	No contact, independent on the emissivity	Complex, signal processing	Frequency domain of a region of the structure right after the excitation of this one	[7, 58, 64]
Lock-in Thermography	No contact, independent on the emissivity	Thickness, time	Temperature magnitude and phase of a region of the structure right after the excitation of this one by a periodic excitation	[7, 47, 55]
X-ray CT-scan	No contact, depth	Time, cost, size, geometry	Detailed information of the internal state of the structure	[25, 59]

2.4 Summary

It has been seen that that in complex structures, there are different types of defects and damage (delamination, debonding, splitting, cracks…) that can appear on the structure affecting its performance and they are not always visible to the naked eye. Therefore, there is need to assess damage that cannot be seen from the outside of the structure. NDE techniques are required to perform this task. The most common NDE techniques only provide information of the existence of defect/damage, but not how it interacts mechanically within the structure. Additionally, multiple NDE techniques are recommended to be used to inspect a sample, as they have different limitations and can identify different features.

This project is focused on the development of data-rich full-field imaging techniques such as TSA [62] and DIC [22], and the use of both simultaneously [18] during testing to provide information on the effect of damage in a structure. In the next Chapter, it will be explained how the damage or defect is revealed as a change in the stress distribution for TSA, and in the DIC displacement and strain fields.

Chapter 3. Full-Field Imaging Methods: TSA and DIC

3.1 Thermoelastic Stress Analysis

3.1.1 Thermoelastic Theory for Isotropic Materials

TSA is based on the thermoelastic effect, which describes the coupling between mechanical deformation and thermal energy in an elastic solid, and was established by Lord Kelvin in 1855 [13]. It states that the change in temperature is proportional to the change of the sum in the principal stresses under adiabatic conditions, and is loaded within the elastic region of the material. This effect is reversible, therefore, when stress is removed the temperature of the specimen returns to the same value. For a linear elastic homogeneous material, the rate of change of the temperature, $\dot{T}$, is as follows [13]:

$$\dot{T} = \frac{T_0}{\rho C_\varepsilon}\frac{\partial \sigma_{ij}}{\partial T}\dot{\varepsilon}_{ij} - \frac{\dot{Q}}{\rho C_\varepsilon} \quad for \;\; i,j = 1,2,3 \tag{3.1}$$

where T_0 is the absolute temperature, ρ is the material density, C_ε is the specific heat at constant strain, σ is the stress tensor, $\dot{\varepsilon}$ is the strain rate tensor, and $\dot{Q}$ is the rate of internal heat generation per unit volume, which is defined as:

$$\dot{Q} = k\nabla^2 T \tag{3.2}$$

where k is the thermal conductivity.

If the thermal conductivity and/or the stress gradient (i.e. temperature gradient) are non-zero, then heat transfer will occur. To minimise the effect of the internal heat generation, the loading frequency must be such that the rate of change of the strain ($\dot{\varepsilon}$) in the first term on the right hand side of equation (3.1) is large. Hence, the $\dot{Q}$ term can be neglected, as the thermal diffusion length decrease and pseudo adiabatic conditions are achieved (effects of thermal diffusion are neglected). Several attempts, e.g. [21, 65], have been made to identify a loading frequency at which these adiabatic conditions prevail, but it is clear that this is specific to the specimen geometry, construction and material.

TSA is a well-established technique that relates the stress change in a material to the temperature change given in equation (3.1). The theory has been simplified by assuming that the temperature change occurs adiabatically (discussed above) and that the material elastic constants are independent of the temperature [66, 67]. Hence, the familiar form of the 'thermoelastic equation' for isotropic materials is defined for specimens subjected to cyclic loading [13]:

$$\Delta T = -\frac{\alpha T_0}{\rho C_p}\Delta\left(\sigma_x + \sigma_y\right) \tag{3.3}$$

where ΔT is the thermoelastic response or peak-to-peak temperature change, T_0 is the mean temperature of the cycle, $\Delta\sigma_x$ and $\Delta\sigma_y$ are the change in the principal stresses, C_p is the specific heat capacity at constant pressure, and α is the coefficient of linear thermal expansion.

The material properties in equation (3.3) are usually expressed as the 'thermoelastic constant':

$$K = \frac{\alpha}{\rho C_p} \tag{3.4}$$

3.1.2 Thermoelastic Theory for Orthotropic Materials

During the last 40 years, there have been studies of TSA applied in orthotropic composite materials [65, 68-70]. In 1988 [71], the relationship between ΔT and the stresses in an orthotropic composite material was first established as:

$$\Delta T = -\frac{T_0}{\rho C_p}(\alpha_1 \Delta\sigma_1 + \alpha_2 \Delta\sigma_2 + \alpha_6 \Delta\sigma_6) \tag{3.5}$$

where $\Delta\sigma_i$ is the change in stress, α_i is the coefficient of linear thermal expansion, the subscripts 1, 2 and 6 (shear in 12) indicate the direction in orthogonal Cartesian coordinate system defined in Figure 3.1 which refers to the principal material axes [34]. It is clear that $\alpha_6 = 0$, because there is no coupling between 1 and 2.

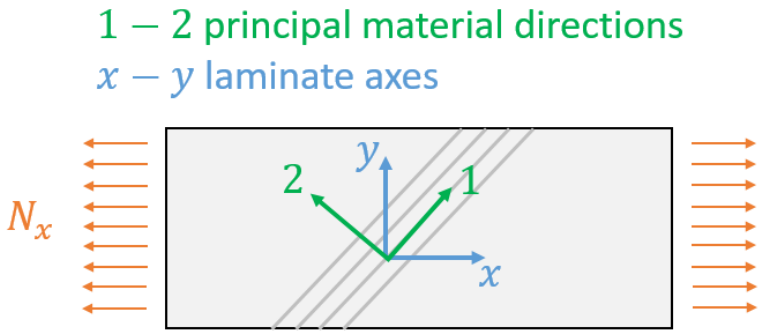

Figure 3.1 Axes systems: Cartesian (x, y) and principal material (1, 2)

Equation (3.5) provides the thermoelastic response from a general orthotropic body, which does not incorporate the features from an actual laminated composite structure. It is valid only when ΔT occurs adiabatically, but as pointed out in [72] ΔT changes ply-by-ply and drives heat transfer. Polymer composite specimens suffer significant internal heating if the deformations are large, therefore keeping the loading frequency low is desirable [65]. Over the decades since the publication of [72], there have been many publications, e.g. [29, 30, 73-80], attempting to interpret the thermoelastic response from laminated polymer composite materials. Zhang et al. [73] studied unidirectional (UD) carbon/epoxy composites and determined that the thermoelastic response became independent of the surface ply for resin-rich surface layers in excess of 30 μm in thickness. Cunningham et al. [74] came

to a similar conclusion for E-glass/epoxy pre-preg material. Pitarresi et al. [75] studied glass/polyester composites and showed that the resin-rich layer acted as an isotropic 'strain witness' (i.e. thermally isolated from the laminate stack so the response is generated by the strain experienced by the resin layer) reproducing the strain field of the laminate underneath, which was later confirmed in [76] using analytical models. Emery et al. [29] determined that in an oven consolidated glass/epoxy laminate the 25 μm thick resin-rich layer was sufficient to provide a strain witness and developed thermoelastic relationships for ply lay-ups in terms of strain. Sambasivam et al. [30] used Classical Laminate Theory (CLT) to derive the thermoelastic response from the surface ply, resin-rich layer, or multidirectional composite laminate, but the outcome was largely inconclusive because of the need to estimate various material properties. In summary, the above works highlight the important influence of the resin-rich surface layer on the thermoelastic response.

Fruehmann et al. [77] showed that variations in fibre volume fraction have significant influence on the thermoelastic response from polymer composite materials and likewise in [78] demonstrated the sensitivity to variations on the fibre volume fraction, resin material and manufacturing methods of glass/epoxy composites. Only one publication [75] thus far has considered the paint coating that is used in TSA to create a uniform and enhanced surface emissivity. It was seen that at low loading frequencies the paint layer acts as an amplifier of the thermoelastic response from the sample, but at high loading frequencies, it acts as a strain witness; similar observations were made in [79] where pure epoxy resin was studied. These effects are attributed to non-adiabatic behaviour, where at higher loading frequencies the thermal diffusion length is small, so the heat cannot diffuse through the paint, and for thicker coating the paint acts as a strain witness and attenuates the thermoelastic response. In [80], laminated carbon fibre epoxy specimens with different stacking sequences were studied. The stacking sequence had a marked effect on the thermoelastic response with some lay-ups showing an increase in response with frequency and others a decrease.

It is clear from the above that ΔT is influenced by the construction of the laminate and its constituent materials. Furthermore, the thickness of the resin-rich layer on the surface of the laminate influences the response, as well as the ply thickness and the fibre volume fraction. The thickness of the resin-rich layer is controlled by the manufacturing process and generally comprises a very low conductivity polymer. The heat transfer between the plies is driven by the thermal conductivity and diffusivity of the constituent materials. The ply-by-ply stresses, and hence, ΔT in each ply, are controlled by the laminate material and fibre orientations, and the relative direction and magnitude of the global applied strain. If ΔT is large, then this may be sufficient to drive substantial heat conduction into the surface layer. The loading frequency controls the heat transfer; as the loading frequency increases, the thermal diffusion length decreases and, depending on the material conductivity, the temperature change occurs under adiabatic conditions. The great number of variables that play a role in the thermoelastic response from laminated orthotropic composites motivates further investigation if the

technique is to be applied to structural components with an aim to provide quantitative information about the material stress state.

3.1.3 TSA Experimental Setup and Data Processing

This section describes the TSA experimental setup and the data processing. The TSA process is broken down into several key aspects:

1. Surface preparation with matt black paint to minimise surface reflection and maximise emissivity.
2. Mechanical loading using a test machine to apply sinusoidal cyclic loading.
3. Data capture using an IR camera positioned in front of the test specimen to capture surface temperature. The camera and test specimen are covered with black cloth to minimise external environmental effects (Figure 3.2).
4. Data processing to generate the mean temperature of the cycle, T_0, the thermoelastic response, ΔT, and phase, ϕ, which are usually obtained using lock-in processing and have recently been further developed by Devivier [81].

The IR camera usually has an analogue input to collect the load at each frame from the test machine, the signal acts as a reference in the TSA post-processing.

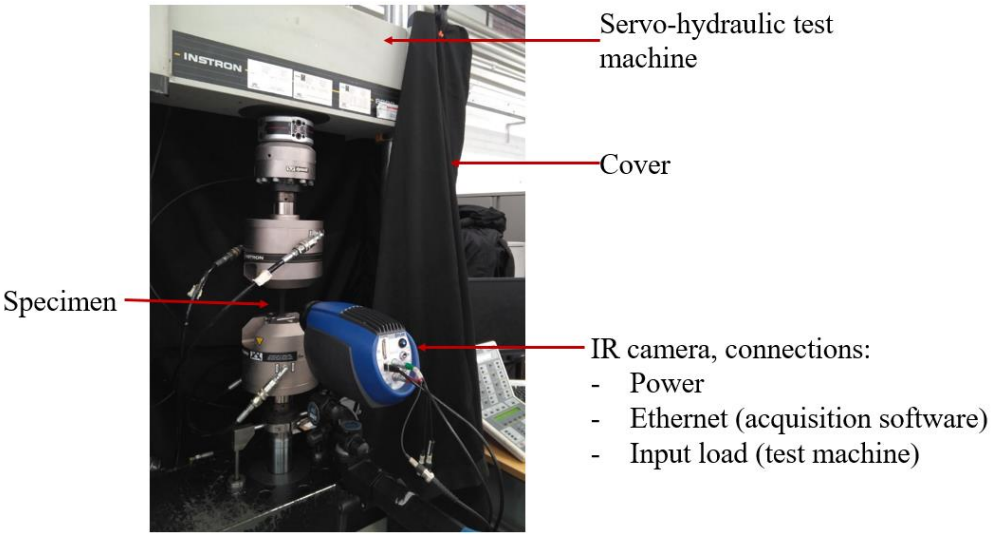

Figure 3.2 TSA setup

In TSA, a series of thermal images is captured at a given frame rate from a specimen that is sinusoidal cyclically loaded at a given frequency, f_0. The thermal image provides a measured temperature, T, for each pixel that is a function of both space and time, that is related to the thermoelastic temperature change, ΔT, as follows:

$$T(x,y,t) = T_0 + 0.5\Delta T(x,y)\cos(2\pi f_0 t + \phi) \tag{3.6}$$

where t is time, f_0 is the specimen loading frequency, ϕ is the phase of ΔT with respect to the stress change, and x and y are the image pixel location coordinates.

To identify the three 'TSA' quantities (T_0, ΔT, ϕ) from a thermal image series using equation (3.6), it is necessary to use an image processing approach. In this PhD project, three different image processing algorithms are used, namely, a lock-in algorithm [22], a Fast Fourier Transform (FFT) [62] and least-squares curve fitting approach [82]. All three image processing procedures implement 'notch filtering' associated with a lock-in amplifier to identify quantities embedded in a noisy signal. Hence, it is necessary that the loading frequency is known accurately for the successful application of TSA.

3.1.3.1 TSA Data Processing: Lock-In Algorithm

The lock-in process is the well-established approach that has been used in TSA since its development using IR cameras. All commercial software developed for TSA implement this approach. Essentially, a reference signal (traditionally the cyclic load signal from the test machine) is used to reconstruct the sinusoidal waveform from the measured signal. In the cases where there is no means of capturing the reference, e.g. natural loading, then a self-referencing approach can be used [83, 84] that employs an FFT. For cameras such as the microbolometers, used in the work described in the later chapters of the thesis, which do not have an analogue input facility into the camera, it is necessary to use the loading frequency applied by the test machine to create a simulated reference signal.

The lock-in algorithm assumes the signal is infinite, but in a real experiment, the signal is discrete and the length of the recorded signal is finite, so the signal is truncated. To approximate the assumption, it is necessary to record a sufficiently large integer number of cycles, otherwise, if the last cycle recorded is incomplete, then spectral leakage occurs causing an underestimation of the signal amplitude. In addition, to avoid scaling the results, the reference signal must have a zero mean and unit amplitude, so it is normalised as follows:

$$r_{norm}(t_i) = \frac{r(t_i) - \bar{r}}{A_r} \tag{3.7}$$

where r_{norm} is the normalised reference signal, t is time vector, i is the sample number, $r(t_i)$ is the reference signal, $\bar{r}$ is the mean of the reference signal and A_r is the amplitude of the reference signal.

A two-phase lock-in amplifier [22] is used as it does not require the reference and measurement signals to be in phase. Hence, the reference signal (X) and its quadrature (Y) are used to obtain the amplitude (Amp) and the phase (ϕ). The quadrature, Y, is obtained using the Hilbert transform of X, which changes the phase of the signal whilst maintaining the frequency content. Additionally, the mean value is obtained by averaging the input signal vector with time. The following expressions are

used for each pixel in the thermal image to calculate the mean temperature of the cycle, T_0, the temperature change, ΔT, and phase, ϕ, maps over the component:

$$X = \frac{1}{N/2}\sum_{i=1}^{N} f(t_i)\sin(\omega t_i + \phi) \tag{3.8}$$

$$Y = \frac{1}{N/2}\sum_{i=1}^{N} f(t_i)\cos(\omega t_i + \phi) \tag{3.9}$$

$$Amp = \sqrt{X^2 + Y^2} \rightarrow \Delta T = 2Amp = 2\sqrt{X^2 + Y^2} \tag{3.10}$$

$$\phi = -\tan^{-1}(X/Y) \tag{3.11}$$

$$mean = T_0 = \frac{1}{N}\sum_{i=1}^{N} f(t_i) \tag{3.12}$$

where N is the total number of images, $f(t_i)$ is the input signal as a function of time, $\sin(\omega t_i + \phi)$ is the reference signal, ω and ϕ are the frequency and phase, respectively, of the reference signal and $\cos(\omega t_i + \phi)$ is the quadrature of the reference signal. The phase is directly related to the load or reference signal.

3.1.3.2 FFT Algorithm

When using a Fast-Fourier Transform (FFT) approach to extract TSA variables, an integer number of cycles is also required, for similar reasons as the lock-in algorithm. Hence, after truncating the image frames to an integer number of load cycles, the FFT of the signal over time, $f(t_i)$, is calculated for each pixel to give the TSA variables as follows:

$$P = FFT(f(t_i)) \tag{3.13}$$

$$T_0 = |P(0)| \tag{3.14}$$

$$\Delta T = 2|P(peak)| \tag{3.15}$$

$$\phi = tan^{-1}\left(\frac{\Im\{P(peak)\}}{\Re\{P(peak)\}}\right) \tag{3.16}$$

where $P(0)$ is the FFT of the first signal value, i.e. $t_1 = 0$ s, $P(peak)$ is the FFT at the loading frequency, which will provide the maximum FFT value, and $\Re$ and $\Im$ extract the real and imaginary parts of a complex number respectively.

It is important to note that the phase value obtained from equation (3.16) is related to the first image collected because in the FFT treatment the reference load signal is not considered. In the case of

camera systems where the load signal can be collected with the image frames, then the phase can be obtained by subtracting the phase of the load signal from the phase obtained from equation (3.16).

3.1.3.3 Least-Squares Algorithm

Each image pixel temperature follows a function given in equation (3.6), which can be fitted to a sinusoidal function using a least-squares treatment. To ease calculations, a sinusoidal function is used that removes the need to directly extract the phase by using sin and cos functions instead, i.e. the in-quadrature amplitudes, as follows:

$$T(t) = T_0 + C\cos 2\pi f_0 t - D\sin 2\pi f_0 t \tag{3.17}$$

where C and D are the amplitudes of cos and sin functions.

Hence, the values of C and D can be extracted using a matrix form:

$$\begin{bmatrix} \cos 2\pi f_0 t_1 & -\sin 2\pi f_0 t_1 & 1 \\ \vdots & \vdots & \vdots \\ \cos 2\pi f_0 t_N & -\sin 2\pi f_0 t_N & 1 \end{bmatrix} \begin{bmatrix} C \\ D \\ T_0 \end{bmatrix} = \begin{bmatrix} T(t_1) \\ \vdots \\ T(t_N) \end{bmatrix} \tag{3.18}$$

where N is the numbers of frames.

Equation (3.18) is solved for every pixel in each image frame to give the coefficients as follows:

$$\begin{bmatrix} C \\ D \\ T_0 \end{bmatrix} = \begin{bmatrix} \cos 2\pi f_0 t_1 & -\sin 2\pi f_0 t_1 & 1 \\ \vdots & \vdots & \vdots \\ \cos 2\pi f_0 t_N & -\sin 2\pi f_0 t_N & 1 \end{bmatrix}^{-1} \begin{bmatrix} T(t_1) \\ \vdots \\ T(t_N) \end{bmatrix} \tag{3.19}$$

The unknowns ΔT and ϕ are:

$$\Delta T = 2\sqrt{C^2 + D^2} \tag{3.20}$$

$$\phi = -\tan^{-1}\frac{C}{D} \tag{3.21}$$

As with the FFT approach, the phase given in equation (3.21) is referred to the first image as a reference signal is not used, but if load data is available, the phase can be obtained in the same way as described for the FFT approach.

3.1.3.4 Advantages and Limitations of the Different Algorithms

The advantages and limitations of each algorithm for TSA post-processing have been summarised in Table 3.1. It is clear from the above that the major drawback for the FFT and lock-in algorithm is that both suffer from spectral leakage if an integer number of periods is not recorded. In contrast, the least-squares approach is immune to any effects of frequency content and hence spectral leakage. Therefore, it does not require truncation of the recorded frames to an integer number of load cycles

and can be applied to any recorded data set removing a data processing step. Due to the microbolometer not having an analogue input to obtain the test machine signal to synchronise the frames to the load, the focus lays on the peak-to-peak temperature magnitude, ΔT. Although the three algorithms considered present some limitations, it can be concluded that they are all valid for TSA post-processing and that they do not present significant differences in terms of extracting the TSA variables [27]. An assessment of the different algorithms is performed in Chapter 4.

Table 3.1 Advantages and limitations summary of the different TSA post-processing algorithms

Algorithm	Advantages	Limitations
Lock-in	- Unaffected by harmonics - Phase related to load if load signal is available	- Integer number of cycles - sensitive to spectral leakage - Longer processing time - Requires a reference signal
FFT	- Phase related to load if load signal is available	- Integer number of cycles - sensitive to spectral leakage
Least-squares	- Does not need an integer number of cycles - Less post-processing time (2-3 times faster than lock-in) - Unaffected by harmonics - Phase related to load if load signal is available	- Waveform must be sinusoidal

3.2 Infrared Cameras

Infrared (IR) cameras [17, 85] provide a means of non-contact temperature measurement. The history of the use of IR cameras for TSA is illustrated in Figure 3.3, which shows the development of different systems for TSA. It starts with the first commercially available equipment, the SPATE (Stress Pattern Analysis by Thermal Emissions) system, which was established in 1980s [86]. It contained a single HgCdTe (mercury-cadmium-telluride) IR photon detector coupled with a two-axis mechanical scanning mirror system. In 1995, SPATE was replaced with a system called Focal-plane Array for Synchronous Thermography (FAST) [87] which contained a detector with multiple sensor elements or ‘pixels’, which reduced the total observation time from hours to minutes. A year after that, Stress Photonics released their system based on a 128 x 128 pixel InSb (Indium Antimonide) array with the name of DeltaTherm. Some years later, the CEDIP company (now part of FLIR), developed a system based on 320 x 256 pixel HgCdTe or InSb array [20]. These two systems were the most commonly used photon detectors for TSA during the next decade. However, both required a cooling system, which makes the cameras expensive, heavy, and bulky. The cooling cycle also limits the life-span of the detector. Thermal detectors were developed originally by Langley in 1881 [88], however, the development of the modern microbolometers took place in the 1990s, but were not introduced for TSA until 2013 [21]. The cost of a microbolometer based camera is one order of magnitude less than the common photon detector, it does not require cooling system and therefore is much more compact, lighter and has a longer life span. Typically, microbolometers incorporate a

Vanadium Oxide (VOx) or Amorphous Silicon (aSi) detector array [89]. However, the drawback in comparison with photon detectors is the response time, which is intrinsic to the sensor. When exposed to a transient signal (such as that used in TSA), microbolometers act as low-pass filters, controlled by the fixed thermal time constant that is dependent on the detector material, resulting in a fixed sensor response time (this is discussed in detail in section 5.2). In TSA the thermal signal is cyclic and presents a major limitation for the technique as the amplitude of the measured thermoelastic response becomes heavily frequency dependent. Nevertheless, for lower loading frequencies below the cut off of the low-pass filtering, calibration procedures can be adopted that enable quantitative TSA [90]. Although the cut off frequency presents a limitation in some applications of TSA, the major cost reduction provides the motivation for adopting microbolometers for TSA. A further motivation is the increased spatial resolution offered by the microbolometer based detectors. In this section, the nature of thermal radiation is described as well as the working principles of the IR cameras used in this project: photon detectors, standard microbolometers and thermal core microbolometers.

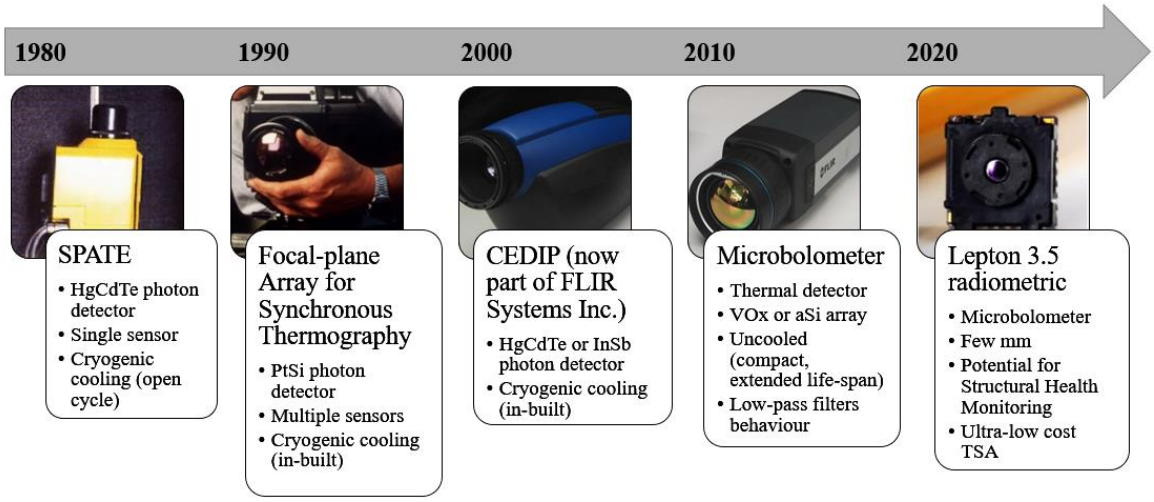

Figure 3.3 Chronological implementation of IR cameras for TSA

3.2.1 Thermal Radiation

All objects emit infrared radiation when their temperature is above absolute zero. Infrared radiation has wavelengths between 0.7 and 1000 µm. Figure 3.4 shows the electromagnetic spectrum with the IR bands made up of five further bands: near-infrared (NIR), short-wavelength infrared (SWIR), mid-wavelength infrared (MWIR), long-wavelength infrared (LWIR) and far infrared (FIR). IR cameras typically work in the following bands:

- Short-wavelength IR (SWIR) between 1.4 and 3 µm.
- Mid-wavelength IR (MWIR) between 3 and 8 µm.
- Long-wavelength IR (LWIR) between 8 and 14 µm.

The radiation in a hemisphere is defined by Planck's wavelength distribution equation [17]:

$$I(\lambda, T) = \frac{2\pi hc^2}{\lambda^5 \left(exp^{\frac{hc}{\lambda k_B T}} - 1 \right)} \tag{3.22}$$

where λ is the wavelength, h is the Planck's constant ($6.626 \cdot 10^{-34}$ Js), c is the speed of light (299,792,458 m/s), k_B is Boltzmann's constant ($1.38065 \cdot 10^{-23}$J/K) and T is the temperature.

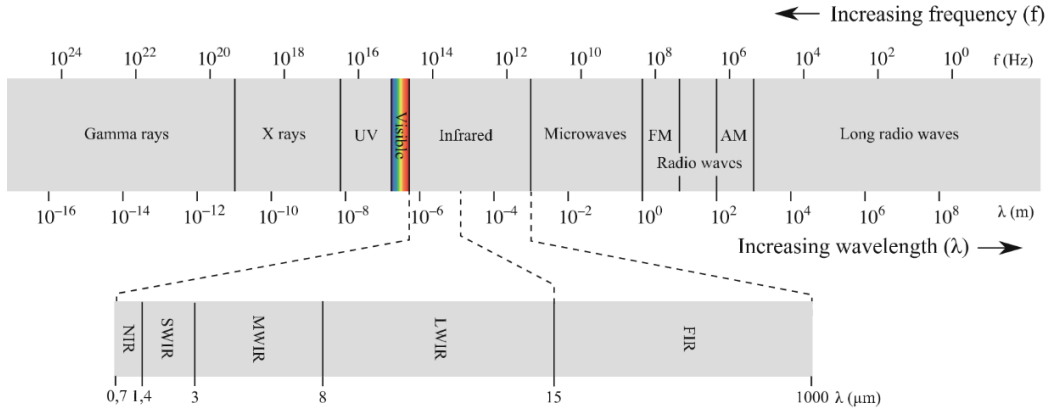

Figure 3.4 Electromagnetic spectrum with details in the IR band [17]

Photon detectors and microbolometers work differently. While photon detectors count the photons that impinge on the detector during an interval of time (integration time), microbolometers rely on IR absorption and thermal conduction [21], i.e. IR radiation is absorbed and there is a change in temperature inside the detector that is converted into an electrical signal by means of an electrical resistance. The operating range of wavelength for different IR cameras is presented in Figure 3.5, i.e. Indium Antimonide (InSb) photon detectors work in the MWIR band and microbolometers in the LWIR band. However, photon detectors are not only InSb [91], they can be Mercury Cadmium Telluride (HgCdTe), which works at LWIR, Platinum Silicide (PtSi) for MWIR, Quantum Well Infrared Photodetector (QWIP), which works at LWIR, and Indium Gallium Arsenide (InGaAs) for SWIR.

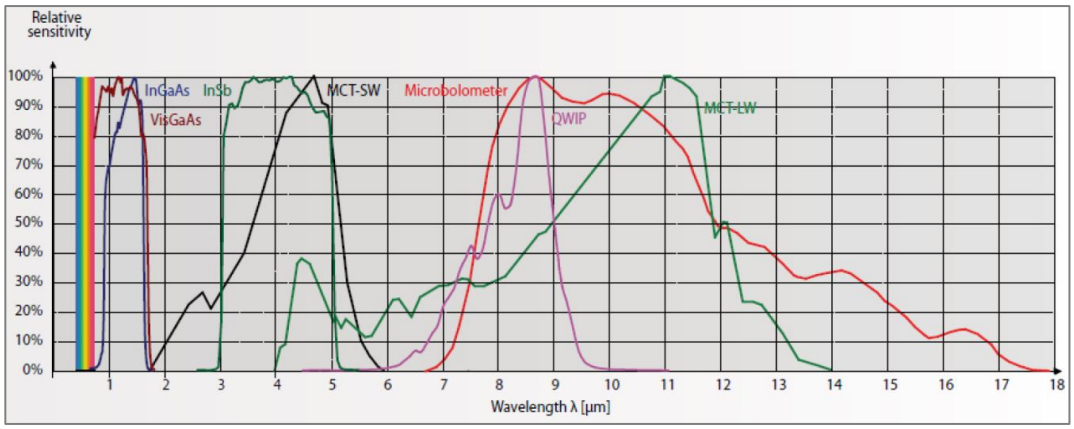

Figure 3.5 Relative response curves for a number of IR cameras [91]

Figure 3.6 shows the radiation intensity with respect to the wavelength [92] of a blackbody at different temperatures. The intensity peaks are at shorter wavelengths when the temperature increases. For TSA, the temperature achieved by the specimens are at around ambient temperature e.g. 20°C, therefore, the emitted radiation is not in the visible range. Therefore, an IR detector is needed to detect the radiation intensity.

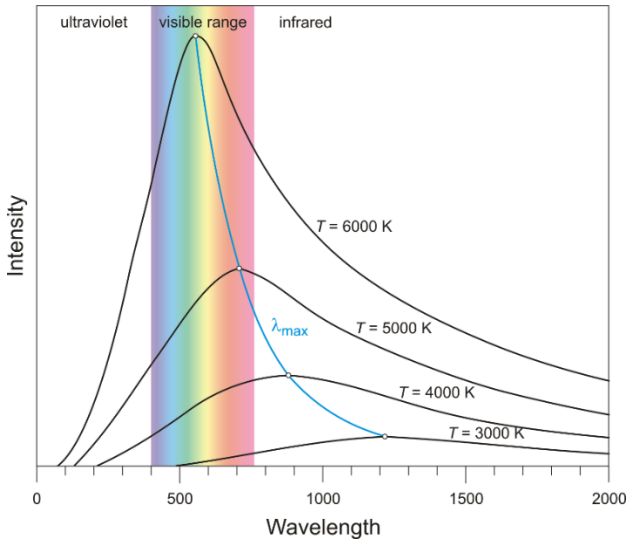

Figure 3.6 Blackbody radiation [92]

To obtain the Stefan-Boltzmann relationship for assessing the radiant emittance (Φ_b), Planck's law is integrated over all wavelengths between zero and infinity.

$$\Phi_b = 2\pi hc^2 \int_0^{\infty} \frac{d\lambda}{\lambda^5 \left(exp^{\frac{hc}{\lambda k_B T}} - 1 \right)} \tag{3.23}$$

By following the steps described in [13], equation (3.23) is simplified by introducing the Stefan-Boltzmann's constant B ($5.67 \cdot 10^{-8}$ J/m^2/s/K^4) over all wavelength (λ_b):

$$\Phi_{\lambda,b} = BT^4 \tag{3.24}$$

However, for a microbolometer (MB) between its working wavelength range (LWIR), i.e. from λ_{min} = 8 µm to λ_{max} = 14 µm, the radiant emittance is:

$$\Phi_{MB} = 2\pi hc^2 \int_{\lambda_{min}}^{\lambda_{max}} \frac{d\lambda}{\lambda^5 \left(exp^{\frac{hc}{\lambda k_B T}} - 1 \right)} \tag{3.25}$$

For an InSb photon detector (PD), it is necessary to obtain the number of photons emitted by a body at a certain temperature (N_{PD}) that is calculated in a similar method. The wavelength range considered is now between λ_{min} = 3 µm and λ_{max} = 8 µm (MWIR – InSb photon detectors).

$$N_{PD} = 2\pi c \int_{\lambda_{min}}^{\lambda_{max}} \frac{d\lambda}{\lambda^4 \left(exp^{\frac{hc}{\lambda k_B T}} - 1 \right)} \tag{3.26}$$

Equations (3.23) to (3.26) consider a black body material, i.e. the incident radiation is totally absorbed and its radiance does not depend on the direction. Nevertheless, real objects do not absorb or emit perfectly, therefore, emissivity is considered, which is the relation between the radiation emitted by the surface of the object and the radiation of a blackbody at the same temperature (Kirchhoff's law [66]).

3.2.2 Photon Detectors

There are different types of photon detectors. The first difference covers the material used in the detector's construction and is broadly divided into intrinsic and extrinsic materials [93]. An intrinsic material considers interband transitions, which are the optical transitions across the band gap from the valence band to the conduction band. It is possible when the photon energy is above the band gap energy. Examples of detectors based on intrinsic materials are lead salt, cadmium sulphide and mercury cadmium selenide. In extrinsic materials, there are additional energy levels introduced by impurities, which provide additional excitation pathways. Examples of extrinsic materials are silicon and germanium doped with arsenic, copper, gold or indium. Therefore, the most common photon detectors are [94-96]:

- Indium Antimonide (InSb): cryogenically cooled via an inbuilt Stirling cooling system, MWIR.
- Indium Gallium Arsenide (InGaAs): cooling system may vary from non-cooled, thermos-electric cooled to cryogenically cooled, capture significant amount of reflected light, SWIR.
- Mercury Cadmium Telluride (HgCdTe): extremely expensive detectors, very non-linear detectors, which make the camera difficult to calibrate and work with, LWIR.
- Super Lattice Structure (SLS): not as sensitive as HgCdTe, but more cost effective and more linear, LWIR.
- Platinum Silicide (PtSi): Schottky-barrier detector, operates at lower temperatures than other photon detectors due to its low quantum efficiency, MWIR.
- Quantum Well Infrared Photodetector (QWIP): relies on electronic intersubband transitions in quantum wells to absorb photons, LWIR.

In general, photon detectors convert the absorbed electromagnetic radiation into a change of the electronic energy distribution in a photovoltaic semiconductor device. A photon detector responds instantaneously when the photons impinge on the detector, and higher frame rates can be achieved that are in the order of hundreds of Hz to kHz. The voltage output allows the photons to be counted

in the form of an analogue signal that is converted to a digital signal using an analogue-to-digital converter (ADC) to create the response output in digital levels (DL). The DL values are converted into temperature by using an in-built radiometric calibration provided by the manufacturer. The calibration procedure involves taking measurements of a blackbody at different known temperatures, and as the detector essentially counts photons, the calibration is dependent on the integration time. The integration time is set by the operator so that the photons are integrated over a predetermined timespan. To extract values of temperature from the photon detector instead of transforming DL to temperature *a posteriori*, a Non-Uniformity Correction (NUC) is performed by using the inbuilt calibration applied to a blackbody plate positioned in front of the lens. The NUC corrects a non-uniformity issue, which is the pixel-by-pixel variations over the detector array that needs to be solved in all camera types. Non-uniformity is noise that depends on time called fixed-pattern noise [97] and is caused by the difference in response of the detector over time.

The characteristics of the two photon detectors used in this project are presented in Table 3.2. Both photon detectors have the possibility to increase the frame rate when sub-windowing, which allows the reduction of pixel rows i.e. less pixels are available, and the frame rate can be increased. It should be noted that the Telops camera, which was newly acquired during the PhD studies, incorporates a different form of calibration, which is independent of integration time and it is not necessary to carry out the NUC. The calibration procedure is described in Appendix A.

Table 3.2 Photon Detectors used in this PhD thesis [98, 99]

Characteristics	**Photon Detector**	
IR Camera	FLIR SC5500	Telops FAST M2k
Detector material	InSb	
Spectral range	2.5 - 5.1 µm	1.5 - 5.4 µm
Pixel dimension	30 µm	25 µm
Cost	~£100,000	
Maximum frame rate at full window	383 Hz	1910 Hz
Frame rate selection	Any value up to 383 Hz	Any value up to 1910 Hz
Reading array	All pixel detectors at the same time	
Integration time	10 - 20,000 µs	0.27 µs to 513 µs
Response time	10 - 20,000 µs	0.27 µs to 513 µs
Sensitivity (NETD)	<20 mK	<25 mK
Resolution	320 x 256 pixels	
Cooling	Yes	
Analogue input	Yes	
Weight	3.8 kg	< 6 kg
Size	310 x 141 x 159 mm	321 x 199 x 176 mm

3.2.3 Standard and Thermal Core Microbolometers

Samuel Langley invented the first uncooled IR sensor, a resistance microbolometer in 1880 which was used in 1914 to detect aircraft and people at long-distances [20]. In 1992, Honeywell developed an uncooled array of thin-film Vanadium Oxide (VOx) for a resistive microbolometer.

Microbolometers are formed by an array of sensing elements that is always exposed to radiation. Each element has an IR radiation absorbing layer (metal or semiconductor) that changes its resistance depending on the amount of absorbed energy. The change in resistance is converted into a voltage that is then converted to a digital signal. The obtained DL is converted into temperature by means of a calibration dependent only on the temperature. Because of the materials used in the construction of a microbolometer, a fixed thermal time constant is associated with the measurement, which is dependent on the sensor material. Therefore, a microbolometer does not instantaneously respond to a temperature change [89, 100] but is a function of the thermal time constant:

$$\frac{ouput(t)}{output(t \to \infty)} = 1 - exp^{-\frac{t}{\tau_{th}}} \tag{3.27}$$

where t is time, and τ_{th} is the thermal time constant.

Figure 3.7 provides a graphical presentation of the response time for 7 and 15 ms time constants, which shows that three times the thermal time constant is required to obtain 95% of the input temperature value and six times the time constant to achieve 99%.

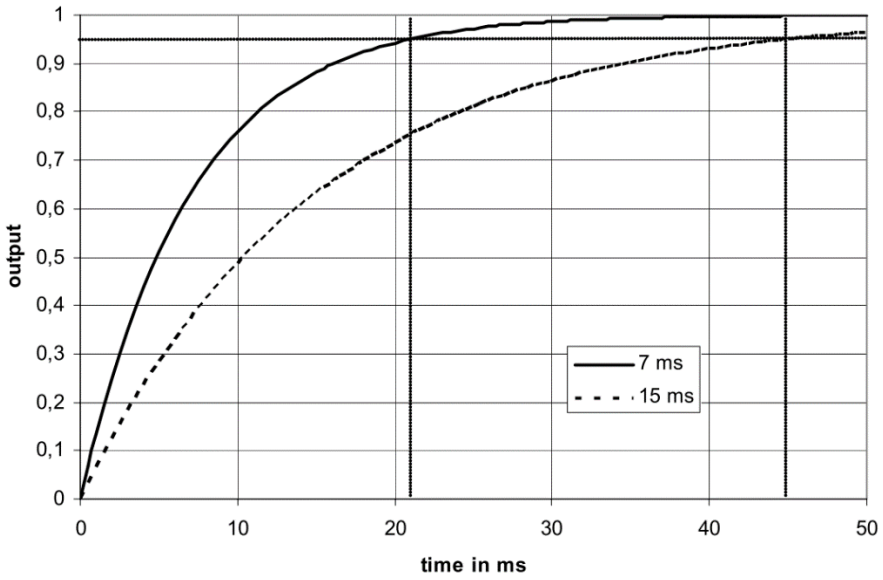

Figure 3.7 Microbolometer time response for 7 and 15 ms time constants [89]

Due to the constant exposure to radiation that constantly changes the microbolometer electrical resistance, measurements of rapid changes in temperature are challenging, such as those occurring as a result of the cyclic loading at relatively high loading frequency in TSA. If the sensor has not had sufficient time to achieve the input temperature, it outputs the current temperature at that time. Hence, the temperature is attenuated, presenting the behaviour of a low-pass filter [21, 100]. A detailed description of the microbolometer performance in the context of TSA is presented in section 5.2.

There have been advances in the IR technology to reduce the size and the weight of uncooled cameras over the last 15 years. FLIR Lepton [101] (non-radiometric), which is a thermal core, has been

available since 2014. It was the size of a golf ball, which by then introduced a significant reduction not only in weight, and size but also in cost of thermal cameras. Since then, it has facilitated developments such as FLIR ONE, which is a smartphone camera attachment, FLIR C2/C3 for inspecting buildings and the FLIR Duo, which was designed for drones. In 2016, FLIR launched Boson [102], a next generation high-performance uncooled thermal camera core, sized between Tau (released in 2010 [103]) and Lepton camera cores. In the case of Boson, it is radiometric, so it can transform digital level to temperature data instead of only providing contrast images in grey scale or RGB (Red Green Blue). Since then, many radiometric thermal cores were available, such as Tau 2, Quark 2, among others. In 2016, FLIR Lepton 3 was also launched [104], which delivers four times the thermal resolution as the previous Lepton generations. In 2018, FLIR Lepton 3.5 radiometric (Figure 3.8) was released [105], being a quantitative microbolometer, and the smallest thermal core available on the market. The development of these thermal cores provides a reduction of more than 10 times the cost of regular uncooled microbolometer cameras, making the IR technology available to a wider public. However, given their recent release, the thermal cores have not yet been used for TSA. Clearly, it would be advantageous to develop thermal cores for TSA, as multiple cameras could be placed in different positions to monitor large structures. Additionally, the significant reduction in cost, means the cameras can be left in-situ and used for continuous monitoring purposes in hazardous and extreme environments. Typical applications could include space, offshore wind turbine systems and nuclear power plants.

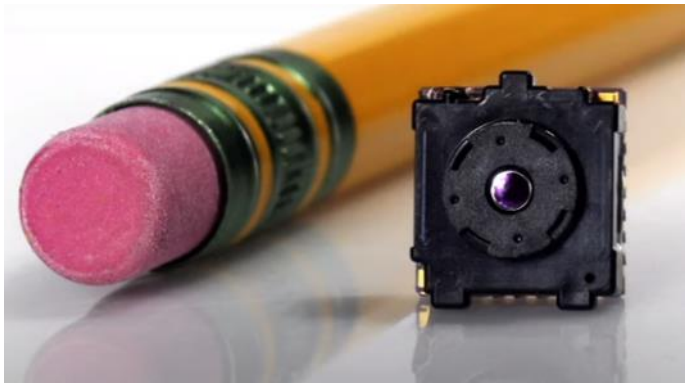

Figure 3.8 FLIR Lepton 3.5 radiometric [105]

The microbolometer maximum frame rate at full frame is lower than for photon detectors and depends on the frequency at which each line of pixels is sampling. All the pixels of a row are absorbing IR radiation at the same time, for this reason, the frame rates that can be selected are dividers of the maximum frame rate, as they are limited by the readout time per pixel row. For example, for the FLIR A655sc microbolometer used in this project (Table 3.3), the maximum readout time is 41.6 µs per row at full frame, considering that there are 480 rows of pixels, the maximum frame rate at full frame is 50 Hz. Hence, the frame rates that can be selected at full window are 50 Hz, 25 Hz, 12.5 Hz, 6.25 Hz and 3.12 Hz, which are divisions of the maximum frame rate of 50 Hz. Therefore, microbolometers need more time to obtain similar results to photon detectors. However,

the setup is much faster as there is no cool-down period required compared to the photon detectors [20]. The NETD of microbolometers is usually higher than photon detectors. For TSA, the post-processing algorithms applied to extract the TSA parameters given in equation (3.6) filter out noise to enable the measurement of the small thermoelastic temperature change.

Table 3.3 Datasheet covering microbolometers used in this PhD thesis [106, 107]

Characteristics	Standard microbolometer	Thermal core microbolometer
IR Camera	FLIR A655sc	FLIR Lepton 3.5 radiometric
Detector material	VOx	VOx
Spectral range	7.5 - 14 µm	8 - 14 µm
Pixel dimension	17 µm	12 µm
Cost	~£10,000	~£500
Maximum frame rate at full window	50 Hz	Limited at 8.7751 Hz
Frame rate selection	50 Hz, 25 Hz, 12.5 Hz, 6.25 Hz, 3.13 Hz	8.7751 Hz
Reading array	Each row of pixels at a time	
Thermal time constant	8 ms - fixed	12 ms
Response time	24 ms (3 x thermal time constant)	36 ms (3 x thermal time constant)
Sensitivity (NETD)	< 30 mK	< 50 mK
Resolution	640 x 480 pixels	160 x 120 pixels
Cooling	No	
Analogue input	No	
Weight	0.9 kg	0.9 g
Size	216 x 73 x 75 mm	10.50 x 12.70 x 7.14 mm

3.2.3.1 Applications of Microbolometers in TSA

Although photon detectors are the most common thermal cameras used in TSA, there are studies that prove the effectiveness of using microbolometers in TSA in metallic and polycarbonate structures [20, 21, 26, 108-110]. It has been demonstrated qualitatively by Rajic et al. in [110] that microbolometers perform well in TSA by testing three wing-attachment bulkheads of aluminium. The microbolometer used was a FLIR A20M, which contains a VOx focal-plane array and has a NETD of 120 mK (one order of magnitude larger than a photon detector NETD). Data from the study was processed using the MiTE software [111] that uses a lock-in approach taking the load signal from the test machine as a reference signal.

To facilitate better signal-to-noise ratio in TSA, it is important to collect a large number of frames. The signal-to-noise ratio is improved as multiple frames are averaged out. It is particularly important in microbolometers to record a large amount of frames as they are noisier detectors than photon detectors. Rajic et al. [110] showed that a microbolometer recording over a time period of 3 minutes at 50 Hz, and obtaining 10,000 frames, demonstrated an improvement in sensitivity scaling with the number of frames acquired. The loading frequency was 0.6 Hz. Rajic and Street [26] tested different uncooled IR detectors (microbolometers) and compared them qualitatively with a photon detector at

different integration times for aluminium alloy tests coupons with a hole at a loading frequency of 5 Hz. It was shown that even though the microbolometers presented higher NETD (by a factor of two or more) compared with the photon detector, the results obtained with the microbolometers outperformed those from the photon detector when 1,500 load cycles or more were recorded with the same number of cycles captured with the photon detector. This can be seen in Figure 3.9 where the coefficient of variation vs the number of cycles is presented for every IR detector studied in the paper [26]. The initial value of the curve should correspond to the NETD of the detector, hence lower NETD's should produce lower coefficient of variation, the results were consistent as the photon detector presents the lower coefficient of variation at the first measurement. The rate of decline in noise is different between photon detector and microbolometer. The trend in microbolometer data is close to log-linear, while it is a tapering rate of decline for a significant part of the photon detector noise. The difference between these two curves (microbolometer and photon detector) leads to intersections between them. Therefore, it can be seen how TSA can evolve to a more cost-effective technique by replacing expensive photon detectors with low-cost microbolometers.

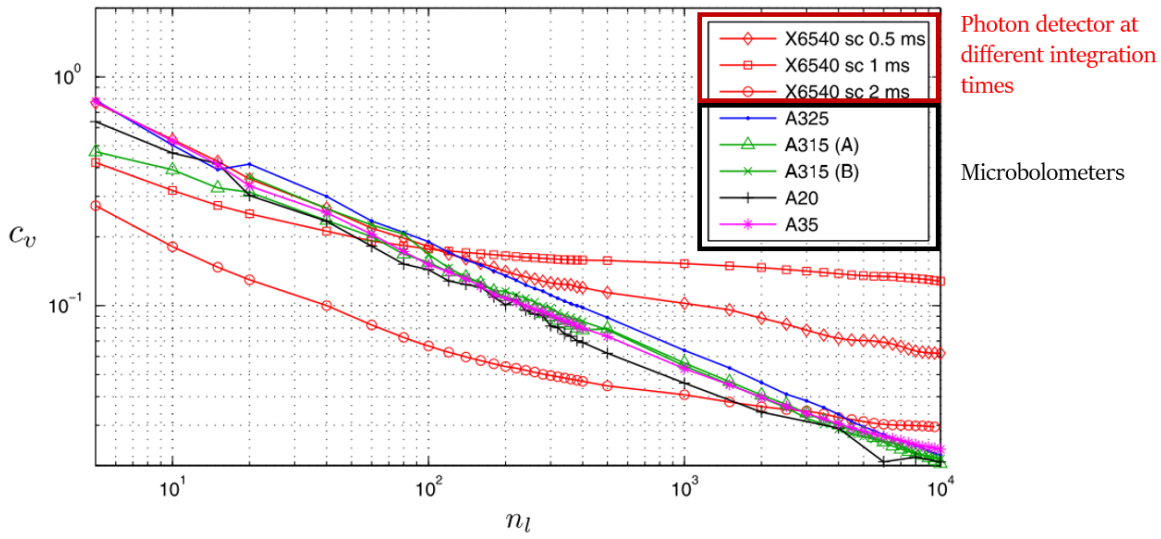

Figure 3.9 Coefficient of variation vs number of loading cycles for different uncooled and cooled detectors [26]

Despite the limitation in thermal time constant, there have been studies using microbolometers for TSA to calculate stress intensity factor and crack growth. As an example, Vieira et al. [109] used TSA to calculate the stress intensity factor and crack growth rate on polycarbonate materials. The experiments were performed using a polycarbonate specimen with a pre-crack and a microbolometer FLIR A655sc, which is the same used in this PhD project. The procedure to perform TSA was different from the one used in this work. In this case, a calibration technique was used, where the amplitude correction is performed by applying a calibration constant and taking measurements in digital level instead of temperature [112]. The digital level is the thermoelastic signal that is uncalibrated in terms of temperature. To calibrate the TSA technique in terms of stress, the load

introduced in the machine and the specimen dimensions are known. The thermoelastic equation can be expressed as:

$$A \cdot DL = \Delta\sigma_1 + \Delta\sigma_2 \tag{3.28}$$

where A is the calibration constant, DL is the thermoelastic signal (uncalibrated) in digital level and $\Delta\sigma$ is the stress change in the principal directions 1 and 2.

The calibration constant, A, depends on the microbolometer properties, loading frequency, specimen surface temperature and the specimen properties i.e. thermoelastic constant and emissivity. Therefore, the calibration constant can be calculated by knowing the stress applied to the specimen and the uncalibrated thermoelastic signal from the camera after the lock-in process, because it is directly related to temperature. Once the calibration constant is known, it can be applied to the uncalibrated thermoelastic signal to obtain the stress field of the specimen tested. However, it is shown that this calibration is time extensive, as it is required to be performed for every testing day, sample type, surface preparation, and loading frequency.

To summarise, microbolometers are low-cost IR cameras that will make TSA an affordable technique facilitating its use in industry. These cameras have been shown to work well for conducting TSA experiments on metallic structures and polycarbonate materials containing cracks. Nevertheless, the use of microbolometers for TSA applications needs to be confirmed for the inspection of composite material structures to understand if they can perform as well as photon detectors. The difference in response between these IR cameras needs to be understood, in particular the low-pass filter behaviour due to the time constant affecting the temperature readout on microbolometers under changing temperatures generated by dynamic cyclic loading.

3.3 Lock-in Digital Image Correlation

3.3.1 Digital Image Correlation

Digital Image Correlation (DIC) [14] consists of recording two or more images of a loaded specimen and extracting the displacement field by tracking the movement of a speckle pattern (Figure 3.10) applied at the surface of the sample. The image is divided into smaller overlapping subsets. The patterns contained within each subset are tracked to obtain the displacement fields. From the displacement fields, the strain fields are derived. The first image (reference image), taken at zero applied load, is compared with the rest of the images when the specimen is loaded in tension or compression. Therefore, the strain field of the sample is determined.

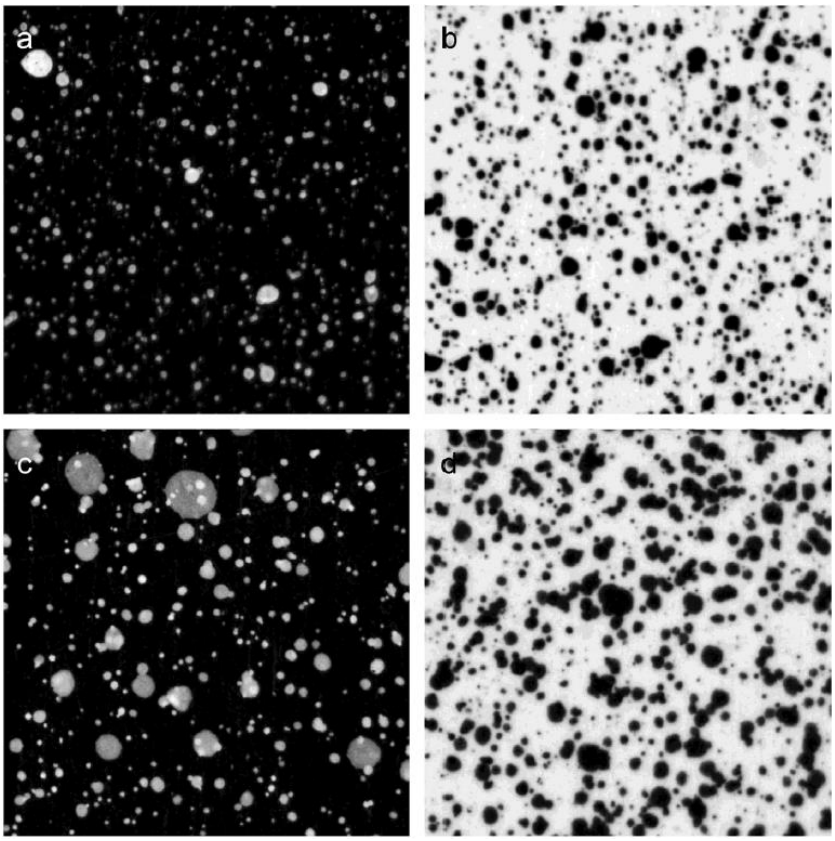

Figure 3.10 Examples of speckle patterns: (a) airbrush - black background, (b) airbrush - white background, (c) spray paint - black background and (d) spray paint - white background [113]

For in-plane displacements, 2D-DIC (Figure 3.11), the movement of the speckles results from the comparison of two images, f and g, at each subset (pixel per pixel region), x, recorded at times t and $t + \Delta t$. Photos f and g are matrices of grey-level [14] values for each pixel. Considering the vector of displacement of the pixel $u(x)$, the local grey-level conservation is:

$$f(x) = g[x + u(x)] \tag{3.29}$$

To measure an adequate $u(x)$ in the region of interest (ROI), the global residual is minimised [14]:

$$\mathcal{T}_{DIC} = \int_{ROI} (f(x) - g[x - u(x)])^2 \, dx \tag{3.30}$$

When more than two images are analysed, subsequent images are referenced against the first image. The following images taken are compared with the reference image to obtain the displacement field relative to the reference image and this process consists of maximizing the correlation product:

$$(f * g)(u) = \int_{ROI} f(x) g(x + u) \, dx \tag{3.31}$$

that can be performed in the Fourier space:

$$f * g = \sqrt{P}\, FFT^{-1}\left[\overline{FFT[f]}\, FFT[g]\right] \tag{3.32}$$

where $\overline{FFT[f]}$ is the conjugate and P is the number of pixels. The ROI size is determined by the user for the pixel per pixel region required to study, it is also called the subset size. Moreover, the shift between two consecutive ROI's is also selected by the user and it is typically chosen as 1/3 of the subset size. The analysis is then performed for each ROI independently. A first value of in-plane displacement correction Δu is obtained from the first FFT but an additional cross-correlation is performed by using the shift-modulation property of the FFT. This procedure is performed to check that the maximum of the interpolated correlation function increases with the number of iterations, otherwise the process is stopped.

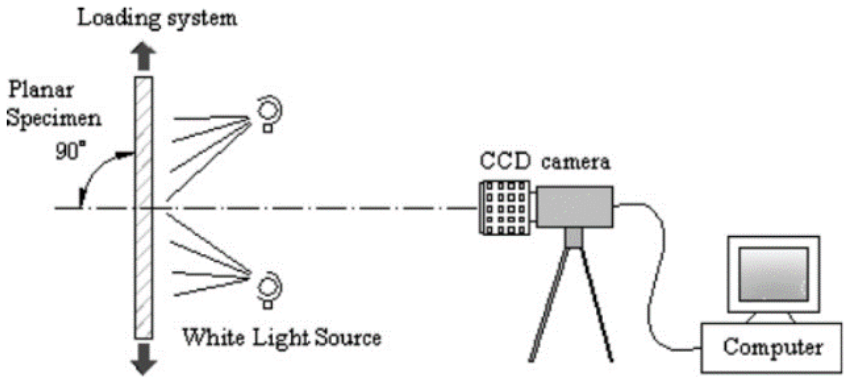

Figure 3.11 2D DIC set up [114]

In 3D or stereo DIC (Figure 3.12), two cameras are required to take into account the out-of-plane displacements. Therefore, from two images taken at two different angles of the same sample, it is possible to detect the out-of-plane displacements and to compensate for in-plane strain measurements caused by artificial scaling of the image as it moves out-of-plane. The transformations between the camera on the left and the camera on the right are determined from the calibration state where a calibration plate (Figure 3.13) of known surface pattern and geometry is used.

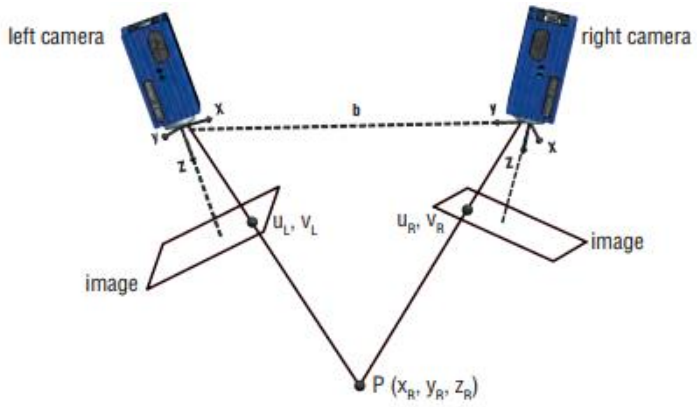

Figure 3.12 Stereo or 3D DIC [115]

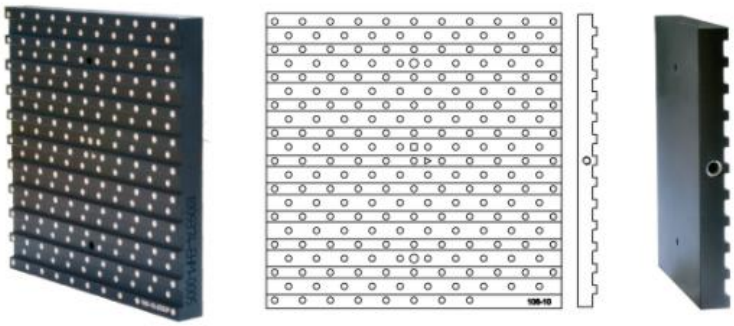

Figure 3.13 Calibration plate example [116]

DIC has been shown to be successful in the detection of damage in composite materials in [117-119]. A 2D braided SiC/SiC composite tube loaded in tension has been studied in [117] to obtain the displacement field. Cracks have been detected and it has been seen that they open normal to the direction of the load. The cracking scenario observed in the experiments matches with the mechanisms considered for these materials. Del Rey Castillo et al. [118] applied DIC to measure strains and displacements in FRP composites used in civil infrastructure. DIC allowed them to analyse strain fields of a complex geometry (FRP anchors) where the use of strain gauges would have been challenging. McKinley et al. [119] studied the effect of weathering on adhesive bonds for wood composites with DIC, showing that there was no significant change in the failure loads after weathering.

When it comes to detecting localised damage, it is important to use higher magnification with DIC. A study has been performed using DIC at different field of views (FOVs) by applying a pattern that is suitable for DIC at low and high magnification [120]. DIC at higher magnification provides a better spatial resolution and strain accuracy measurement for localised strain concentrations in comparison with low magnification DIC. The trade off to consider is that at higher magnification, there is a smaller FOV. One approach to maximise the efficiency of the technique is to use low resolution DIC to measure a general strain response of a structure over a wider field of view, and identify areas of concern, which can be studied in detail by increasing the resolution on that specific area without the need to repaint the speckle pattern. This type of speckle pattern would be useful to inspect large structures as there may be regions that would require a higher magnification. Bomarito et al. [120] studied the inclusion of local greyscale biases in the pattern by applying it to numerical and physical experiments at different contrasts showing a smaller error at 0.5 mean greyscale. In Figure 3.14, an example of the multiscale pattern applied on an aluminium specimen with a hole is shown. It can be seen that the high magnification of DIC measurements has a better resolution to accurately measure the deformation around the hole than the low magnification, which smears the deformation. This kind of multiscale pattern would be interesting to be applied to inspect large structures and being able to change the FOV without the need of changing the surface treatment. The general strain response of the structure can be seen at a larger FOV (low magnification) and more detailed

information on regions of strain concentrations can be analysed on a smaller FOV (high magnification).

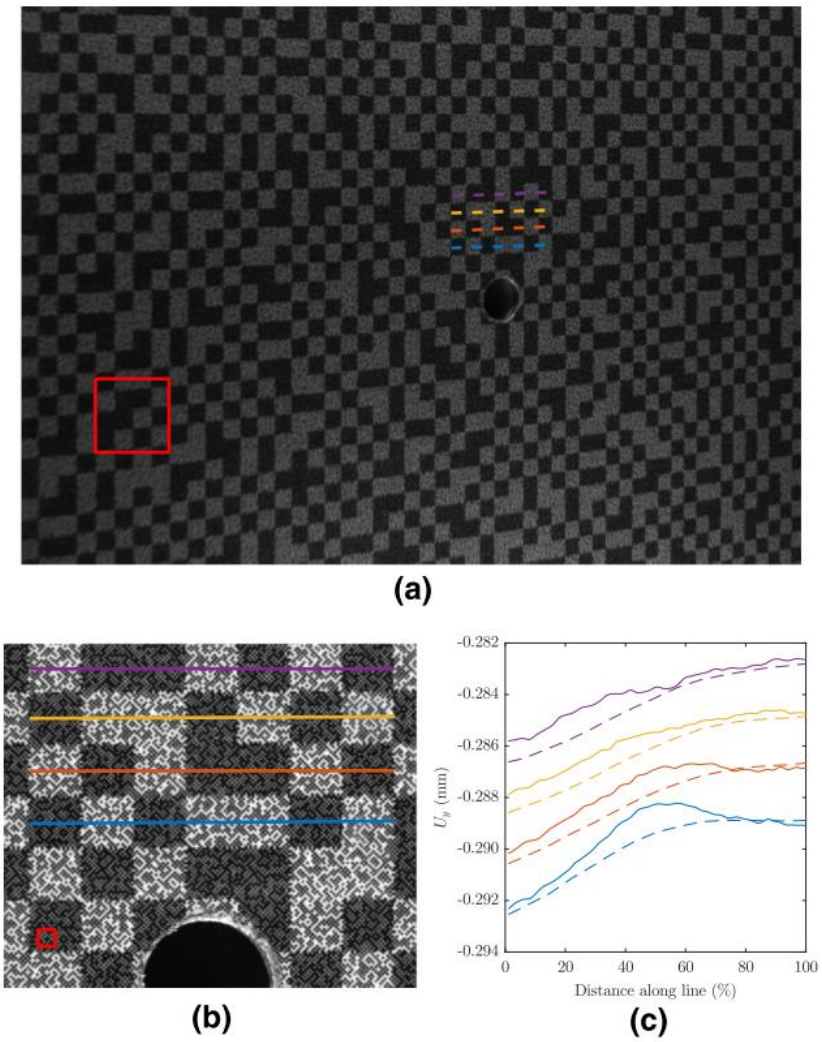

Figure 3.14 Pattern applied in an aluminium sample for low magnification **(a)** and high magnification **(b)** and a comparison of the cross-sections shown in (a) and (b) of the DIC displacement fields under load **(c)** [120]

3.3.2 Lock-in Digital Image Correlation

Dynamic loading such as cyclic loading usually requires high-speed cameras to capture strain information for DIC or complex camera triggering to capture peak-to-peak change in strains during a loading cycle. One simpler approach that has been proposed by Fruehmann et al. [22] is to apply a lock-in DIC (LIDIC) process, enabling inexpensive white light cameras with relatively low frame rates (<10 Hz) to capture peak-to-peak strain information on cyclic loaded components, which would lead to undersampled data. The approach was demonstrated by capturing many images over a long time period. By applying LIDIC, it is possible to extract the change in strain information without the need of synchronising the images to the maximum and minimum loads in the cycle. The lock-in algorithm used for DIC data is the same process as the one used in TSA and described in section 3.1.3.1. As the data is undersampled the recording does not follow the cyclic load signal. But as the

lock-in is performed at an apparent frequency that is lower than the cyclic frequency, more data is needed and therefore the images must be recorded over a longer period of time, so that several cycles at the apparent frequency are analysed. To apply the lock-in amplifier to DIC, first the displacement and then the strain fields with respect to the first image (mean load image) are obtained for each ROI as a function of time, then the lock-in algorithm extracts the amplitude (strain change: $\Delta\varepsilon$) and phase maps over the component. The frame rate and loading frequency selected do not need to fulfil the Nyquist-Shannon criterion [22, 83], which is that the frame rate must be greater than two times the loading frequency, to apply the lock-in amplifier.

In Figure 3.15, an example of under-sampled signal is shown. The actual signal is the signal from the test machine at which the sample is loaded and has a high frequency (7.1 Hz), the crosses are the images taken with the white light cameras and they are represented with a low frequency (2 Hz) which gives a discrete signal. The sampling points coincide with a 0.9 Hz signal. Therefore, the lock-in algorithm is applied by assuming an apparent frequency of 0.9 Hz, so the reference signal for undersampled data is a signal at 0.9 Hz, not the loading frequency extracted from the test machine.

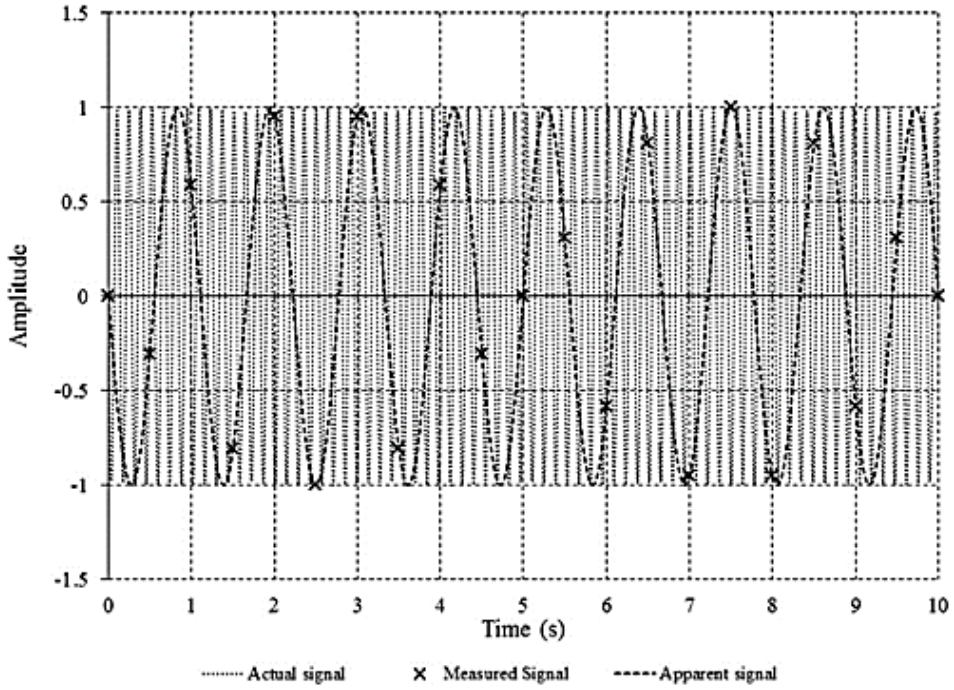

Figure 3.15 Under-sampled signal example [22]

Fruehmann et al. [22] tested LIDIC using an aluminium Brazilian disc in diametric compression at different loading frequencies greater than the frame rate of the camera and accurate strain fields were obtained. The LIDIC strains were verified by the closed form solution for the stresses of the Brazilian disc [28] transformed to strains knowing the elastic properties. This technique was also used in [121] and [25] to inspect damaged cross-ply CFRP specimens and a CFRP corner of a wing spar, respectively, both using TSA and LIDIC.

3.4 Integration of Infrared Images and DIC

An objective of this project is to combine TSA and DIC to construct a constitutive parameter that would provide a measurement of the structural state. Therefore, a review of the literature has been done to identify the advances in IR images and DIC integration on metallic and composite components.

Cholewa et al. [122] combined IR thermography and stereo-DIC to measure spatial and temporal fields of temperatures and displacements. The technique has been called IR Thermography and Digital Image Correlation (TDIC). The IR cameras were calibrated using the DIC system and a calibration plate with laser imprinted circles, which were heated at about 40°C, provided a high emissivity contrast for the IR images. TDIC has been applied to sandwich composite panels under compression load and exposed to heat on one side. It allowed the identification of transient events during the tests, which would not have been detected with the use of only one experimental method. The transient events include blister formation and growth, and out-of-plane deflections. This methodology was demonstrated to be applicable to different scale components from 50 to 1000 mm.

Wang et al. [24] used the displacement field extracted from DIC to motion compensate the TSA data to improve the accuracy of TSA when using high magnification imaging equipment. The methodology was validated by comparing the experiments and the finite element model on an aluminium sample with a circular hole at the centre loaded in tension. Additionally, it was applied to a double cantilever beam sandwich specimen to demonstrate the application on complex and discontinuous motion produced by the debonding of the specimen face sheet.

The speckle patterns used in [122] and [24] provide contrast on the white light spectrum, but have a uniform emissivity on the IR spectrum of the IR cameras used. Therefore, the speckle pattern does not have an effect on the IR images.

Chen et al. [18] applied LIDIC and TSA techniques to monitor crack growth in welded and non-welded T-joints. The motion compensation technique used in this work is the same as in [24]. The stress intensity factors (SIF) of mode I and mode II have been calculated from both experimental methods and compared with an extended Finite Element Model. The SIF from LIDIC and TSA agree between them, as well as with the theoretical value. However, the SIF obtained with the Finite Element Model, which is based on the linear region of the Paris' law, are larger than the experimental results.

Battams and Dulieu-Barton [121] used DIC and TSA techniques simultaneously to track damage progression on CFRP composites under fatigue loading. DIC can provide shear strains and capture shear damage, and TSA can capture subsurface damage due to non-adiabatic behaviours. Therefore, both techniques are combined to detect a greater number of damage features that would not be possible to obtain by using a single methodology. DIC images were captured at the points of

maximum and minimum load of the cycle. Transverse cracking, longitudinal splitting and delaminations and their evolution were identified on TSA and DIC data sets, which were confirmed on X-ray CT-scans after the experiments.

TSA and LIDIC were applied by Bull et al. [25] to study the damage progression of a wrinkle defect in an aerospace component demonstrating the capabilities of both techniques in complex structures. Both techniques showed delaminations induced by the subsurface wrinkle and its surroundings that was further analysed by X-ray CT-scans.

There are studies where DIC and TSA have been used simultaneously [23, 123]. The damage of an adhesively bonded composite double butt strap joint was analysed by applying TSA and DIC to obtain the stress and strain fields respectively [23]. The results of combining both techniques showed good agreement, validating these experimental methods. In [123] the localised through thickness load transfer and damage initiation of the double butt strap joint was performed by applying DIC at a mesoscopic scale, which clearly showed the damage initiation and its growth.

It can be seen that several work on using DIC and TSA simultaneously has been done. The literature has focused on using both techniques complementary to validate them, and to apply motion compensation from DIC data to TSA. However, further development on the integration of both techniques is required so that a quantitative parameter can be extracted. The constitutive parameter would provide information on the sample stiffness. Additionally, the use of DIC and TSA will allow further understanding on the thermoelastic response of laminated composites, as DIC will provide an independent measurement of the strains without any influence of heat transfer, which can be used to calculate the thermoelastic response considering different hypotheses. The DIC calculated thermoelastic response will be compared with the TSA measured thermoelastic response.

3.5 Summary

It has been seen that most of the NDE techniques [7] inform of the presence of a defect and damage on a structure, but most NDE techniques are unable to characterise defects and damage in terms of stress and strain, or how they influence the structure when loaded. LIDIC and TSA are two NDE methods that are capable of extracting the strain and stress fields (data-rich information) on the surface of the sample. Therefore, the defect or damage are characterised and their combination in a strain based NDE methodology would provide quantitatively the state of the structures stiffness due to the combination of the strain and stress fields.

It has been seen that there is a range of IR cameras available in the market at different costs from ~£500 (microbolometer thermal cores) to ~£100k (photon detectors) and with diverse performances. Additionally, different algorithms can be used to post-process temperature data in TSA. Therefore, Chapter 4 presents the analysis of the advantages and limitations of the IR microbolometers presented

in this section as well as TSA algorithms performance using a Brazilian disc [28] with closed form solution for the stresses.

Regarding the TSA technique, it was seen that it is mainly applied by using the expensive IR photon detectors and that the application with microbolometers is currently under development in this PhD thesis. There are examples [20, 21, 109, 110] of applications showing that microbolometers can be applied for TSA tests, but calibration is needed. Rajic and Rowlands [26] applied calibration, considering that the microbolometer acts as a low-pass filter, prior to the TSA process and to high signal-to-noise ratio data. Additionally, Vieira et al. [109] applied another calibration technique considering the digital level [112] of the microbolometer that needed a known stress to be applied to the structure. This technique works well for coupons, but it is complex for the application of TSA to large structures. Therefore, there is need for a faster processing, low signal-to-noise ratios, and no dependency on previous knowledge of the structure and of the structure materials. Study of different variables affecting the thermoelastic response measured with microbolometers and a developed calibration technique is shown in Chapter 5.

The development of DIC to be applied in cyclic loading tests opens the possibility to study the thermoelastic response obtained from TSA by using an independent measure of the strain. The same post-processing algorithm can be used to obtain the peak-to-peak strain from DIC and the thermoelastic response from TSA; the least-squares algorithm was selected i.e. least-squares DIC (LSDIC). Therefore, the purpose of Chapter 6 is to understand the nature of the thermoelastic response by using the full-field LSDIC to calculate the thermoelastic response from measured strains (independent of heat transfer) and compare it with the thermoelastic response measured with TSA to understand the influence of the resin-rich layer, the orthotropic surface ply and the global laminate behaviour.

Previous work on integrating TSA and LIDIC to study damage in composites has focused on coupon level tests. However, there is a need to understand the behaviour on large structures that exhibit complex loading configurations and multiple materials. One example is the loading configuration in a wind turbine T-joint containing wood, resin-rich areas, and glass fibre with complex stress/strain interactions. Additionally, industry is relying more on models to simulate the behaviour of a structure to reduce the number of required tests that are typically expensive and time consuming to perform [25]. This has created the need of detailed experimental data to validate models that can be provided through experiments such as DIC and TSA to extract data-rich strain and stress fields respectively of a large structure. Chapter 7 presents initial work on the extraction of strain and stress fields from DIC and TSA that can be used to validate FEA (Finite Element Analysis) models.

Chapter 4. Microbolometer Infrared Cameras and Algorithms Comparison for TSA Using a Brazilian Disc

4.1 Introduction

The contents of this chapter are the results of a close collaboration with Dr Cédric Devivier, who developed the Matlab scripts for post-processing of the TSA and the camera model simulations, based on work presented in [124]. The author of the thesis carried out all the experimental work described in the chapter and the analysis of the results.

As a first step in understanding the capabilities of microbolometers applied to TSA, the work described in the chapter focused on a comparison between the FLIR A655sc microbolometer [106] and FLIR Lepton 3.5 radiometric microbolometer thermal core [107]. A summary of the IR cameras specifications is provided in Table 3.3. A camera simulation is set up similar to that given in [124] using a Brazilian disc instead of the single edge notched specimen. The closed form solution for the Brazilian disc [28] is well known and has been used widely in calibration studies for TSA. In brief, the camera model is obtained collecting black body data at different temperatures to obtain expressions that define the noise content produced by the camera and define its responsivity (i.e. it is the linear relationship between the emission and the outputted image in DL). The camera model allows a simulation of the experiments to be created and, hence, provides the basis for comparison between a processed image based on theory and a nominally identical image obtained experimentally.

The aim of this chapter is to study the suitability of different microbolometer cameras and algorithms for TSA. Over the years, there has been a massive development on the technology of IR cameras, therefore, this chapter assesses two microbolometer cameras of different cost range for TSA. Additionally, there are various algorithms that can be used to extract T_0, ΔT and ϕ from the cyclic temperature signal, although traditionally, the lock-in process has been the most used for TSA. Rajic and Street [26] studied the performance of various VOx microbolometers but of similar characteristics (frame rate, response time) in comparison with a photon detector demonstrating similar results among them and in particular with the photon detector. Nevertheless, before further application of microbolometers to TSA, a quantitative understanding of their performance for TSA is required particularly in respect of recent ultralow cost IR camera developments, such as the Lepton thermal core.

The chapter includes an overview of the simulation approach to produce a ‘model’ of each camera, which provides the basis for the performance comparison between each camera. The image processing procedure to extract the three TSA parameters from equation (3.6) is described. Finally, experimental results from the Brazilian disc are obtained for the two cameras and integrated with the simulated results to enable the derivation of comparable camera performance parameters for the application of TSA.

The work presents a new procedure to evaluate the performance of different IR cameras for TSA by incorporating the inherent noise and sensitivity of the IR camera to produce a camera model with identical spatial resolution to that of the actual detector array for each camera. By comparing the model data with experimental data, a new means of evaluating performance is presented, that establishes the accuracy and precision of the TSA parameters derived from IR images. Furthermore, for the first time, it is shown that it is possible to obtain TSA measurements from a miniaturised thermal core, which will enable the application of TSA to large structural tests by deploying multiple thermal cores in regions of interest around the structure.

4.2 Overview of Camera Model

The procedure for producing the camera model [124] is such that it can be adapted to operate with information extracted from images using a variety of cameras. To fully describe the procedure given in [124], it is necessary to visualise how an IR camera processes the emittance from an object at a given temperature, T, to a logic signal displayed as an image as shown in the schematic diagram in Figure 4.1. The heat flux or radiance is passed through the camera lens system and impinges on the IR detector array, a voltage signal reads out from the sensor, which is converted to a digital signal, by an analogue to digital converter (ADC), which is then captured by the frame grabber to give an image on the computer display. It is important to note that the camera model developed here is represented by the dotted line in Figure 4.1 and includes the lens. Each of the sensors in the detector array responds to the radiance; in the case of the microbolometer a change of resistance occurs, the photon detector counts the photons that cross the band gap in the semi-conductor. It is here that the sensitivity, or ‘responsivity’, of the camera system is determined. The analogue readout is then converted to a digital signal and, hence, the responsivity determined for the camera model also includes the bit depth of the ADC. The ADC also rounds the value of the voltage output to the nearest integer value. At each stage in the process, ‘noise’ is introduced from the detector array, during the readout and by the ADC, so the camera model also includes the system noise.

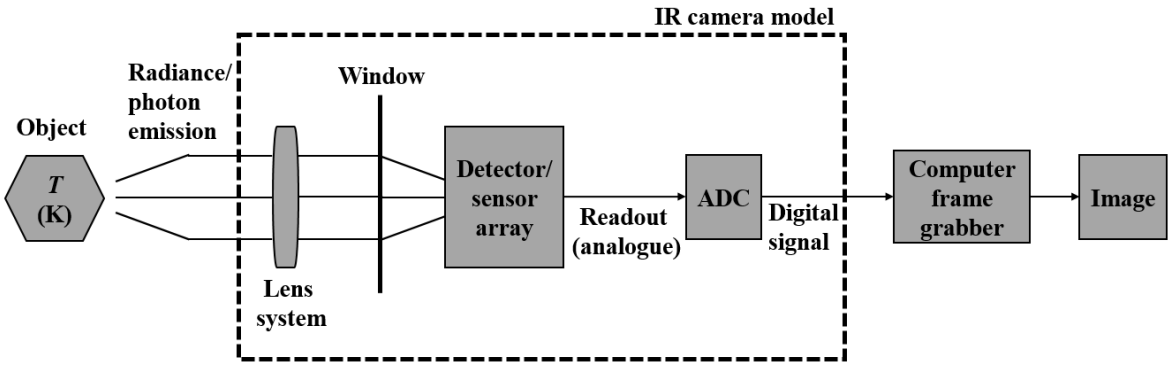

Figure 4.1 Implementation of the camera model

To implement the camera model for the two camera systems used in the chapter, a procedure adapted from [124] was followed. Images were collected from a temperature controlled blackbody over a temperature range of 20 to 70 °C at different frame rates as summarised in Table 4.1.

Table 4.1 Matrix of experiments performed to obtain the camera performance

IR camera	**Frame rate (Hz)**	**Blackbody temperature (°C)**
Microbolometer FLIR A655sc	50, 25, 12.5, 6.25	20, 30, 40, 50, 60, 70
Microbolometer thermal core FLIR Lepton 3.5 radiometric	8.7751	

To obtain the responsivity for each camera system, the following expression was used for the microbolometers:

$$DL = a_{\mu b}\, R + b_{\mu b} \tag{4.1}$$

where DL is the output digital levels, R the radiance impinging on the sensor (W sr^{-1} m^{-2}), $a_{\mu b}$ the responsivity (DL W^{-1} sr m^2), and $b_{\mu b}$ the offset (DL).

Noise is then added to the map of DLs using the following equation:

$$NL = c\, DL + d \tag{4.2}$$

where NL the noise level (DL), c the noise amplification (-) and d the intrinsic noise (DL).

The noise level and responsivity are determined by fitting equations (4.1) and (4.2) to the experimental data extracted from the blackbody images. The values obtained for the two cameras used in the present work are reported in Table 4.2.

In the model, the radiance (R) is scaled in the digital domain using equation (4.1) after which the noise is added. These perturbed DLs are rounded to the nearest integer according to the camera's bit depth or clipped within the camera's bit depth to give the algorithm for the model.

Table 4.2 Summary of the performance for the different cameras

Camera		**FLIR A655sc**	**FLIR Lepton 3.5 radiometric**
Sensitivity	$a_{\mu b}$	168.75	59.58
	$b_{\mu b}$	4230.4	141.66
Noise	c	0	0
	d	17.99	4.82

4.3 Simulation of the Thermoelastic Response

To simulate the thermoelastic response using the camera models, it is necessary to generate a temperature input that is representative of a typical experiment. Hence, the ΔT field generated the Brazilian disc [28] is used as the starting point for the simulation. Figure 4.2 (a) shows the nomenclature for the Brazilian disc, so the stresses can be expressed in a Cartesian coordinate system as follows:

$$\sigma_{xx} = \frac{F}{\pi t R} - \frac{2F}{\pi t}\frac{(R-y)x^2}{[x^2+(R-y)^2]^2} - \frac{2F}{\pi t}\frac{(R+y)x^2}{[x^2+(R+y)^2]^2} \tag{4.3}$$

$$\sigma_{yy} = \frac{F}{\pi t R} - \frac{2F}{\pi t}\frac{(R-y)^3}{[x^2+(R-y)^2]^2} - \frac{2F}{\pi t}.\frac{(R+y)^3}{[x^2+(R+y)^2]^2} \tag{4.4}$$

$$\sigma_{xy} = \frac{2F}{\pi t}\frac{(R-y)^2 x}{[x^2+(R-y)^2]^2} - \frac{2F}{\pi t}\frac{(R+y)^2 x}{[x^2+(R+y)^2]^2} \tag{4.5}$$

where F is the peak-to-peak applied load, t the thickness of the disk, and R the radius of the disc.

Equations (4.3) - (4.5) are expressed in Cartesian coordinates as the data in an infrared image is presented on an x - y grid corresponding to the projected area of each sensor in the detector array on the object under investigation. It should also be noted that equation (3.3) provides the sum of principal stresses, which is an invariant, so that $\Delta(\sigma_1 + \sigma_2) = \Delta(\sigma_{xx} + \sigma_{yy})$. As the principal stress directions are being considered to generate ΔT, it is necessary only to add equations (4.3) and (4.4).

Throughout the experimental work, a disc made from aluminium alloy (Al 6081 T6) of diameter 80 mm and 6 mm in thickness was used. To simulate the ΔT from the disc, the first step in the process is to establish the image pixel size at the stand-off distance of the camera in each experiment as given in Table 3.3 and Table 4.3. If the diameter of the disc is known, then it is a straightforward matter to establish the pixel size and generate an x - y grid in an identical form to that of the image that is captured experimentally. This is an important step in the simulation procedure as it enables the

simulated and experimental images to be integrated and quantitatively compared at an identical resolution.

As an example, Figure 4.2 (b) and (c) present the coordinates stresses at the spatial resolution of the the FLIR A655sc camera for the disc with a load range of $F = 4.5$ kN; similar data were generated for the Lepton 3.5 camera.

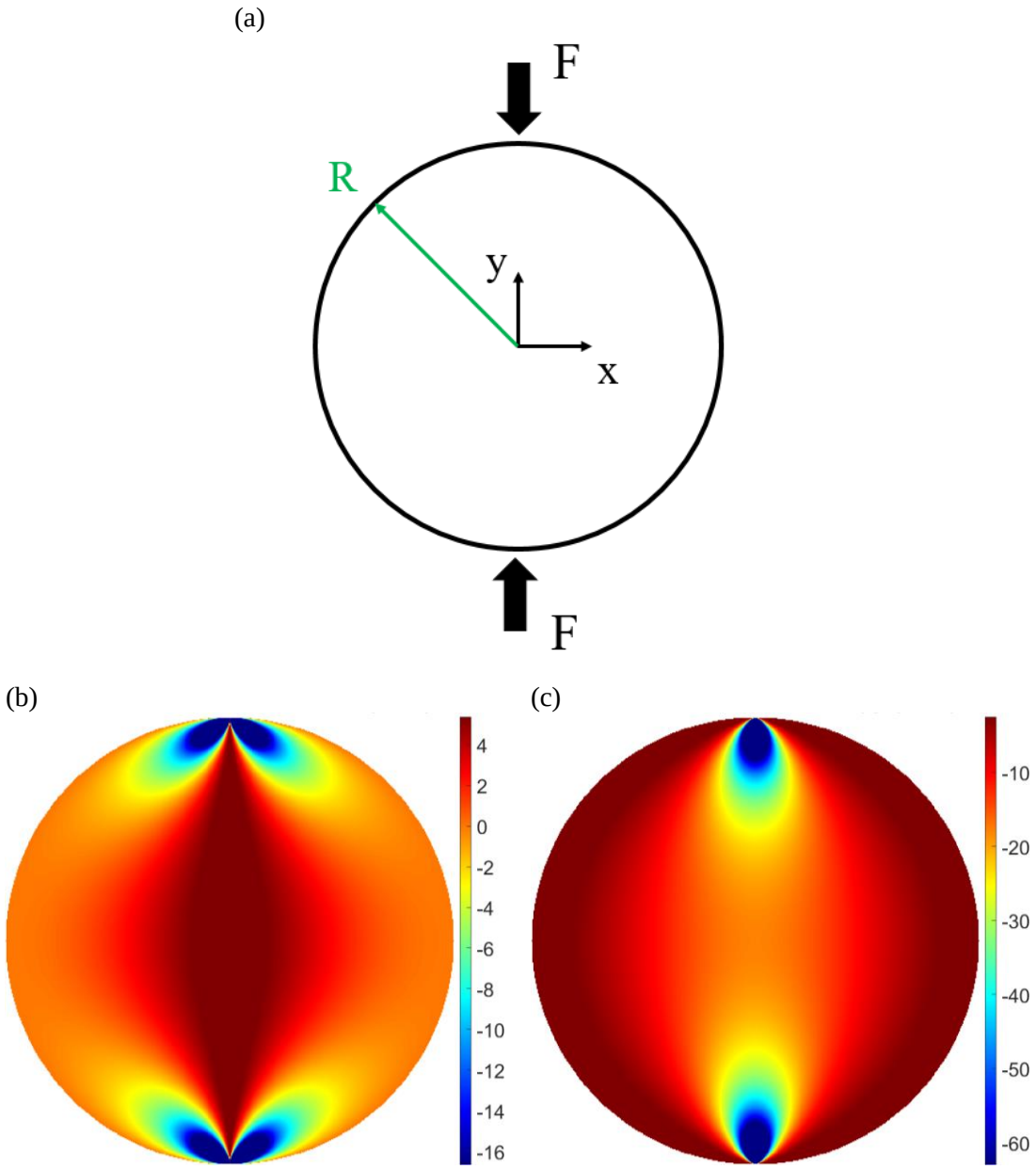

Figure 4.2 (a) Brazilian disc nomenclature and coordinate stress fields (MPa): (b) σ_{xx}, and (c) σ_{yy}

To convert the stresses to ΔT, it is necessary to multiply the stresses by the thermoelastic constant, K, which was determined experimentally as $9.51 \cdot 10^{-6}$ MPa^{-1}. To generate ΔT across the disc, it is necessary to introduce a base temperature, T_b, because laboratory temperatures vary. Therefore, to make meaningful comparison, it is essential that T_b is the actual temperature of the specimen. Hence, T_b was obtained directly by taking the spatial average of a 40 x 40 pixel region at the centre of the

disc and using the manufacturer's inbuilt calibration to obtain a value in Kelvin, so that the following expression relating the stresses calculated from equations (4.3) and (4.4) to ΔT was established:

$$\Delta T^t(x,y) = -K\,T_b\left(\sigma_{xx}+\sigma_{yy}\right) \tag{4.6}$$

where the superscript t indicates a 'theoretical' value.

Figure 4.3 (a) shows $\Delta T^t(x,y)$, i.e. the spatially varying thermoelastic temperature change field derived from equation (4.6) for the FLIR A655sc camera using the stress fields given in Figure 4.2. Now it is necessary to derive a theoretical temperature field, $T^t(x,y,t)$, representing the temperature variations in the cyclically loaded disc, similar to equation (3.6), but in the form:

$$T^t(x,y,t) = T_b + \Delta T^t(x,y)\cos(2\pi f_0 t) \tag{4.7}$$

The next stage is to create a cyclic reference signal, L, from the test machine load cell to extract the TSA variables using the image processing techniques described in the previous chapter (section 3.1.3). L is synchronised with T^t at different time steps, determined by the camera frame rate as follows:

$$L(t) = L_0 - \frac{F}{2}\cos(2\pi f_0 t) \tag{4.8}$$

where L_0 is the applied mean load.

Now $T^t(x,y,t)$ can be generated as simulated image frames at different times; an example is shown in Figure 4.3 (b) to (d) for the disc shown in Figure 4.3 (a) at loading frequency of 5.1 Hz with $L_0 = -5$ kN.

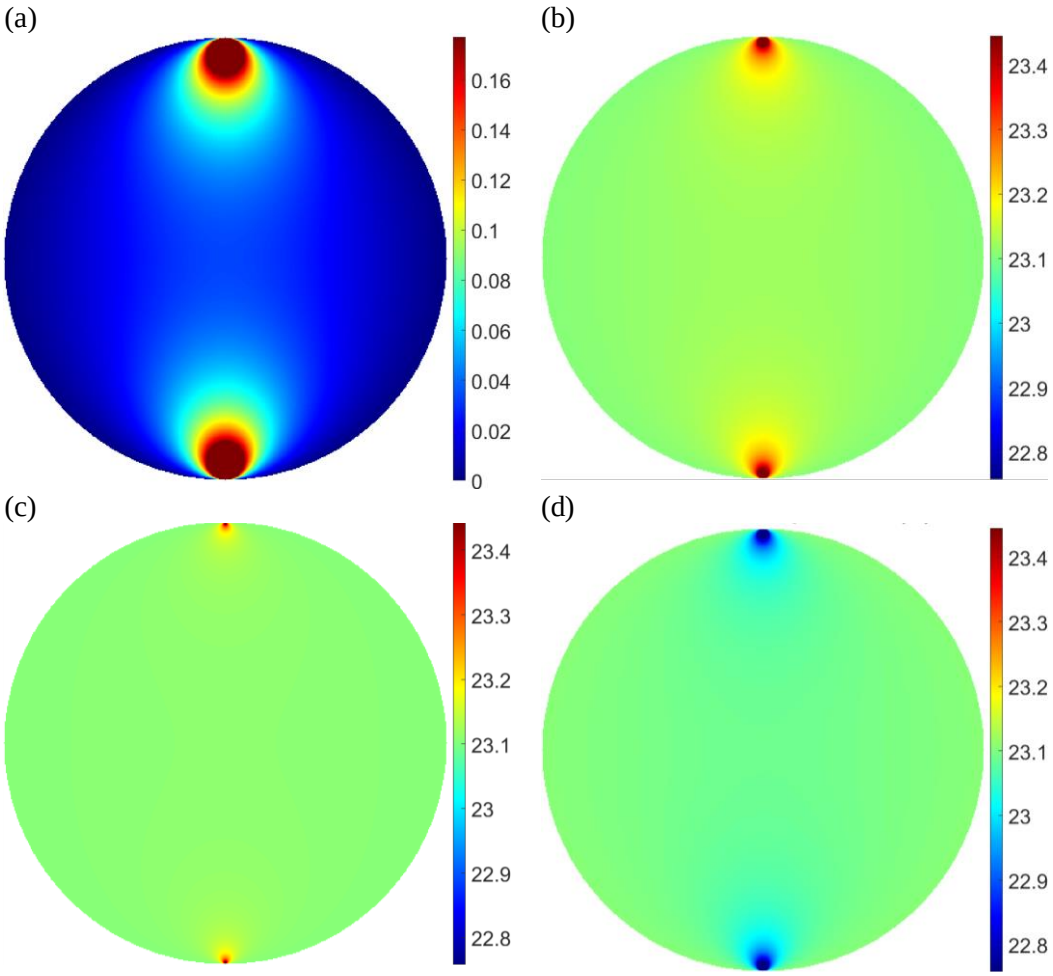

Figure 4.3 Temperature fields (°C) for the painted disc (a) $\Delta T^t(x,y)$; $T^t(x,y,t)$ at: (b) $t = 0$ s, (c) $t = 0.05$ s, and (d) $t = 0.1$ s

To determine the camera response to the temperature field given by equation (4.7), it is necessary to convert the temperature field to a radiant emittance using Planck's law. For the microbolometer, the radiance (R) [13] over the detector operating wavelengths (as given in Table 3.3) is calculated using:

$$R(x,y,t) = e\int_{\lambda_{min}}^{\lambda_{max}} \frac{2\,h\,c^2\,\lambda^{-5}}{exp^{\frac{h\,c}{k_B\,\lambda\,T^t(x,y,t)}} - 1} d\lambda \tag{4.9}$$

where e is the emissivity, h is Planck's constant, c is the speed of light, λ is the wavelength, k_B is Boltzmann's constant.

Figure 4.4 (a) and (b) present the simulated radiance for the FLIR A655sc and the Lepton 3.5 cameras respectively at $t = 0\ s$ with an applied load range of 4.5 kN, and loading frequency of 5.1 Hz.

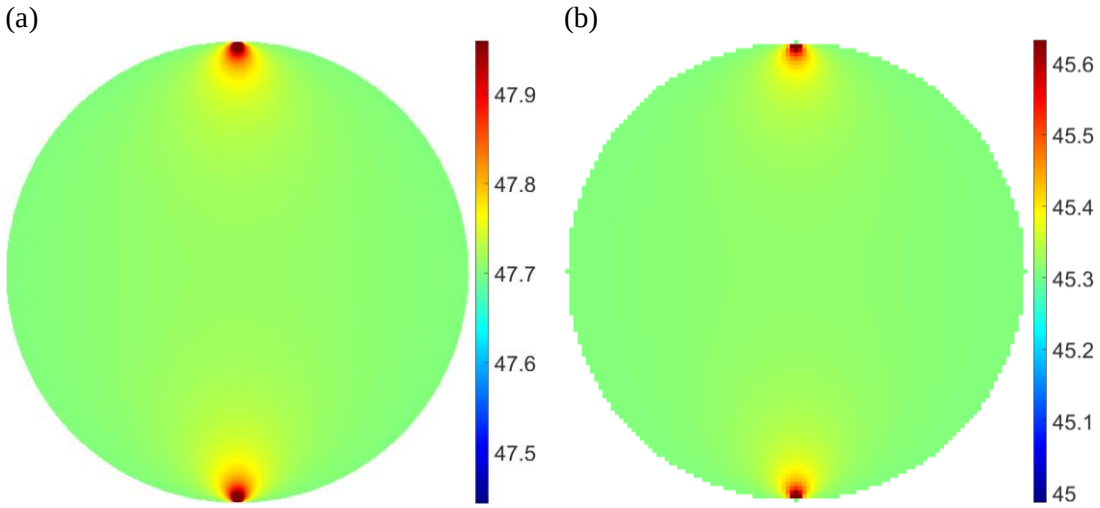

Figure 4.4 Example of radiance fields for: (a) the FLIR A655sc microbolometer (W sr^{-1} m^{-2}), and (b) the Lepton 3.5 microbolometer (W sr^{-1} m^{-2})

The radiances can be processed by the camera models as defined in section 4.2 to obtain the final digital levels as illustrated in Figure 4.5 for the FLIR A655sc camera, for a load of 4.5 kN, and a loading frequency of 5.1 Hz. An identical procedure was carried out to generate simulated DL images of the temperature variation with cyclic load from the Brazilian disc for the Lepton 3.5 camera. Table 4.3 provides the experimental parameters used for each camera to create the simulated DL temperature maps.

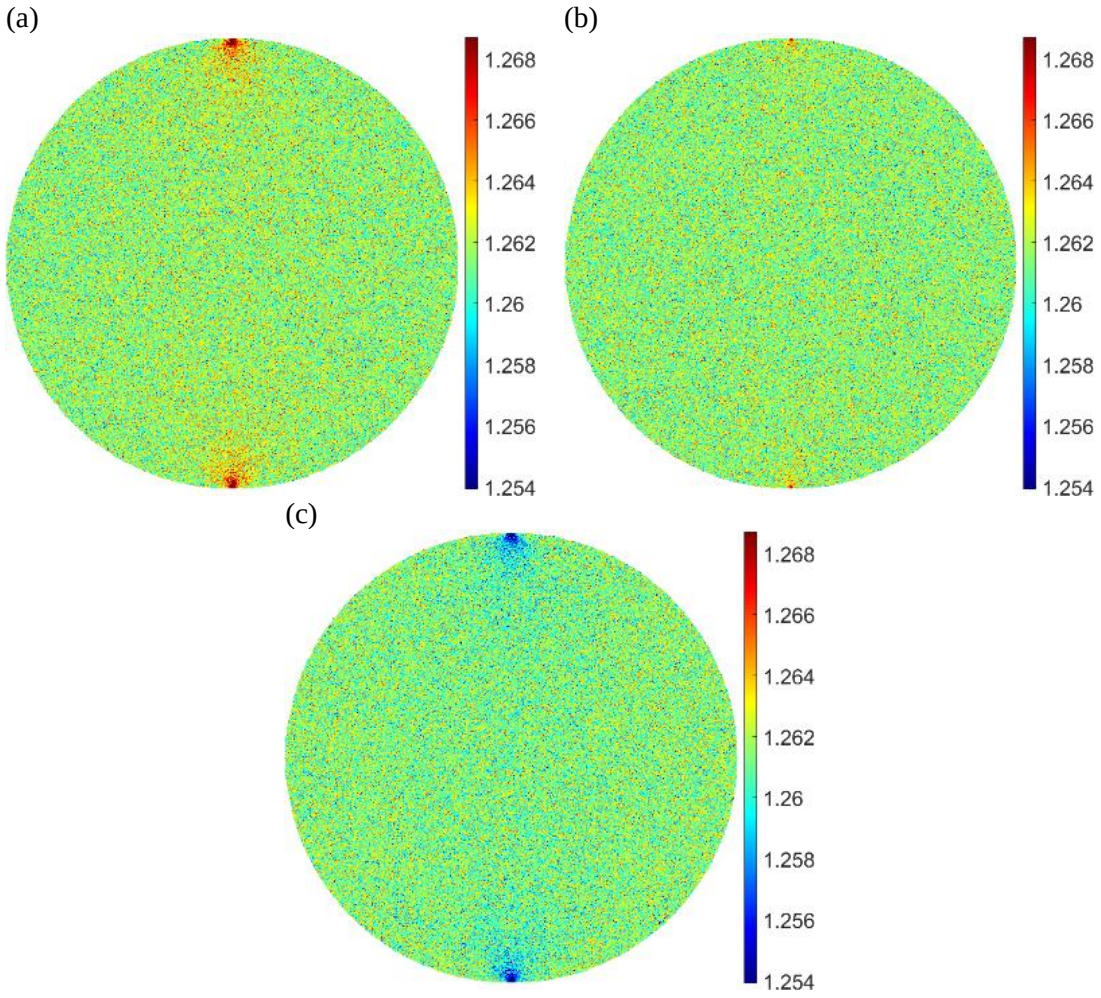

Figure 4.5 Example of digital level fields generated by the FLIR A655sc camera model: (a) at $t =$ 0 s ($\cdot 10^4$ DL), (b) at $t = 0.05$ s ($\cdot 10^4$ DL), and (c) at $t = 0.1$ s ($\cdot 10^4$ DL)

Table 4.3 Simulation parameters

Camera	**FLIR A655sc**	**FLIR Lepton 3.5 radiometric**
Sample to camera distance	~27 cm	~10 cm
Effective pixel dimension	0.1896 mm/pix	0.7207 mm/pix
Frame rate (full window)	50 Hz	8.7751 Hz
Number of frames collected	2500	5000

The procedure described above allows simulated images to be generated in DL with an identical pixel resolution and noise content to that generated by the cameras. Thus, enabling and evaluation of the image capture and processing procedure used to extract the TSA variables from equation (3.6). Firstly, a comparison between each of the three images processing algorithms is made. The algorithm assessment is performed analytically by creating a sinusoidal temperature vector (simulating a single data point or pixel) with the inputs T_0 and ΔT shown in Table 4.4 at 5.1 Hz of loading frequency. A

sampling rate of 50 Hz and 2,500 points were considered, which are the experimental parameters used with the FLIR A655sc. The temperature vector had a non-integer number of cycles to demonstrate the effect on the FFT and lock-in approaches. For the lock-in algorithm, it was necessary to create a load vector as reference, which corresponded to the Brazilian disc load signal at 4.5 kN load range, i.e. -5 ± 2.25 kN. The three algorithms i.e. lock-in, least-squares and FFT, described in section 3.1.3 were used to extract T_0 and ΔT.

Table 4.4 shows the TSA variables, T_0 and ΔT, obtained with the three algorithms and the relative difference with respect to the input value, calculated as

$$Relative\ difference\ (\%) = \frac{\left(D_{algorithm} - D_{input}\right)}{D_{input}} \cdot 100 \tag{4.10}$$

where D_{input} is the input value, and $D_{algorithm}$ is the value obtained with the algorithm (lock-in, least-squares or FFT).

It can be seen that the least-squares algorithm is the most accurate and fast procedure in comparison to the lock-in and FFT algorithms. The spectral leakage that the lock-in and FFT suffer due to the non-integer number of cycles is highlighted in the extraction of ΔT, but it is not significant in T_0. For this reason, the lock-in and FFT algorithms require an additional processing step to consider an integer number of cycles to extract the TSA variables accurately. The time difference of a single data point is not significant, but it is scaled up when the post-processing is required for thermal images of multiple data points i.e. 640 x 480 pixels. Therefore, the least-squares process is selected for processing the remainder of the thermal image data sets presented throughout the thesis as it is not being affected by non-integer cycle counts and has the shortest processing time.

Table 4.4 Comparison of the performance algorithms used in TSA

	T_0 (K)	T_0 relative difference (%)	ΔT (K)	ΔT relative difference (%)	Time (s)
Input	293	-	0.050	-	-
Lock-in	293.00	$3.41 \cdot 10^{-4}$	0.051	0.44	0.1238
Least-squares	293.00	$3.88 \cdot 10^{-14}$	0.050	0.00	0.0863
FFT	293.00	$3.41 \cdot 10^{-4}$	0.049	-0.42	0.1204

Figure 4.6 presents the simulated values T_0 and ΔT in terms of DL and the phase obtained using the least-squares algorithm for the FLIR A655sc camera, for a load of 4.5 kN, and a frequency of 5.1 Hz. It is clear the plasticity at the loading points is not included in the simulation, because the phase data is showing a consistent 180° value apart from at the edges of the disc where the response is obscured by the noise.

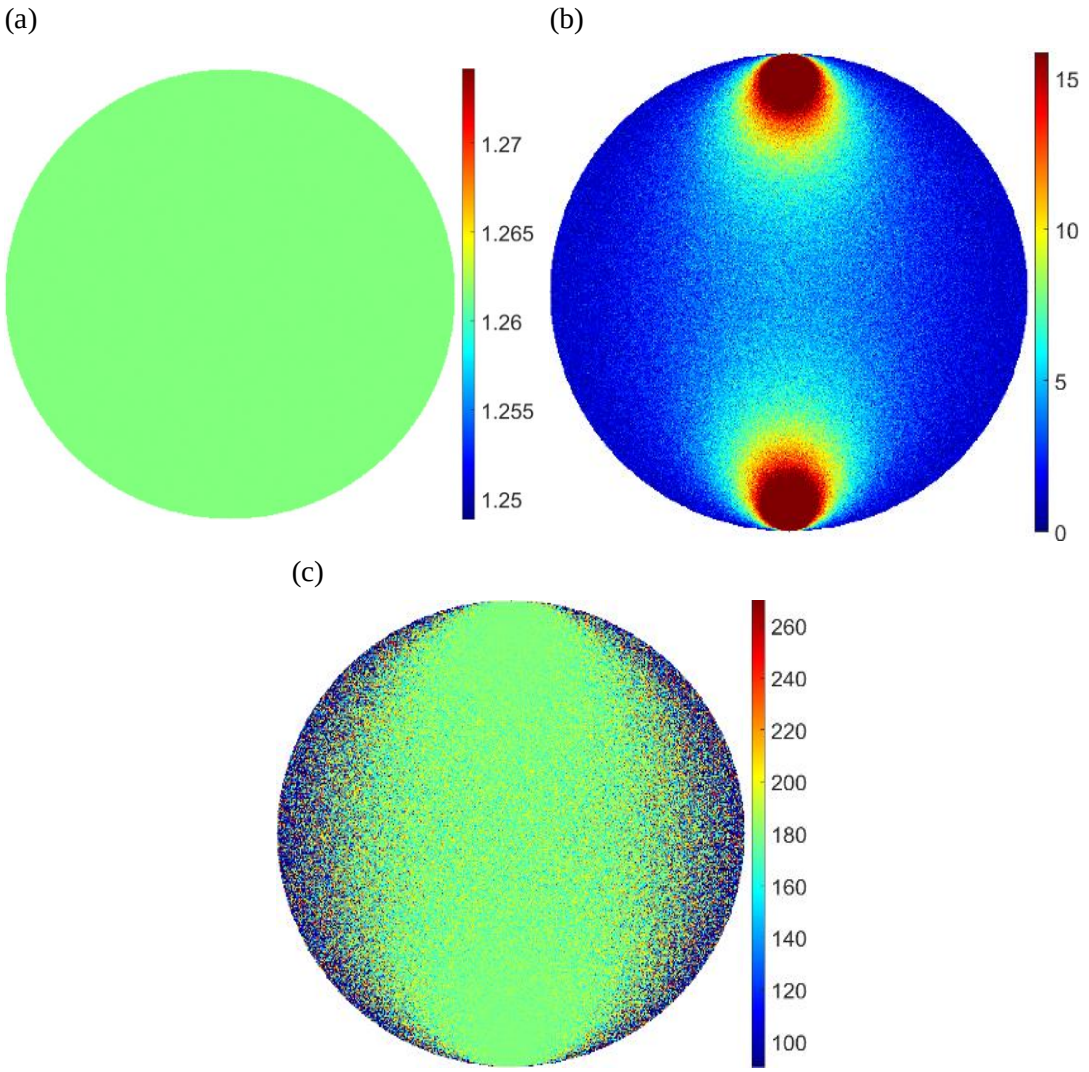

Figure 4.6 Example of TSA results: **(a)** mean temperature T_0 ($\cdot 10^4$ DL), **(b)** temperature amplitude ΔT (DL), and **(c)** phase ϕ (°)

4.4 Comparison of the Experimental Results with the Simulation

The simulations and experimental results obtained with the two microbolometer cameras are compared using the Brazilian disc loaded at 4.5 kN (-5 ± 2.25 kN) and 9 kN (-5 ± 4.5 kN). The loading frequencies considered are 2.1, 5.1 and 10.1 Hz to avoid aliasing, particularly, when using the FLIR A655sc at 50 Hz frame rate. Additionally, the experiments were performed on two different types of test machines, a servo-hydraulic Instron 8802 of the type usually used to provide the cyclic loading in TSA, and an electrodynamic machine, an Instron ElectroPuls E10000. It was shown that there was practically no difference in the results hence, for brevity, the data collected for the specimen loaded in the ElectroPuls test machine is provided.

For the two microbolometers, full-field plots of both the simulated and experimental TSA variables (T_0, ΔT and ϕ) are generated. To make a quantitative comparison, plots of the difference between

the two data sets are provided, which provide the basis for the performance assessment of the two microbolometer cameras for TSA. The experimental data showed the disc slightly tilted with respect the vertical axis. Hence, to facilitate the comparison, it was necessary to correct the experimental data so that both loading points were directly aligned and in an identical position to that of simulated data. As only a small rotation of the data was required, the correction was achieved using a simple linear interpolation procedure.

4.4.1 Microbolometer FLIR A655sc

The experimental data considered are those performed on the Brazilian disc at the 4.5 kN peak-to-peak applied load with the FLIR A655sc operating at 50 Hz frame rate. Figure 4.7 shows full-field plots of T_0, ΔT and ϕ for simulations (a)-(c), experiments (d)-(f) and the simulation and experiments difference (g)-(i) of the Brazilian disc at 5.1 Hz loading frequency. In the experiments, the FLIR A655sc had the noise reduction feature off, therefore, although it acts as a low-pass filter, its time constant is 8 ms and does not show significant attenuation on the ΔT magnitude, as it would happen if the noise reduction feature was on. The noise reduction feature of the FLIR A655sc camera is studied in detail in Chapter 5. It can be seen that the simulations and experiments match closely, and that the plasticity region can only be seen on the experimental data. The difference between the simulation and experimental data on T_0 is about 1000 DL. In the phase data for the experiment, the region of plasticity close to the loading points is clearly visible. There is also a shift in the phase data from the top to the bottom of the disc, the reason for this has not been established but may be attributed to a slight misalignment of the disc during the test.

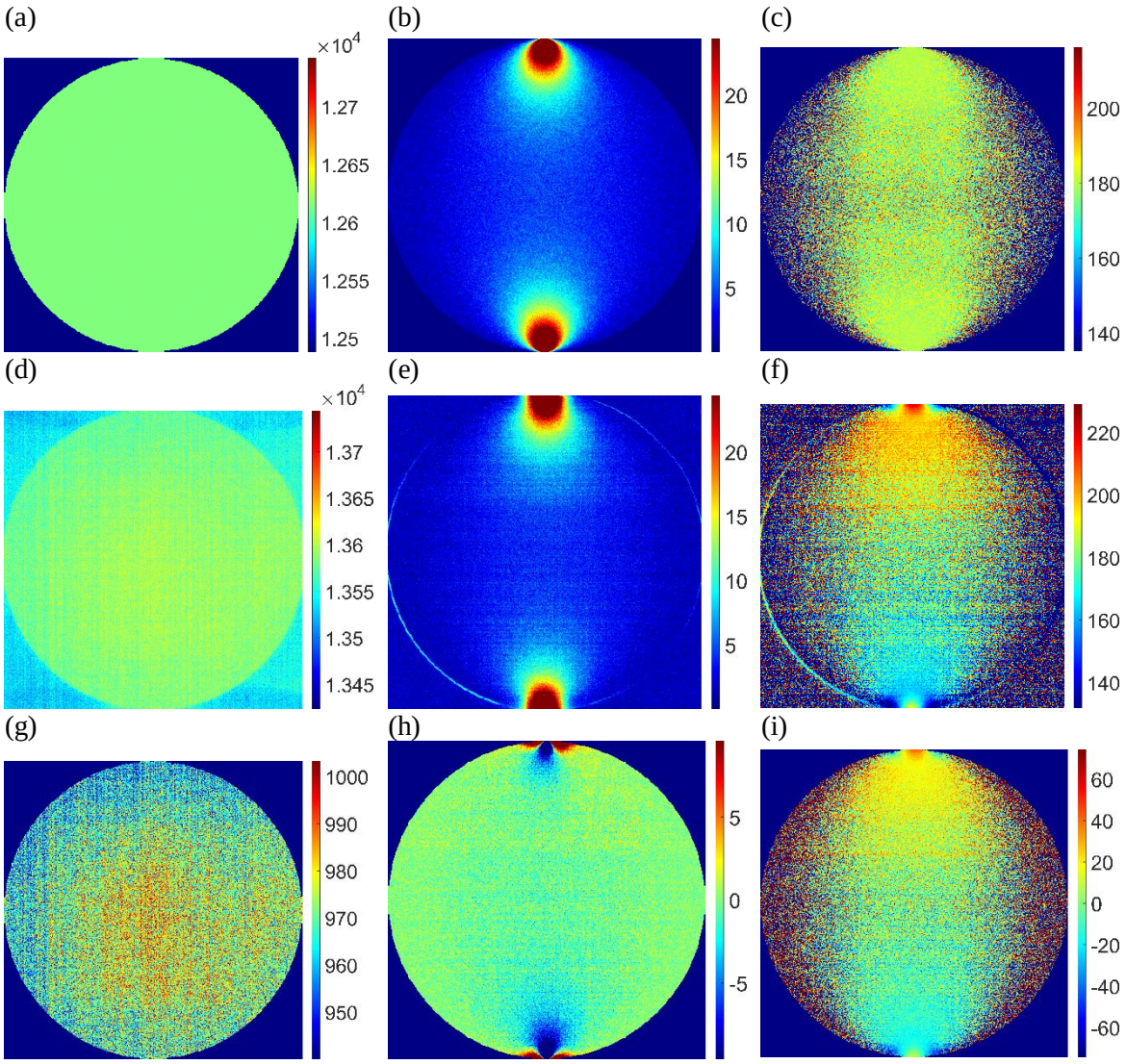

Figure 4.7 FLIR A655sc T_0, ΔT and ϕ fields for 4.5 kN peak-to-peak applied load at 5.1 Hz loading frequency: (a)-(c) simulations with added camera noise, (d)-(f) experiments, (g)-(i) difference between simulation and experiment. (a), (d), and (g) are the mean temperature T_0 (DL), (b), (e), and (h) are the temperature amplitude ΔT (DL), and (c), (f), and (i) are the phase ϕ(°)

Figure 4.8 shows a line plot of the relative difference of ΔT calculated using equation (4.10) along the centre line of the disc for the 4.5 kN peak-to-peak load at 5.1 Hz loading frequency. A slight sign of the low-pass filter behaviour can be detected at 5.1 Hz loading frequency as it shows a small deviation from 0%, which is expected as for a time constant of 8 ms as the cut-off frequency is 20 Hz, as described in Chapter 5.

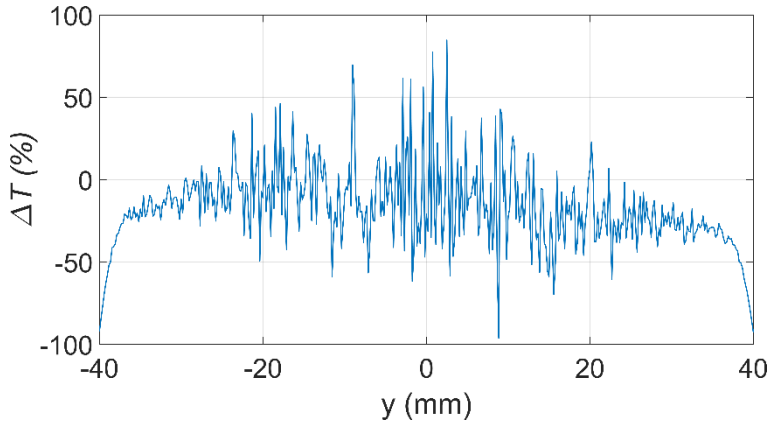

Figure 4.8 Relative difference of ΔT vs vertical position comparison between simulations and experiments for the 4.5 kN peak-to-peak applied load at 5.1 Hz loading frequency using the FLIR A655sc microbolometer IR camera

Figure 4.9 shows the T_0 and ΔT mean values of a 40 x 40 pixel region at the centre of the disc for both simulation and experiments with respect to the loading frequency. Both loading cases are considered. The T_0 and ΔT simulation data is shown in Figure 4.9 (a) and (b) with the experimental data T_0 and ΔT shown in (c) and (d). The experimental data has been normalised with the simulation values and is shown in Figure 4.9 (e) and (f). T_0 given by the experiments is slightly greater (~7%) than the simulations with an indication of a very small dependence in the loading frequency. Regarding the experimental ΔT, it can be seen that, as expected, the magnitude reduces when the loading frequency increases, as microbolometers act as low-pass filters. However, the magnitude reduction difference between the simulation and experimental data goes from ~5% at 2.1 Hz loading frequency to ~20% at 10.1 Hz loading frequency. In the next chapter, it will be shown that if the thermal time constant of the microbolometer is known, the TSA data can be calibrated for the loading frequency of the test.

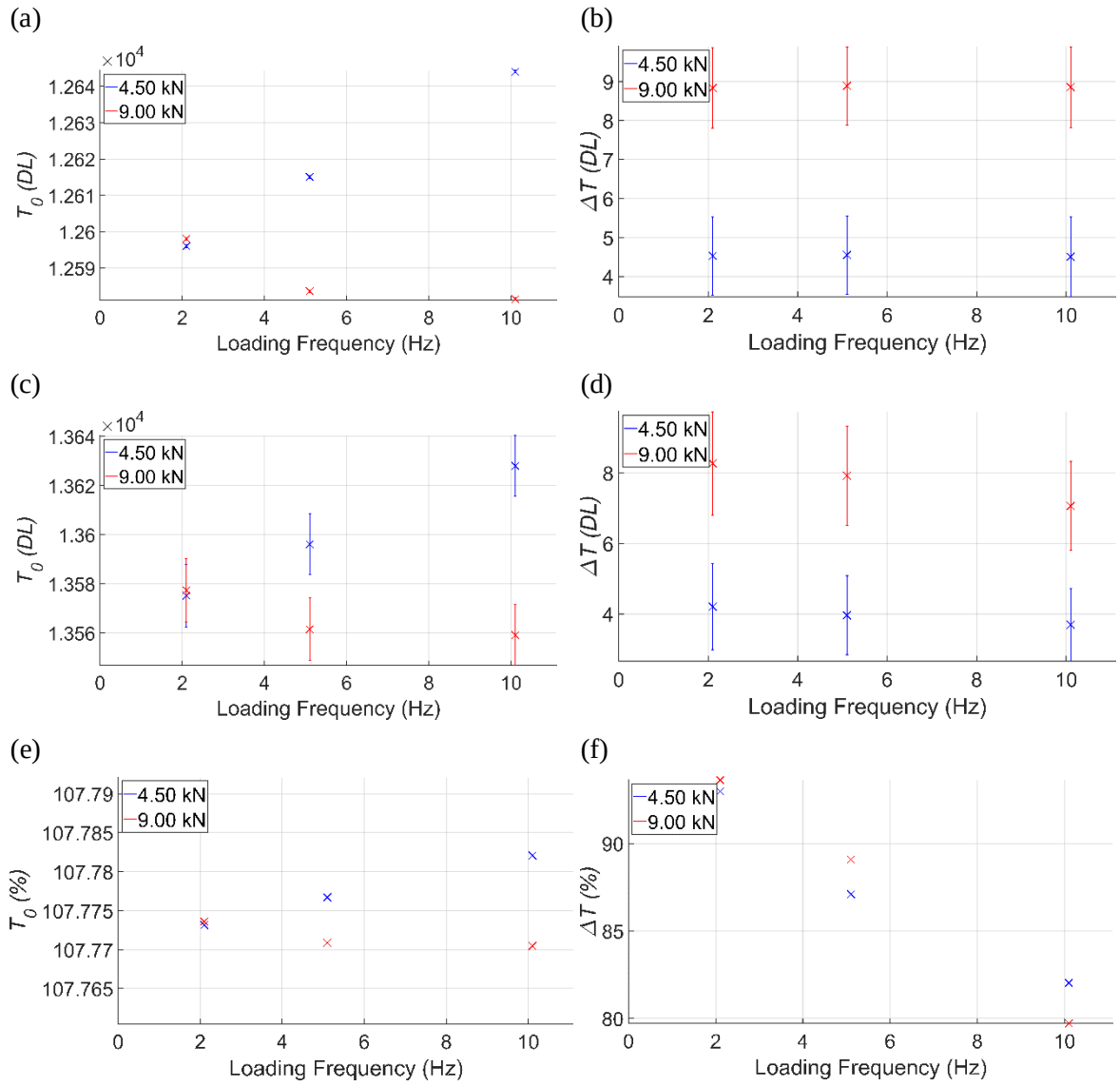

Figure 4.9 FLIR A655sc single pixel data vs loading frequency of (a) simulated T_0, (b) simulated ΔT, (c) experimental T_0, (d) experimental ΔT, (e) normalised experiments over simulations of T_0 and (f) normalised experiments over simulations of ΔT

4.4.2 Thermal Core Lepton 3.5 Radiometric

The experimental data considered is when the Brazilian disc is loaded to 4.5 kN peak-to-peak applied load at 2.1 Hz. As shown in the previous section, the thermoelastic response is attenuated when the loading frequency increases. Hence, as the Lepton has a larger time constant than the FLIR A655sc, the lowest loading frequency was selected to minimise the low-pass filter effect. Figure 4.10 shows the full-field maps of the T_0, ΔT and ϕ for the simulations (a)-(c), experiments (d)-(f) and difference between simulation and experimental data (g)-(i). It can be seen that the experimental value of T_0 is quite close to the simulation showing ~100 to 120 DL difference. The experimental value of ΔT is significantly lower than that given by the simulation, however, the stress gradient is visible. The

experimental ϕ map matches closely the simulation one and the plasticity region close to the loading points is visible, which is encouraging for damage and defects inspections.

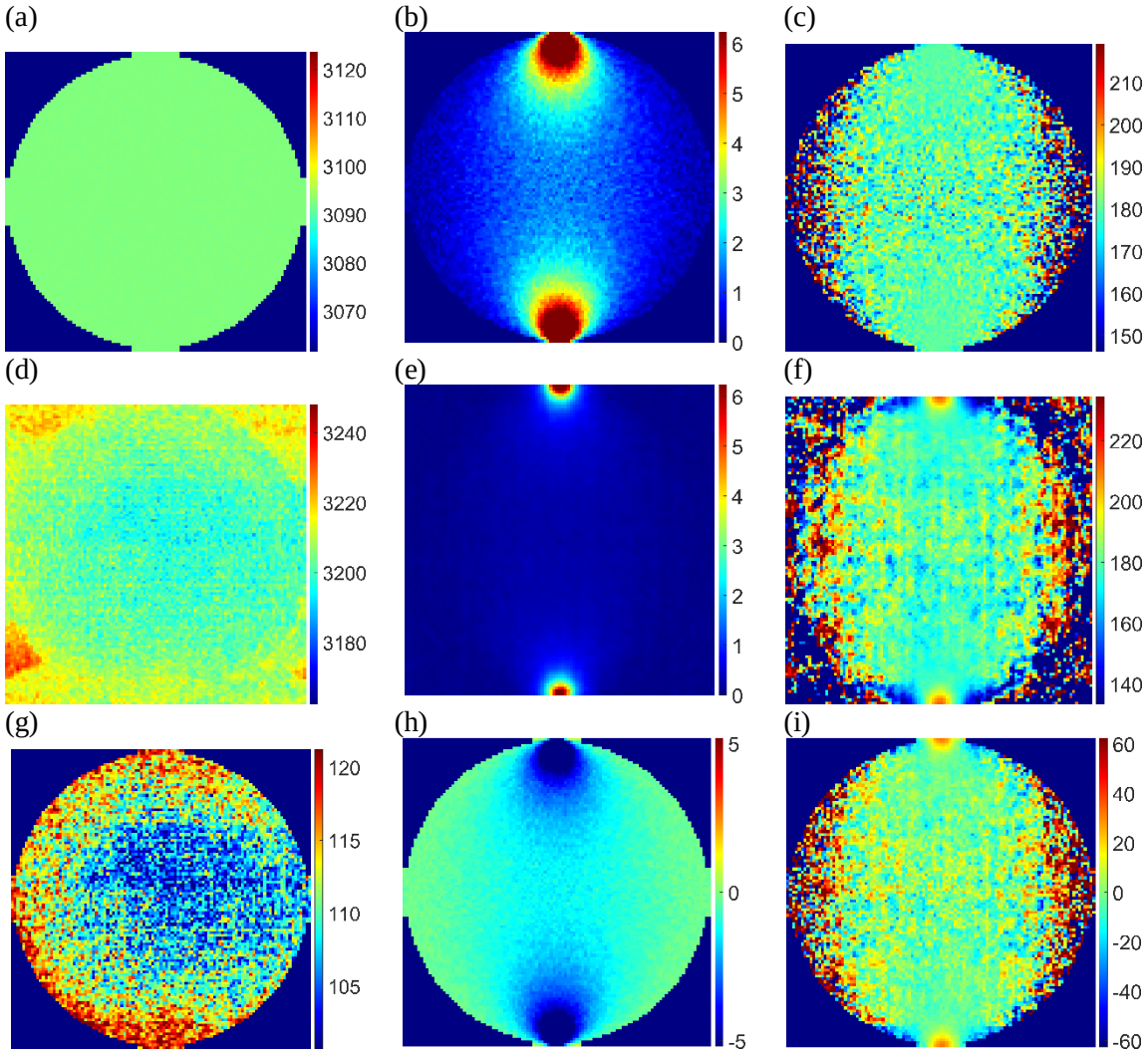

Figure 4.10 Thermal core FLIR Lepton 3.5 radiometric T_0, ΔT and ϕ fields for 4.5 kN peak-to-peak applied load at 2.1 Hz loading frequency: (a)-(c) simulations with added camera noise, (d)-(f) experiments, (g)-(i) difference between simulation and experiment. (a), (d), and (g) are the mean temperature T_0 (DL), (b), (e), and (h) are the temperature amplitude ΔT (DL), and (c), (f), and (i) are the phase ϕ (°)

Figure 4.11 shows a line plot of the relative difference of ΔT calculated using equation (4.10) along the centre line of the disc for the 4.5 kN peak-to-peak load at 2.1 Hz loading frequency. It can be seen that there is ~15% between the simulation and experimental data at the centre of the disc. This is much greater than that of the FLIR A655sc, but cannot be attributed to just the low-pass filtering effect unless the quoted time constant is much greater than that given by the manufacturer.

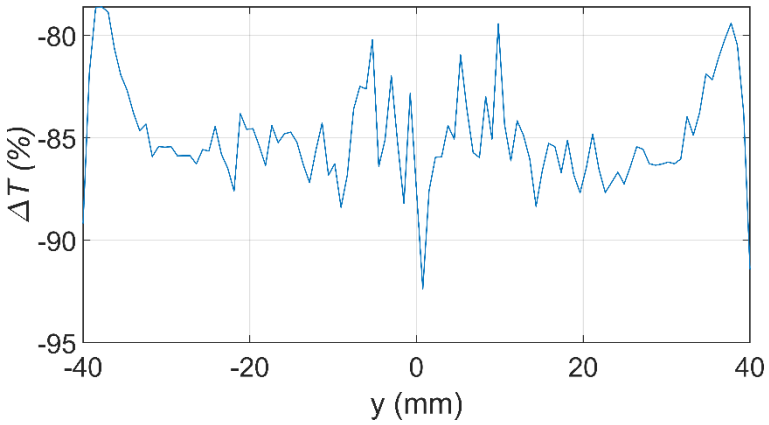

Figure 4.11 Relative difference of ΔT vs vertical position comparison between simulations and experiments for the 4.5 kN peak-to-peak applied load at 2.1 Hz loading frequency using the FLIR Lepton 3.5 thermal core microbolometer IR camera

Figure 4.12 shows the T_0 and ΔT mean values of a 40 x 40 pixel region at the centre of the disc for both simulation and experiments with respect to the loading frequency for both loading cases. The T_0 and ΔT simulation data is shown in Figure 4.12 (a) and (b) with the experimental data T_0 and ΔT in Figure 4.12 (c) and (d). The experimental data has been normalised with the simulation values and is shown in Figure 4.12 (e) and (f). It can be seen that the T_0 values from the experiments and simulations match closely with only ~4% difference. However, the normalised ΔT shows a deviation of up to ~90% from the experimental data with respect the simulation, and as indicated above cannot be attributed to the low-pass filtering alone. It may be a sampling issue, as the Lepton camera is capable of sampling at about 26.3 Hz, but it is limited to 8.7751 Hz by USA government regulations [107] - Engineering Data Sheet.

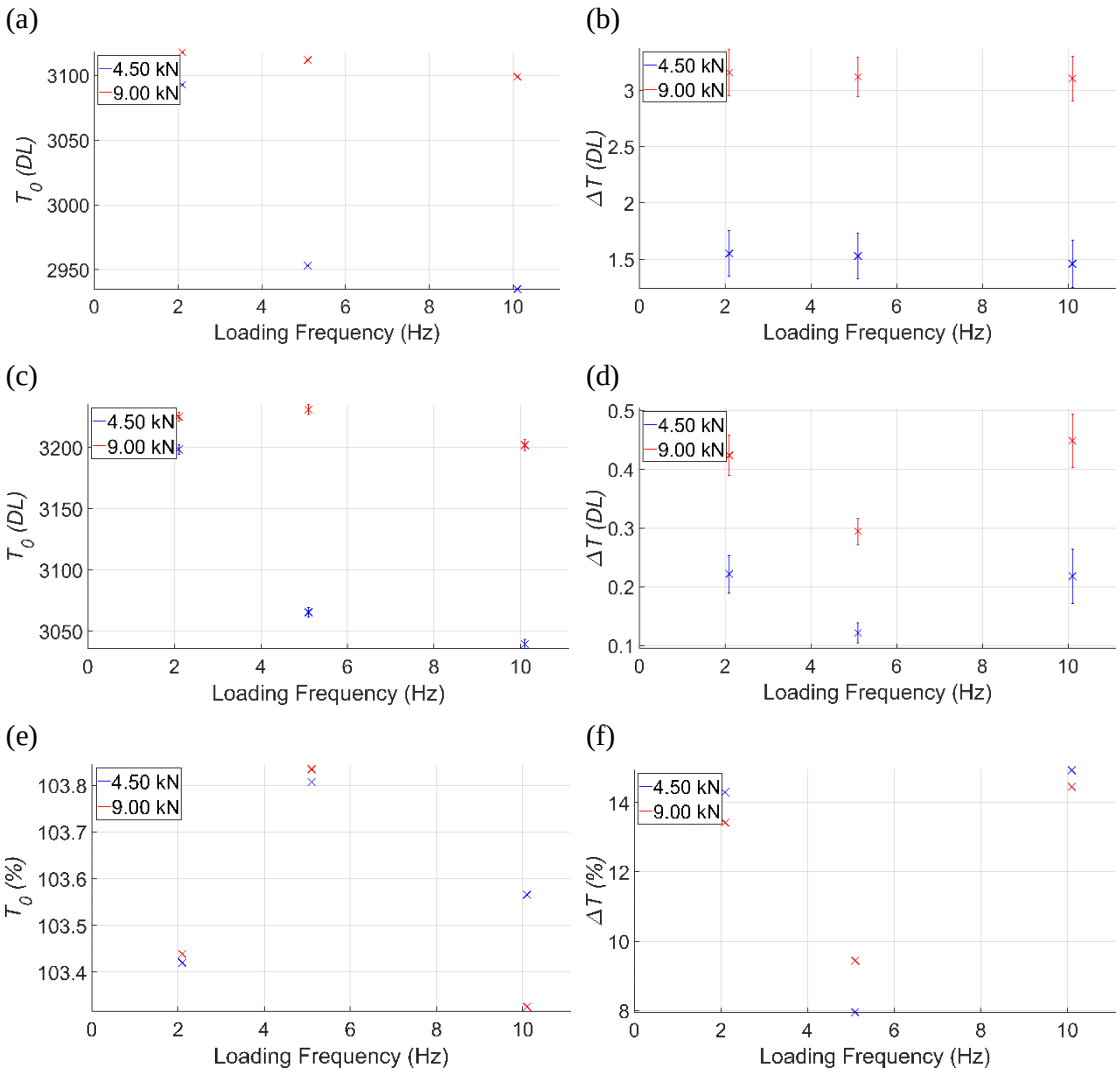

Figure 4.12 Lepton 3.5 single pixel data vs loading frequency of (a) simulated T_0, (b) simulated ΔT, (c) experimental T_0, (d) experimental ΔT, (e) normalised experiments over simulations of T_0 and (f) normalised experiments over simulations of ΔT

4.5 Summary

The performance for TSA of two microbolometers has been assessed by comparing simulations based on a camera model developed in [124] and experimental data. The FLIR A655sc microbolometer is an order of magnitude less expensive than a common photon detector, is compact and does not require any cooling system; however, it is clearly shown it acts as a low-pass filter in TSA unless low loading frequencies are used. The Lepton 3.5 thermal core is an ultra-low cost IR camera in comparison with the FLIR A655sc microbolometer, it is only a few millimetres in size, but attenuates the thermoelastic response that cannot be attributed to the low-pass filtering alone.

Three different algorithms to obtain the TSA data have been assessed, in particular, least-squares fitting, lock-in and FFT algorithms. The least-squares algorithm presented the best results in terms

of ΔT than the lock-in and the FFT algorithms, as these two are affected by spectral leakage due to non-integer number of cycles. The T_0 obtained with the different algorithms was similar in all analysed cases. In terms of processing time, the least-squares algorithm was faster than both the lock-in and FFT algorithms. Hence, the least-squares algorithm was selected as the preferred image processing approach for TSA.

Camera models have been developed to simulate the camera behaviour analytically and compare the simulations with the experiments. The comparison has been done through full-field maps, assessing the thermoelastic response obtained along the vertical central line of the disc, as well as at a region at the centre of the Brazilian disc. It was seen that both simulation and experimental data matched closely using the FLIR A655sc with a time constant of 8 ms for low loading frequencies. The results obtained with the microbolometer highlights the low-pass filter behaviour, which is further investigated in Chapter 5, including the presentation of a calibration procedure and an in-depth study of additional variables that should be considered when using a microbolometer for TSA.

The results obtained with the thermal core are promising, showing the stress gradients on the disc. However, at present, it is clear that the thermal core can only be used in a qualitative sense, as it has a very low response alongside significant attenuation caused by the low-pass filtering effect and possible sampling issues due to the camera frame rate being limited, as the attenuation curve is not as expected for low-pass filter behaviour. Further work is required to understand fully the capabilities of Lepton for quantitative TSA.

Chapter 5. Evaluation of the Performance of Microbolometers for TSA

5.1 Introduction

Previous work [21, 100] that have studied microbolometers for TSA showed that the fixed thermal time constant that controls the response time (as described in Chapter 3) attenuates the temperature reading. This is because in TSA the temperature of the object is changing rapidly so that the relatively slow response has the same effect as a low-pass filter. The overarching purpose of the work described in this chapter is to devise a procedure to evaluate the performance of microbolometers and their suitability for TSA. Hence, a model is developed that allows a variety of inputs to be applied separately to the microbolometer camera system to assess their effect on the output as follows:

- Firstly, it is demonstrated that the working principle of the microbolometer can be compared to an electrical equivalence system consisting of a series resistance-capacitor (RC) circuit (low-pass filter).
- The microbolometer behaviour is modelled with a series RC circuit using Simulink to understand the effects of different input variables on thermoelastic behaviour such as waveforms, signal-to-noise ratio, and wavelengths variations.
- A means of independently experimentally determining the microbolometer thermal time constant using an optical chopper is presented.
- Understand the impact of an in-built noise reduction (NR) feature in the FLIR A655sc microbolometer used in the work on the thermoelastic response.
- Introduce a new unified calibration approach that enables quantitative TSA with microbolometers, which can be implemented in a straightforward manner by non-expert practitioners. This is demonstrated on samples from a variety of materials.

Throughout the chapter the least-squares algorithm (presented in Chapter 3) was used for TSA post-processing as in Chapter 4 it was shown to be the most accurate approach in comparison with the lock-in and FFT algorithms.

5.2 Microbolometer Compared to Electrical Circuit

The thermal sensor is formed of a resistor that changes its value when infrared radiation is absorbed. The electrical resistance change results in a change in output voltage or current [17]. Put simply, thermal radiation sensors transform radiant flux (Φ_s) into an electric signal (voltage V_s or current I_s)

on the sensor, and this signal is processed via a calibration lookup table into a temperature measurement.

Figure 5.1 (a) [100] shows the principle working model of a microbolometer. It is assumed that the absorption of the radiant flux causes a temperature distribution in the sensor. The heat energy of the incident radiant flux, $\Delta\Phi_s$, heats the sensor element with its thermal capacity, C_{th}. The heat conduction to the surroundings can be represented as thermal resistance, R_{th}, or thermal conductance, $G_{th} = 1/R_{th}$. Therefore, the energy balance or power balance is

$$A_{th}\Delta\Phi_s(t) = P_C(t) + P_G(t) \tag{5.1}$$

where t is time, A_{th} is the absorbance, P_C and P_G are the power flow through the heat capacity and the thermal conductance or resistance, respectively, to the thermal ground (Figure 5.1 (b)).

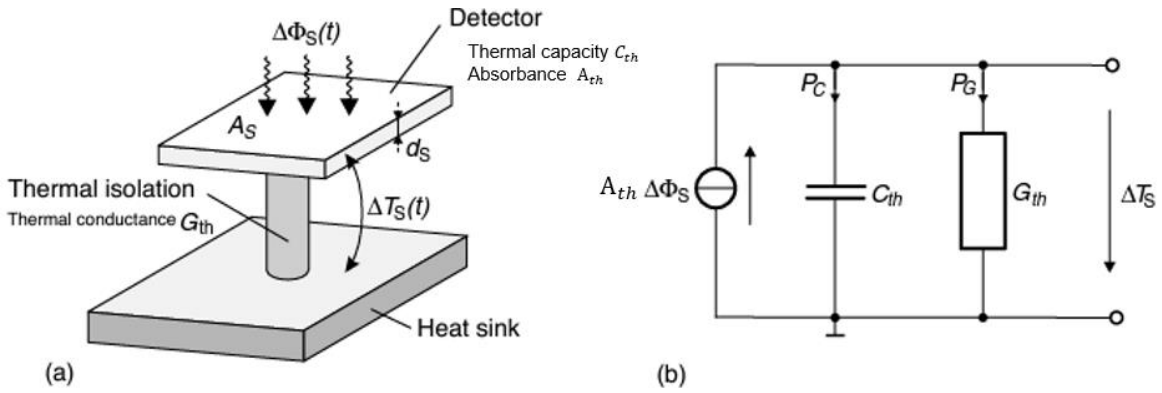

Figure 5.1 Simple model of a thermal IR sensor: (a) Principle; (b) thermal network model [100]

By following the procedure shown in [100] and considering that the radiant flux is a sinusoidal time function, such as in TSA, with a frequency $\omega = 2\pi f_0$, equation (5.1) can be expressed in frequency domain for an input sinusoidal radiant flux:

$$A_{th}\Delta\Phi_S(\omega) = (j\omega C_{th} + G_{th})\Delta T_S(\omega) \tag{5.2}$$

Therefore, the temperature change in the detector element is:

$$\Delta T_S(\omega) = \frac{A_{th}\Delta\Phi_S}{G_{th}}\frac{1}{1 + j\omega\tau_{th}} \tag{5.3}$$

where τ_{th} is the thermal time constant:

$$\tau_{th} = \frac{C_{th}}{G_{th}} = C_{th}R_{th} \tag{5.4}$$

The effective value of the temperature change is the amplitude of equation (5.3) and the phase, ϕ, can be calculated as a function of the frequency:

$$|\Delta T_S(\omega)| = \frac{A_{th}\Delta\Phi_S}{G_{th}} \frac{1}{\sqrt{1+\omega^2\tau_{th}^2}} \tag{5.5}$$

$$\phi(\omega) = \tan^{-1}(-\tau_{th}\omega) \tag{5.6}$$

It should be noted that for a sinusoidal input signal, the microbolometer output temperature amplitude and phase is affected by the thermal time constant, τ_{th}, in the frequency domain.

The input temperature change can be defined as

$$\Delta T_{S\,input} = \frac{A_{th}\Delta\Phi_{S\,input}}{G_{th}} \tag{5.7}$$

which can be used to normalise equation (5.5) with the input measurement of the temperature.

The construction of the microbolometer circuit can be compared to a series RC circuit or low-pass filter circuit [125] as shown in Figure 5.2. The equation of the electrical series RC circuit [125] is found by using Kirchhoff's law applied at the node where voltage is v_C, between the resistor R and the capacitor C.

$$\frac{v_C - v_I}{R} + C\frac{dv_C}{dt} = 0 \tag{5.8}$$

where v_C is the voltage at the capacitor, v_I is the input voltage, R is the resistor and C is the capacitor.

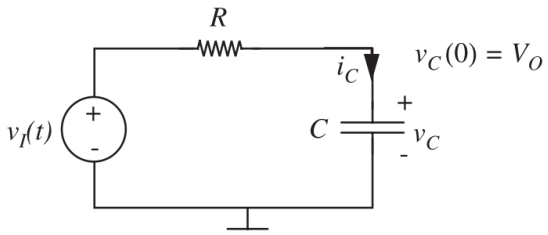

Figure 5.2 Series RC circuit [125]

By dividing by C and rearranging terms:

$$\frac{dv_C}{dt} + \frac{v_C}{RC} = \frac{v_I}{RC} \tag{5.9}$$

The solution for the differential equation (5.9) for a sinusoidal input signal, like for TSA, in the frequency domain is

$$v_C(\omega) = v_I(\omega)\frac{1}{1+j\omega\tau} \tag{5.10}$$

where τ is the time constant $\tau = RC$.

Hence, the effective value of the capacitor voltage, $|v_C(\omega)|$, and the phase, $\phi_C(\omega)$, is

$$|v_C(\omega)| = |v_I(\omega)| \frac{1}{\sqrt{1+\omega^2\tau^2}} \tag{5.11}$$

$$\phi_C(\omega) = \tan^{-1}(-\tau\omega) \tag{5.12}$$

It is clearly seen that equations (5.5) and (5.6) from the microbolometer internal circuit can be compared with equations (5.11) and (5.12) from a low-pass filter circuit formed by a resistor and a capacitor in series. By normalising these equations with the input temperature or voltage, they can be used to calibrate the output depending on the frequency.

The cut-off frequency (f_c) is the frequency at which the filter changes its behaviour. For the case of a low-pass filter, when the frequency is below the cut-off frequency, the filter passes all the signal, but when the frequency is above the cut-off frequency, the filter attenuates the signal. The cut-off frequency point takes place at -3 dB ($20\log(v_c/v_I)$), which corresponds to an output that provides 70% of the input, and depends on the time constant. The cut-off frequency for a low-pass filter is defined as:

$$f_c = \frac{1}{2\pi\tau} \tag{5.13}$$

For the case of the FLIR A655sc microbolometer used in this work, where the thermal time constant provided by the manufacturer is 8 ms, the cut-off frequency is at 20 Hz, at which the attenuation is 30% of the input value.

Figure 5.3 shows the frequency response, $H(j\omega) = v_C/v_I$, with respect the frequency (ω) for an RC circuit of 0.05 s time constant, which gives a cut off frequency, $\omega_C = 20$ rad/s or $f_c = 3.2$ Hz. This type of plot, i.e. logarithmic scale in the y-axis and ω in the x-axis, is shown as Bode diagram. It shows clearly the low-pass filter behaviour and the effect on the normalised response and phase.

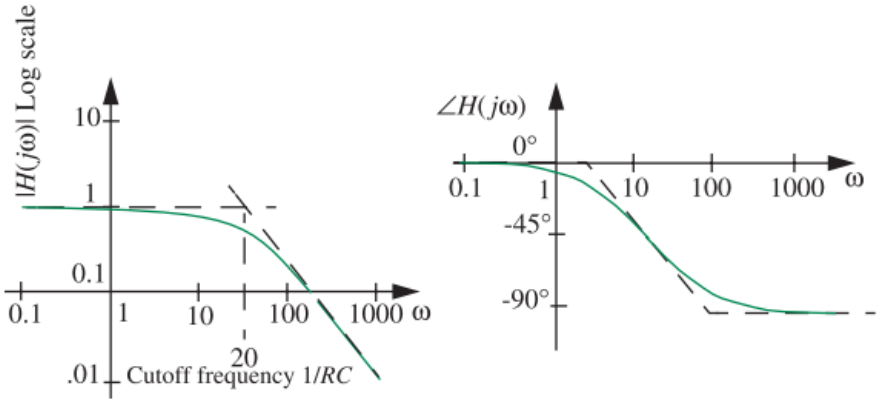

Figure 5.3 Frequency response of a simple RC circuit being $\tau = 0.05$ s [125]

Based on the comparison of this subsection, a low-pass filter circuit provides a suitable basis to simulate the microbolometer FLIR A655sc in the following section and study different parameters affecting the microbolometer behaviour.

5.3 Simulations of the Thermoelastic Response from a Microbolometer

A Simulink model and Matlab scripts were developed to study different parameters affecting the output of microbolometers and their effect on the TSA variables extracted from the least-squares algorithm. An obvious parameter for study is the effect of the loading frequency on the thermoelastic response. Other factors such as high noise level in the thermal response and the in-built noise reduction (NR) feature are studied. To apply the least-squares fit to the thermal data, the assumption is that the input signal is sinusoidal, hence, variations in the input waveforms are studied. A further concern with the microbolometer systems is a drift in the mean temperature reading, which is also studied. Figure 5.4 shows a block diagram of the Simulink model, which allows known inputs to be processed using the least-squares algorithm to better understand how different input signals affect the output response processed by the algorithm and hence the thermoelastic response. The Simulink model consists of a low-pass filter, constructed as a block or RC circuit, with a thermal time constant of 8 ms as defined by the manufacturer of the FLIR A655sc. The input of the low-pass filter is a signal of 1 V amplitude with the same noise level as the NETD of the microbolometer (30 mK). The input signal can be any cyclic signal (triangular, sawtooth, rectangular, sinusoidal, etc.) and a slope can be added to simulate mean drifting. The outputs are a visualisation window with the plot of the final signal (visualisation block) and a variable called ‘simout’ that allows discrete-time sampling of the output data. This output data is then imported into Matlab to be processed by the least-squares algorithm to calculate the change in voltage, ΔV. The simout is sampled at 50 Hz matching the 50 Hz frame rate of the camera. The ΔV is normalised with the expected value, that is 2 V peak-to-peak amplitude.

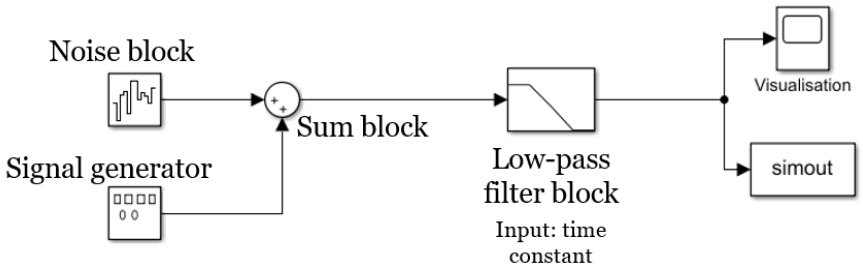

Figure 5.4 Simulink model of a microbolometer based TSA measurement system

TSA depends on the load amplitude, which in turn affects the signal to noise ratio, i.e. a greater stress results in a larger thermoelastic response. Hence, signals of different amplitudes are studied to give different signal to noise ratio. This will also simulate the effect of different materials and surface emissivity's as these determine the magnitude of the thermoelastic response. Although under adiabatic conditions the thermoelastic response is independent of frequency, it is clear from the description of the operating principles of a microbolometer that changing the loading frequency will have an effect on the thermoelastic response obtained from a microbolometer; hence, different loading frequencies are studied.

As mentioned above, the microbolometer camera parameters also have an impact on TSA results, these include: the thermal time constant fixed by the sensor material, the frame rate of the camera, the NETD and the noise reduction feature. The thermal time constant is provided by the manufacturer, to verify this, a means of measuring the thermal time constant using an optical chopper is presented.

To underpin the simulations, experimental work was conducted on stainless steel and aluminium alloy test specimens, which are described in Table 5.1. A servo-hydraulic test machine (Instron 8802) was used to apply a sinusoidal cyclic load. TSA was performed with the standard microbolometer (FLIR A655sc - Table 3.3) at different frame rates and with the NR feature on and off. Matt black paint with a thickness between 15 to 25 μm [126] was applied to reduce reflections and create a surface with a uniform emissivity of 0.95 corresponding to the MBP (matt black paint) Electrolube emissivity [127]. The cyclic loading amplitude for each material was calculated to achieve a theoretical temperature change of 50, 80 and 100 mK. The target loading amplitudes were calculated from equation (3.3) and is presented in Table 5.2. The experiments were carried out at different loading frequencies (0.25 - 11 Hz).

Table 5.1 Metallic samples dimensions and thermoelastic constants

Specimen	**Gauge Length (mm)**	**Width (mm)**	**Thickness (mm)**	**Thermoelastic constant (MPa^{-1})**
Al 6081 T6	50	15	6	$9.5 \cdot 10^{-6}$ [128]
316L Stainless Steel	237	30	2	$4.6 \cdot 10^{-6}$ [129]

Table 5.2 Loading cases for the metallic specimens to achieve a target ΔT of 50, 80 and 100 mK

Coupon	Loading case 1 (kN)	Loading case 2 (kN)	Loading case 3 (kN)
Al 6081 T6	2 ± 0.81	2 ± 1.30	2 ±1.62
316L Stainless Steel	3 ± 1.12	3 ± 1.79	3 ± 2.24
Predicted ΔT (mK)	50	80	100

5.3.1 Influence of the Loading Frequency Input

To study the influence of the loading frequency input, experimental data of 316L stainless steel data and it is analysed with the least-squares algorithm. As with any 'notch' filter, it is essential that the loading frequency at which the test was conducted is input accurately, so the least-squares algorithm can fit to the data correctly. For microbolometer camera systems in general, an analogue input to take on-board a reference signal to sample the input loading signal with the camera frames is not available. Hence, this has to be input into the algorithm to perform the matching and least-squares fit. The loading frequency can be obtained from the test machine, which may be inaccurate, hence, the first step in the evaluation of the performance is to establish the effect of variation in the loading frequency.

In this section, the sensitivity of the loading frequency as a user entered input variable into the least-squares algorithm is studied. The experimental data is from the 316L stainless steel coupon subjected to a cyclic load of 3 ± 1.79 kN at 6 Hz loading frequency. The loading amplitude was chosen to achieve a theoretical 80 mK ΔT response from the test specimen, as described above, and the microbolometer camera was set to obtain images at a frame rate of 25 Hz and 50 Hz, with the NR feature switched on.

The least-squares algorithm processed the same dataset with loading frequencies entered into the software ranging from 5.8 to 6.2 Hz. Figure 5.5 shows the ΔT with respect the loading frequency input into the software for experimental data collected at 50 Hz (a) and 25 Hz (b). This illustrates that it is vitally important that the exact loading frequency is used, otherwise the thermoelastic response will be significantly attenuated. It is noteworthy that even at the exact 6 Hz loading frequency, the maximum ΔT peak is at 25 mK instead of 80 mK; this is associated with the NR feature, which is discussed later in this chapter.

To conclude, the notch filter behaviour of the least-squares algorithm has the advantage to filter out all the unwanted noisy signals and is the key enabler for TSA. However, if the incorrect frequency is used, a few percent away from the actual loading frequency, the signal is attenuated. A way of mitigating this would be to use an FFT on the load signal from the test machine to check the loading frequency applied was the same as that requested in the test machine set-up or the self-referencing approach as described in [83, 84] could be used to determine an exact loading frequency.

(a) (b)

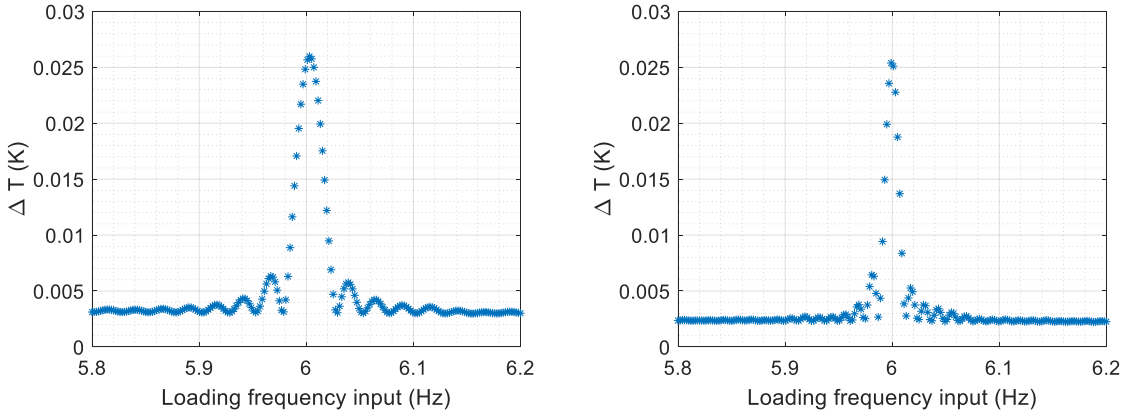

Figure 5.5 ΔT vs loading frequency (LF) input on 316L stainless steel at 6 Hz sampled at (a) 50 Hz frame rate and (b) 25 Hz frame rate

5.3.2 Influence of High Noise Level

The influence of the noise level corresponding to 30 mK NETD is analysed using simulations. Usually, in TSA the ΔT is of the order of few mK, therefore, there is typically a low signal-to-noise ratio. To study if noise has any influence on the output of TSA data, a simulated signal formed by summing a cyclic sinusoid signal and a noise signal is constructed and used as an input to the model. The noise signal has been created by uniformly distributed random numbers centred at 0 with 30 mK amplitude. The sinusoidal signal has a mean of 293 K, simulating ambient temperature and peak-to-peak amplitudes (varied from 0.02 K to 0.1 K). The simulated data allows different SNR to be studied with varying levels of input signal against a fixed level of noise, and is also tested at different frequencies ranging from 0.25 Hz to 11 Hz, with the time constant set to zero for this study to remove any dependence on frequency. The simulated data was sampled at 50 Hz and processed using the least-squares algorithm to extract the thermoelastic response, ΔT, and is plotted against the frequency in Figure 5.6. It can be seen that the output of the least-squares algorithm corresponds to the known input amplitude. Therefore, the level of noise has no significant influence on the extraction of the thermoelastic response, ΔT, when the input is a cyclic sinusoidal signal.

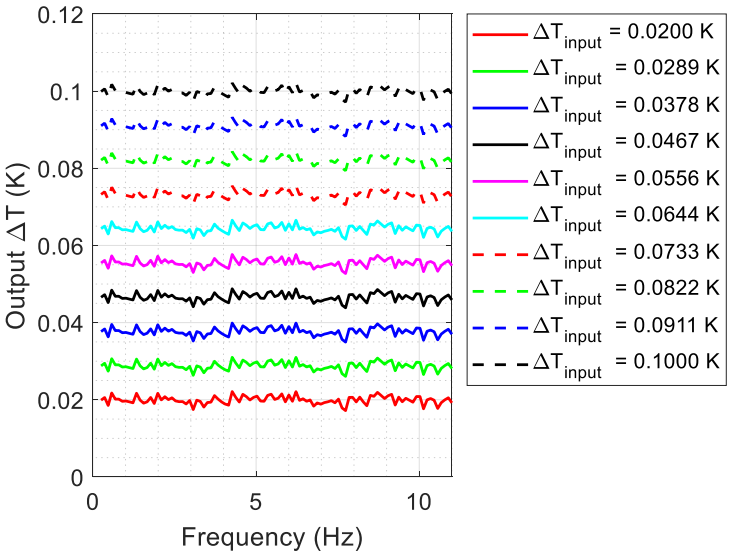

Figure 5.6 Peak-to-peak amplitude vs loading frequency simulating different SNR

5.3.3 Determining the Thermal Time Constant Experimentally using an Optical Chopper

The setup used to determine the time constant was presented in [21] and consists of a blackbody [130] and an optical chopper placed in front of it. The blackbody is set to 30°C, a higher temperature than the optical chopper, as the optical chopper is at room temperature (nominally 21 °C in a temperature controlled room). The optical chopper used is the MC2000B-EC with MC1F2 blade [131], which can produce rotating frequencies from 4 to 200 Hz. The optical chopper with the installed blade generates rectangular (square) waves at certain frequencies. Figure 5.7 shows four images taken with the microbolometer where the blackbody temperature is seen at the background, and the optical chopper at the front. The top row images (a) and (b) correspond to noise reduction feature on, while the bottom images (c) and (d) were taken with the noise reduction off on a different day. The black symbols are single data points considered in the study (Figure 5.7 (a), (c)) and a 10 x 10 pixels region comprised by the 4 points shown in Figure 5.7 (b), (d). The optical chopper rotation frequencies considered are 4 - 40 Hz, i.e. those of interest for TSA. The microbolometer recorded frames at 25 and 50 Hz frame rate and with the noise reduction feature on and off.

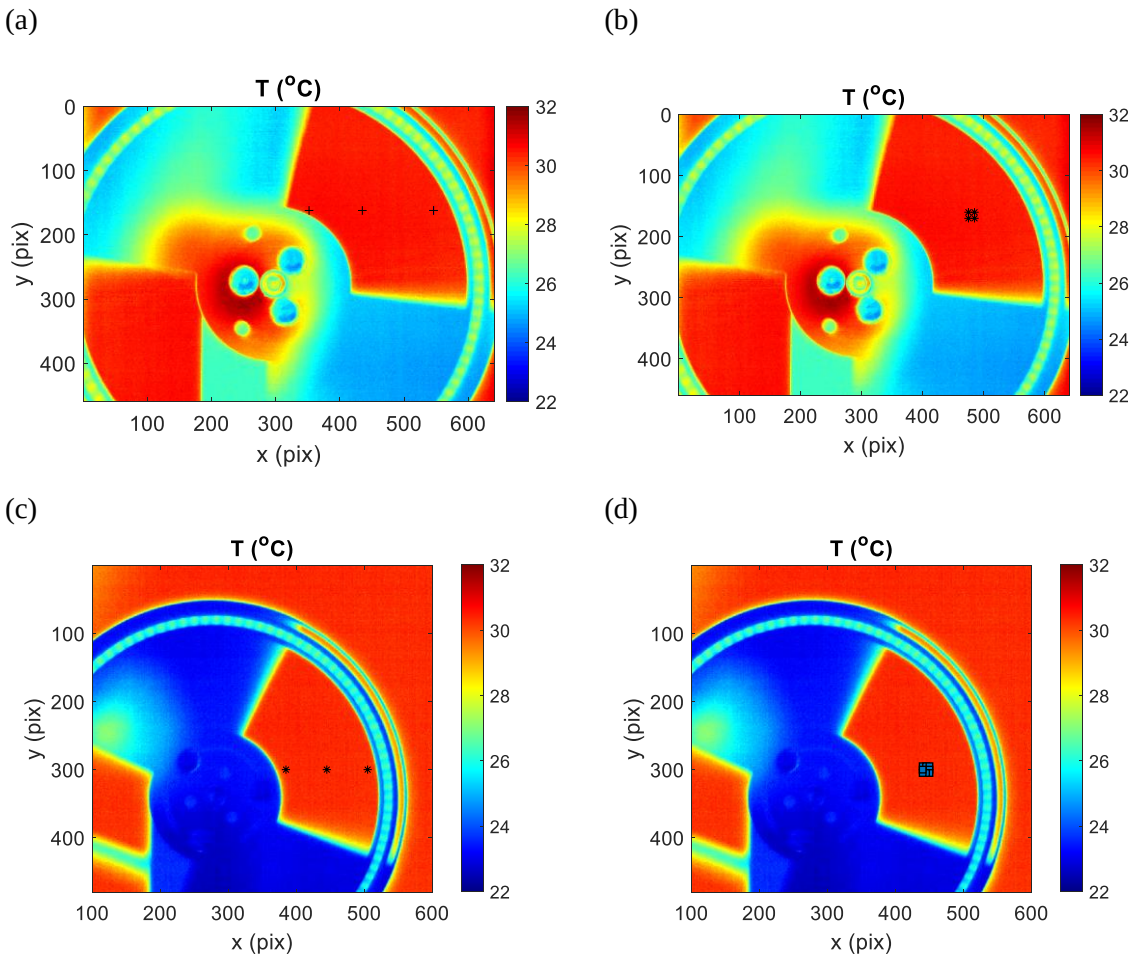

Figure 5.7 Temperature (°C) field images of the optical chopper placed in front of the blackbody showing the (a) single pixel measurement points (NR on), (b) an averaged 10x10 pixel region (NR on), (c) single pixel measurement points (NR off) and, (d) an averaged 10 x 10 pixel region (NR off)

The signal obtained with the microbolometer on a single pixel measurement point has been analysed using Fast Fourier Transform (FFT) to check the input of rotation frequencies into the chopper rotating system. Figure 5.8 shows the frequency obtained with the FFT plotted against the optical chopper input frequency. Figure 5.8 (a) corresponds to the microbolometer with the noise reduction on, recording at 50 Hz frame rate, and (b) at 25 Hz frame rate. It can be seen in Figure 5.8 (a) that from 4 Hz to 11 Hz, the optical chopper input frequencies do not match the values extracted with the FFT, probably because the optical chopper is designed to operate at larger rotational speeds. However, from 12 Hz up to 24 Hz the frequencies from the optical chopper input and FFT extraction match. It can be seen that the folding frequency is at 25 Hz that is when the optical chopper frequency is half the frame rate (Nyquist frequency [22]). After 25 Hz, the FFT frequency reduces as the optical chopper rotation is undersampled. Similar behaviour can be seen in Figure 5.8(b). The frequencies obtained from the FFT do not match the input frequency of the optical chopper. There are three folding frequencies at $n \cdot 12.5Hz$, where n is a natural number and 12.5 Hz corresponds to the Nyquist frequency [22] for 25 Hz frame rate. It is clear that the optical chopper cannot rotate as

requested at the lower loading frequencies, hence, the frequencies considered to calculate the thermal time constant are those obtained with the FFT of the experimental data.

(a) (b)

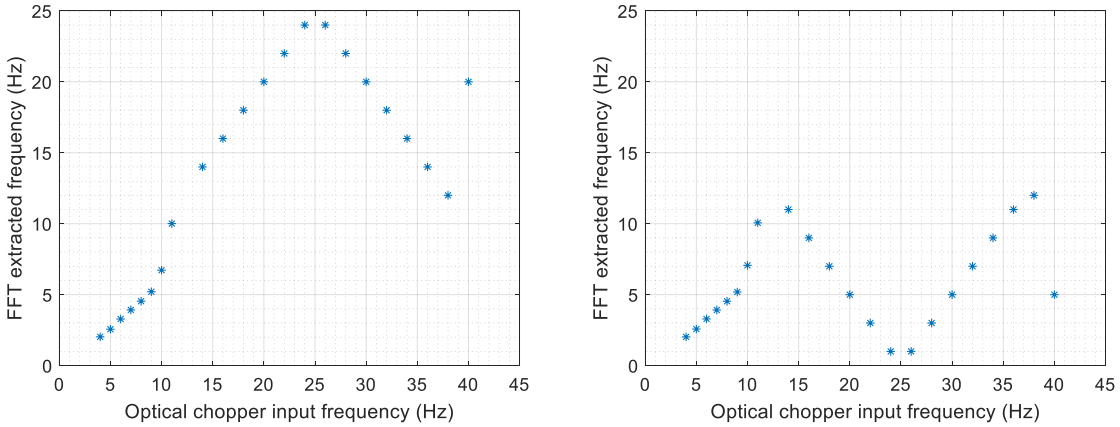

Figure 5.8 Frequency obtained with FFT vs Optical Chopper Frequency with the microbolometer recording with noise reduction applied at (a) 50 Hz frame rate and (b) 25 Hz frame rate

The thermal time constant is obtained by finding the minimum of equation (5.5) rewritten as follows with the Nelder-Mead Simplex algorithm [21]:

$$\min_{\{\tau,C\}} \sum_{i} \left(\Delta T(\omega_i) - \frac{C}{\sqrt{1+\omega_i^2 \tau^2}} \right)^2 \tag{5.14}$$

where $\Delta T(\omega_i)$ is the magnitude obtained with the microbolometer, i.e. peak-to-peak temperature, ω_i is the chopper frequency in rad/s ($\omega = 2\pi f$ where f is frequency in (Hz)), the subscript i corresponds to a particular rotating frequency, τ is the thermal time constant, C is a constant grouping the variables in equation (5.5). τ and C are unknowns and are the parameters that the Nelder-Mead Simplex algorithm [21] find.

The thermal time constant obtained for each single point and region with and without noise reduction applied in the microbolometer is presented in Table 5.3. It can be seen that in all cases the time constant obtained is smaller than 8 ms, which corresponds with the 'below 8 ms' as stated by the manufacturer in [106]. It can be observed that the results obtained without the noise reduction applied are more precise ranging from 5.2 ms to 5.9 ms, while the results with the noise reduction activated varies from 4.3 ms to 7.2 ms, showing that the noise reduction feature influences ΔT.

Table 5.3 Thermal time constant obtained from optical chopper experiments at different single points and an averaged 10 x 10 pixel region with the microbolometer collecting data with the noise reduction activated and deactivated

Noise reduction		**On**		**Off**	
Frame Rate		**50 Hz**	**25 Hz**	**50 Hz**	**25 Hz**
Regions	**Region**	5.6 ms	5.2 ms	5.6 ms	5.2 ms
	Single outer pixel	4.3 ms	6.8 ms	5.5 ms	5.6 ms
	Single inner pixel	4.4 ms	6.9 ms	5.9 ms	6.2 ms
	Single central pixel	4.6 ms	7.2 ms	5.7 ms	5.9 ms

Figure 5.9 shows the experiments fit to model extracted from equation (5.14) for different frame rates and with the noise reduction on and off. It can be seen in Figure 5.9 that the experiments fit better with the model when the noise reduction is off than when it is activated. The offset in magnitude between figures (a) and (b) with (c) and (d) is due to the difference in ambient temperature of 3 °C, and hence the temperature of the chopper, on the days of the experiments.

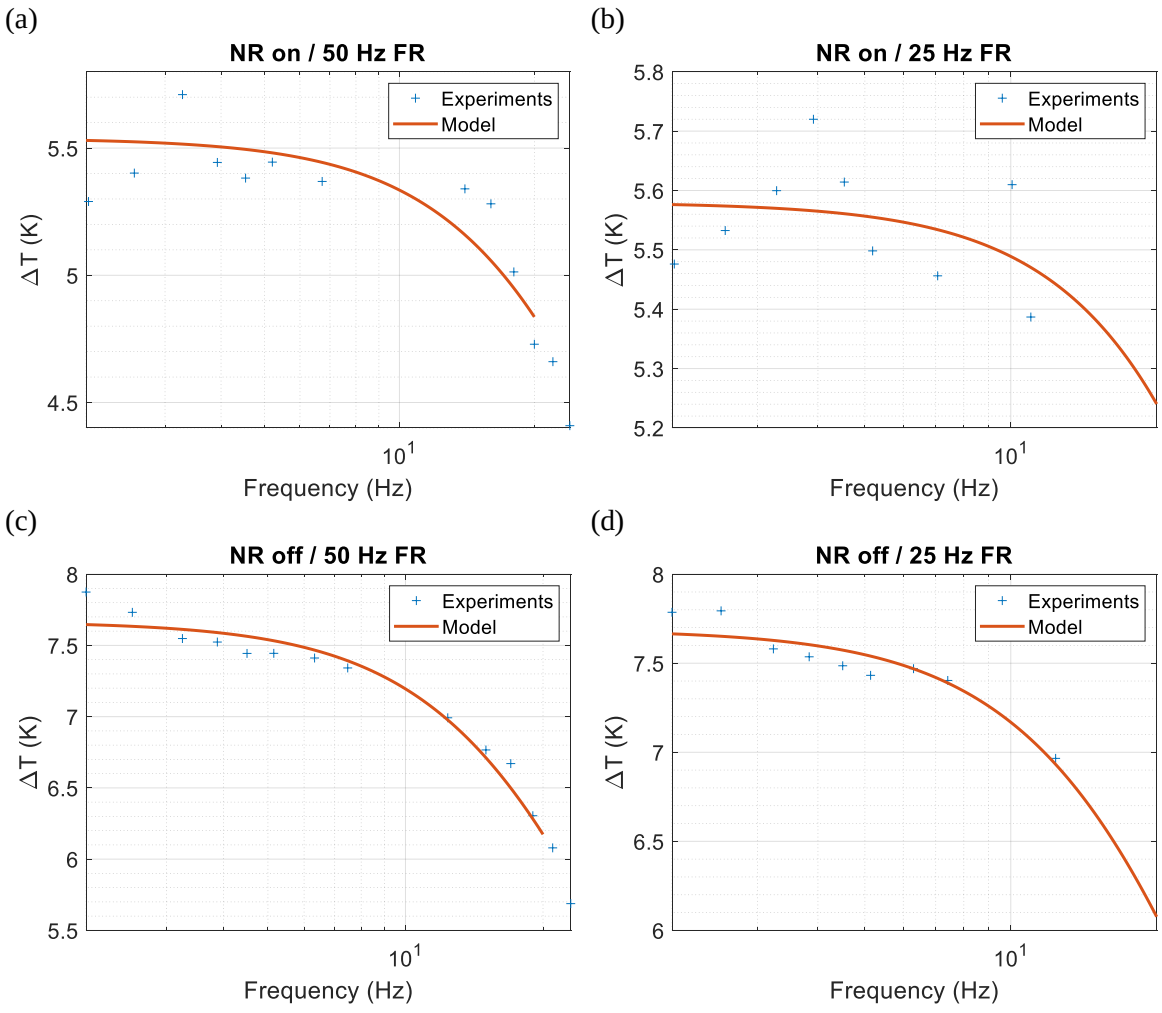

Figure 5.9 Experiments fit to model (a) noise reduction on and 50 Hz frame rate, (b) noise reduction on and 25 Hz frame rate, (c) noise reduction off and 50 Hz frame rate, and (d) noise reduction off and 25 Hz frame rate

5.3.4 Noise Reduction Simulation

It is clear from Figure 5.9 that the NR feature has an effect on the signal recorded by the microbolometer. The exact nature of the NR feature is not described by the manufacturer. Clearly, it is useful in reducing the noise for a stationary signal. However, in TSA the signal is transient and, hence, any averaging of the response will result in further filtering. To identify the effect of the NR feature, it is assumed that the NR feature performs a temporal averaging of the thermal data points to reduce the standard deviation in the readings. Therefore, the NR feature is represented as a rolling average in a simulated model with the magnitude of the noise reduction scaled by varying the number of data points averaged (N) from 2 to 7. The simulation consists of creating a sinusoidal signal of a certain frequency (loading frequency (LF) for TSA experiments) and normalised amplitude sampled at 50 Hz, which is the maximum frame rate of the FLIR A655sc in full frame window mode. The signal is passed through a low-pass filter of 8 ms simulating the behaviour of the FLIR A655sc. A simple rolling average is applied to the output, which calculates the mean of the following N data points. Finally, the least-squares algorithm is used to extract the equivalent thermoelastic response. The simulation is done for a range of (loading) frequencies (ranging from 2.1 to 6.1 Hz) to get similar plots to those in Figure 5.9, and to extract the time constant for each level of averaged points, N. An example of the process is illustrated in Figure 5.10 for the case of a signal of 4.1 Hz loading frequency (LF) and $N = 6$ averaged points.

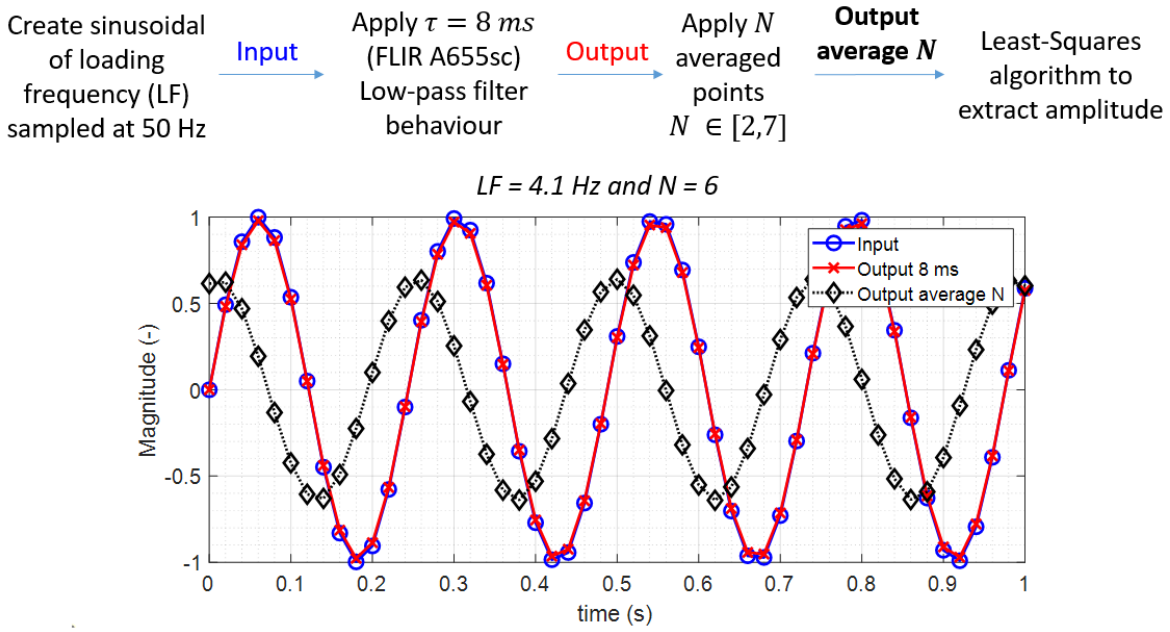

Figure 5.10 Noise reduction simulation procedure for 4.1 Hz loading frequency and 6 averaged points

The normalised peak-to-peak amplitude with respect to the loading frequency is shown in Figure 5.11 for different N. It can be seen that the magnitude reduces when the frequency increases due to the low-pass filter behaviour, and is further reduced when the number of average points increases.

The time constant for each case of N is obtained following equation (5.14). Figure 5.12 shows the time constant obtained with respect to N, where it can be seen that the increase of N produces a significant increase in the time constant, therefore, producing a significant low-pass filter effect far greater than the 8 ms time constant of the detector.

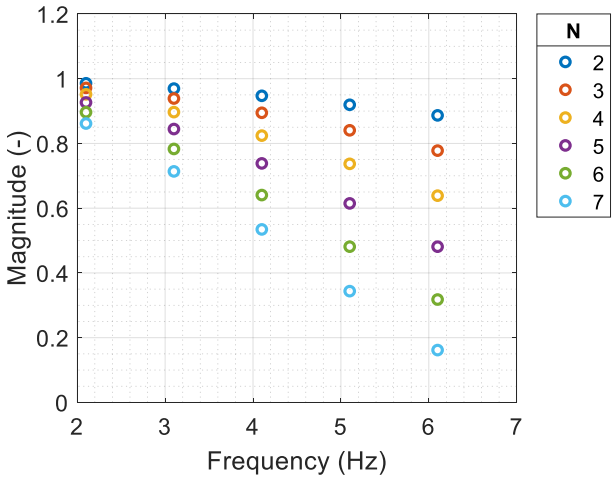

Figure 5.11 Magnitude vs frequency for each average number of data points

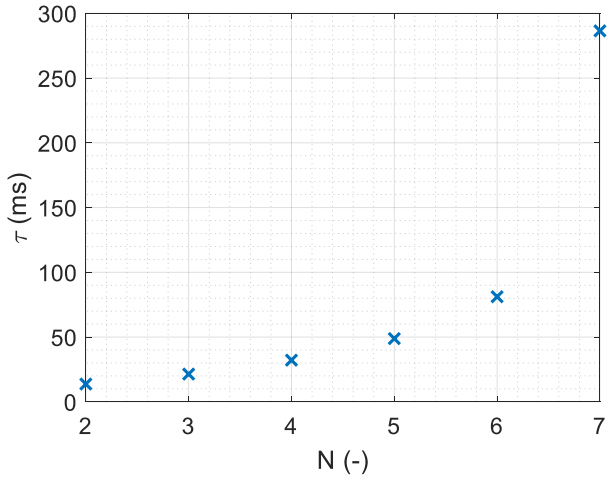

Figure 5.12 Time constant vs average number of data points

5.3.5 Influence of Camera Frame Rate, Loading Frequency and NR on the Thermoelastic Response

In this section, experimental data is used to analyse the influence of different parameters. Simulated data is generated to compare the experimental results obtained with the NR on and off. The experimental results were normalised by dividing the measured ΔT over the target ΔT for both aluminium and 316L stainless steel samples to be comparable for all the loading cases and sample materials. The normalised response ($\Delta T_{measured}/\Delta T_{known}$) is shown in Figure 5.13 with respect to different variables:

(a). **Frame rate**: for a given material, aluminium in this case, loading amplitude (810 N) and frequency (1 Hz), the frame rate does not have an effect on the measured thermoelastic response.

(b). **Loading amplitude**: for a given material (aluminium), loading frequency (1 Hz) and frame rate (25 Hz), the loading amplitude does not modify the measured thermoelastic response.

(c). **Loading frequency and material**: considering aluminium and steel samples, for a given loading amplitude (810 N for aluminium and 1120 N for stainless steel - 50 mK target ΔT) and frame rate (25 Hz), there is an attenuation with loading frequency, as expected as the microbolometer behaves as a low-pass filter.

(d). **Loading frequency with noise reduction on and off**: for noise reduction on and off, for a given material (aluminium), frame rate (25 Hz) and loading amplitude (810 N). It can be seen that with the NR switched on, there is a much higher attenuation with respect to the loading frequency than with NR off. A Simulink model with a time constant of 80 ms (solid red line), which is 10 times higher than the thermal time constant provided by the manufacturer, matched the NR on experimental results. However, a Simulink model with 8 ms time constant (solid black line) matches the NR off experiments.

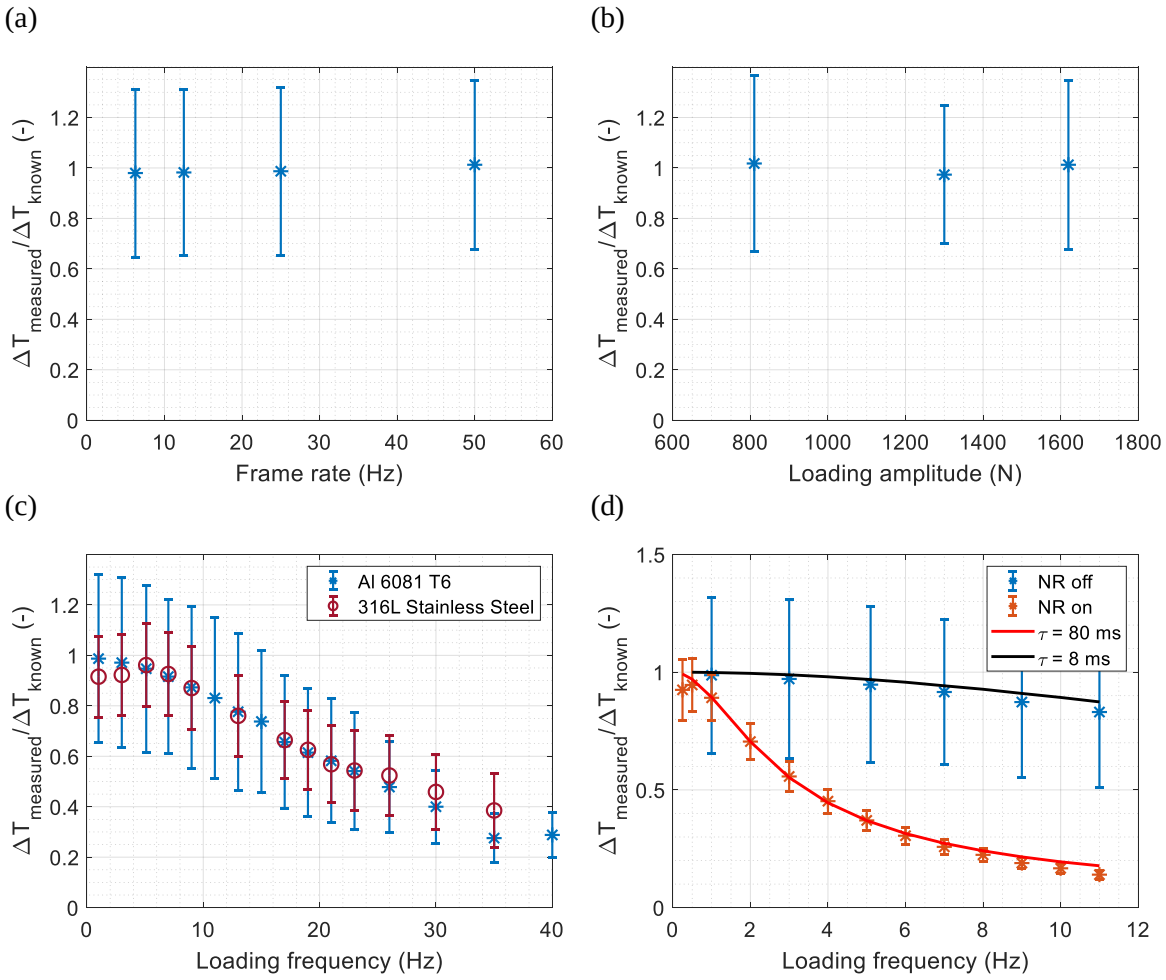

Figure 5.13 Normalised thermoelastic response to study different factors affecting TSA: (a) frame rate (aluminium), (b) loading amplitude (aluminium), (c) loading frequency and material, and (d) noise reduction (aluminium)

To sum up, it has been seen that the microbolometer performance only depends on the loading frequency, and that the noise reduction feature turned on produces a higher attenuation, i.e. higher time constant. It is suggested that the noise reduction on feature averages a number of frames and outputs this average, which is a disadvantage for a sinusoidal load that is continuously changing with time. The simulation carried out in section 5.3.4 suggests that the NR feature may be averaging six frames, as this matches a time constant of 80 ms. In [132], the same IR microbolometer camera was used for TSA, and the results obtained with the NR on, but the effect of this NR feature on the thermoelastic response output from the camera was not studied. Instead, the dependency on the loading frequency, i.e. low-pass filter behaviour, was accounted for by 'calibrating' the data at loading frequency, with the NR feature enabled. However, it is recommended from the work above that NR feature is disabled to avoid adding extra attenuation, especially when testing materials at high loading frequencies (> 10 Hz) to achieve adiabatic behaviour. Nevertheless, a calibration can be obtained for both noise reduction on and off options, which is described and validated in section 5.4.

5.3.6 Impact of Input Waveforms and Mean Temperature Drift Simulation

For microbolometer based TSA experiments, it is necessary to collect data for a long period of time to reduce noise and improve the final TSA results. The downside to capturing data over long periods of time is the potential for drift of the mean temperature on the test specimen. It is therefore important to model the impact of temperature drift on the TSA output. Figure 5.14 shows an example of the normalised temperature signal shifted to zero along time for a single pixel obtained during a TSA experiment with the microbolometer FLIR A655sc. In particular, a central single pixel from a Brazilian disc (as described in Chapter 4) loaded at - 5 ± 2.25 kN at 2.1 Hz loading frequency and sampled at 50 Hz frame rate. It is shown that the signal is obscured by noise, and that the mean temperature drifts over time. Therefore, in this section, the study of different input waveform shapes and signals with a drift to the mean is performed. As previously, extraction of the magnitude ΔV (representative of ΔT) has been done using the least-squares algorithm.

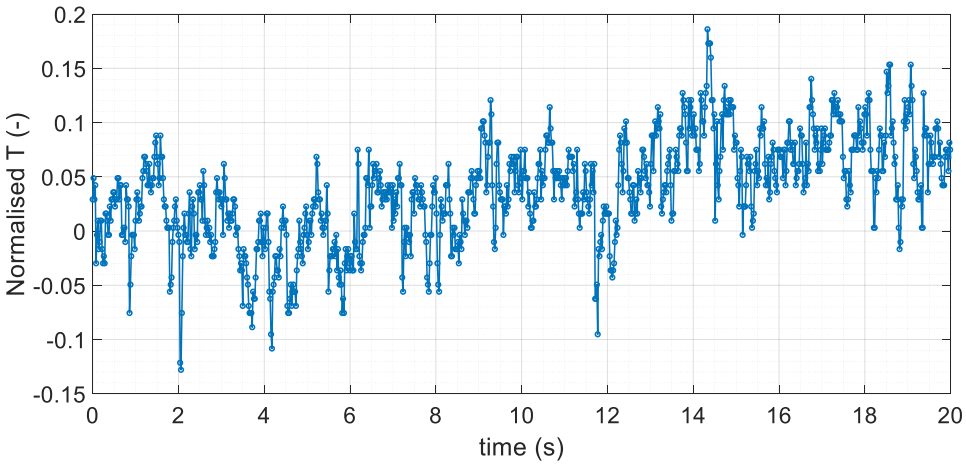

Figure 5.14 Example of normalised temperature shifted to zero vs time of a single pixel during a sinusoidal test of a Brazilian disc loaded at - 5 ± 2.25 kN at 2.1 Hz loading frequency

Variations to the model presented in Figure 5.4 have been done accordingly to produce different waveforms:

- Sinusoid with change in mean drift simulated with the addition of a slope
- Sawtooth wave with a harmonic
- Sawtooth wave with a harmonic and increased in mean
- Variable wave passed through another low-pass filter, which gives rectangular, 'sea wave', and triangular signals depending on the loading frequency

The effect of change in mean has been studied using a sinusoid of 5 Hz frequency and adding to it different values of slope from 0 to 5 gradient levels, hence, there is no constant mean. It can be seen in Figure 5.15 that increasing the slope attenuates the output ΔV. The equation of the curve presented in Figure 5.15 is fitted to

$$\Delta V = -0.0372 \cdot slope + 0.9591 \tag{5.15}$$

Therefore, extra attenuation will take place scaling with the magnitude of mean drift, but the slope values shown in Figure 5.15 are unrealistic for TSA experiments. As an example, for a 2 gradient slope, it means that after 1 second the signal goes up from 0 V to 2 V (which can be translated in terms of temperature as an increase of 2 K in 1 second). However, it would not be possible in any TSA experiment, as the increase in temperature during a cyclic test is of the order of ~0.1 K in 1 second.

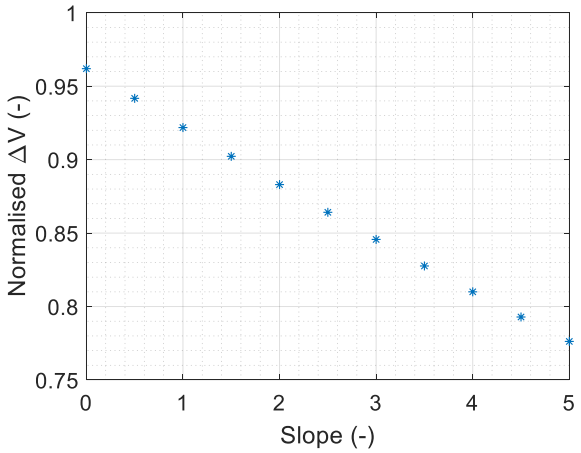

Figure 5.15 Normalised output of 5 Hz frequency sinusoid vs slope added

Figure 5.16 (a) and (b) show the normalised output (normalised ΔV), calculated as $\Delta V_{output}/\Delta V_{input}$, with respect to the loading frequency in (a) for a sawtooth with a harmonic at 10.1 Hz frequency and (b) the same signal as previously but with the addition of a 0.5 gradient slope. The Nelder-Mead Simplex algorithm [21] has been used to extract the time constant of the curves shown in Figure 5.16 (a) and (b) obtaining 7.7 ms and 5.1 ms time constants, respectively. It shows that the least-squares algorithm underestimates the output when the signal is triangular, which is expected as the least-squares algorithm requires a sinusoidal signal. The addition of the slope attenuated the output even more. This demonstrated that the quality of the sinusoidal waveform applied is a consideration; however, it would be unlikely that triangular waveforms would be used during a test and, if they were, then possibly the lock-in or the FFT algorithms should be used to fit the thermal data instead of the least-squares approach.

(a) (b)

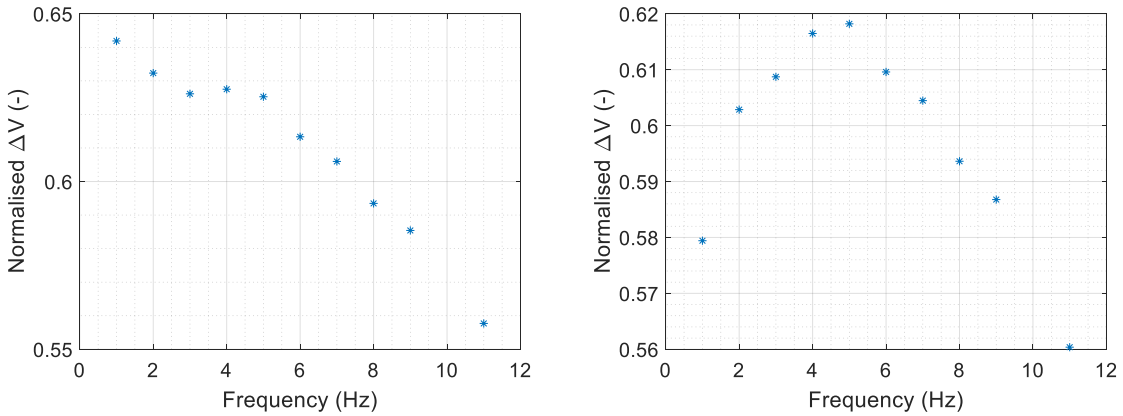

Figure 5.16 Normalised output vs loading frequency of sawtooth signal with (a) an harmonic at 10.1 Hz and (b) an harmonic at 10.1 Hz and 0.5 slope

Figure 5.17 shows the modification to the Simulink model to assess how a variable wave input effects the TSA data extracted from a microbolometer system. Due to the addition of a low-pass filter set at 100 ms or 25 ms, a rectangular signal, constructed by the signal generator, is transformed at the output of the low-pass filter to a 'sea wave' signal at low frequencies and triangular waves at higher

frequencies (see Figure 5.18). The output of this first low-pass filter is extracted to Matlab workspace (first_low_pass variable) to analyse the peak-to-peak amplitude, which is used to normalise the output of the second low-pass filter (simout variable) of 8 ms time constant that simulates the microbolometer. The output of the first low-pass filter is the input to the second low-pass filter.

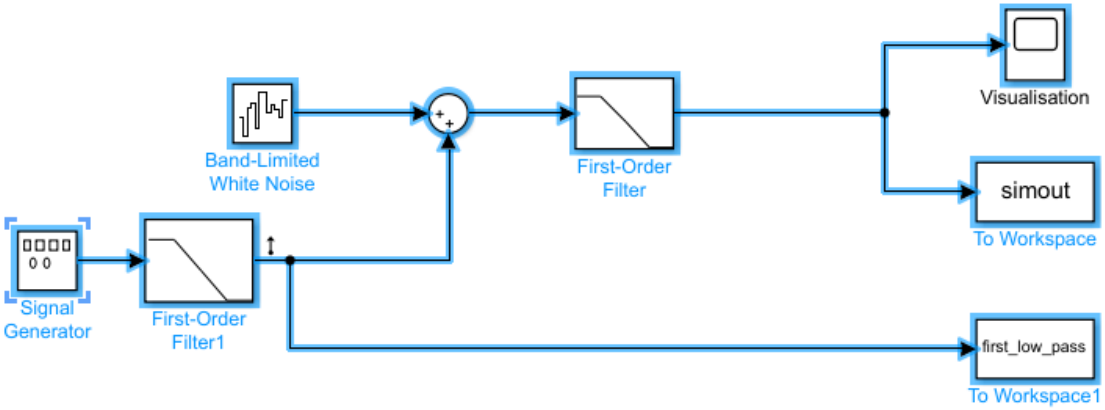

Figure 5.17 Variable wave Simulink model

(a)

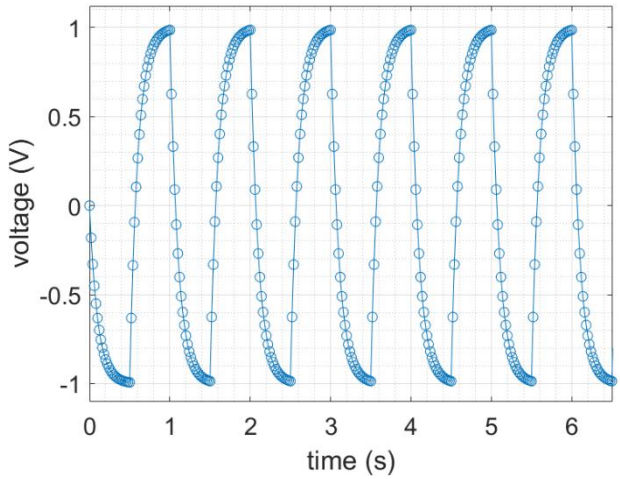

(b)

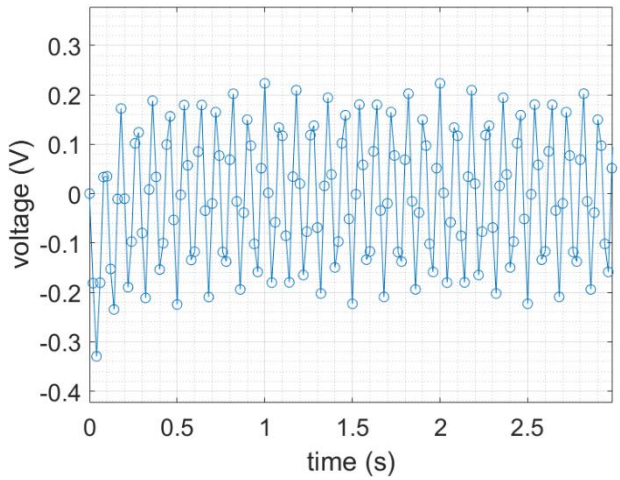

Figure 5.18 100 ms time constant low-pass filter output signal (a) 1 Hz and (b) 11 Hz loading frequencies

Figure 5.19 (a) and (b) show the normalised output of the Simulink model with respect the input frequencies of initial low-pass filters of 100 ms and 25 ms time constant, respectively. It is shown that at lower frequencies, where rectangular and sea waves are present, the least-squares algorithm over predicts the response. However, at higher frequencies, the output is below 1, showing attenuation due to the nature of low-pass filters. Examples can be found in Figure 5.20 where the voltage is shown against time. It demonstrates that the least-squares algorithm requires a sinusoidal signal to output the correct peak-to-peak amplitude, confirming that for different waveform inputs, other algorithms should be considered.

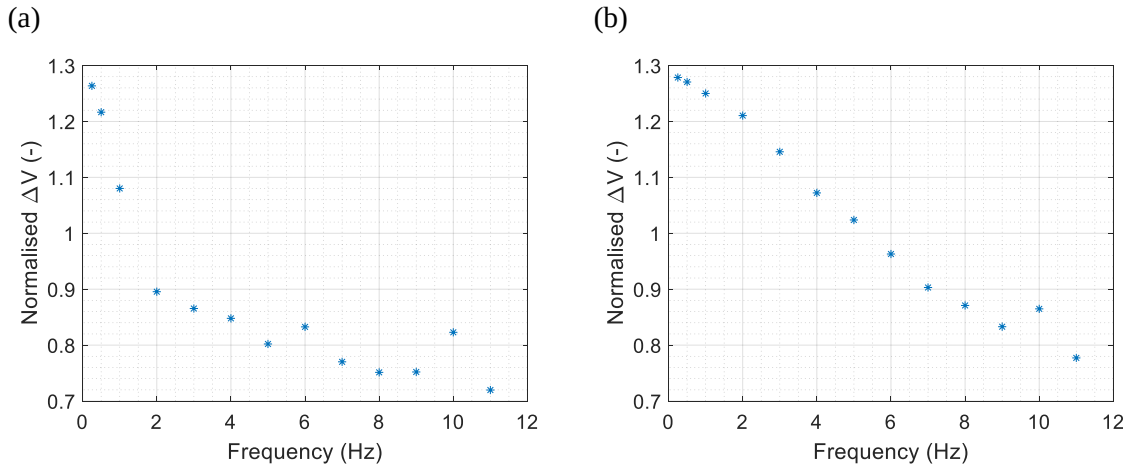

Figure 5.19 Normalised output vs frequency for a variable wave with (a) 100 ms low-pass filter, (b) 25 ms low-pass filter

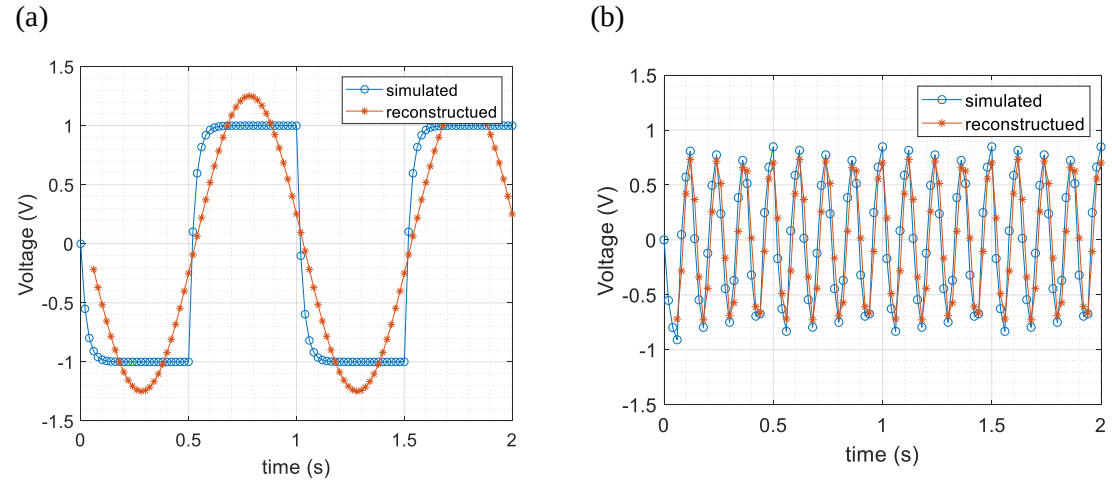

Figure 5.20 Output signal from the model compared with the reconstructed signal from the TSA algorithm of the the 25 ms time constant variable wave at (a) 1 Hz frequency and (b) 8 Hz frequency

5.4 New Unified Calibration Approach to Account for Attenuation in Signal due to Loading Frequency and Noise Reduction

5.4.1 Calibration Technique

To develop the calibration technique, the aluminium and stainless steel samples described earlier were used. Additionally, composite materials were included in the study to investigate any effect of material anisotropy. The GFRP specimens considered are shown in Table 5.4. The GFRP laminate is a 10 ply glass/epoxy prepreg that has been cured in an autoclave for 1h at 120 °C and 4 bar. Both specimens have end tabs of the same thickness and the same unidirectional direction. The length of the 0 UD and 90 UD specimen end tabs are 65 and 55 mm, respectively, and were bonded to the composite laminate using an adhesive film. For the GFRP specimens, the photon detector (FLIR SC5500 - Table 3.2) was used simultaneously with the microbolometer in a back-to-back test to

check that the thermoelastic constant values obtained from the literature given in Table 5.4 are appropriate for the GFRP material and assess the accuracy of the predicted temperature change given in Table 5.5. In contrast with the metallic samples, the GFRP specimens were tested without applying paint as the epoxy resin has a high emissivity [29]. The photon detector frame rate and the integration time were 383 Hz and 1332 μs respectively [133]. Data acquisition for both the photon detector camera and the microbolometer were started at the same time for the composite specimens, but observed on the opposite sides of the composite surface. Both IR detectors collected 2,000 frames in each measurement, however, due to the differences in frame rate of both IR cameras, the microbolometer was capturing data over a much longer time period compared with the photon detector.

Table 5.4 GFRP sample dimensions and thermoelastic constant of each specimen

Specimen	**Gauge Length (mm)**	**Width (mm)**	**Thickness (mm)**	**Thermoelastic constant (MPa^{-1})**
0 UD GFRP	150	33.77	2.36	$3.7 \cdot 10^{-6}$ [29]
90 UD GFRP	152	45.54	2.37	$21.6 \cdot 10^{-6}$ [29]

Table 5.5 Loading cases for the different specimens to achieve a target ΔT of 50, 80 and 100 mK

Coupon	**Loading case 1 (kN)**	**Loading case 2 (kN)**	**Loading case 3 (kN)**
0 UD GFRP	2 ± 1.84	3 ± 2.94	4 ± 3.68
90 UD GFRP	1 ± 0.43	1 ± 0.69	1 ± 0.87
Predicted ΔT (mK)	50	80	100

It was seen that the estimated ΔT values obtained using properties from the literature for a typical UD GFRP did not match with the photon detector measurements. This could be because the properties from the literature were generic, and not for the specific RP-528 pre-preg. It could also be the case that the assumptions in deriving ΔT were not correct; this is the object of the work described in the next chapter of the thesis. For the purposes of the comparative study described here, it was considered that using the measured ΔT values from the photon detector to normalise the measured ΔT values from the microbolometer would be sufficient. The normalising values of ΔT from the photon detector are 68, 115 and 141 mK for the 0 UD sample, and 52, 84, 105 mK for the 90 UD coupon.

Previously in section 5.3.5, only particular cases on the aluminium and stainless steel samples were compared. However, it is possible to show all the experiments on the same figure to show that the only variables affecting microbolometer based TSA measurements are the loading frequency and the NR feature. Figure 5.21 shows a general comparison, where the normalised thermoelastic response vs the loading frequency of all the experiments (materials, frame rates, and loading amplitudes) is presented for the noise reduction on (a) and off (b). The cut-off frequency, calculated using equation (5.13), is 1.99 Hz when the noise reduction is on ($\tau = 80$ ms), but 19.89 Hz when noise reduction is not applied ($\tau = 8$ ms). Figure 5.21 can be linearized by presenting it as a gain Bode diagram (Figure

5.22), i.e. common logarithmic scale, where it can be seen that the attenuated parts of the thermoelastic response follow a linear tendency for loading frequencies higher than the cut-off frequency, as it was shown in section 5.2.

(a)

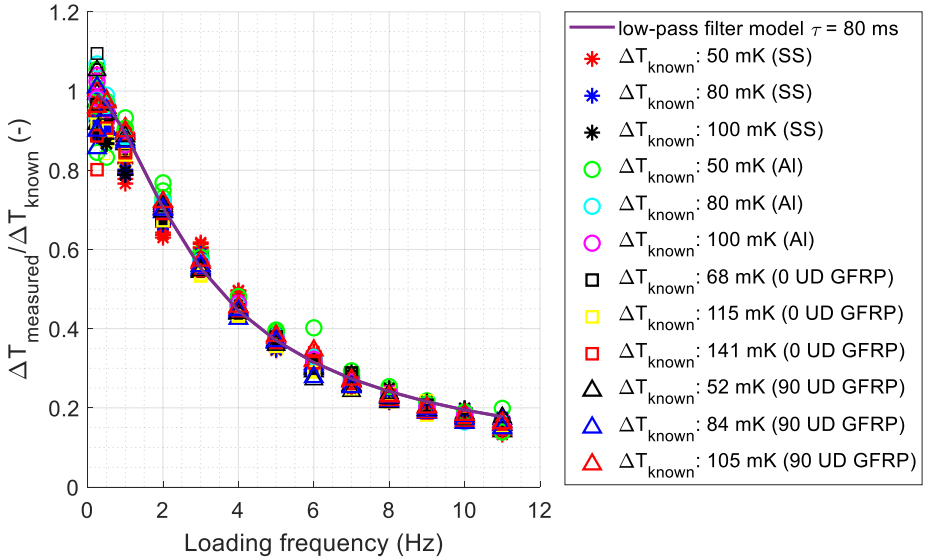

(b)

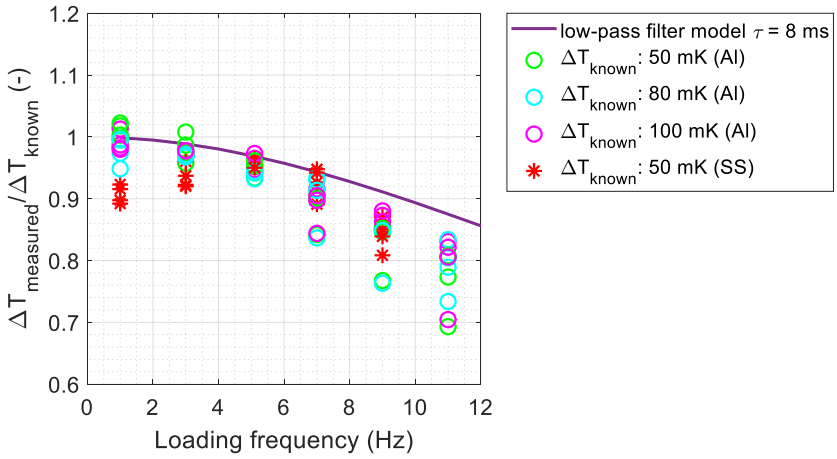

Figure 5.21 Simulink and experimental data comparison (a) NR on and (b) NR off

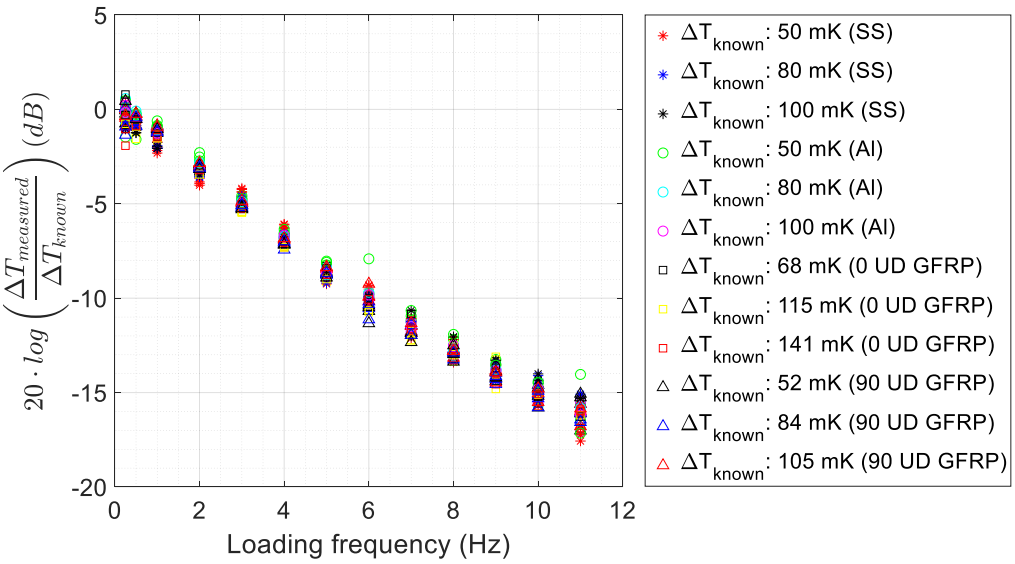

Figure 5.22 Normalised measured temperature change vs loading frequency with the noise reduction on

Figure 5.22 shows that the attenuation is independent of material and depends exclusively on the loading frequency. Based on this finding, a suitable calibration technique that corrects for the dependency on loading frequency when applying TSA with microbolometer can be devised. The proposed approach simply requires a coupon specimen with a known thermoelastic constant such as the 316L stainless steel. The coupon is loaded in tension, with an applied stress that produces a known ΔT, and thermal image series are collected with the NR on and off over a range of loading frequencies. The calibration parameter, CP, is defined as follows:

$$CP = \frac{\Delta T_{known}}{\Delta T_{measured}} \tag{5.16}$$

where ΔT_{known} is the calculated temperature change for the applied stress and $\Delta T_{measured}$ is the measured temperature change obtained from the microbolometer thermal image series using the image processing algorithm.

When the common logarithmic fit is performed to the calibration parameter, and presented with respect to the loading frequency, the trend is linear as shown in Figure 5.22, the following relationship can be defined:

$$20 \log CP = A \cdot f_0 + B \tag{5.17}$$

where f_0 is the loading frequency (Hz), A is the slope (Hz^{-1}) and B is the intercept (-).

The CP can be extracted from equation (5.17) as follows :

$$CP = \sqrt{A \cdot f_0 + B} \tag{5.18}$$

so that it can be used to calibrate other materials when using TSA with the microbolometer system and NR feature considered for a particular f_0.

If the time constant of the microbolometer is known, which for this particular microbolometer depends on the NR feature setting, the CP can also be obtained analytically from the normalisation and inverse of equation (5.5) or (5.11) as follows:

$$CP = \sqrt{1 + \omega^2 \tau^2} \tag{5.19}$$

where $\omega = 2\pi f_0$. Therefore, the CP for the NR feature on requires an input of $\tau = 80$ ms while for the NR disabled option a $\tau = 8$ ms.

As an example, the calibration curves for the NR feature activated are shown in Figure 5.23 for the frame rates 6.25, 12.5, 25 and 50 Hz, respectively, and for all experiments. For a more detailed comparison, the slope and intercept are presented in Table 5.6 for every frame rate and sample material showing a good agreement among them.

Table 5.6 Slope (A) and intercept (B) for different frame rates and sample materials

Frame rate	**Coupons**	**A (Hz^{-1})**	**B (-)**	**R^2 (-)**
50 Hz	**Stainless Steel**	1.547	0.3773	0.9911
	Aluminium	1.584	0.07332	0.9938
	0UD GFRP	1.56	0.4916	0.9940
	90 UD GFRP	1.611	0.01913	0.9913
25 Hz	**Stainless Steel**	1.453	0.6782	0.9901
	Aluminium	1.53	0.05394	0.9907
	0UD GFRP	1.496	0.4899	0.9897
	90 UD GFRP	1.53	0.279	0.9891
12.5 Hz	**Stainless Steel**	1.442	0.629	0.9907
	Aluminium	1.484	0.1536	0.9854
	0UD GFRP	1.476	0.6235	0.9896
	90 UD GFRP	1.507	0.3199	0.9845
6.25 Hz	**Stainless Steel**	1.418	0.7458	0.9907
	Aluminium	1.528	0.01126	0.9940
	0UD GFRP	1.5	0.5326	0.9908
	90 UD GFRP	1.527	0.2625	0.9834

Considering all the experimental data, the mean calibration fitting for TSA with the FLIR A655sc and the NR feature on is

$$20 \log CP = 1.512 \cdot f_0 + 0.3627 \tag{5.20}$$

with 0.9915 R^2 value.

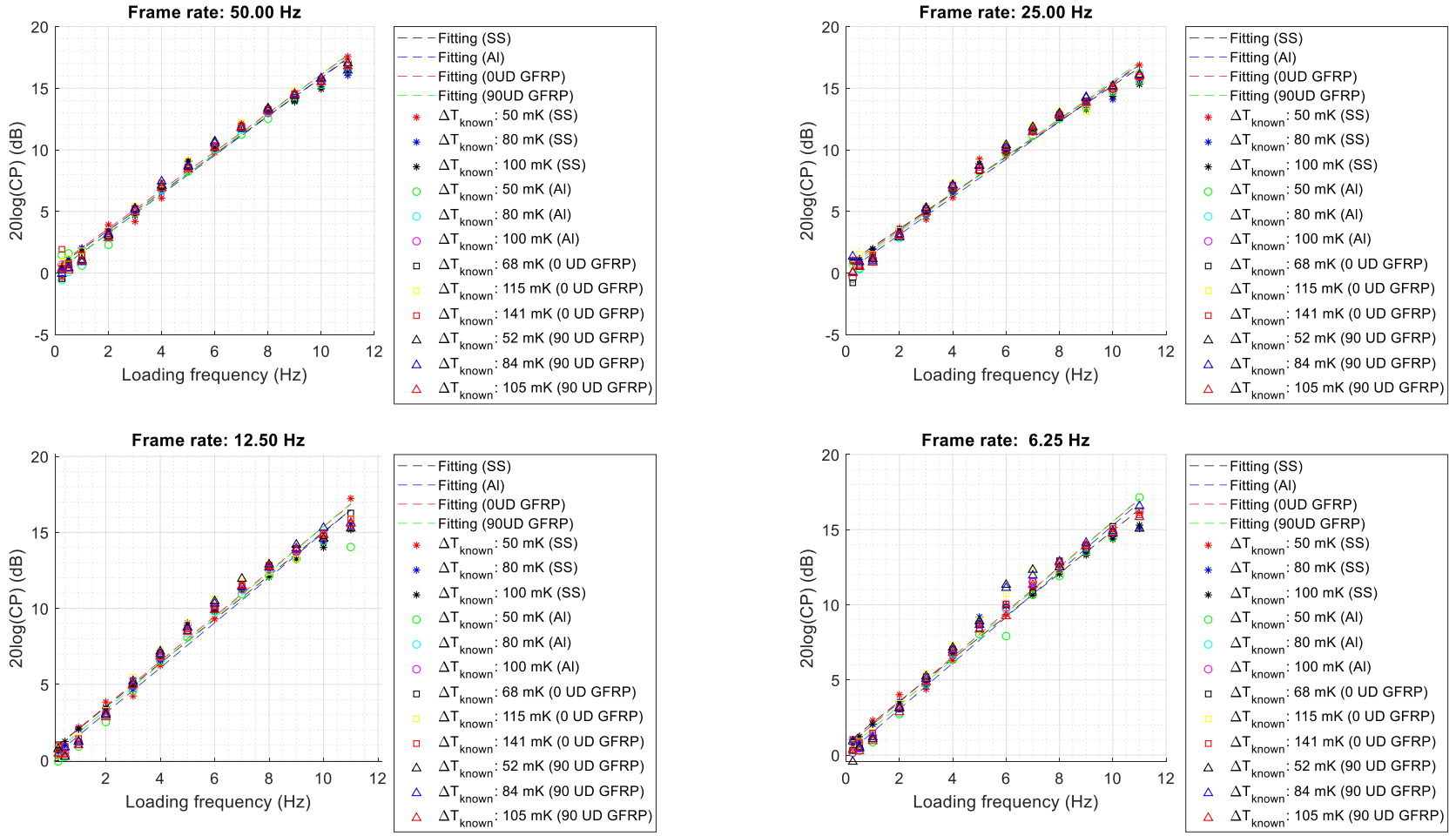

Figure 5.23 Calibration fitting for stainless steel, aluminium and 0 UD and 90 UD GFRP specimens (noise reduction on)

The calibration for TSA measurements with the NR off can be performed following the same procedure based on experimental data, however, it is possible to use a Simulink model to obtain the CP as the time constant is provided by the manufacturer. On the contrary, when the NR is on, it was observed that the time constant provided by the manufacturer is no longer valid for TSA, hence, experiments are essential to determine the CP.

The calibration is performed after ΔT has been obtained by the image processing and simply involves multiplying the measured ΔT by the calibration parameter, CP. Hence, previous knowledge of the structure in terms of geometry or material is not required as suggested in [109]. The calibration technique presented here is also different than the one performed by Rajic and Rowlands in [21] where the calibration was performed before the processing of the thermal data series, hence, applied to all the collected frames, which requires a longer processing time than the calibration presented in this thesis.

Validation of the calibration technique is presented in the following section. A damaged CFRP specimen was inspected with the FLIR A655sc microbolometer and a photon detector. The calibrated ΔT measured with the microbolometer is compared with the ΔT measured with a photon detector along a vertical line. Furthermore, the Brazilian disc was used to validate the microbolometer calibration for both NR options against the analytical solution for the stress.

5.4.2 Application of the Calibration Parameter to Experimental Data

5.4.2.1 Damaged CFRP Specimen

It was demonstrated that the calibration technique does not depend on the sample material, specimen temperature or magnitude of response, only on the loading frequency and the NR feature. Therefore, it can be used to calibrate the results obtained with the microbolometer on a range of materials, and on systems exhibiting variations of thermoelastic response, e.g. in the presence of a crack or stress gradients.

To validate the capability of using a calibration parameter, a demonstrator in the form of a damaged CFRP specimen was used. This was manufactured using unidirectional carbon fibre prepreg containing an embedded manufacturing defect in the form of artificial fibre waviness. The schematic of the artificial waviness can be seen in Figure 5.24 showing that the lay-up of the sample is $[0,90]_{6s}$. The inserted defect developed a delamination crack after an application of 67.5 MPa stress level, which was detected on an X-ray CT-scan (Figure 5.25 and Figure 5.26). The specimen was loaded at 25 kN mean and 20 kN amplitude at 5 Hz loading frequency. The dimensions are 150 mm long,

35.81 mm wide and 5.16 mm thick. Figure 5.27 presents a sketch of the CFRP sample with the dimensions and location of the crack following the coordinate system shown in Figure 5.25.

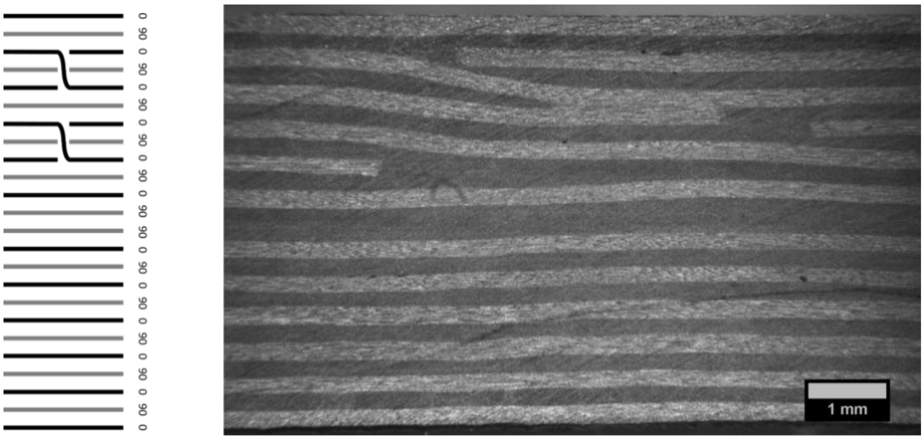

Figure 5.24 CFRP sample lay-up with embedded defect, thickness view

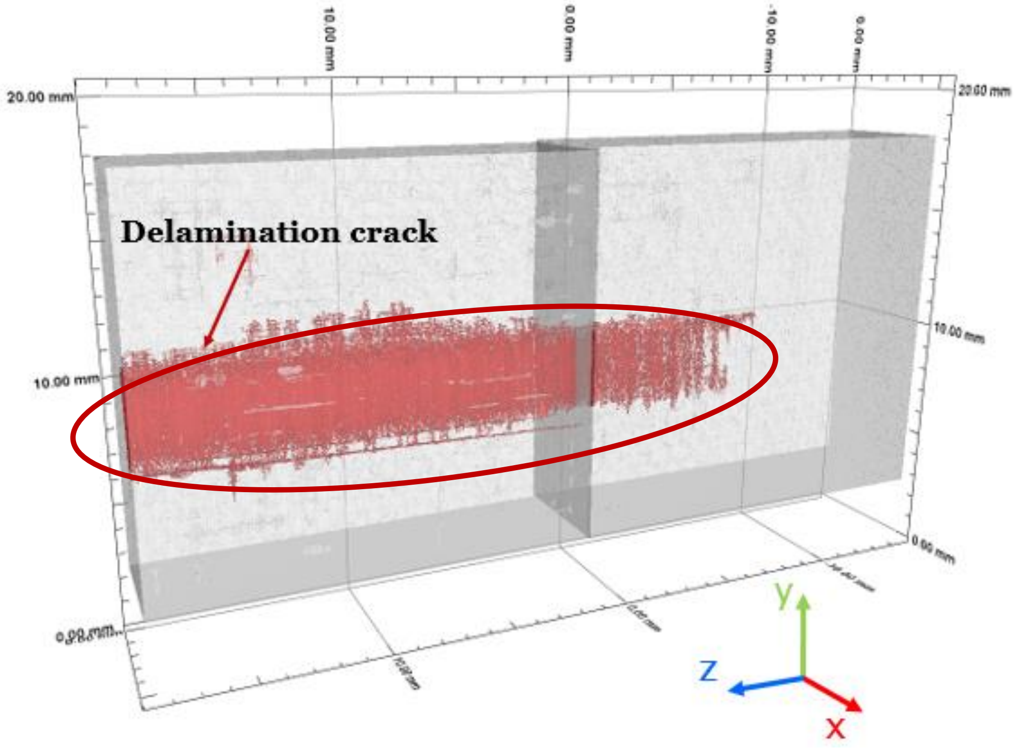

Figure 5.25 3D CT-scan of the developed delamination crack after 67.5 MPa stress level

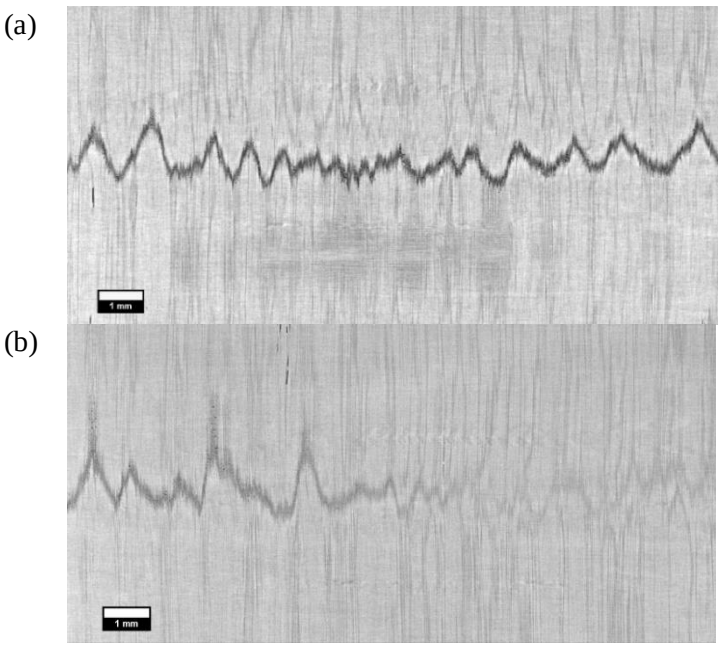

Figure 5.26 CT-scan images front view, (a) main body of the cracked region, (b) towards the edge of the cracked region

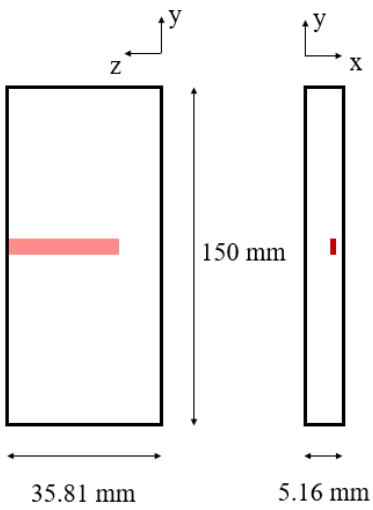

Figure 5.27 CFRP specimen dimensions and location of the crack

The TSA results for the CFRP sample are presented in Figure 5.28 where the ΔT is shown in (a) for the uncalibrated microbolometer, in (b) for the calibrated microbolometer and in (c) for the photon detector. Bicubic image interpolation was applied to downsample the microbolometer IR data to have the same dimensional resolution as the photon detector, which is 0.46 mm/pix, to compare quantitatively the thermoelastic response of the sample captured with both IR detectors. The microbolometer was calibrated by scaling the magnitude of ΔT by 2.78, which corresponds to the CP at 5 Hz loading frequency (NR on). It is shown that the full-field temperature change maps from the photon detector and the calibrated microbolometer are nearly identical in terms of ΔT magnitude. The similarity between the photon detector and calibrated microbolometer is further confirmed by

comparing a line profile (x = 8 mm) across the surface shown in Figure 5.29. It can be seen that there is more noise present in the photon detector data in comparison with the microbolometer data. The lower noise can be attributed to more frames collected with the microbolometer (8,000 frames) versus the photon detector camera (1,000 frames). Additionally, the photon detector used in this study (FLIR SC5500 - Table 3.2) was at the end of its life, which can also increase camera noise. The microbolometer ΔT fields present edges effects due to the motion that affects all the data. The photon detector data was motion compensated by applying pencil markers on the surface and tracking the movement with Altair software. Hence, motion compensation routines are required to improve microbolometer TSA field data.

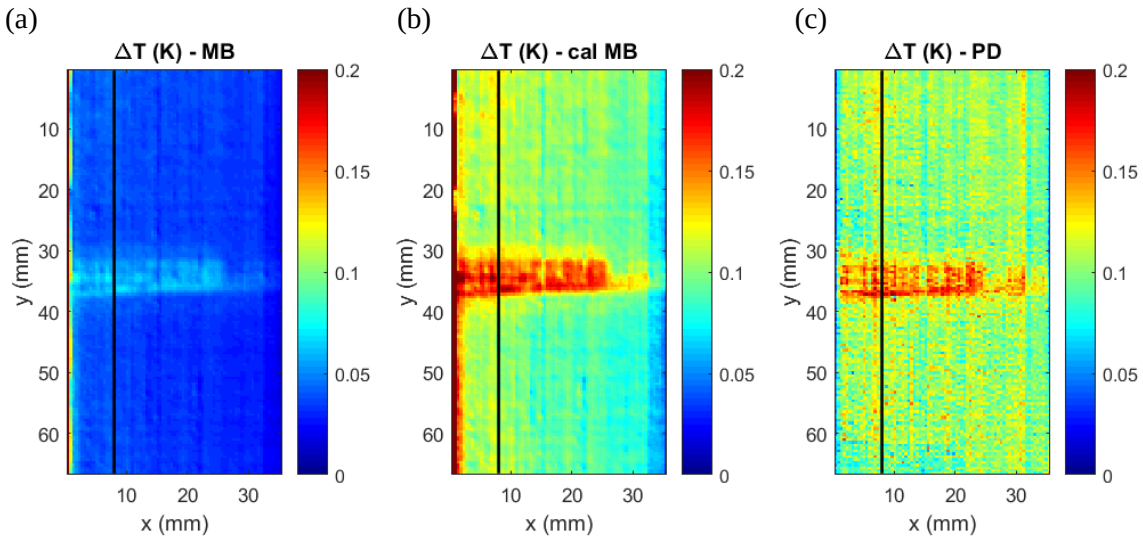

Figure 5.28 ΔT results obtained in a CFRP specimen with (a) uncalibrated (uncal) microbolometer (MB), (b) calibrated (cal) microbolometer (MB) and (c) photon detector (PD)

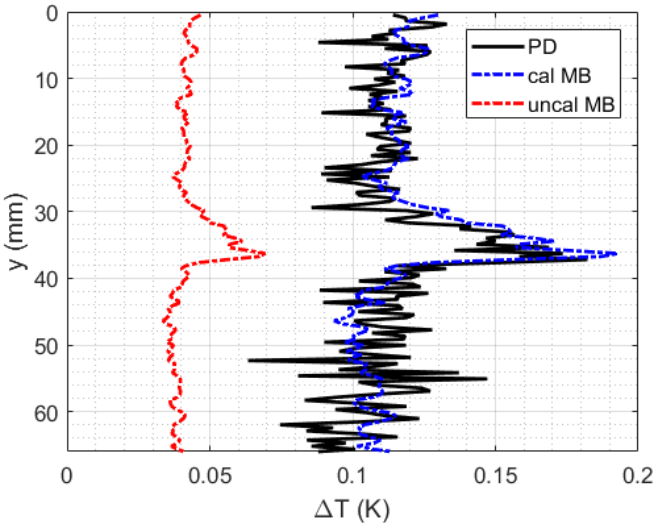

Figure 5.29 Temperature change of the CFRP specimen obtained with TSA along the vertical length at 8 mm from the left edge with the photon detector (PD) and the calibrated (cal) and uncalibrated (uncal) microbolometer (MB)

5.4.2.2 Aluminium Brazilian Disc Specimen

The aim of this section is to validate the calibration for both NR on and off on an isotropic material sample with stress gradient, that is a Brazilian disc. The experiments were conducted, as described in Chapter 4, with the microbolometer NR on and off, at different loading frequencies (2.1, 5.1 and 10.1 Hz), and a sinusoidal load of - 5 ± 4.5 kN.

Figure 5.30 shows the ΔT field of the experiments at 2.1 Hz loading frequency obtained at 50 Hz frame rate with the NR feature activated in (a) and disabled in (b), showing that ΔT with the NR off is much higher than with the NR on.

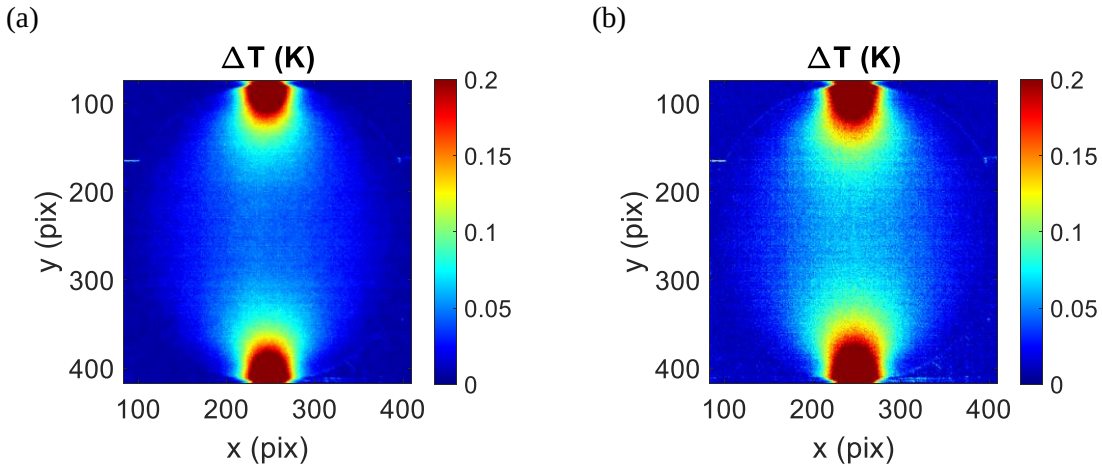

Figure 5.30 ΔT field obtained with the microbolometer camera at 50 Hz frame rate and loaded at 2.1 Hz loading frequency for (a) NR on and (b) NR off

The ΔT mean of a 4 x 4 pixel region at the centre of the disc was compared across the loading frequencies considered and for both NR feature options. The results are shown in Figure 5.31, where it can be seen that the ΔT attenuation when the loading frequency increases is significant when the noise reduction feature is on. Additionally, the error bars are significantly larger for the noise reduction off than on, as expected.

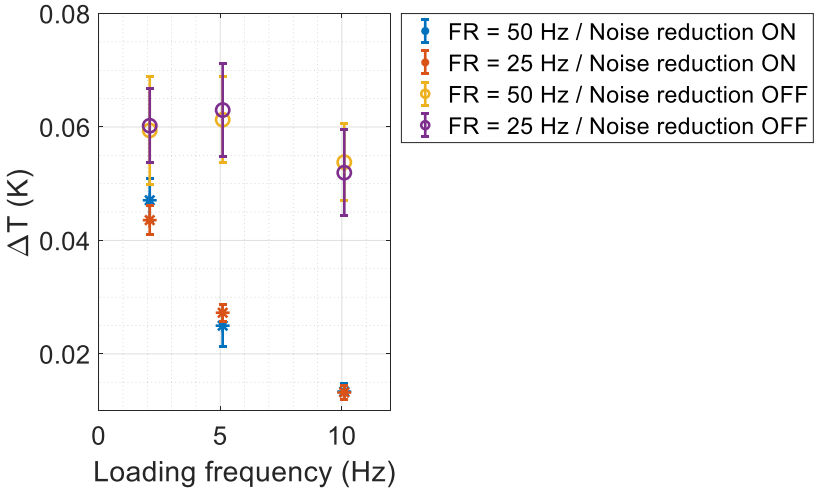

Figure 5.31 ΔT mean value over a central 4x4 pixel area vs loading frequency comparing 25 and 50 Hz frame rates of the FLIR A655sc and the noise reduction feature

Using equation (4.6) and using the thermoelastic constant given in Chapter 4, Figure 5.32 shows an example of the stress field obtained from the disc loaded at 10.1 Hz loading frequency and with the microbolometer camera collecting data with the NR off. The vertical line through the centre of the disk shows the region used to compare experimental and analytical data.

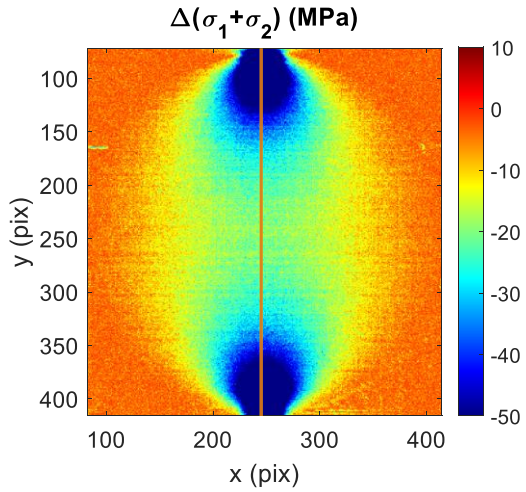

Figure 5.32 Stress field of the 10.1 Hz loading frequency experiment with the noise reduction off and 50 Hz frame rate

The comparison between the experimental data and the theory is done along the vertical line (x = 0 mm for the analytical stresses presented in equations (4.3) and (4.4)), which corresponds to the experimental data at 250 pix. Therefore, the theoretical stresses along the vertical line are

$$\sigma_{xx}^{x=0} = \frac{F}{\pi t R} \tag{5.21}$$

$$\sigma_{yy}^{x=0} = \frac{F}{\pi t R}\left[1 - \frac{4R^2}{R^2 - y^2}\right] \tag{5.22}$$

Figure 5.33, Figure 5.34, and Figure 5.35 show the stress comparison between the experiments and theory along the vertical line for the experiments performed at 2.1, 5.1 and 10.1 Hz loading frequency, respectively. They show the comparison between the NR feature on and off before and after the calibration. It can be seen that there is significant attenuation in all frequencies when the NR is on before calibrating the data, but once the data has been calibrated, no difference can be seen between the NR feature on and off.

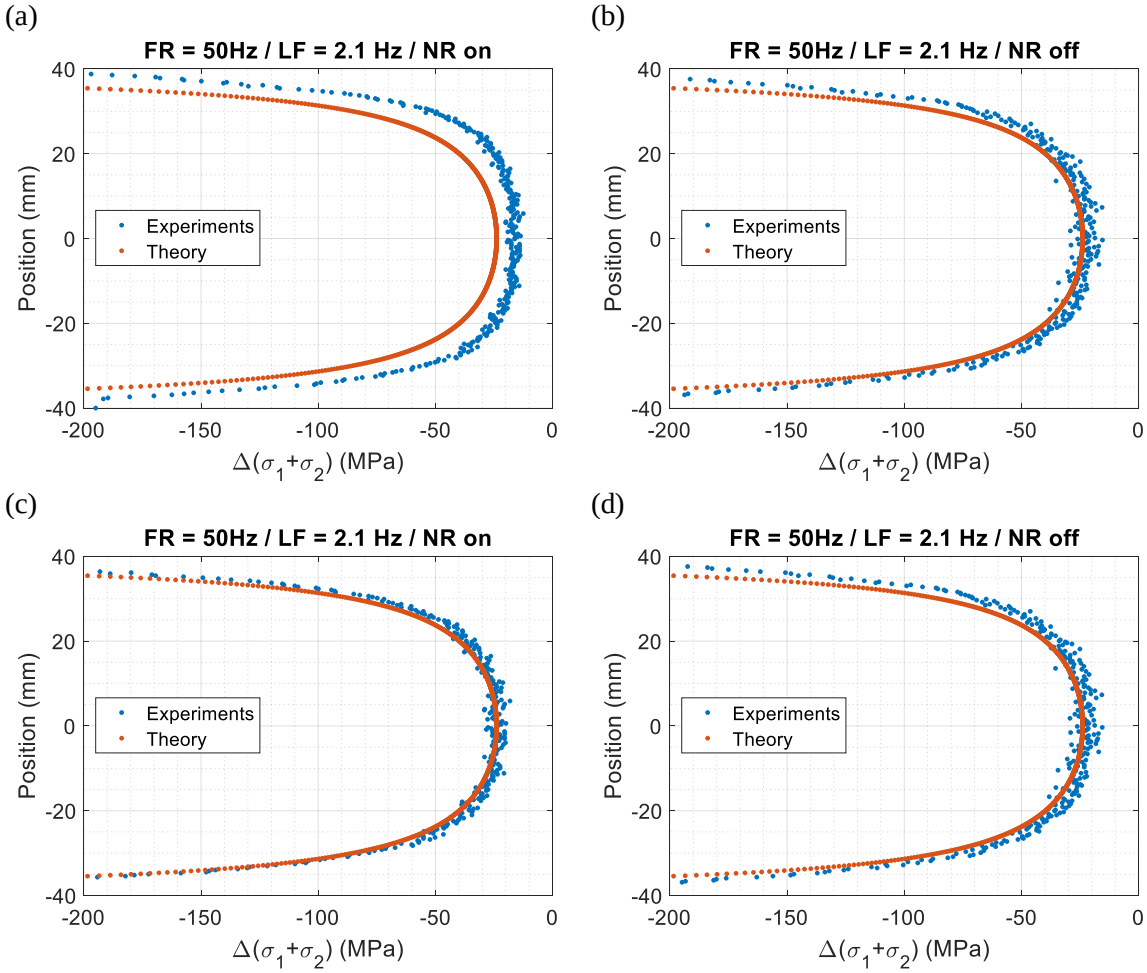

Figure 5.33 Vertical position vs stress of the Brazilian disc experiment at 9 kN peak-to-peak load and 2.1 Hz loading frequency with FLIR A655sc recording at 50 Hz frame rate (a) uncalibrated noise reduction on (b) uncalibrated noise reduction off, (c) calibrated noise reduction on and (d) calibrated noise reduction off

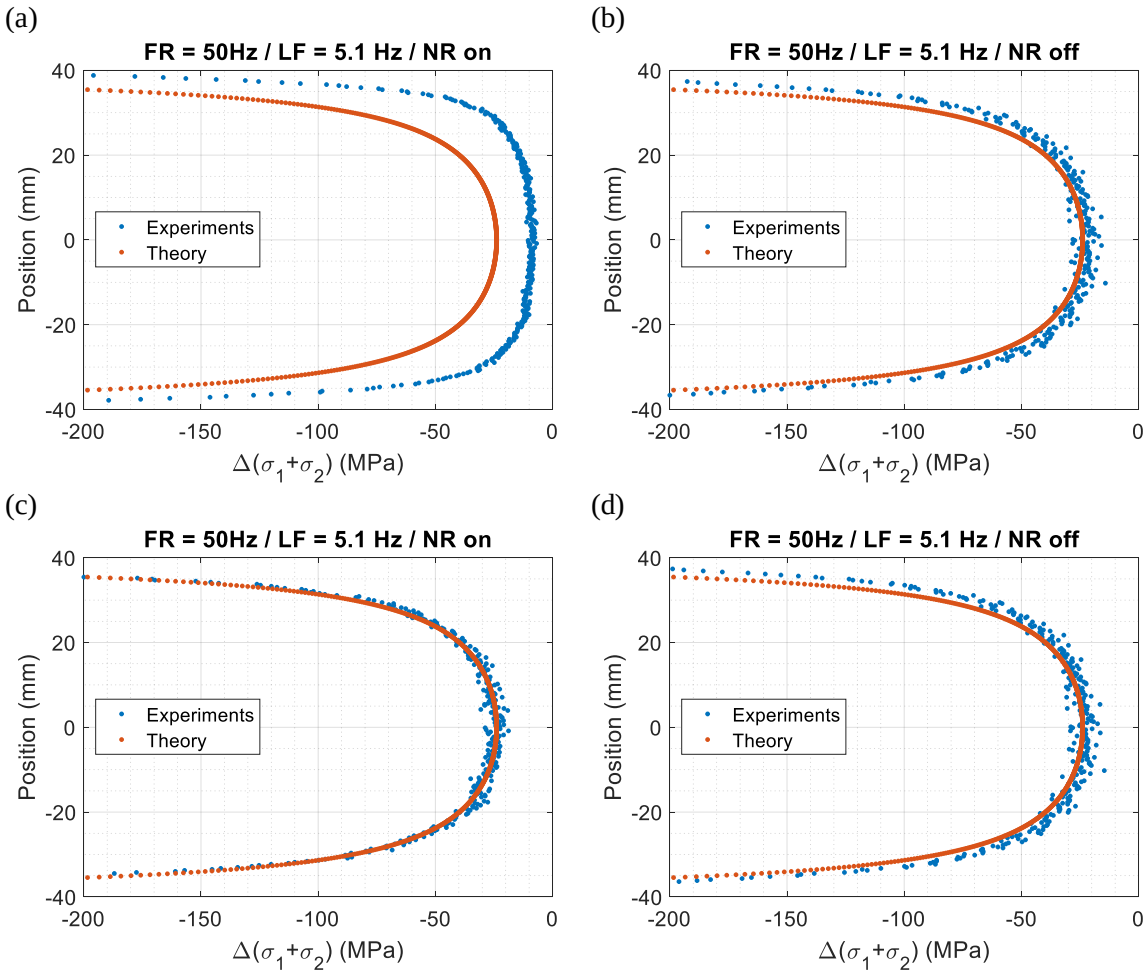

Figure 5.34 Vertical position vs stress of the Brazilian disc experiment at 9 kN peak-to-peak load and 5.1 Hz loading frequency with FLIR A655sc recording at 50 Hz frame rate (a) uncalibrated noise reduction on (b) uncalibrated noise reduction off, (c) calibrated noise reduction on and (d) calibrated noise reduction off

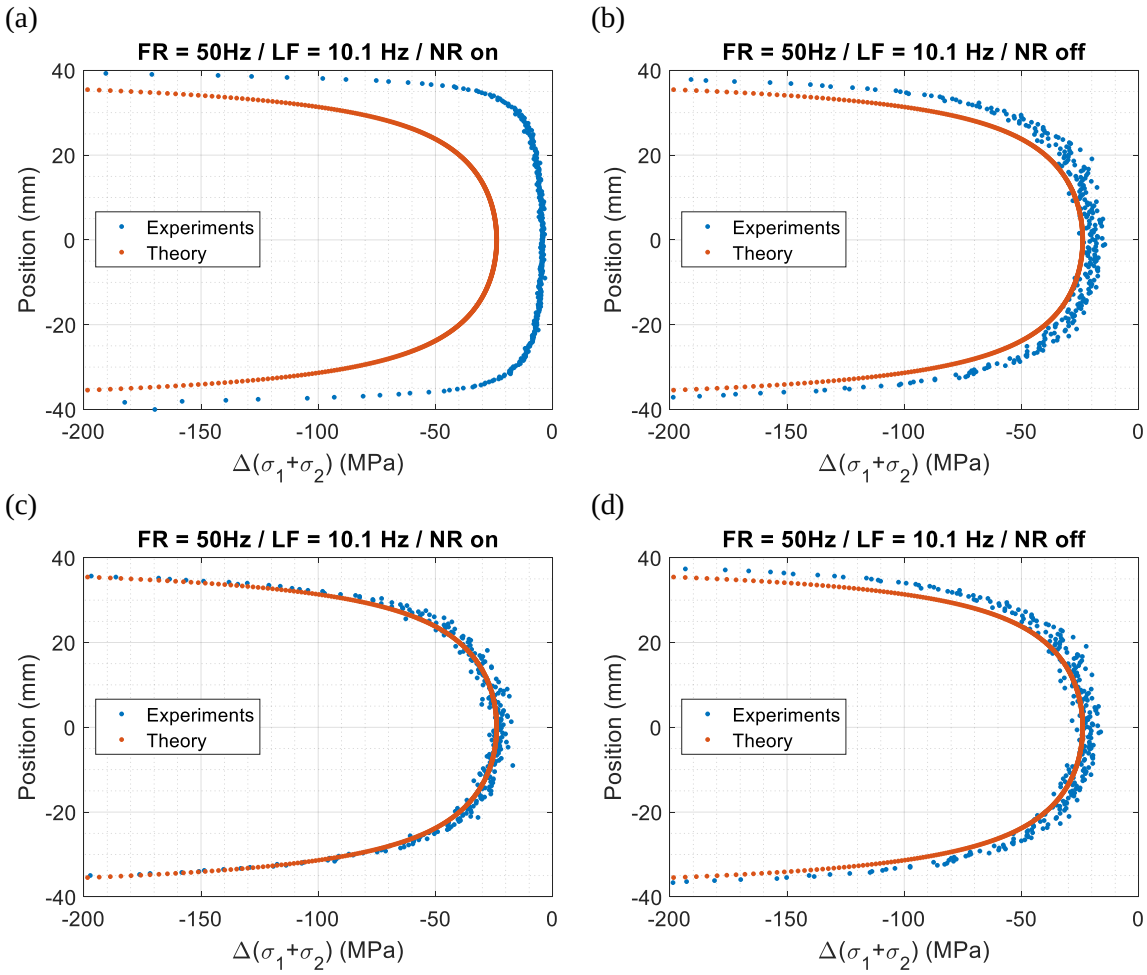

Figure 5.35 Vertical position vs stress of the Brazilian disc experiment at 9 kN peak-to-peak load and 10.1 Hz loading frequency with FLIR A655sc recording at 50 Hz frame rate (a) uncalibrated noise reduction on (b) uncalibrated noise reduction off, (c) calibrated noise reduction on and (d) calibrated noise reduction off

5.5 Summary

An analytical procedure based on Matlab Simulink was devised to assess how various features in the thermal image series affect the application of microbolometers to TSA. It was seen that for dynamic tests such as cyclic loading, and, particularly, at higher loading frequencies, the microbolometer behaves as a low-pass filter, which has an effect on attenuating the output magnitude and shifting the phase of the recorded temperature. The low-pass filter behaviour is driven by an inherent fixed time constant of the microbolometer sensor material, associated with the physical principles of how it converts IR radiation to an electrical signal.

It was shown that in-built NR feature further attenuates the thermal data from a transient scene and effectively increases the time constant which has a significant effect on the ΔT derived from the thermal image series. Using an optical chopper, the thermal time constant with NR off was

determined as ‘below 8 ms’, which matched with the value provided by the manufacturer. However, with the NR on, the time constant measured did not match the manufacturer’s value as accurately as with the NR off. To model the NR feature, a rolling average approach was used, allowing the level of noise reduction to be adjusted by changing the number of averaged data points in the signal. The model tested different numbers of averaged points (to change the level of NR) across different loading frequencies to test the attenuation on the TSA data. The study showed an increase of the time constant leading to an exponential attenuation when the number of averaged data points increased. Different TSA experiments were carried out to assess the effect of the camera frame rate, loading frequency, NR feature and material. It was shown the low-pass filter behaviour of the microbolometer and the increase of 10 times the time constant occurred only when the NR feature was activated. However, the camera frame rate, material, and loading amplitude did not have an effect on the measured ΔT with the microbolometer.

Due to the lack of an analogue input port in the camera to capture the load signal from the test machine, the loading frequency is inputted manually by the user into the least-squares algorithm. Results show that the algorithm behaves as a notch filter that rejects signals outside the loading frequency, and therefore improves the signal to noise in the system. Hence, it is important that the loading frequency is correctly and accurately entered into the software. The analysis of the SNR showed that the NETD does not have a large effect, as the output for different SNR was extracted and matched with the input. Therefore, although the NETD is of the order of the thermoelastic response usually obtained with TSA, the least-square algorithm is capable of removing the noise due to the NETD, which is related to the notch filter behaviour.

The shape of the signal waveform was shown to affect the level of attenuation in the TSA data. Different signal shapes were tested and processed with the least-squares algorithm. It is shown that the least-squares algorithm overpredicts rectangular and sea-wave signal shapes, but underpredicts triangular signals. It is therefore important that a sinusoidal waveform is used with the least-squares algorithm. For signals such as rectangular and triangular, other algorithms such as lock-in are better suited.

To compensate for signal attenuation in the processed ΔT, a calibration technique, which depends on the loading frequency and the NR feature, was constructed. The calibration approach was applied and validated on a CFRP test specimen with an embedded crack. The experiments were performed with a photon detector and a microbolometer with the NR feature on. The comparison of ΔT between the calibrated microbolometer, and photon detector at the same spatial resolution matched closely. Additionally, the calibration parameter was demonstrated on a Brazilian disc sample with the NR featured turned on and off. The study showed that as long as the time constant of the camera and the different features of the camera are known and well understood, the new developed calibration

parameter can be successfully applied for quantitative TSA. The calibration parameter is shown to be tied to the loading frequency and noise reduction feature, but is independent of the camera's frame rate, and the material of the test specimen studied.

The next step is to understand the source of the thermoelastic response in orthotropic composite materials, as it was seen that the estimated ΔT for GFRP coupons did not match with the ΔT measured with a photon detector. Chapter 6 presents a procedure to quantify the thermoelastic response from orthotropic laminated composite materials using DIC. Additionally, the microbolometer based TSA technique should be validated for use on composite structures, i.e. T-joint formed by different materials. Hence, Chapter 7 presents the initial work on the T-joint testing with microbolometer based TSA and DIC performed simultaneously to integrate both data sets.

Chapter 6. Quantification of Thermoelastic Response from Laminated Composites by Combining TSA and DIC

6.1 Introduction

The thermoelastic response from orthotropic laminated composites is driven either by the temperature change in the resin-rich surface layer or the fibre reinforced substrate layers and is dependent on the loading frequency used in the experiments, where heat transfer plays an important role. However, definitively identifying the 'source' of the thermoelastic response for a general fibre reinforced polymer composite material has remained elusive. In this chapter, a procedure is established and demonstrated on two well-characterised glass and carbon reinforced composite material systems that enables identification of the source of the thermoelastic response. The procedure is based on the application of Digital Image Correlation (DIC) at the same time as the TSA. As TSA requires a cyclic load, a new approach is devised where the strains obtained from the DIC are processed using the least-squares algorithm developed for TSA, which is named 'Least-Squares DIC' (LSDIC). The procedure follows the same concept for undersampled data as LIDIC. However, it presents the same advantages as the least-squares algorithm for TSA, i.e. reduced processing time and not affected by non-integer number of load cycles. The LSDIC procedure is validated in Appendix B. In this work, the camera used was the Telops FAST M2K photon detector as it was essential to use loading frequencies greater than the cut-off frequency associated with the microbolometer to assess when adiabatic conditions had been achieved in the composite laminates. Although the calibration procedure described in Chapter 5 could have been adopted to account for the reduction in response, it was decided that the calibration would integrate an additional potential inaccuracy. The measurement of the strain fields enables an independent 'measure' of the thermoelastic response to be calculated using Classical Laminate Theory (CLT), without any influence of heat transfer. The theoretical thermoelastic response based on the LSDIC strains is calculated for the resin-rich layer, the surface ply and homogenised through the entire laminate from specimens with different stacking sequences and compared with the measured thermoelastic response. The strains obtained from the LSDIC are validated against strain gauge measurements. The thickness of the paint and surface resin-rich layer are obtained from micrographs and included in the analysis. It is demonstrated that the new approach enables the source of the thermoelastic response to be established categorically. The effect of differences in fibre volume fraction and surface resin layer resulting from the manufacturing process are highlighted, as well as the influence of paint

coating. Thereby emphasising the importance of the experimental calibration, facilitated by the procedure proposed in this chapter, for quantitative TSA of laminated composite components.

The purpose of the work described in this chapter is to understand the nature of the thermoelastic response by introducing an independent measure of the in-plane strains without any influence of heat transfer using the Digital Image Correlation (DIC) technique [14]. In DIC, a speckle pattern applied to the surface of the sample is tracked while the sample is deforming. For sinusoidal loading conditions, it is possible to obtain the change in strain, $\Delta\varepsilon$, from DIC by using the same algorithm as for TSA [22]. In this work, the process used is based on the least-squares algorithm, and the methodology is referred to as 'Least-Squares DIC' (LSDIC). The strains derived from the LSDIC are validated against strain gauge readings, and it is demonstrated that TSA can be conducted with LSDIC to provide full-field data relating to both the stress (TSA) and strain (DIC) fields. The application of LSDIC alongside TSA not only removes the need to have a priori knowledge of many mechanical properties, but also any inconsistencies in the loading by eliminating the need to calculate the stresses from the applied load.

Strips of multidirectional symmetrically laminated composite material loaded in tension are studied. Assuming there is no damage in the material in its virgin as manufactured state, the DIC measure of surface strain allows the global (overall laminate) and the ply-by-ply stresses to be determined using only the measured elastic constants. Section 6.2 describes the three different scenarios that are considered for the source of the thermoelastic response: 1) the stresses in the resin-rich surface layer, 2) the stresses in the orthotropic surface ply and 3) the global laminate mechanical response. The nomenclature is explained diagrammatically in Figure 6.1.

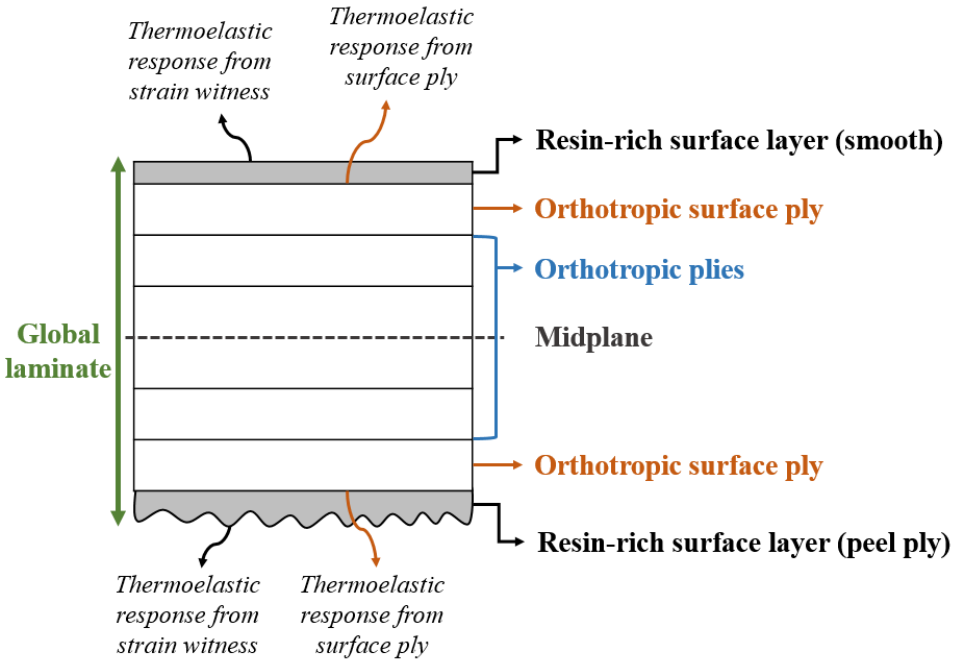

Figure 6.1 Cross-section of multi-directional symmetric laminate showing the nomenclature

Both low conductivity Glass Fibre Reinforced Polymer (GFRP) and high conductivity Carbon Fibre Reinforced Polymer (CFRP) are studied, manufactured from two well characterised composite material systems, RP-528 [134] and IM7/8552 [135, 136], respectively. A detailed survey of the literature alongside a comprehensive mechanical testing campaign provides the relevant material properties to calculate ΔT from the LSDIC strains for the three scenarios. Factors such as paint coating, resin-rich layer thickness and fibre volume fraction are considered. Importantly, the effect of surface emissivity of the material is included in the approach facilitated by measurements against a blackbody source. A significant amount of experimental data has been generated to provide the results described through the chapter. All data supporting this study are openly available from the University of Southampton repository at https://doi.org/10.5258/SOTON/D1828.

The work presents a new procedure for calibration of TSA for use on orthotropic laminated polymer composites. It is demonstrated that such a calibration procedure is necessary to interpret the thermoelastic response from complex structural composites in any quantitative manner. Furthermore, the research presented brings together, for the first time, a means of assessing the significance and influence of many variables that thus far have been considered to be a barrier to deploying TSA in studies of the performance of composite materials and structures

6.2 Derivation of Thermoelastic Response from Measured Strains

To establish the effect of heat transfer on the thermoelastic response, it is proposed that a comparison between the measured ΔT obtained from TSA is made with a calculated value determined from the

measured strains obtained with LSDIC. The latter is independent of any heat transfer effects and therefore provides the basis for establishing the effect of different materials and stacking sequences on the thermoelastic response. The theoretical considerations are based on a multidirectional laminated coupon type specimen with a symmetrical stacking sequence loaded in uniaxial tension; the coordinate systems and notation used throughout the chapter follows Chapter 2 and is shown in Figure 3.1. The laminate/coupon axes and the principal material directions are denoted in Figure 3.1 with the load (N_x) applied in the coupon x-direction.

Using the nomenclature shown in Figure 3.1 and by assuming that strain compatibility is retained through the laminate stack (i.e. laminate does not exhibit bend or twist coupling behaviour), it is possible to calculate ΔT from the measured LSDIC laminate strains for three different scenarios as follows:

1) Resin-rich surface layer

The resin-rich surface layer is an isotropic material, so ΔT in the resin, ΔT_r, is related to the stress change in the resin, $\Delta(\sigma_x + \sigma_y)_r$, by the following expression:

$$\Delta T_r = -\frac{eT_0\alpha_r}{\rho_r C_{p_r}}\Delta(\sigma_x + \sigma_y)_r \tag{6.1}$$

where e is the emissivity of the specimen surface, α_r is the coefficient of thermal expansion of the resin, ρ_r is the density of the resin, and C_{p_r} is the specific heat capacity of the resin at constant pressure.

It is important to note that the term $\Delta(\sigma_x + \sigma_y)_r$ in equation (6.1) is an invariant and therefore independent of direction. In the set-up shown in Figure 3.1, the $x - y$ axes are coincident with the axes of principal stress in the laminate and hence the change in the shear stress, $\Delta\sigma_{xy}$, is neglected (zero) in equation (6.1), but the term is retained in the following treatment. By obtaining the laminate strain, $[\Delta\varepsilon]_{x,y}$, from the LSDIC, $\Delta\sigma_{x_r}$ and $\Delta\sigma_{y_r}$ are calculated as follow:

$$\begin{bmatrix}\Delta\sigma_x\\ \Delta\sigma_y\\ \Delta\sigma_{xy}\end{bmatrix}_r = [Q]_r\begin{bmatrix}\Delta\varepsilon_x\\ \Delta\varepsilon_y\\ \Delta\varepsilon_{xy}\end{bmatrix} = \begin{bmatrix}\frac{E_r}{1-\nu_r^2} & \frac{\nu_r E_r}{1-\nu_r^2} & 0\\ \frac{\nu_r E_r}{1-\nu_r^2} & \frac{E_r}{1-\nu_r^2} & 0\\ 0 & 0 & G_r\end{bmatrix}\begin{bmatrix}\Delta\varepsilon_x\\ \Delta\varepsilon_y\\ \Delta\varepsilon_{xy}\end{bmatrix} \tag{6.2}$$

where E_r is the Young's modulus of the resin, ν_r is the Poisson's ratio of the resin and G_r is the shear modulus, which is calculated directly from E_r and ν_r as the resin is assumed to be isotropic.

From equations (6.1) and (6.2) above, the 'normalised' thermoelastic response can be calculated as

$$\frac{\Delta T_r}{T_0} = -\frac{e\alpha_r}{\rho_r C_{p_r}}\left[\frac{E_r}{1-\nu_r}\left(\Delta\varepsilon_x + \Delta\varepsilon_y\right) + G_r\Delta\varepsilon_{xy}\right] \tag{6.3}$$

In equation (6.3) the normalising factor, T_0, is the mean of the cyclic temperature change and is obtained from the least-squares processing of the IR images series captured for the TSA. Normalising the thermoelastic response in this manner removes the effect of any variations in specimen temperature during the experiments. It is clear from equation (6.3) that to calculate the thermoelastic response from measured strains, the elastic constants, density, specific heat capacity and coefficient of thermal expansion are required alongside the emissivity of the surface. The coupon is loaded so that the $x-y$ axes are axes of principal stress and strain (shear strain is zero). However, it is important to note the normal stress/strain sum is an invariant, so issues such as misalignments in the coupon and its clamping can be neglected and, as the resin is isotropic, the coefficient of thermal expansion can be expressed as a scalar quantity.

In the treatment above, it is assumed that the resin-rich surface layer is thermally isolated from the laminate stack and the response is generated by the strain experienced by the resin layer, hence the terminology 'strain witness'. Clearly, this is dependent on the magnitude of ΔT in the layer below, if ΔT in the substrate is greater than that in the resin layer then heat will be transferred to the resin layer and vice versa. However, if the thermal conductivity of the resin and the substrate layer is low, then heat transfer between the two can be considered to be negligible, thus creating the so-called strain witness reported in [29, 74-76]. Additionally, the thickness of the resin layer and the substrate layers play a role in the thermal diffusion conditions, indicating a minimum thickness of resin for the strain witness assumption to be valid.

2) Orthotropic surface ply

As with scenario 1, the surface ply is treated as an isolated ply and any heat transfer effects are neglected. The nomenclature given in Figure 3.1 is used and the directional elastic properties and coefficients of thermal expansion are considered. Here the thermoelastic response is calculated as a function of the properties in the principal material direction of the surface ply, i.e. $\alpha_6 = 0$. Hence, using the measured strains from the LSDIC, the normalised thermoelastic response for the surface ply can be determined as

$$\frac{\Delta T_{surface\ ply}}{T_0} = -\frac{e}{\rho C_p}\begin{bmatrix}\alpha_1 & \alpha_2 & 0\end{bmatrix}[Q]_{1,2}[T_\varepsilon]\begin{bmatrix}\Delta\varepsilon_x \\ \Delta\varepsilon_y \\ \Delta\varepsilon_{xy}\end{bmatrix} \tag{6.4}$$

where $[T_\varepsilon]$ is the transformation matrix of the strains from 1-2 in the principal material directions to the global coordinate system x and y as shown in Figure 3.1 and defined in equation (2.5), $[Q]_{1,2}$ is the ply stiffness matrix (terms defined in equation (2.4)), C_p is the specific heat capacity, α_1 and α_2 are the coefficients of thermal expansion longitudinal and transverse to the fibre direction respectively, and $[\Delta\varepsilon]_{x,y}$ is the LSDIC measured change in strain.

Unlike scenario 1, the term G_{12} in equation (6.4) is independent of the other elastic properties, however, it is coupled with $\alpha_6 = 0$. Moreover, in the loading configuration shown in Figure 3.1 the laminate axes are axes of principal strain and hence $\Delta\varepsilon_{xy}$ is zero. Nevertheless, the elastic properties longitudinal and transverse to the fibre direction are required to determine the normalised thermoelastic response.

3) Global laminate

In contrast to scenario 1 and 2, here the response is considered to be generated by the homogenised laminate and, hence, all quantities are referenced to the laminate axes shown in Figure 3.1:

$$\frac{\Delta T_{laminate}}{T_0} = -\frac{e}{\rho C_p}[\alpha_x \quad \alpha_y \quad \alpha_{xy}][A^*]\begin{bmatrix}\Delta\varepsilon_x \\ \Delta\varepsilon_y \\ \Delta\varepsilon_{xy}\end{bmatrix} \tag{6.5}$$

where $[A^*]$ is the in-plane stiffness matrix of the laminate normalised by the laminate thickness, t, i.e. $[A^*] = \frac{1}{t}[A]$ [34], where $[A]$ has been defined in equation (2.11), $[\alpha]_{x,y}$ the matrix of global coefficients of thermal expansion of the laminate shown in equation (2.15), and $[\Delta\varepsilon]_{x,y}$ is the measured change in strain from the LSDIC.

In scenario 3, the properties $[A^*]$ and $[\alpha]_{x,y}$ includes the thickness and stiffness contributions of each ply, and in the present work includes also the thickness and stiffness of the resin-rich surface layer.

The methodology presented above shows the parameters that are required to obtain the normalised thermoelastic response from measured strain data for the three scenarios. Obtaining the thermoelastic response from measured strain data eliminates any variations due to the loading, as the strains obtained from the LSDIC and ΔT derived from the TSA are generated by the same load if the DIC and TSA are performed during the same cyclic loading test. Equations (6.3), (6.4) and (6.5) contain all the parameters that are required to determine ΔT from the measured strain. The next section of the chapter details how each of the parameters was obtained so that ΔT calculated from the LSDIC, ΔT_{LSDIC}, can be compared with ΔT derived from the TSA to identify the effect of heat transfer for different materials and stacking sequences.

6.3 Test Specimens and Material Properties

6.3.1 Test Specimen Manufacture and Geometry

All the test specimens were manufactured from either GFRP (RP-528 pre-preg [134]) or CFRP (IM7/8552 pre-preg [135, 136]). Panels of the material were manufactured in an autoclave following the manufacturer recommended curing cycles. All panels were made so that peel ply was employed only on the vacuum bag side of the panels, hence each side of the panels has either a 'smooth' surface, which was in contact with the aluminium mould, or a rough surface containing the characteristic peel ply imprint. Strips of material were cut from the panels to make the specimens, to which end tabs were bonded with epoxy resin.

UD specimens, $[0]_{10}$ and $[90]_{10}$, and $[\pm 45]_{3s}$ samples were made for the mechanical testing according to ASTM D3039 and ASTM D3518 standards, respectively. For the TSA and LSDIC, test coupons of stacking sequences $[0,90]_{3s}$, $[90,0]_{3s}$ and $[\pm 45]_{3s}$ were prepared. An overview of the final test specimen dimensions is given in Table 6.1. The stacking sequences were chosen because the two cross-ply laminates have the same stiffness, with different ply-by-ply stresses and thermoelastic constant of the surface ply, and displaying no shearing coupling, hence, little or no heating. For $[\pm 45]_{3s}$, the ply-by-ply stresses are identical and in theory, the plies are in thermal equilibrium with no opportunity for heat transfer, although the shearing may cause some heating at higher loading frequencies.

Table 6.1 Specimen dimensions

Specimen type	GFRP			CFRP		
	Length (mm)	Width (mm)	Thickness (mm)	Length (mm)	Width (mm)	Thickness (mm)
0 UD: $[0]_{10}$	270	15	2.36	220	25*	1.31
90 UD: $[90]_{10}$	235	25	2.36	175	25	1.31
$[0,90]_{3s}$	220	25	2.76	220	25	1.527
$[90,0]_{3s}$	220	25	2.76	220	25	1.527
$[\pm 45]_{3s}$	250	25	2.76	220	25	1.527

* This does not conform the recommended width in the standard because a wider sample was required for the TSA work on the UD carbon to give more measurement points

Table 6.2 shows the theoretical thermoelastic response for the different considered plies, resin and laminate approaches at a constant strain using the CLT theory described in Chapter 2 and the thermoelastic response equations (6.3), (6.4) and (6.5) for the different approaches. It can be seen that ΔT for the 0° and 90° GFRP plies is similar, due to the contributions of the coefficients of thermal expansion and stresses, hence, for both GFRP cross-ply laminates adiabatic conditions should prevail i.e. no heat transfer will occur. However, there is an order of magnitude difference for the ΔT of 0°

and 90° CFRP plies, hence, at low loading frequencies there should be heat transfer in both CFRP cross-ply laminates, but adiabatic conditions should be met when the loading frequency increases i.e. thermal diffusion length decreases. For both GFRP and CFRP $[\pm 45]_{3s}$ laminates, there will be no heat transfer between plies as the $+45°$ and $-45°$ plies have the same ΔT, and adiabatic conditions will be met. If the resin layer is thick, it will act as a strain witness (adiabatic behaviour), but if it is thin or ΔT from the subsurface ply is very different in comparison with the resin one, heat transfer should occur (non-adiabatic behaviour). Regarding the laminate approach, if ΔT is equivalent to the laminate, a homogenised value should be obtained that is based on non-adiabatic behaviour. Therefore, to study adiabatic and non-adiabatic effects, the loading frequency of the experiments is changed to modify the diffusion length i.e. varying the rate of the change of strain.

Table 6.2 Theoretical ΔT for 0°, 90°, 45° plies, resin and laminate for a constant strain

ΔT (K)	0° ply	90° ply	±45° ply	Resin	Laminate
GFRP	0.1028	0.1014	0.0758	0.1180	0.1029
CFRP	0.0155	0.1186	0.0178	0.1438	0.0676

6.3.2 Elastic Properties

The elastic properties of the GFRP and CFRP materials were determined in tensile tests on UD and $[\pm 45]_{3s}$ specimens according to ASTM D3039 or ASTM D3518. A detailed analysis is presented in Appendix D. As the specimens were not tested to failure, several repeat tests were carried out on the same specimen. The strains were determined by using stereo DIC on one side of the specimen and a T strain gauge rosette (CEA-13-125UT-350) on the other. The density of the TSA and DIC coupons ($[0,90]_{3s}$, $[90,0]_{3s}$ and $[\pm 45]_{3s}$) was also evaluated by using the specimen measurements given in Table 6.1 and the mass of the specimens. A summary of the elastic properties and density for both materials is given in Table 6.3. The DIC results differ slightly from those of the strain gauges possibly resulting from a small misalignment in the loading and for this reason, the mean value between DIC and strain gauges was used. G_{12} is included as it is required to calculate the overall laminate stiffness.

Table 6.3 Material properties

Property	GFRP			CFRP		
	DIC	Strain gauge	Average	DIC	Strain gauge	Average
E_1 (GPa)	38.87 $\pm$ 0.09	37.32 $\pm$ 0.07	38.10 $\pm$ 0.83	150.75 $\pm$ 0.50	146.86 $\pm$ 0.02	148.80 $\pm$ 2.27
ν_{12}	0.311 $\pm$ 0.02	0.272 $\pm$ 0.001	0.291 $\pm$ 0.021	0.35 $\pm$ 0.01	0.34 $\pm$ 0.01	0.34 $\pm$ 0.01
E_2 (GPa)	10.74 $\pm$ 0.02	11.43 $\pm$ 0.10	11.08 $\pm$ 0.38	9.11 $\pm$ 0.04	9.27 $\pm$ 0.03	9.19 $\pm$ 0.10
G_{12} (GPa)	3.87 $\pm$ 0.06	3.86 $\pm$ 0.18	3.86 $\pm$ 0.13	5.12 $\pm$ 0.15	5.01 $\pm$ 0.01	5.06 $\pm$ 0.07
ρ (kg/m^3)	-	-	1861.6 $\pm$ 3.4	-	-	1556.75 $\pm$ 72.5

The orthotropic elastic properties were obtained experimentally for both GFRP and CFRP materials. However, to calculate the normalised thermoelastic response for the different scenarios, the resin, the thermal properties of GFRP and CFRP, as well as the surface emissivity are also required. The determination of these properties is discussed in sections 6.3.3, 6.3.4 and 6.3.5.

Sambasivam et al. [30] obtained the elastic properties for the actual resin used in the prepreg and showed that there was little difference in the elastic properties quoted from the literature for a 'pure epoxy' and the measured values. Hence, rather than procure the actual resin used in the prepreg and conduct a testing campaign, it was considered to be acceptable to use properties taken from the literature [34, 77] for a pure epoxy, these are given in Table 6.4.

Table 6.4 Epoxy resin elastic properties

Resin property	Value
$\boldsymbol{\rho_r}$ $(\mathbf{kg/m^3})$	1153
$\boldsymbol{E_r}$ $(\mathbf{GPa})$	3.8
$\boldsymbol{\nu_r}$	0.35
$\boldsymbol{G_r}$ $(\mathbf{GPa})$	1.41

6.3.3 Specimen Volume Fraction and Resin Layer Thickness

The specific heat and coefficient of thermal expansion of composite material are difficult to measure in a standard laboratory environment and literature values show a large variation. This is because both properties are dependent on the fibre volume fraction, V_f, which is determined by the constituent materials and the curing process. Hence, a sensible starting point to determine the thermal properties is to obtain the V_f for the cured materials. The thickness of the resin-rich surface layer and the paint also play a role in the heat transfer and, therefore, have an effect on the measured ΔT, hence, it is essential to measure these to properly compare measured ΔT from TSA with ΔT_{LSDIC}.

The V_f and the thickness of the resin-rich surface layer were determined using micrographs of both the GFRP and CFRP $[0,90]_{3s}$, $[90,0]_{3s}$ and $[\pm 45]_{3s}$ materials. The fibre diameter was measured to calculate the V_f by considering the number of fibres contained in the micrograph area. As the DIC and the TSA were performed on the smooth side of the laminates, the resin-rich surface layer thickness was obtained at the smooth side. Additional experiments were performed on painted smooth and peel ply sides of GFRP specimens to analyse the effect of the surface finish and the paint on thermoelastic response measurements. Therefore, the thicknesses of the resin-rich surface layer and the paint were measured on GFRP specimens. The CFRP specimens were painted with a very thin layer of paint to avoid reflection, hence, it was considered not necessary to measure the paint thickness on the CFRP samples. A summary of the V_f, resin and paint thicknesses is presented in Table 6.5. It can be seen that V_f is lower for the GFRP compared with the CFRP and that the resin-

rich layer thickness is almost double for the case of the GFRP in comparison with the CFRP. The higher V_f, and thinner resin-rich surface layer in the CFRP can be attributed to differences in the curing cycles for both material systems, in particular, the higher pressure applied to CFRP panels (i.e. 7 bar versus 4 bar for the GFRP). It should be considered that the carbon fibres are much thinner resulting in better compaction, than can be achieved with the thicker glass fibres (see Table 6.5). Additionally, for the GFRP results, the resin-rich layer and paint are almost doubled on the peel ply side compared with the smooth side. Figure 6.2 shows that the paint seems to fill the texture on the peel ply side and to add the same thickness layer as on the smooth side.

Table 6.5 Volume fraction and resin-rich layer thickness

			GFRP	CFRP
Fibre diameter (µm)			13.59 ± 0.92	5.0 ± 0.3
Micrograph area (µm^2)			23,400	5,570
V_f			0.54 ± 0.06	0.63 ± 0.03
Resin-rich layer thickness (µm)	**Smooth side**		16.66 ± 9.69	5.10 ± 3.69
	Peel ply side		28.62 ± 8.47	-
Paint thickness (µm)	**Smooth side**	**Used in Section 6.4.3**	18.32 ± 2.73	-
		Used in Section 6.4.4	12.94 ± 2.65	-
	Peel ply side - Used in Section 6.4.4		23.17 ± 5.32	-

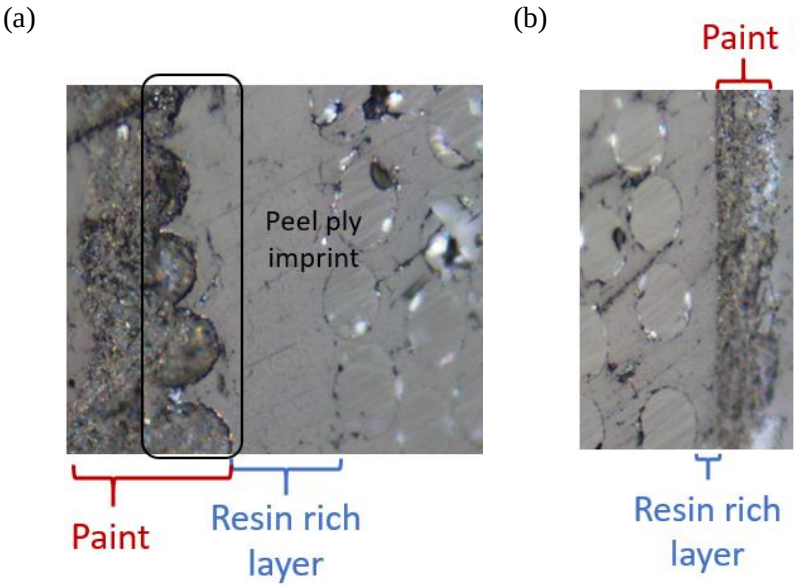

Figure 6.2 Micrographs from GFRP specimens (a) peel ply side and (b) smooth side

6.3.4 Thermal Properties

As described in the previous section, it was not possible to measure with any accuracy the thermal properties of the material. Instead, it was decided to compare literature values with those determined from the rule of mixtures for C_p and Schapery's equations for the coefficients of thermal expansion [34], using V_f. The starting point for applying these approaches are the values for the constituent materials, which are given in Table 6.6 for E-glass fibre and epoxy resin.

The C_p was determined in [29] and [30] as 882 J $kg^{-1}K^{-1}$ and 843 J $kg^{-1}K^{-1}$ respectively. As V_f was given in [29] and [30], these values can be verified against the rule of mixtures [34]. Figure 6.3 (a) shows C_p plotted against V_f with the values obtained from [29] and [30] indicated in the plot. It is clear that the value from [30] is incorrect or the constituent materials are different, particularly the resin. However, the value from Emery [29] matches closely the expected results, and provides some confidence in the properties given for the constituent material. Hence, C_p provided by the rule of mixtures for $V_f = 0.54 \pm 0.06$ was used for the calculation of $\Delta T/T_0$ for the orthotropic surface ply and global laminate scenarios as is indicated in Figure 6.3 (a) with a *.

In a similar way to calculating C_p, the V_f and properties of the constituent materials given in Table 6.6 were used to obtain α_1 and α_2 for the GFRP using Schapery's equations [34] and plotted in Figure 6.3 (b). Values were taken from the literature, [34], [29] and [30]. The value chosen for $\alpha_1 = 7 \cdot 10^{-6}\ K^{-1}$ is from [34] as it matches the Schapery's equation for α_1. It is important to note that for α_1 the value from [29] also corresponds with the Schapery's equation, with the value from [30] once again not corresponding with the theoretical value. In the case of α_2, there is considerable scatter in the literature values with the value from [30] being close to the theoretical prediction. Hence, it was decided to use an average value from [34], [29] and [30], i.e. $\alpha_2 = 30.7 \cdot 10^{-6}\ K^{-1}$, as in general, rule of mixtures type formulations are less reliable transverse to the fibre direction [34].

Table 6.6 Glass fibre and resin thermal properties

	$C_p\ (\mathbf{J\ kg^{-1}K^{-1}})$	$\alpha\ (\cdot \mathbf{10^{-6}\ K^{-1}})$
E-glass fibre	810 [137]	5 [34]
Resin	1100 [138]	53.5 (mean value from [34])

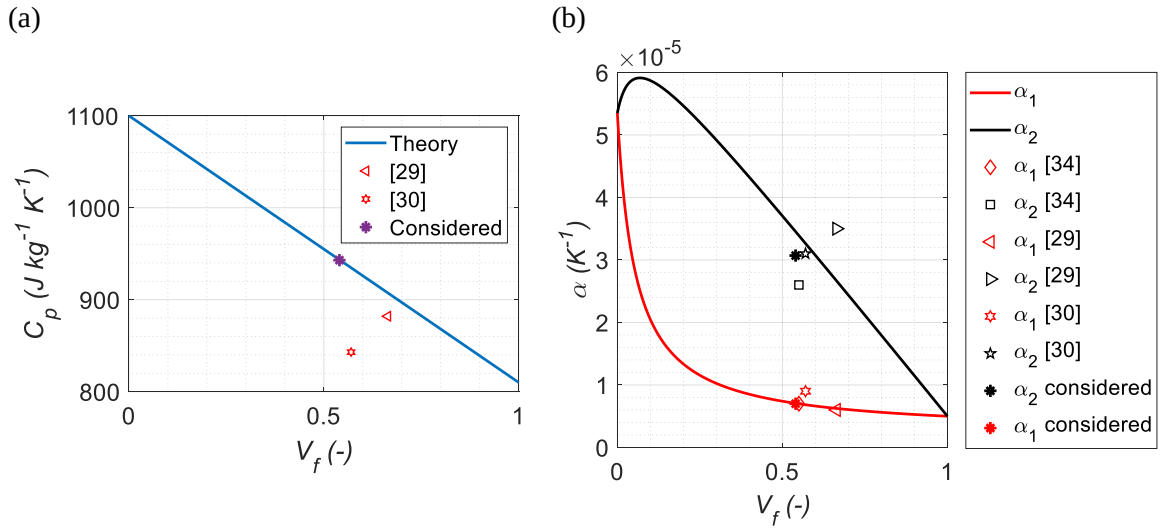

Figure 6.3 (a) C_p plotted against V_f for GFRP using the rule of mixtures, (b) α_1 and α_2 plotted against V_f for GFRP using the Schapery's equations

Regarding the CFRP, as the fibre IM7 is anisotropic [34], it is not straightforward to apply the rule of mixtures or use Schapery's equation to determine the coefficients of thermal expansion of the ply [139]. Additionally, there are no reliable properties for the 8552 epoxy resin published in the open literature. Therefore, as IM7/8552 is a very well characterised material, the thermal properties were taken from the literature [140-142] as $C_p = 857\ \mathrm{J\,kg^{-1}K^{-1}}$ [140] and the coefficients of thermal expansion were taken as the mean of the values found in [141] and [142] shown in Table 6.7, i.e. $\alpha_1 = -0.3 \cdot 10^{-6}\ \mathrm{K^{-1}}$ and $\alpha_2 = 28.4 \cdot 10^{-6}\ \mathrm{K^{-1}}$, as the V_f are close to the measured $V_f = 0.63 \pm 0.03$.

Table 6.7 Coefficients of thermal expansion for IM7/8552 from literature

	Reference [141]	**Reference [142]**
$\boldsymbol{V_f}$	0.591	0.577
$\boldsymbol{\alpha_1\ (\cdot 10^{-6}\ K^{-1})}$	-0.5	-0.1
$\boldsymbol{\alpha_2\ (\cdot 10^{-6}\ K^{-1})}$	25.8	31

The ratio of α_2/α_1 can also be verified experimentally performing TSA on UD samples, with the load applied in the x and y directions (see Figure 3.1). This allows the thermoelastic constants, K_1 and K_2, to be obtained as follows [80]:

$$K_1 = \frac{\alpha_1}{\rho C_p} = \frac{\Delta T}{T_0 \Delta \sigma_x} \text{ and } K_2 = \frac{\alpha_2}{\rho C_p} = \frac{\Delta T}{T_0 \Delta \sigma_y} \tag{6.6}$$

where ΔT and T_0 are obtained experimentally, and $\Delta\sigma_x$ and $\Delta\sigma_y$ are the applied stresses.

Hence, the ratio of K_2/K_1 can be determined experimentally and compared with α_2/α_1 obtained from the literature. Table 6.8 shows that the experimental and theoretical values for both GFRP and

CFRP are in close correspondence further verifying the values of coefficients of thermal expansion used in the analysis.

Table 6.8 Ratio of coefficients of thermal expansion

Properties	GFRP	CFRP
$\boldsymbol{\alpha_1 \left(\cdot 10^{-6}\,\mathrm{K}^{-1}\right)}$*	7	-0.3
$\boldsymbol{\alpha_2 \left(\cdot 10^{-6}\,\mathrm{K}^{-1}\right)}$*	30.7	28.4
$\boldsymbol{\alpha_2/\alpha_1}$	$\mathbf{4.4}$	$\mathbf{94.7}$
$\boldsymbol{K_1 \left(\mathrm{MPa}^{-1}\right)}$**	4.4 ± 0.4	0.17 ± 0.06
$\boldsymbol{K_2 \left(\mathrm{MPa}^{-1}\right)}$**	18.7 ± 1.8	16.0 ± 1.0
$\boldsymbol{K_2/K_1}$	$\mathbf{4.3 \pm 0.6}$	$\mathbf{94.1 \pm 0.5}$

* obtained from the literature; ** determined experimentally

6.3.5 Surface Emissivity

In the literature, the emissivity of a glass fibre epoxy material ranges from 0.79 [29] to 0.95 [143]. Therefore, assuming a value for the emissivity can have a significant effect on the calculated thermoelastic response. To make an estimation of the emissivity of the GFRP material, an experiment was conducted using a temperature controlled blackbody (Infrared Systems Development Corporation, IR-2106/301 [130]) with a known emissivity of 0.96 ± 0.02. Two GFRP coupons were placed in front of the blackbody with the smooth side at the front, one without any background paint applied and the other prepared with a matt black background paint with white speckles, as used for the capture of images for the DIC and TSA. Figure 6.4 shows an IR image of the specimens attached to the blackbody, collected with a Telops FAST M2K [99] photon detector camera. The blackbody and the coupons had a thermocouple attached to their surface to verify they were all at the same temperature. The temperature of the blackbody was adjusted until it was at the same temperature as the specimens of 24 °C. The scene was recorded at 383 Hz frame rate and 1000 image frames were collected and averaged to reduce the temporal noise. The emissivity, e, of GFRP epoxy resin and matt black paint, MBP Electrolube [144], were determined from the following relationship:

$$\frac{\mathrm{DL_S}}{\mathrm{DL_{BB}}} = \frac{e_\mathrm{S}}{e_\mathrm{BB}} \tag{6.7}$$

where the subscript S refers to GFRP epoxy or paint, BB to blackbody, and DL is digital level measured with the IR camera.

The $\mathrm{DL_{GFRP\ epoxy}}$ and $\mathrm{DL_{paint}}$ were obtained by averaging an area shown in Figure 6.4 of 120 x 40 pixels for each sample, and $\mathrm{DL_{BB}}$ was obtained by averaging a 120 x 123 pixel area, also indicated on Figure 6.4. A summary of the digital levels and emissivity can be seen in Table 6.9. The GFRP epoxy resin and paint have a similar emissivity. To verify the results further, another experiment was

conducted with the coupon positions interchanged, which yielded an identical result. As the CFRP was slightly painted, the emissivity for the paint could be used for the experiments on the CFRP.

Table 6.9 Digital level and emissivity for each element

	DL	e
Blackbody	21407.21 ± 20.52	0.96 ± 0.02
GFRP epoxy (smooth)	21287.09 ± 26.48	0.95 ± 0.02
Paint on GFRP epoxy (smooth)	21285.94 ± 29.74	0.95 ± 0.02

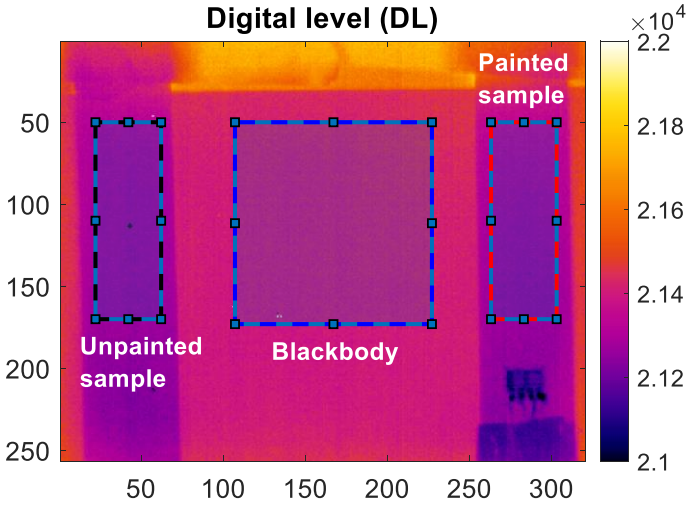

Figure 6.4 IR image of the comparative experiment to obtain emissivity in DL: GFRP specimens without paint (left) and with paint (right) applied to the surface

6.4 Thermoelastic Response

6.4.1 Experimental Arrangements

In the previous section, all the material properties for the laminated composite materials, resin and surface properties were established, so that the normalised thermoelastic response for the different scenarios as presented in section 6.2 can be calculated from the strains obtained from the DIC. For convenience, a summary of all the material properties used in the analysis is given in Table 6.10 and Table 6.11.

Table 6.10 Summary of the properties used in the calculations for orthotropic GFRP and CFRP materials

Property	GFRP	CFRP
E_1(GPa)	38.10 ± 0.83	148.80 ± 2.27
ν_{12}	0.291 ± 0.021	0.34 ± 0.01
E_2 (GPa)	11.08 ± 0.38	9.19 ± 0.10
G_{12} (GPa)	3.86 ± 0.13	5.06 ± 0.07
ρ (kg/m^3)	1861.6 ± 3.4	1556.75 ± 72.5
C_p (J kg^{-1}K^{-1})	940	857
α_1 ($\cdot 10^{-6}$ K^{-1})	7	−0.3
α_2 ($\cdot 10^{-6}$ K^{-1})	30.7	28.4

Table 6.11 Resin properties used

Property	Resin
E_r (GPa)	3.8
ν_r	0.35
G_r (GPa)	1.41
ρ_r (kg/m^3)	1153
C_{p_r} (J kg^{-1}K^{-1})	1100
α_r ($\cdot 10^{-6}$ K^{-1})	53.5

To make the comparison between the TSA and the DIC by applying the equations in section 6.2, it is important that the applied loads do not damage the specimens. Therefore, the applied tension loads for the experiments were determined by establishing the first ply failure (FPF) stress for the multidirectional laminated coupons. The FPF was established using the material properties given in [134, 145] and [141, 146] for the GFRP and CFRP respectively using Puck and LarC03 [39] criteria, which is overviewed in Chapter 2. Table 6.12 shows the FPF stress and the applied cyclic load and maximum applied stress used in the experiments. A detailed analysis of the FPF can be seen in Appendix C. To determine the effect of any heat transfer, the tests were carried out at different loading frequencies from 3.1 to 30.1 Hz. It should be noted that the tests on the GFRP were carried out at about 50% of the FPF stress, whereas in the CFRP the test were carried out at about 30%. This was because the test machine was not able to achieve the target load range accurately at higher frequencies.

Table 6.12 Applied load and stress and FPF for the different stacking sequences and materials

	$[0,90]_{3s}$ and $[90,0]_{3s}$			$[\pm 45]_{3s}$		
	Applied load (kN)	**Applied stress (MPa)**	**FPF stress (MPa)**	**Applied load (kN)**	**Applied stress (MPa)**	**FPF stress (MPa)**
GFRP	2 ± 1.67	53	115.63	2 ± 1.24	47	78.07
CFRP	4 ± 3.4	194	542	1 ± 0.9	50	174

The GFRP coupons were painted with MBP Electrolube matt black background paint to increase the emissivity for TSA, and white spray-painted speckles were applied to dehomogenise the surface for DIC. The CFRP coupons were painted with a very thin layer of black matt paint to reduce reflections on the smooth side due to the surface finish. Images of the speckle patterns applied on a 300 x 300 pix area for GFRP and CFRP samples are shown in Figure 6.5. The speckle pattern size was between 3 and 5 pixels [147]. To understand the effect of the painting, TSA was performed on unpainted GFRP coupons; this was not possible with the CFRP due to a high level of interference due to reflection. Additionally, GFRP specimens were used to compare the effect of the peel ply imprint by performing TSA and DIC on both sides of the samples.

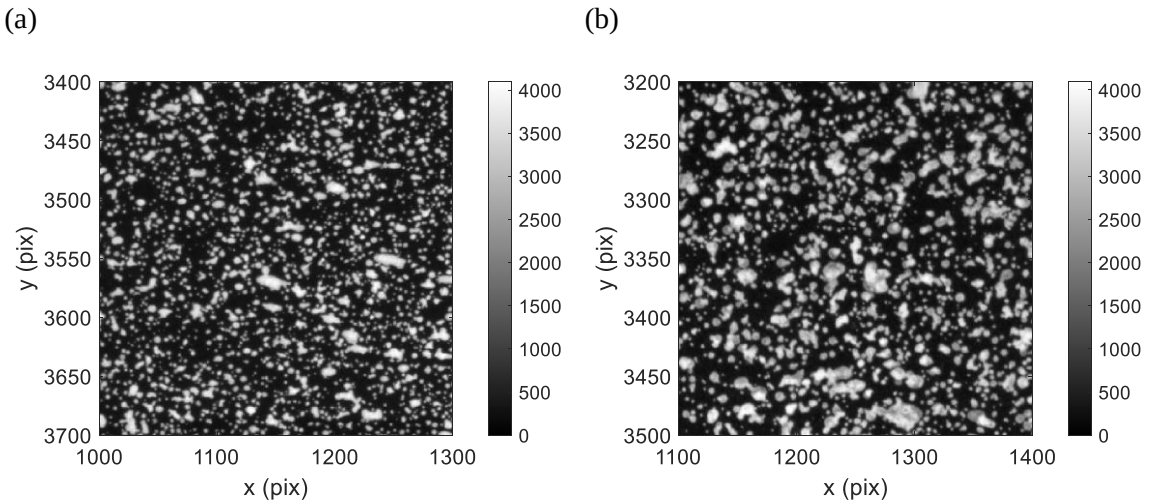

Figure 6.5 Speckle pattern in a 300 x 300 pix area (grey levels) in (a) GFRP, and (b) CFRP surfaces

Figure 6.6 shows a schematic with the position of the IR and white light cameras used for capturing the images for the TSA and stereo DIC. It was decided to do stereo DIC instead of 2D-DIC to have room for the IR camera in the centre of both white light cameras. The DIC setup was performed considering the iDICs guide [147]. It was not necessary to synchronise the IR and white light image capture. Instead, the lock-in approach used to process the IR images was also used on the strains derived from the DIC [22]. The cameras used for the LSDIC were E-lite 5M by LaVision, where a camera frame rate of 1.5 Hz was used, which is below the loading frequencies studied. Hence, the data is undersampled but, as the frame rate and the loading frequency are known, it is possible to reconstruct the signal and obtain the peak-to-peak amplitude using the least-squares algorithm [82]. The DIC performance characteristics are shown in Table 6.13 and Table 6.14 for GFRP and CFRP samples respectively; more details of the methods to obtain the values given in the tables are provided in Appendix B. It should be noted that the noise content is different for the GFRP and CFRP experiments because of adjustments in the illumination of the specimens.

As mentioned previously, the IR camera was a Telops FAST M2K, which is capable of capturing at very high frame rates e.g. ~1,000 frames per second. However, it was decided to limit the number of images captured for TSA, and hence a frame rate of 383 Hz was used for the IR camera to minimise aliasing effects, which has been demonstrated to be sufficient, e.g. [124, 148]. So, the IR camera collected 2,000 frames over 5 seconds immediately after the LSDIC images were collected. To verify the LSDIC strain measurements, a T strain gauge rosette (CEA-13-125UT-350) was mounted on the peel ply side of the coupons. The data extracted from the strain gauges was sampled at 500 Hz.

The normalised thermoelastic response from LSDIC measured strains was obtained using equations (6.3), (6.4) and (6.5) for the resin-rich surface layer, orthotropic surface ply and global laminate approaches, respectively. The strain changes, $\Delta\varepsilon_x$ and $\Delta\varepsilon_y$ were obtained from the LSDIC and strain gauges using the least-squares 'lock-in' algorithm on the measured strains.

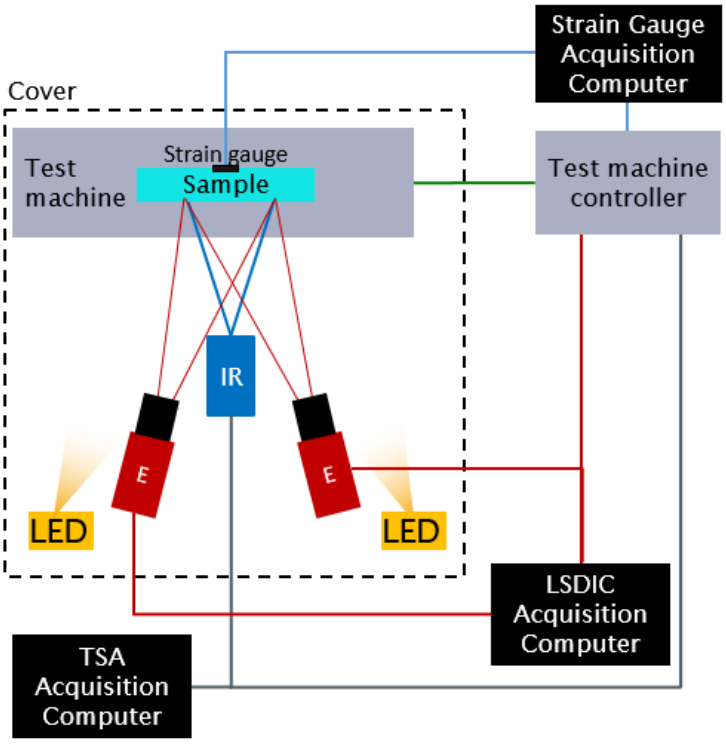

Figure 6.6 Experimental setup

Table 6.13 3D-DIC performance evaluation for GFRP samples

Technique used	**3D Digital Image Correlation**	
	Camera 1	**Camera 2**
Sensor and digitization	2448 x 2050, 12-bit	
Camera noise (% of range)	0.66%	0.65%
Lens and imaging distance	50 mm F-mount, 1.1 m	
Total number of images	2 (1.5 Hz)	
Pixel to mm conversion	1 pixel = 0.067 mm	
ROI (mm)	140 x 25 mm	
Subset, step	61, 20	
Interpolation, shape functions, correlation criterion	Bicubic (6^{th} order spline), affine, ZNSSD	
Pre-smoothing	None	
Displacement resolution	$1.73 \cdot 10^{-4}$ mm	
Strain		
Smoothing technique	Local polynomial - affine least-squares fit	
Strain window	3 data points	
VSG	102 pixels	
Resolution	0.0041 %	

Table 6.14 3D-DIC performance evaluation for CFRP samples

Technique used	**3D Digital Image Correlation**	
	Camera 1	**Camera 2**
Sensor and digitization	2448 x 2050, 12-bit	
Camera noise (% of range)	1.57%	1.78%
Lens and imaging distance	50 mm F-mount, 1 m	
Total number of images	2 (1.5 Hz)	
Pixel to mm conversion	1 pixel = 0.059 mm	
ROI (mm)	113 x 25 mm	
Subset, step	61, 20	
Interpolation, shape functions, correlation criterion	Bicubic (6^{th} order spline), affine, ZNSSD	
Pre-smoothing	None	
Displacement resolution	$2.78 \cdot 10^{-4}$ mm	
Strain		
Smoothing technique	Local polynomial - affine least-squares fit	
Strain window	3 data points	
VSG	102 pixels	
Resolution	0.0048 %	

6.4.2 Comparing Measured and CLT Predicted Strains

The aim of this section is to validate the LSDIC measured strains by comparing them with the strains obtained with the strain gauges. The advantage of using LSDIC with respect to strain gauges is that

it provides a full-field measurement that allows the detection of strain gradients. Therefore, LSDIC would be suitable for testing of structural components. Additionally, the measured strains from LSDIC and strain gauges were compared with the predicted strains at the laminate mid-plane using CLT.

Figure 6.7 shows the comparison of longitudinal, $\Delta\varepsilon_x$, and transverse, $\Delta\varepsilon_y$, strains for the three GFRP laminates considered. Generally, the LSDIC and strain gauges measured strains show good agreement, and validates the LSDIC technique. However, at the highest frequency, in some cases there is a mismatch between the strain gauge and LSDIC measurements, probably caused by errors in the fitting of the undersampled LSDIC data. The most important observation, most prominently observed in the $\Delta\varepsilon_x$ values for the $[0,90]_{3s}$ and $[90,0]_{3s}$ laminates, is the reduction in strain with frequency. This is caused by the inability of the test machine to maintain a constant load range at higher loading frequencies, and justifies the need to make strain measurements rather than rely on outputs from the test machine. It was confirmed by an analysis of the test machine data that the displacement range was reducing with loading frequency even though control features such as 'amplitude control' were initiated. In the $\Delta\varepsilon_y$ values obtained for the $[0,90]_{3s}$ and $[90,0]_{3s}$ laminates there is little evidence of this behaviour because the Poisson's ratio of the laminate is close to zero. Conversely in the $[\pm 45]_{3s}$ laminate, $\Delta\varepsilon_x$ decreases whilst $\Delta\varepsilon_y$ increases with loading frequency due to the Poisson's ratio of the laminate.

In all three laminates, the magnitude $\Delta\varepsilon_x$ predicted by the CLT is higher than the measured values, whereas the measured and predicted $\Delta\varepsilon_y$ match more closely. The difference between the measured and predicted strains highlights the uncertainties on the GFRP material properties. Additionally, the LSDIC measured shear strain, $\Delta\varepsilon_{xy}$, was obtained and it was practically zero in all cases, because the x and y axes are axes of principal stress and strain.

It should be noted that a similar exercise was carried out on the CFRP specimens and it was seen that measured and CLT predicted strains showed a good agreement validating the CFRP material properties. However, the LSDIC measured strains showed a similar reduction in magnitude with respect to the loading frequency as also seen for the GFRP laminates.

The outcome from this section is that an independent measure of strain is required in any TSA calibration process to account for heat transfer effects, as using the target applied load from the test machine will introduce large uncertainties as loading frequencies increase. Hence, in the following section, the strains obtained from the LSDIC are used to provide a predicted $\Delta T/T_0$ that is compared with the measured $\Delta T/T_0$, with the certainty that the LSDIC and TSA are experiencing exactly the same loading conditions. In the current experimental campaign, it is not necessary to use full-field measurements to obtain the strain, as the field is uniform, so the readings from the strain gauge would

be sufficient to monitor the load behaviour. However, the full-field strain measurements allow non-uniform loading to be monitored. Moreover, for typical components, the surface strain field will be non-uniform and, hence, a reading from a single strain gauge will not be sufficient for calibration purposes.

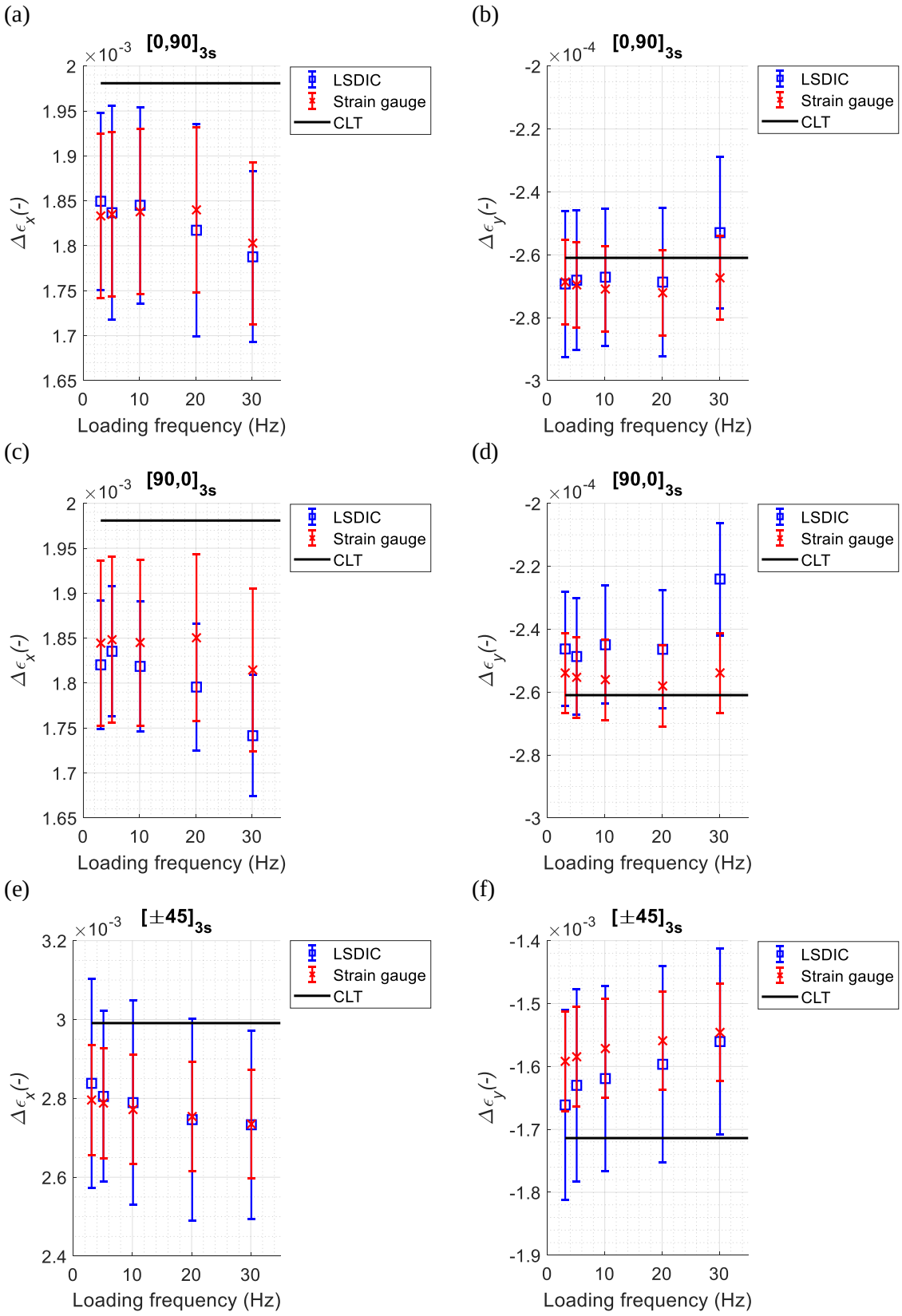

Figure 6.7 GFRP strain comparison LSDIC, strain gauge and CLT being (a) and (b) the $\Delta\varepsilon_x$ and $\Delta\varepsilon_y$ of the $[0,90]_{3s}$ sample; (c) and (d) the $\Delta\varepsilon_x$ and $\Delta\varepsilon_y$ of the $[90,0]_{3s}$ sample; and (e) and (f) the $\Delta\varepsilon_x$ and $\Delta\varepsilon_y$ of the $[\pm 45]_{3s}$ sample

6.4.3 Comparison of $\Delta T/T_0$ derived from TSA, LSDIC and Strain Gauges

Figure 6.8 shows the normalised thermoelastic response for the three GFRP coupons with respect to the loading frequency. The actual measure of the thermoelastic response is shown, alongside the predicted response using the LSDIC measured strains for the three scenarios formulated in section 6.2. In all cases, the unpainted specimens provide a greater measured $\Delta T/T_0$ than the painted specimens. Moreover, the response from the painted specimens reduces significantly with loading frequency; this is not evident in the unpainted specimens indicating that the paint thickness causes attenuation of the thermoelastic response when it is greater than 18.32 ± 2.73 μm, as this is the value measured for the paint thickness (see Table 6.5). Further analysis on the paint thickness is shown in section 6.4.4. As the loading frequency increases, the response reduces further indicating that the thermal diffusion length generated within one cycle is not large enough for the response to diffuse through the paint coating.

Focusing on the thermoelastic response from the unpainted specimen and comparing with the predicted response from the LSDIC, it is clear in all three cases that the actual $\Delta T/T_0$ corresponds most closely with the predicted values for the resin. A further observation is that the response does not vary with loading frequency indicating clearly, as concluded in previous works [29, 74-76], that the thermoelastic response is that of the isolated isotropic resin-rich layer. However, it is the case that the predictions of $\Delta T/T_0$ do not match exactly the measured data. For the $[90,0]_{3s}$ (Figure 6.8 (b)), the measurements and the predictions are very close, with predictions slightly greater than the measurements. For the other two laminates, the difference between the measurements and the predictions is much greater, with the predictions being less than the measured values. Interestingly, the predicted LSDIC values for the surface ply and the laminate are very close for the $[0,90]_{3s}$ and $[90,0]_{3s}$ specimens, with $\Delta T/T_0$ being $\sim 3.2 \cdot 10^{-4}$. This is because the combination of the stress carried by the ply and the coefficients of thermal expansion of the ply results in a similar value for both lay-ups. Considering the potential systematic errors in the material property values and scatter in the data indicated by the error bars (standard deviation) in Figure 6.8, it is difficult to make any further conclusions regarding the heat transfer characteristics in the GFRP specimens.

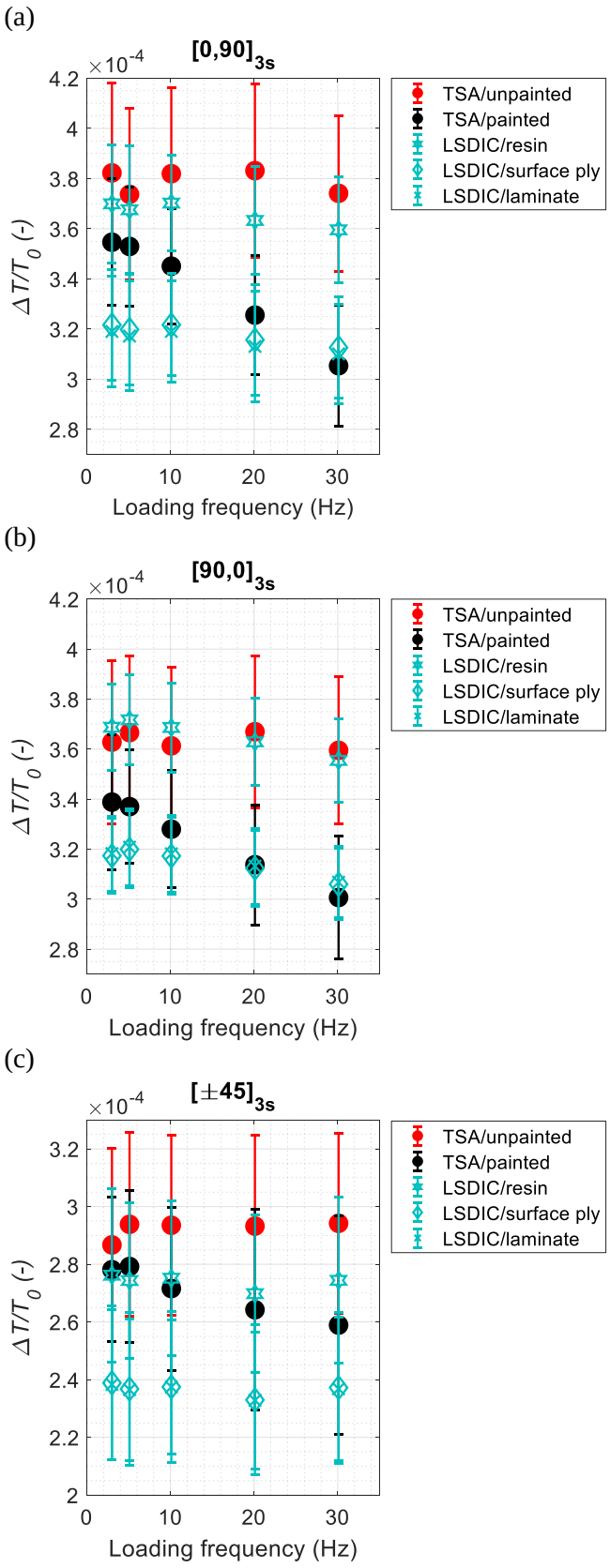

Figure 6.8 Normalised thermoelastic response $\Delta T/T_0$ vs loading frequency of (a) $[0,90]_{3s}$, (b) $[90,0]_{3s}$ and (c) $[\pm 45]_{3s}$ GFRP specimens

Figure 6.9 shows the normalised thermoelastic response for the three CFRP coupons with respect to the loading frequency. Figure 6.9 shows for the $[0,90]_{3s}$ sample that the measured $\Delta T/T_0$ decreases and for the $[90,0]_{3s}$ laminate $\Delta T/T_0$ increases when the loading frequency increases, similar to [80]. Therefore, it can be concluded that heat transfer is occurring due to the difference in the stress induced temperature change between the 0° and 90° plies. In the $[0,90]_{3s}$, the stress induced temperature change in the 90° subsurface ply is greater than in the 0° surface ply, hence, at lower frequencies there is heat transfer from the subsurface ply to the surface ply, which at higher frequencies does not occur as the thermal diffusion length reduces. In the $[90,0]_{3s}$, as in the 0° subsurface ply the stress induced temperature change is lower than in the 90° surface ply, heat transfers from the surface ply to the subsurface ply, which is possible at low frequencies, but at higher frequencies, as the thermal diffusion length decreases, heat transfer reduces and the thermoelastic response of the surface ply is larger. Figure 6.9 shows that for both the cross-ply laminates $\Delta T/T_0$ corresponds to the homogenised global laminate response at low loading frequencies and to the orthotropic surface ply at high loading frequencies. Regarding the $[\pm 45]_{3s}$ specimen, (Figure 6.9 (c)), the stress induced temperature change is the same for every ply, so heat transfer cannot occur and $\Delta T/T_0$ is constant over the frequency range, with the predicted values for the laminate and the surface ply being equal.

To sum up, in comparison with the CFRP, the GFRP stress induced temperature change between the 0° and 90° plies is similar, hence there is no opportunity for heat transfer, and $\Delta T/T_0$ is unaffected by the loading frequency. The difference between the thermoelastic response from CFRP and GFRP corresponds with a much thinner resin-rich surface layer for the CFRP (5.10 ± 3.69 μm) in comparison with the GFRP (16.66 ± 9.69 μm), which allows heat transfer to the surface, highlighted by the $[0,90]_{3s}$ and $[90,0]_{3s}$ laminates, as the stress induced temperature change of the 0° and 90° plies is significantly different. Another consideration is the volume fraction of the fibres, in the CFRP this is higher than in the GFRP (0.63 ± 0.03 compared to 0.54 ± 0.06). Additionally, although the epoxy resin has a low thermal conductivity, unlike the glass fibre, carbon fibre is conductive, with the larger fibre volume fraction of the CFRP, more fibres will be in contact across plies aiding heat transfer from ply-to-ply. Hence, the explanation of adiabatic and non-adiabatic conditions described in section 6.3.1 based on theoretical ΔT values was demonstrated for both materials.

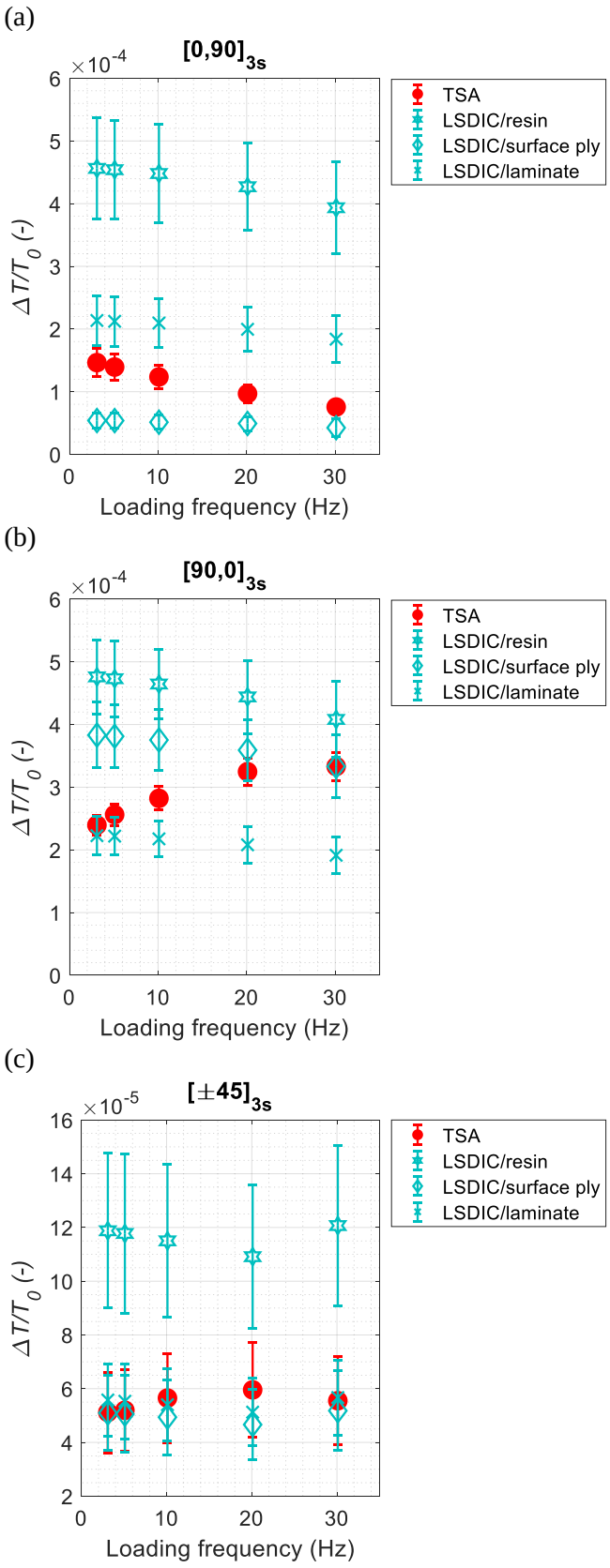

Figure 6.9 Normalised thermoelastic response $\Delta T/T_0$ vs loading frequency of (a) $[0,90]_{3s}$, (b) $[90,0]_{3s}$ and (c) $[\pm 45]_{3s}$ CFRP specimens

6.4.4 Peel Ply Imprint

To examine the effect of the peel ply imprint on the thermoelastic response, three painted GFRP specimens are studied. The samples were different to those used in section 6.4.3, but were cut from the same panels. Hence, these specimens were painted with a focus on achieving a thinner layer of paint, as thick paint layers were seen to have a detrimental effect in the previous section. Figure 6.10 shows the normalised thermoelastic response on the smooth and peel ply sides with respect to the loading frequency of painted GFRP specimens. As the results presented in the previous section showed that the thermoelastic response of the GFRP material is driven by the resin, only the predicted thermoelastic response obtained for the resin-rich surface layer is presented. It is clear from Table 6.5 that the resin is much thicker on the peel ply side than on the smooth side, making the laminate non-symmetrical. Notwithstanding that the resin layer stiffness is small, it could have an effect on the strains. This was checked against CLT predictions, with the calculated strains for the non-symmetrical laminate being practically identical to the symmetrical laminate, i.e. strain sum, $\Delta(\varepsilon_x + \varepsilon_y)$, $1.264 \cdot 10^{-3}$ versus $1.277 \cdot 10^{-3}$ for $[\pm 45]_{3s}$ laminates. Additionally, as the peel ply imprint causes aliasing in the DIC, the LSDIC strains were obtained from the smooth side; as no damage was occurring, this is justified as strain compatibility is maintained.

The results in Figure 6.10 show that the $\Delta T/T_0$ from the peel ply side attenuates severely when the loading frequency increases. This is attributed to the thickness of the paint, which is almost double to that on the smooth side (see Table 6.5). $\Delta T/T_0$ from the smooth side converges in all cases between 10.1 and 20.1 Hz, indicating adiabatic conditions are prevailing. This result is in contrast to the results given in Figure 6.8, where there is no indication of convergence to a constant value suggesting that the paint is thinner than on the specimens presented in section 6.4.3. The paint thickness was measured and compared (see Table 6.5), on the smooth side it was 18.32 ± 2.73 μm for the GFRP specimens in section 6.4.3 versus 12.94 ± 2.65 μm for the specimens in this section. The paint thickness plays an important role on the thermoelastic response and a layer of $\sim 23.17 \pm 5.32$ μm, as seen on the peel ply side, attenuates the response significantly when the loading frequency increases. The variability of the measured thermoelastic response from specimens with different paint thickness applied highlights the dependency on the operator applying the paint and the care required when applying the paint, and where possible tests should be conducted without paint.

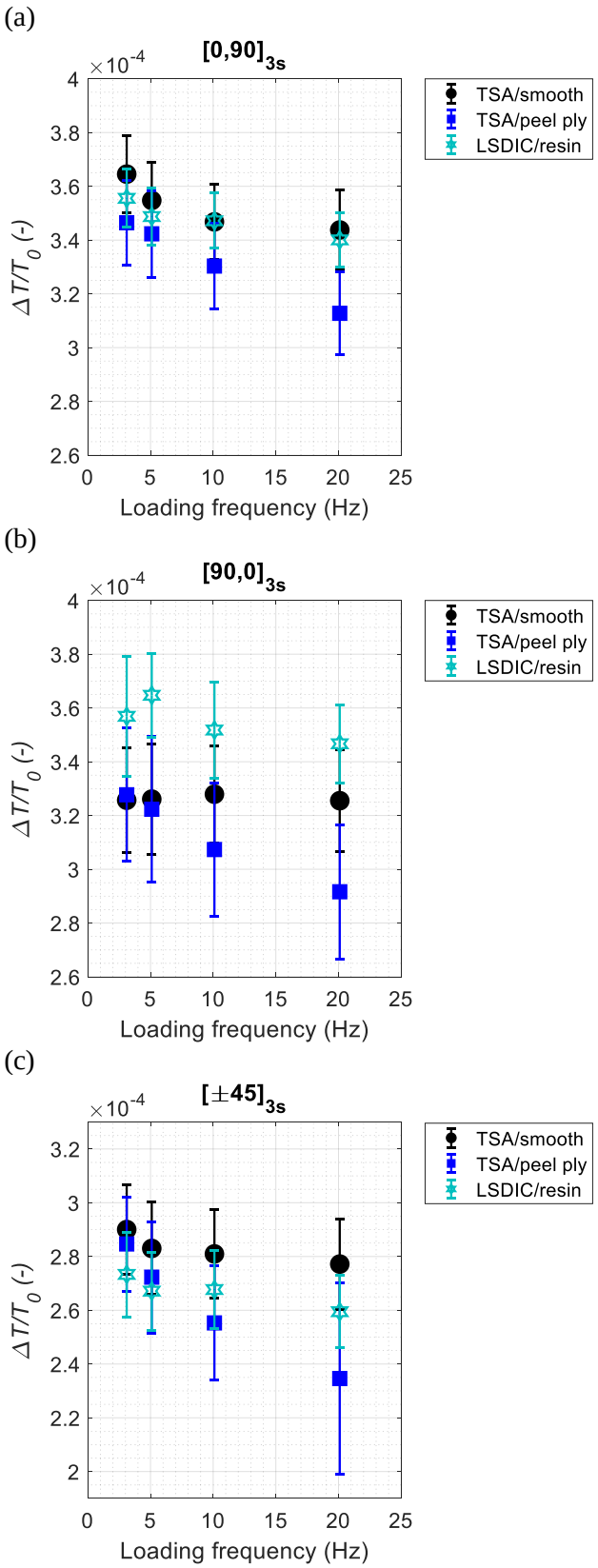

Figure 6.10 Normalised thermoelastic response $\Delta T/T_0$ vs loading frequency of painted (a) $[0,90]_{3s}$, (b) $[90,0]_{3s}$ and (c) $[\pm 45]_{3s}$ GFRP specimens comparing smooth and peel ply surface finish

6.5 Summary

A new means of analysing the nature or source of the thermoelastic response has been presented that is based on using a measured strain determined from DIC and strain gauge measurements. The approach allows uncertainties in the loading to be accounted for, particularly those associated with test machine capability to achieve a consistent peak to peak load range at high loading frequencies. The new approach utilises the 'lock-in' processing for TSA based on a least-squares fit to the strains from images obtained at low frame rates derived by the DIC (LSDIC) high resolution strain data. The approach was verified using strain gauges, which confirmed that the LSDIC measured strains corresponded directly to the strains measured with the strain gauges. The combination of TSA and the LSDIC establishes a means of monitoring the strain (DIC) alongside the thermal response (TSA) in a full-field manner, which could be applied to larger structures that contain strain gradients and for the monitoring of damaged composite structures.

The focus of the chapter is to determine the source of the normalised thermoelastic response, $\Delta T/T_0$. Both the temperature change and the mean surface temperature are measured quantities extracted from an IR image series. The measured $\Delta T/T_0$ was compared with predicted values based on the strain measurements, enabling the source of the thermoelastic response to be identified categorically. A detailed experimental campaign and literature review provided well-documented values for two typical material types: a GFRP and a CFRP. Micrographs were used to obtain paint and resin-rich layer thicknesses as well as fibre volume fraction. A study of the material thermal properties with respect to the fibre volume fraction was carried out to verify the thermal properties obtained from the literature. Different laminate stacking sequences were studied, i.e. two cross-ply ($[0,90]_{3s}$, $[90,0]_{3s}$) and a shear dominated laminate ($[\pm 45]_{3s}$). $\Delta T/T_0$ was calculated from the LSDIC measured strains using three different scenarios (considering the resin-rich surface layer, orthotropic surface ply and global laminate), and compared with the $\Delta T/T_0$ obtained directly from the IR images using TSA.

It was shown that the measurement of the strain using LSDIC enables an independent 'measure' of the thermoelastic response to be calculated without any influence of heat transfer. Comparing this with the measured $\Delta T/T_0$ values demonstrated that in the GFRP the source of the thermoelastic response was the resin-rich surface layer. In the GFRP laminates, the stress induced temperature change ply-by-ply is similar because of the combination of coefficients of thermal expansion and material stiffness. Hence, even if the resin-rich surface layer was removed, no heat transfer could take place and, for any symmetrical laminate stacking sequence with these material properties, ΔT would occur adiabatically. The outcome results in a very important conclusion that for most glass fibre based composite laminates (including those with resins other than epoxy that have a similar ratio of coefficients of thermal expansion and stiffness), the thermoelastic relationship given in

equation (3.5) is always valid as ΔT will always occur adiabatically, as ply-by-ply the material is in thermal equilibrium. Moreover, when the resin-rich surface layer thickness is greater than 16.66 ± 9.69 μm, the response follows equation (6.3), which is a combination of orthotropic elastic properties and isotropic thermal properties. Further work is required to establish the minimum thickness of the resin-rich surface layer where equation (6.3) can be applied. However, controlling the thickness of the resin and maintaining a uniform surface represents a challenge in manufacturing as this is determined by resin bleed out during curing.

For the CFRP, the response was heavily influence by heat transfer, as the ply-by-ply stress induced temperature change for the $[90,0]_{3s}$ and $[0,90]_{3s}$ is markedly different, and because the fibre volume fraction is higher, and the resin-rich surface layer much thinner than for the GFRP laminates. An attenuation in response with frequency was evident for the $[0,90]_{3s}$ laminate, as the subsurface ply was transferring heat to the surface ply. Conversely for the $[90,0]_{3s}$ laminate, the response was amplified with frequency as the surface ply was transferring heat to the subsurface ply. At approximately 30 Hz the response tended to that predicted for the orthotropic surface ply, whilst at low loading frequencies the response tended to that predicted for the global laminate. In the $[\pm 45]_{3s}$ lay-up for CFRP, the ply-by-ply stress induced temperature change is identical and hence this laminate displayed an adiabatic response regardless of loading frequency. As with the GFRP, some important conclusions can be drawn from this work. Namely, for the given fibre volume fraction and resin-rich surface layer thickness, equation (3.5) is only valid for frequencies of around 30 Hz. However, this result cannot be considered universal for carbon fibre laminated composites. The ability to transfer heat is not just driven by the temperature gradient between the plies, but also the thermal conductivity of the carbon fibre itself, in turn, aspects such as ply thickness will also have an effect. The IM7/8552 material used here has a ply thickness of 0.131 mm and is considered a 'thin ply' material. Clearly, future work could consider thicker plies to determine their effect on heat transfer. The high fibre volume fraction of the CFRP material also plays a role and this means greater contact between fibres and better paths for conduction. A further conclusion that can be drawn is that the resin-rich surface layer is about 5.10 ± 3.69 μm for this material, and hence indicates a possible minimum resin-rich surface layer thickness for equation (6.3) to be valid, particularly, as the stress induced temperature change in the $[0,90]_{3s}$ CFRP is much less than of the GFRP.

The work described has also exposed a further and little considered matter relating to the effect of the paint coating on the response. The paint thickness plays an important role by attenuating the TSA response at high loading frequencies if the paint thickness is high i.e. ~23 μm. The peel ply imprint on the surface of composite components often means it is not necessary to paint the material as this generally has a greater emissivity. This was not explored and is clearly an avenue for more research. However, it was shown that painting over the peel ply imprint significantly attenuated the thermoelastic response. A major conclusion is the paint application, which is operator dependent, is

of significant importance. Thus, if paint is necessary, the paint layer thickness should be as thin as possible and uniform, otherwise the measured thermoelastic response will vary over the region of interest making any quantitative comparisons very difficult.

The indications are that GFRP is an easier material to deal with in terms of TSA, but in general these materials are not as well characterised and are usually manufactured by a process that results in lower quality material with variations in fibre volume fraction over the laminate. In contrast, CFRP lends itself to more consistent manufacturing with a focus on high quality (aerospace) laminates with well-characterised properties. The overarching conclusion is that accurate interpretation of the thermoelastic response from laminated orthotropic composites is possible. However, it is dependent on several competing factors, and it is recommended that a careful experimental calibration procedure is carried out, as described in this chapter to determine the source of the thermoelastic response, prior to embarking on an experimental campaign on actual components.

This chapter has focused on undamaged composite materials. However, the thermoelastic response changes when damage occurs as the sample may suffer plasticity and localised changes in stiffness. Hence, the next step is to understand how the thermoelastic response is affected when damage occurs. Additionally, the use of LSDIC simultaneously with TSA to obtain the strain and stress fields, respectively, could provide a constitutive parameter related to the stiffness of the sample. Therefore, Chapter 7 presents initial work on understanding the thermoelastic response on damaged GFRP coupons, and the extraction of the constitutive parameter in GFRP coupons and a T-joint substructure.

Chapter 7. Integration of TSA and LSDIC for Damage Assessment

7.1 Introduction

The thermoelastic response from an orthotropic material provides a stress metric (i.e. $\alpha_1\sigma_1 + \alpha_2\sigma_2$) and the LSDIC provides the strain. If the stress metric from TSA and the strain measurement from LSDIC are integrated, a new constitutive parameter can be defined that is related to the overall structural stiffness. To verify if the parameter is useful in assessing the condition of composite components, an experimental campaign has been conducted on GFRP coupons with different stacking sequences. The samples have been incrementally loaded to different stress levels to create damage. After each load increment, the load is reduced to the same level so that TSA and LSDIC can be carried out. The X-ray CT-scans were conducted to identify any internal damage.

To demonstrate further the efficacy of using microbolometer for TSA with the calibration approach defined in Chapter 5, both TSA and LSDIC were applied simultaneously on a T-joint taken from a wind turbine blade spar. The T-joint is made-up from several different materials and provides an initial structural demonstrator for combining both TSA and LSDIC in a low-cost configuration. Instead of simply aligning data sets, as conducted in the past, e.g. [23], the data has been integrated using an interpolation approach similar to that used in Chapter 5 to present the TSA data from the microbolometer and the photon detector to the same spatial resolution. The work performed on the T-joint substructure validates the microbolometer TSA approach and demonstrates the potential of the constitutive parameter applied to substructural components.

7.2 Constitutive Parameter Study

It can be seen in the TSA equation (3.3) that the thermoelastic response depends on the stiffness as well as the coefficients of thermal expansion, while DIC only depends on the stiffness. Therefore, the damage parameter or constitutive parameter will consider not only the degradation in stiffness, but also in coefficients of thermal expansion. The constitutive parameter will provide an indication of the material state such as stiffness.

7.2.1 Overview of the Methodology

To study the constitutive parameter, GFRP laminates were used, constructed in an identical manner to those described in Chapter 6, i.e. two cross-ply laminates, with stacking sequence $[0,90]_{3s}$ and

$[90,0]_{3s}$, with the same global stiffness but different surface ply orientation, and a shear dominated laminate, $[\pm 45]_{3s}$. The assessment of the constitutive parameter was performed following the procedure shown in Figure 7.1. The FPF was determined analytically using ESAComp, as described in section 2.1 and shown in Appendix C, and assessed experimentally with DIC. The study on the FPF determines the cyclic load level used to inspect the specimens using TSA and LSDIC. The specimens are loaded quasi-statically incrementally to different levels, between each load increment the specimen is unloaded to the mean level of the cyclic load. During the quasi-static loading, images were collected for DIC. A cyclic load is then applied and the TSA and LSDIC are carried out, after which the specimen was removed from the test machine and inspected using X-ray CT-scans. This enabled damage evolution in the samples to be tracked at each load increment and help to understand what the failure mechanism is and how damage is initiated and evolved. After the X-ray images were collected, the specimen was returned to the test machine and loaded to the next load increment and then unloaded to the same mean load used in the previous TSA and LSDIC inspection and so on. The constitutive parameter was extracted by dividing the normalised thermoelastic response, $\Delta T/T_0$, over the change in the sum of strains, $\Delta(\varepsilon_{xx} + \varepsilon_{yy})$.

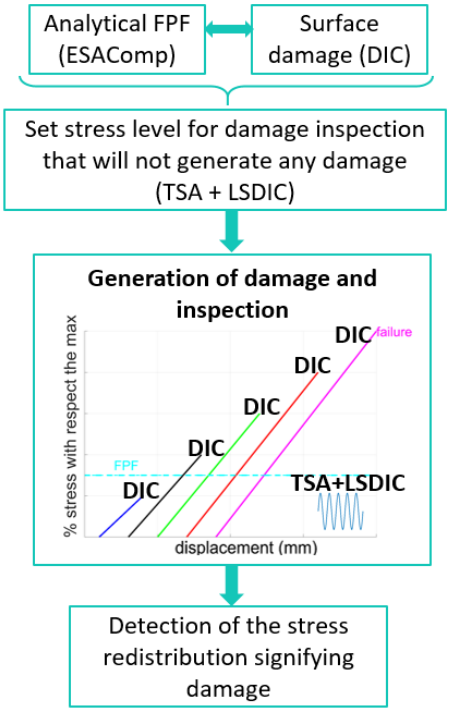

Figure 7.1 Constitutive parameter methodology

7.2.2 First Ply Failure using DIC

2D-DIC experiments have been performed using $[\pm 45]_{3s}$ and $[90,0]_{3s}$ samples to investigate the possibility of capturing damage on the surface ply and to validate the analytical FPF results obtained with ESAComp. The $[90,0]_{3s}$ was assessed because the 90° ply fails first and is on the surface. One

camera (Camera 1 (C1)) was positioned to view the smooth side of the sample and a second camera (Camera 2 (C2)) to view the peel ply side. The parameters used in the DIC are given in Table 7.1 and Table 7.2 for the $[\pm 45]_{3s}$ and $[90,0]_{3s}$ samples. The analysis carried out is shown in Appendix B. The specimens were painted with a white speckle pattern on a black background as described in Chapter 6.

Table 7.1 2D-DIC performance evaluation for $[\pm 45]_{3s}$ samples

	Sample 1		**Sample 2**		**Sample 3**	
	Camera 1 - smooth	**Camera 2 - peel ply**	**Camera 1 - smooth**	**Camera 2 - peel ply**	**Camera 1 - smooth**	**Camera 2 - peel ply**
Sensor and digitization	2448 x 2050, 12-bit	2448 x 2050, 12-bit	2448 x 2050, 12-bit	2448 x 2050, 12-bit	2448 x 2050, 12-bit	2448 x 2050, 12-bit
Camera noise (% of range)	1.15%	0.99%	0.52%	0.53%	0.52%	1.06%
Lens and imaging distance	150 mm F-mount, 0.7 m	150 mm F-mount, 0.5 m	50 mm F-mount, 0.7 m	50 mm F-mount, 0.5 m	50 mm F-mount, 0.7 m	50 mm F-mount, 0.5 m
Total number of images	2 (2 Hz)					
Pixel to mm conversion	1 pixel = 0.028 mm	1 pixel = 0.020 mm	1 pixel = 0.062 mm	1 pixel = 0.04 mm	1 pixel = 0.06 mm	1 pixel = 0.04 mm
ROI (mm)	57 x 25 mm	40 x 24 mm	112 x 23 mm	80 x 20 mm	115 x 22 mm	81 x 16 mm
Subset, step sizes (pix)	21, 7	45, 15	21, 7	21, 7	21, 7	21, 7
Interpolation, Shape functions, correlation criterion	Bicubic (6^{th} order spline), affine, ZNSSD					
Pre-smoothing	None					
Displacement resolution	0.001 mm	0.001 mm	$6.8 \cdot 10^{-4}$ mm	0.05 mm	$7.7 \cdot 10^{-4}$ mm	0.05 mm
Strain						
Smoothing technique	Local polynomial - affine					
Strain window	3 data points					
VSG	35 pixels	59 pixels	35 pixels	35 pixels	35 pixels	35 pixels
Resolution	0.091 %	0.034 %	0.035 %	0.058 %	0.037 %	0.074 %

Table 7.2 2D-DIC performance evaluation for $[90,0]_{3s}$ samples

	Sample 1		**Sample 2**	
	Camera 1 - smooth	**Camera 2 - peel ply**	**Camera 1 - smooth**	**Camera 2 - peel ply**
Sensor and digitization	2448 x 2050, 12-bit	2448 x 2050, 12-bit	2448 x 2050, 12-bit	2448 x 2050, 12-bit
Camera noise (% of range)	0.48%	0.89%	0.48%	1.23%
Lens and imaging distance	50 mm F-mount, 0.7 m	50 mm F-mount, 0.5 m	50 mm F-mount, 0.7 m	50 mm F-mount, 0.5 m
Total number of images	2 (2 Hz)			
Pixel to mm conversion	1 pixel = 0.07mm	1 pixel = 0.04 mm	1 pixel = 0.07mm	1 pixel = 0.07 mm
ROI (mm)	133 x 20 mm	82 x 19 mm	136 x 23 mm	133 x 22 mm
Subset, step sizes (pix)	21,7	21, 7	45, 15	45, 15
Interpolation, Shape functions, correlation criterion	Bicubic (6^{th} order spline), affine, ZNSSD			
Pre-smoothing	None			
Displacement resolution	$7.6 \cdot 10^{-4}$ mm	0.05 mm	$2.1 \cdot 10^{-4}$ mm	0.005 mm
Strain				
Smoothing technique	Local polynomial - affine			
Strain window	3 data points			
VSG	35 pixels	59 pixels	59 pixels	59 pixels
Resolution	0.048 %	0.055 %	0.01 %	0.063%

The samples were loaded in tension, as shown in Figure 3.1, in a servo-hydraulic test machine to failure at quasi-static rate of 2 mm/min. As one of the $[90,0]_{3s}$ failed at the grips in the first test, only data from two tests on this laminate were analysed. The gripping pressure was reduced in the tests following this failure and all other specimens failed away from the grips. The stress vs strain curve can be seen in Figure 7.2 and Figure 7.3 for the $[\pm 45]_{3s}$ and $[90,0]_{3s}$ samples, respectively, showing strain fields before and after the FPF (80 and 115 MPa for $[\pm 45]_{3s}$ and $[90,0]_{3s}$). The strain field data at a lower stress is constant, while at higher stress cracks aligned with the fibres can be observed. It can be seen that for each laminate all the specimens follow the same stress vs strain curve. As expected, the $[\pm 45]_{3s}$ laminate presents a linear behaviour prior to the first ply failure followed by a non-linear behaviour in which progressive damage occurs. The $[90,0]_{3s}$ specimen has a practically linear behaviour to failure. The ultimate stress for the $[\pm 45]_{3s}$ is ~ 240 MPa, and ~480 MPa for the $[90,0]_{3s}$ laminate, which dictates the load range and the increments that can be applied to the samples to create progressive damage.

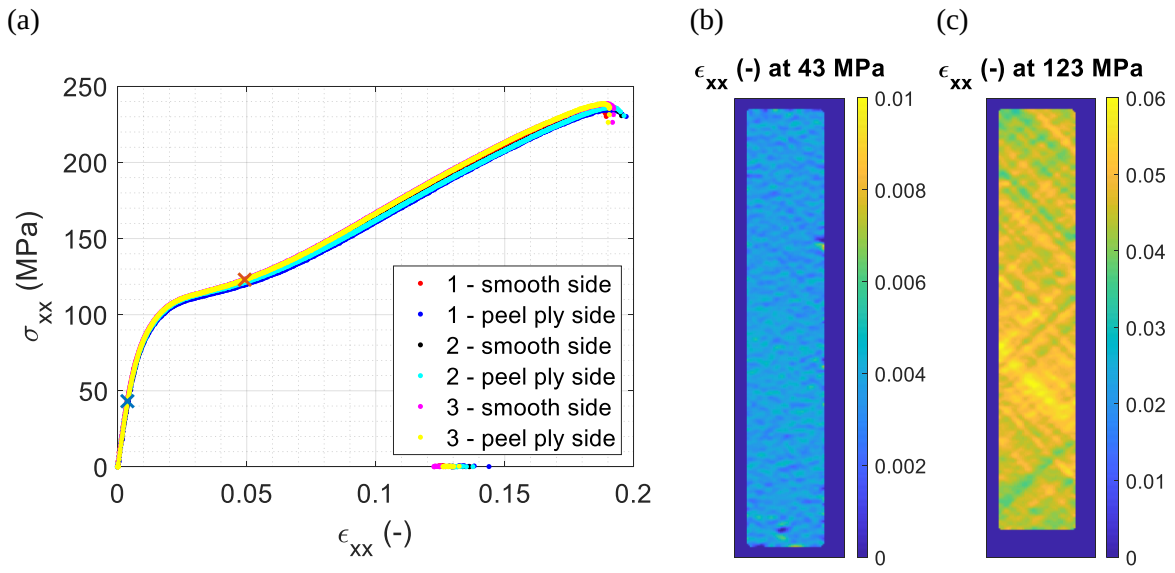

Figure 7.2 $[\pm 45]_{3s}$ (a) stress vs strain and strain fields (smooth side - C1) at (b) 43 MPa (blue marker) and (c) 123 MPa (orange marker) obtained with 2D-DIC

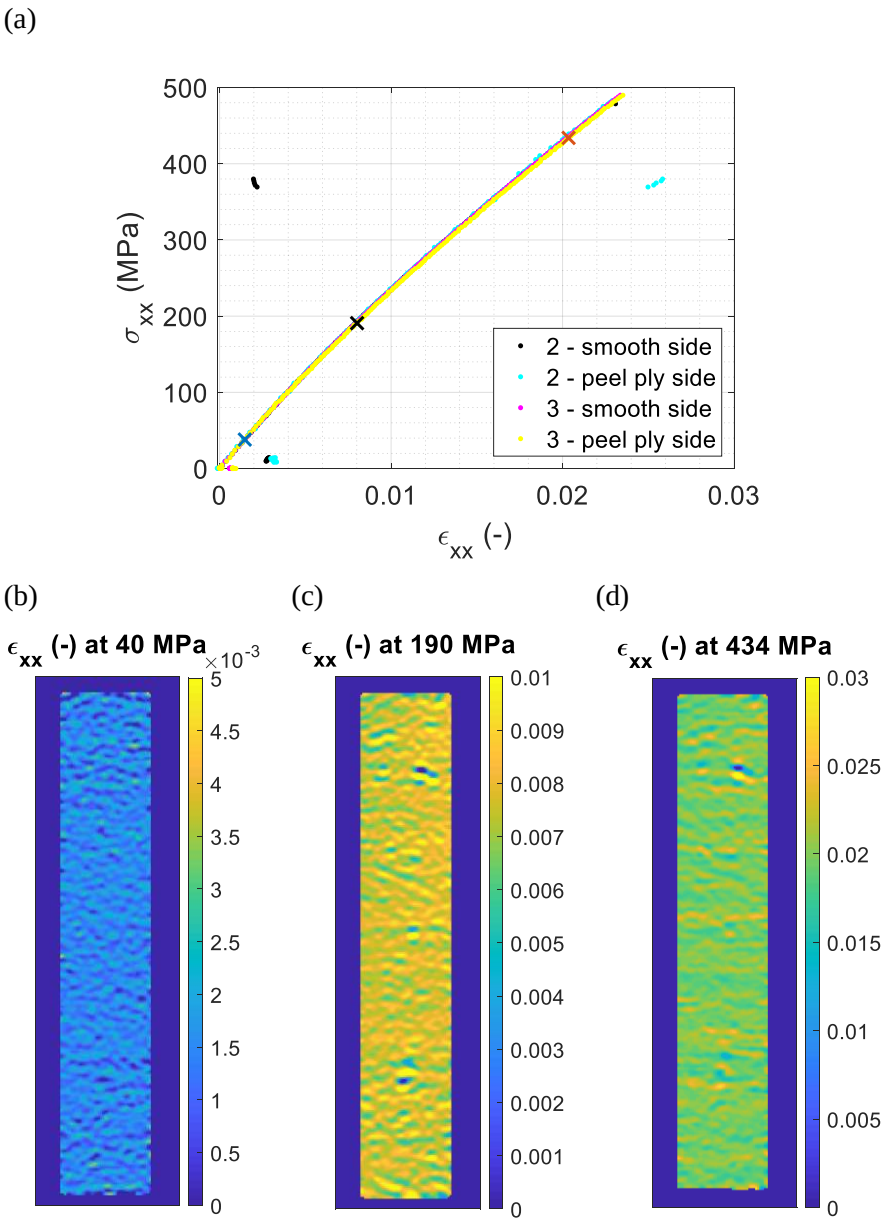

Figure 7.3 $[90,0]_{3s}$ (a) stress vs strain and strain fields at (b) 40 MPa (blue marker), (c) 190 MPa (black marker), (d) 434 MPa (orange marker) obtained with 2D-DIC

It is clear from the full-field images that damage is occurring progressively in the $[\pm 45]_{3s}$ and in the 90° plies of the $[90,0]_{3s}$ laminate. As the stress-strain curves use an average value of strain across the whole specimen, the progressive nature of the damage is not visible in the stress-strain plots. However, it is clear in the full-field data. To provide a better visualisation and utilise the full-field 2D-DIC strain data, it is possible to obtain contour plots of the longitudinal strain (ε_{xx}) for the central vertical position (line plot) vs the stress. Any changes in the strain field with respect to the vertical position along the specimen shows a possible deviation to uniform strain signifying damage at the surface ply. When the strain contour plot becomes inhomogeneous at a given stress this signifies localised changes in strain or strain concentrations signifying damage at that position, which can be

compared to the stress at which the FPF is predicted using the failure criteria obtained from ESAComp (see Appendix C).

Figure 7.4 presents the contour strain plots obtained for the $[\pm 45]_{3s}$ laminate for both the smooth and peel ply sides. The plot shows the vertical position on the sample for the applied homogenised stress in the laminate (force over area). The blue contour along the vertical position indicates that the strain is uniform at low stresses, but at high stresses the strain contour is no longer uniform. The contour plot appears to taper because the specimen moves in the field of view as the test progresses. The space at the back of the test machine, where C2 was positioned, was limited, so a smaller section of the sample than in C1 was inspected. The contour plot on the smooth side shows two vertical lines corresponding to 43 and 123 MPa strain fields provided in Figure 7.2. At position = 80 mm, there are changes in the strain profile which begins at a stress level of ~ 50 MPa on both the smooth and peel ply side. The FPF laminate stress obtained with ESAComp (see Appendix C) is in the 45° ply at ~ 80 MPa, the FPF stress level obtained experimentally is below than the ESAComp result. Therefore, 36 MPa was selected as the maximum stress level at which to perform each of the LSDIC and TSA inspections, to limit any further damage being introduced and in the initial linear-elastic region of the laminate, as also seen in Figure 7.2.

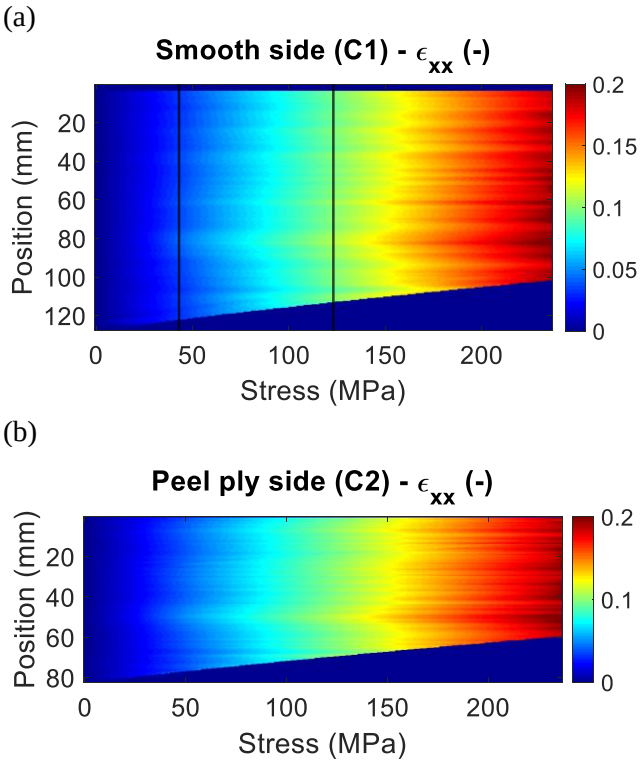

Figure 7.4 $[\pm 45]_{3s}$ strain contour - vertical position vs stress (a) C1 - smooth side, and (b) C2 - peel ply side

Figure 7.5 shows the $[90,0]_{3s}$ strain contour plot, where the vertical lines on the smooth side correspond to the strain fields shown in Figure 7.3. It can be seen that there is a change in the strain

along the vertical line at about 50 MPa, and at ~ 100 mm on the smooth side. At this stress level, more horizontal lines can be seen, highlighting that the strain is no longer uniform along the vertical position. The FPF obtained with ESAComp (see Appendix C) for the 90° ply in $[90,0]_{3s}$ or $[0,90]_{3s}$ laminate is 115 MPa. The DIC data actually indicates the FPF is closer to that for a $[90]_{10}$ (51 MPa), hence, stress level considered at which it does not create damage is 48 MPa.

(a)

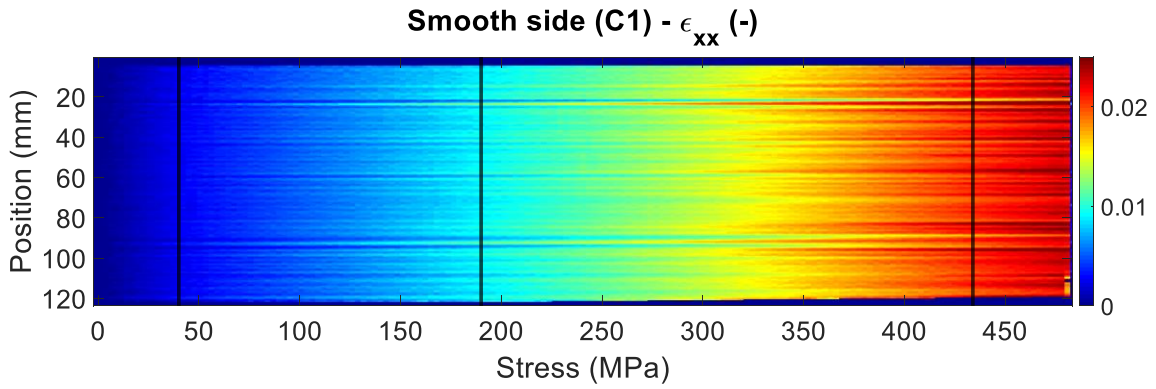

(b)

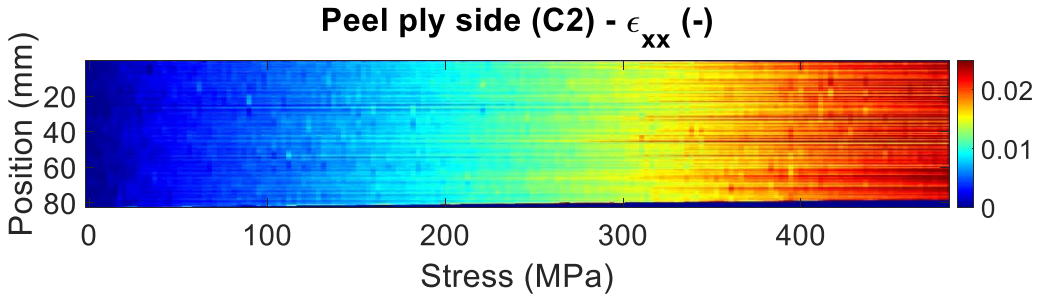

Figure 7.5 $[90,0]_{3s}$ strain contour - vertical position vs stress (a) C1 - smooth side, and (b) C2 - peel ply side

7.2.3 Determination of the Experimental Test Matrix

The inspection level was determined for the laminates analysed, $[\pm 45]_{3s}$, and cross-ply $[90,0]_{3s}$ and $[0,90]_{3s}$, as well as the ultimate stress. Therefore, the different load steps were set for the $[\pm 45]_{3s}$ and for both cross-ply laminates as given in Table 7.3 and Table 7.4, respectively. The global homogenised stress was calculated with the initial width of the sample, i.e. 25 mm. Table 7.3 and Table 7.4 provide the parameters to perform DIC while the sample is being loaded, and the parameters for the TSA and LSDIC while the sample is being inspected. The experiments start with a quasi-static test from 0 kN to a stress level that is 15% of the ultimate stress. After the static test, the load was reduced to the mean cyclic load to perform the inspection with TSA and LSDIC. Once cyclic loading stabilised at about 100 load cycles, both TSA and LSDIC were triggered to start collecting frames together during the same time period. After TSA and LSDIC are performed, the

sample is taken out of the test machine to perform X-ray CT-scan. Once the CT-scan is completed, the sample is placed into the test machine at the same position as it was before, and the same procedure is repeated using the next level of quasi-static load.

Table 7.3 Test matrix for the $[\pm 45]_{3s}$ sample

Stress level with respect to ultimate stress	**Estimated stress (MPa)**	**TSA+LSDIC**	**DIC**
15 %	47		0 kN to 3.24 kN 0.1 mm/s 1.5 Hz frame rate
	36	2 ± 1.24 kN at 10.1, 5.1 and 3.1 Hz loading frequency TSA: 25 Hz frame rate 5250 frames and 383 Hz frame rate LSDIC: 1.5 Hz frame rate 316 frames	
35%	83		0 kN to 5.75 kN 0.1 mm/s 1.5 Hz frame rate
	36	2 ± 1.24 kN at 10.1, 5.1 and 3.1 Hz loading frequency TSA: 25 Hz frame rate 5250 frames and 383 Hz frame rate LSDIC: 1.5 Hz frame rate 316 frames	
50%	119		0 kN to 8.3 kN 0.1 mm/s 1.5 Hz frame rate
	36	2 ± 1.24 kN at 10.1, 5.1 and 3.1 Hz loading frequency TSA: 25 Hz frame rate 5250 frames and 383 Hz frame rate LSDIC: 1.5 Hz frame rate 316 frames	
75%	178		0 kN to 12.41 kN 0.1 mm/s 1.5 Hz frame rate
	36	2 ± 1.24 kN at 10.1, 5.1 and 3.1 Hz loading frequency TSA: 25 Hz frame rate 5250 frames and 383 Hz frame rate LSDIC: 1.5 Hz frame rate 316 frames	
90%	215		0 kN to 14.85 kN 0.1 mm/s 1.5 Hz frame rate
	36	2 ± 1.24 kN at 10.1, 5.1 and 3.1 Hz loading frequency TSA: 25 Hz frame rate 5250 frames and 383 Hz frame rate LSDIC: 1.5 Hz frame rate 316 frames	

Table 7.4 Test matrix for the cross-ply $[90,0]_{3s}$ and $[0,90]_{3s}$ samples

Stress level with respect to ultimate stress	**Estimated stress (MPa)**	**TSA+LSDIC**	**DIC**
15 %	53		0 kN to 3.67 kN 0.1 mm/s 1.5 Hz frame rate
	48	2 ± 1.67 kN at 10.1, 5.1 and 3.1 Hz loading frequency TSA: 25 Hz frame rate 5250 frames and 383 Hz frame rate LSDIC: 1.5 Hz frame rate 316 frames	
35%	169		0 kN to 11.7 kN 0.1 mm/s 1.5 Hz frame rate
	48	2 ± 1.67 kN at 10.1, 5.1 and 3.1 Hz loading frequency TSA: 25 Hz frame rate 5250 frames and 383 Hz frame rate LSDIC: 1.5 Hz frame rate 316 frames	
50%	242		0 kN to 16.7 kN 0.1 mm/s 1.5 Hz frame rate
	48	2 ± 1.67 kN at 10.1, 5.1 and 3.1 Hz loading frequency TSA: 25 Hz frame rate 5250 frames and 383 Hz frame rate LSDIC: 1.5 Hz frame rate 316 frames	
75%	363		0 kN to 25.1 kN 0.1 mm/s 1.5 Hz frame rate
	48	2 ± 1.67 kN at 10.1, 5.1 and 3.1 Hz loading frequency TSA: 25 Hz frame rate 5250 frames and 383 Hz frame rate LSDIC: 1.5 Hz frame rate 316 frames	
90%	437		0 kN to 30.15 kN 0.1 mm/s 1.5 Hz frame rate
	48	2 ± 1.67 kN at 10.1, 5.1 and 3.1 Hz loading frequency TSA: 25 Hz frame rate 5250 frames and 383 Hz frame rate LSDIC: 1.5 Hz frame rate 316 frames	
95%	458		0 kN to 30.15 kN 0.1 mm/s 1.5 Hz frame rate
	48	2 ± 1.67 kN at 10.1, 5.1 and 3.1 Hz loading frequency TSA: 25 Hz frame rate 5250 frames and 383 Hz frame rate LSDIC: 1.5 Hz frame rate 316 frames	

It was seen in Chapter 6 that a thick paint had a detrimental effect in TSA. Hence, TSA and LSDIC in this chapter have been performed in specimens without background paint. Black speckles were applied with a thin black marker to obtain speckles of the same size, an example can be seen in Figure 7.6 for a 200 x 200 pix region. The DIC and LSDIC performance evaluation is shown in Table 7.5, based on the analysis shown in Appendix B.

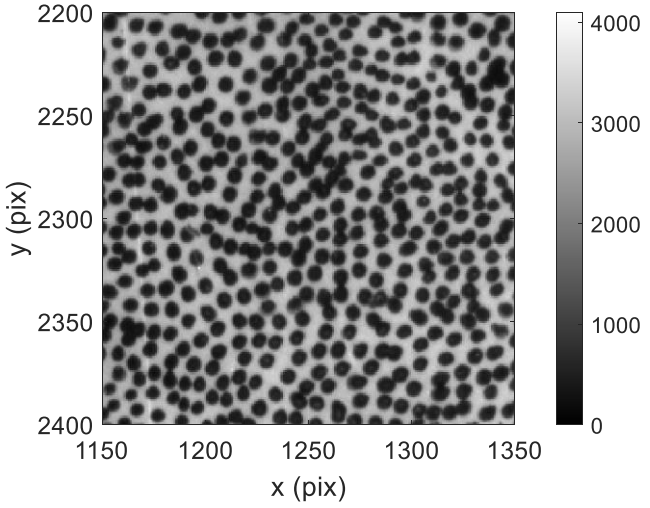

Figure 7.6 Speckle pattern applied on GFRP without background paint (grey levels)

Table 7.5 LSDIC and DIC performance evaluation

Technique used	**3D Digital Image Correlation**	
	Camera 1	**Camera 2**
Sensor and digitization	2448 x 2050, 12-bit	
Camera noise (% of range)	0.85%	0.90%
Lens and imaging distance	50 mm F-mount, 1 m	
Total number of images	2 (1.5 Hz)	
Pixel to mm conversion	1 pixel = 0.094 mm	
ROI (mm)	137 x 25 mm	
Subset, step	61, 20	
Interpolation, shape functions, correlation criterion	Bicubic (6^{th} order spline), affine, ZNSSD	
Pre-smoothing	None	
Displacement resolution	$4.85 \cdot 10^{-4}$ mm	
Strain		
Smoothing technique	Local polynomial - affine least-squares fit	
Strain window	3 data points	
VSG	102 pixels	
Resolution	0.0085 %	

7.2.4 Results

Figure 7.7 shows the $\Delta T/T_0$ average across the specimen plotted against the homogenised stress applied to the laminate in each loading step, indicated as the 'damaging stress' on the x-axis of the plot. The three different laminates and three different loading frequencies are shown. It is important to remember that the load range applied to each of these samples is the inspection load range given in Table 7.3 and Table 7.4. From Chapter 6, it was concluded that the source of the thermoelastic response of GFRP laminates was the resin-rich layer. Hence, only the damage on the resin-rich layer is detected in $\Delta T/T_0$ vs damaging stress plots. It can be seen that for the $[0,90]_{3s}$ laminate, $\Delta T/T_0$ is constant for each 'damaging stress' indicating that the resin-rich layer of the specimen is not damaged. The $[90,0]_{3s}$ laminate shows a slight reduction of $\Delta T/T_0$ at higher stresses due to the resin-rich layer being degraded, as the 90° ply in contact with the resin-rich layer has been damaged at the last load steps. The degradation of the resin-rich layer is highlighted for the $[\pm 45]_{3s}$ laminate as it suffers much more deformation when the stress increases, and hence, higher degradation in the resin-rich layer. The $[\pm 45]_{3s}$ specimen did exhibit plastic deformation in the test coupon, where the coupon length elongated at higher stresses. Additionally, there is a linear reduction of $\Delta T/T_0$ when the stress is higher than 83 MPa. Across all the three test specimens, the X-ray CT-scans did not show any damage except for the last scan of the $[\pm 45]_{3s}$ laminate, where a crack was observed at the centre of the stacking sequence (Figure 7.8), but it was not visible in the TSA as the heat is not transferred in the GFRP laminate. Full-field ΔT for each specimen at the first and last damaging stresses are shown in Figure 7.9 to enable a detail inspection of the specimen surfaces and confirm the conclusions extracted from Figure 7.7. It can be seen that the resin-rich layer has been damaged for the $[90,0]_{3s}$ and the $[\pm 45]_{3s}$ laminates as both specimens show an attenuation on ΔT and cracks at the last damaging stress. However, $[0,90]_{3s}$ laminate does not show any difference in the ΔT field between the first and last damaging stress due to no heat transferring from the possible damaged subsurface 90° ply to the resin-rich layer. Hence, it can be concluded from Figure 7.7 and Figure 7.9 that the $[0,90]_{3s}$laminate is not suitable to analyse damage progression as $\Delta T/T_0$ was constant with respect to the damaging stress and no damage was seen in ΔT field. Additionally, $[90,0]_{3s}$ laminate only showed a change in $\Delta T/T_0$ at the last damaging stress, which was confirmed by the ΔT field, but did not show any damage progression as seen in the $[\pm 45]_{3s}$ specimen.

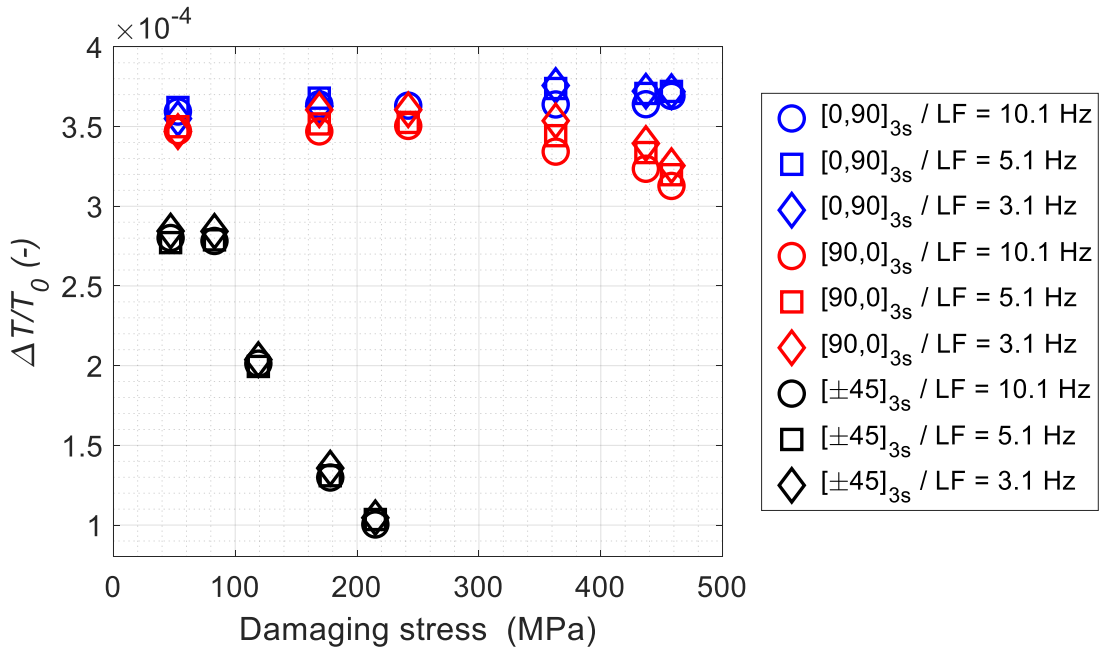

Figure 7.7 TSA results $\Delta T/T_0$ vs damaging stress

Figure 7.8 Crack shown in centre of the stacking sequence $[\pm 45]_{3s}$

(a) $[0,90]_{3s}$ after 53 MPa (b) $[90,0]_{3s}$ after 53 MPa (c) $[\pm 45]_{3s}$ after 47 MPa

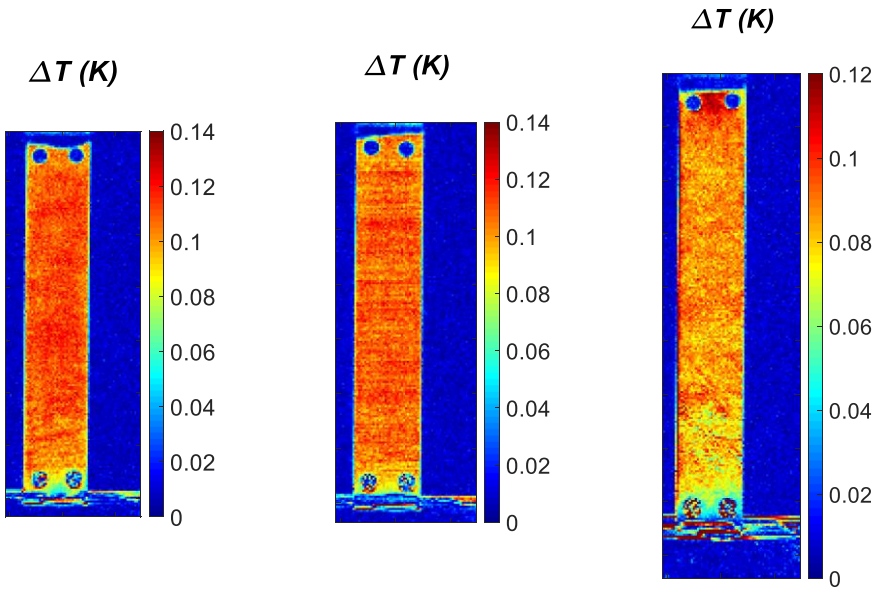

(d) $[0,90]_{3s}$ after 458 MPa (e) $[90,0]_{3s}$ after 458 MPa (f) $[\pm 45]_{3s}$ after 215 MPa

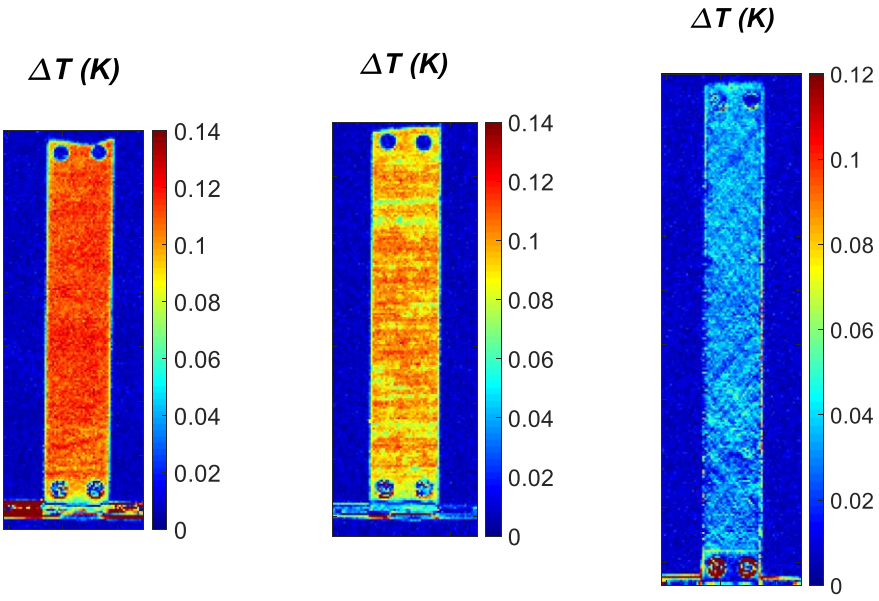

Figure 7.9 Full-field ΔT at first (a)-(c) and last (d)-(f) damaging stresses at 5.1 Hz loading frequency

Figure 7.10 shows the LSDIC results for the three laminates and loading frequencies, in particular, the $\Delta(\varepsilon_{xx} + \varepsilon_{yy})$ against the previous applied stress. It can be seen that for both cross-ply samples there are no changes in $\Delta(\varepsilon_{xx} + \varepsilon_{yy})$ except at the last applied stress, where it is marginally reduced. Therefore, the stiffness of both cross-ply laminates remains almost unchanged throughout the damaging stress. However, regarding the $[\pm 45]_{3s}$ sample, there is a reduction in $\Delta(\varepsilon_{xx} + \varepsilon_{yy})$ when the stress is higher than 83 MPa, which implies that the stiffness has changed. Full-field $\Delta(\varepsilon_{xx} + \varepsilon_{yy})$ plots at first and last damaging stress of the three laminates are shown in Figure 7.11, which

confirm the conclusions obtained from Figure 7.10. The change in stiffness of the $[\pm 45]_{3s}$ laminate is due to the fibres reorienting towards the 0° ply by ~8° as seen in the CT-scans, and Figure 7.13. It can be seen that the rate of decrease of $\Delta T/T_0$ with respect the damaging stress (Figure 7.7) is steeper than the rate of descend of $\Delta(\varepsilon_{xx} + \varepsilon_{yy})$ against the damaging stress (Figure 7.10), which can also be seen in Figure 7.13. It is suggested that the $[\pm 45]_{3s}$ laminate also suffers degradation of the coefficients of thermal expansion as presented in the literature [31, 149] due to possible micro-cracks taking place at the resin-rich layer that were not detected on the CT-scans. It is evident in the TSA results as there is a steeper reduction in response when the stress increases, which is associated to the fibre reorientation and the degradation of the coefficients of thermal expansion.

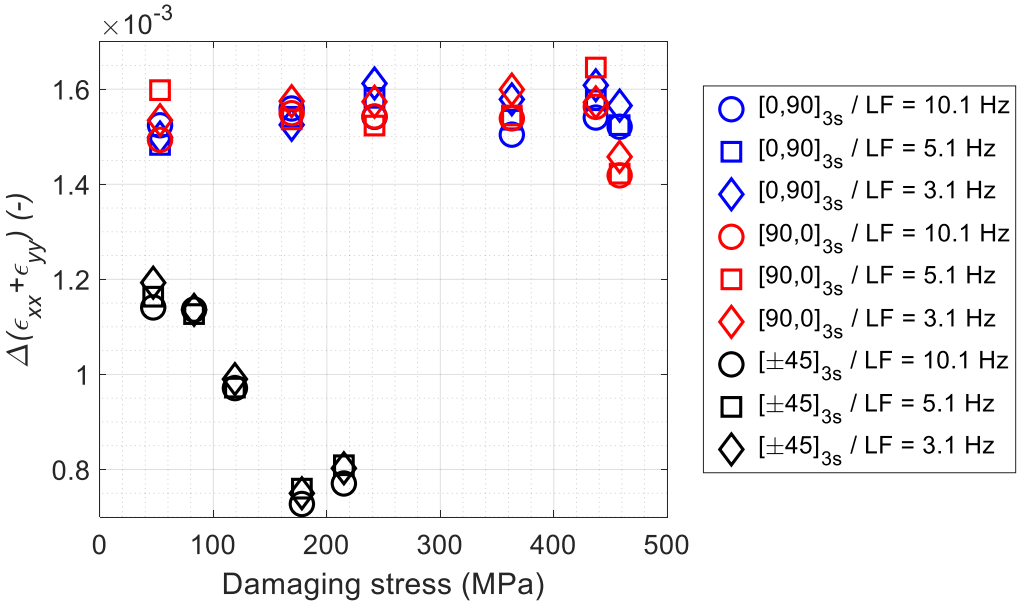

Figure 7.10 LSDIC results $\Delta(\varepsilon_{xx} + \varepsilon_{yy})$ vs damaging stress

(a) $[0,90]_{3s}$ after 53 MPa (b) $[90,0]_{3s}$ after 53 MPa (c) $[\pm 45]_{3s}$ after 47 MPa

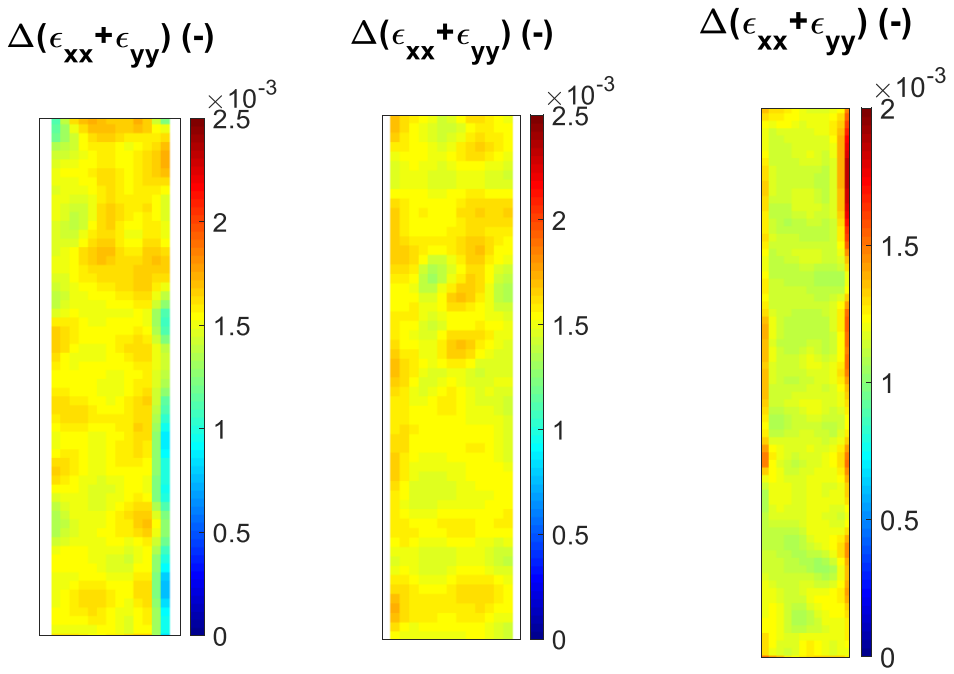

(d) $[0,90]_{3s}$ after 458 MPa (e) $[90,0]_{3s}$ after 458 MPa (f) $[\pm 45]_{3s}$ after 215 MPa

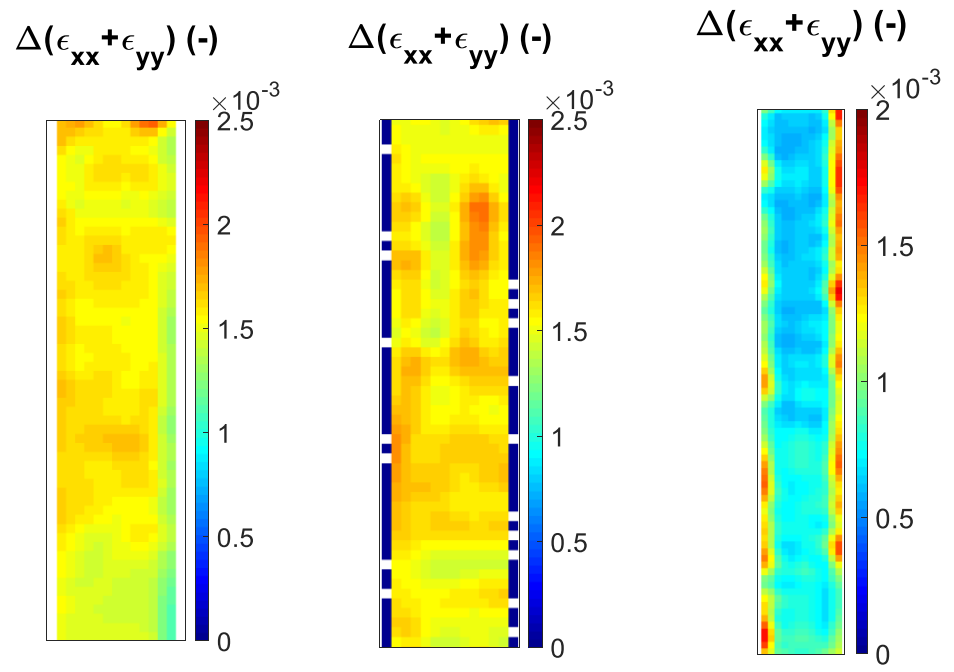

Figure 7.11 Full-field $\Delta(\varepsilon_{xx} + \varepsilon_{yy})$ at first (a)-(c) and last (d)-(f) damaging stresses at 5.1 Hz loading frequency

From the LSDIC, TSA, and CT-scan data, it is possible to determine the fibre angle after each damaging stress. To obtain theoretical fibre angles from the LSDIC measured strains, CLT has been used for a range of $[\pm\theta]_{3s}$ laminates. From CLT, the strains for different $[\pm\theta]_{3s}$ laminates are extracted to obtain a plot of strain vs fibre angle, θ (shown in Figure 7.12) that is then used as a look

up graph, to determine the fibre angle θ that corresponds to the $\varepsilon_{xx} + \varepsilon_{yy}$ obtained with LSDIC measured strains. For the extraction of the fibre angle from TSA, the coefficients of expansion α_1 and α_2 at a stress level lower than 115 MPa have been taken from the literature (Table 6.12). It was considered that α_1 and α_2 change due to both damage and reorientation of the fibres. From the literature [31, 149], it was seen that α_2 is significantly more affected by damage than α_1, that is 80% reduction in α_2 versus 20 % reduction in α_1. Therefore, an arbitrary selection of α_1 and α_2 has been carried out following this criterion, shown in Table 7.6. These were adjusted so that TSA matches the same rate of θ reduction obtained with the CT-scans and LSDIC. Equation (6.4) is used to obtain ΔT for a range of $[\pm\theta]_{3s}$ laminates considering the different values of coefficients of thermal expansion. Therefore, instead of having a single look up plot (as was used to obtain θ from LSDIC measured strains), there is a look up graph for each set of α_1 and α_2 parameters considered, i.e. for each stress. Therefore, knowing the measured ΔT, it is possible to obtain θ for each case. Finally, for the CT-scan, the angle between the fibres in $+\theta$ ply and the $-\theta$ ply is measured after each damaging stress and divided by 2 to obtain the θ with respect the longitudinal axis, i.e. the same axis as the loading direction. The θ obtained with LSDIC, TSA, and CT-scans is shown in Figure 7.13 (b), where it can be seen that the rate of reduction of θ is similar among the three different methods, otherwise, the TSA would provide much different fibre angles if α_1 and α_2 are considered to be unchanged (Figure 7.13 (a)).

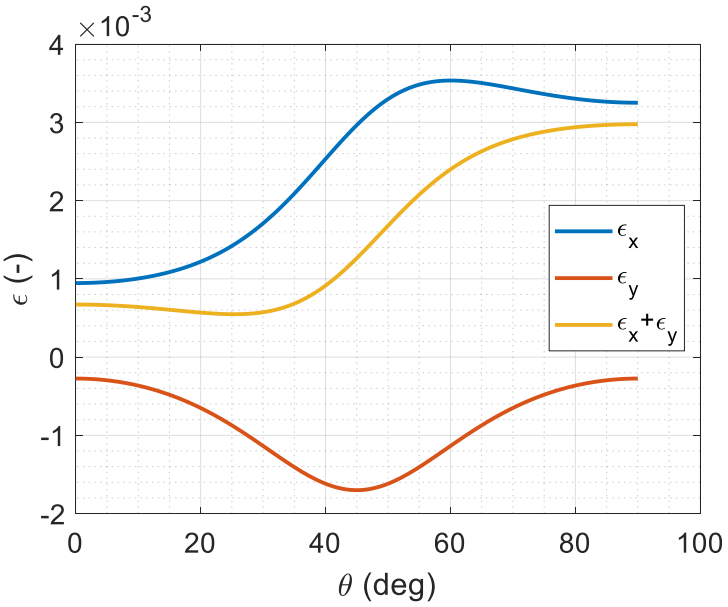

Figure 7.12 Strain vs fibre angle

Table 7.6 Considered coefficients of thermal expansion to extract fibre angles from TSA data

Damaging stress (MPa)	**Damaging load (kN)**	$\boldsymbol{\alpha_1(\cdot 10^{-6}\ 1/K)}$	$\boldsymbol{\alpha_2(\cdot 10^{-6}\ 1/K)}$
119	8.3	6.3	18.1
178	12.41	5.6	6.1
215	14.85	4.2	3.6

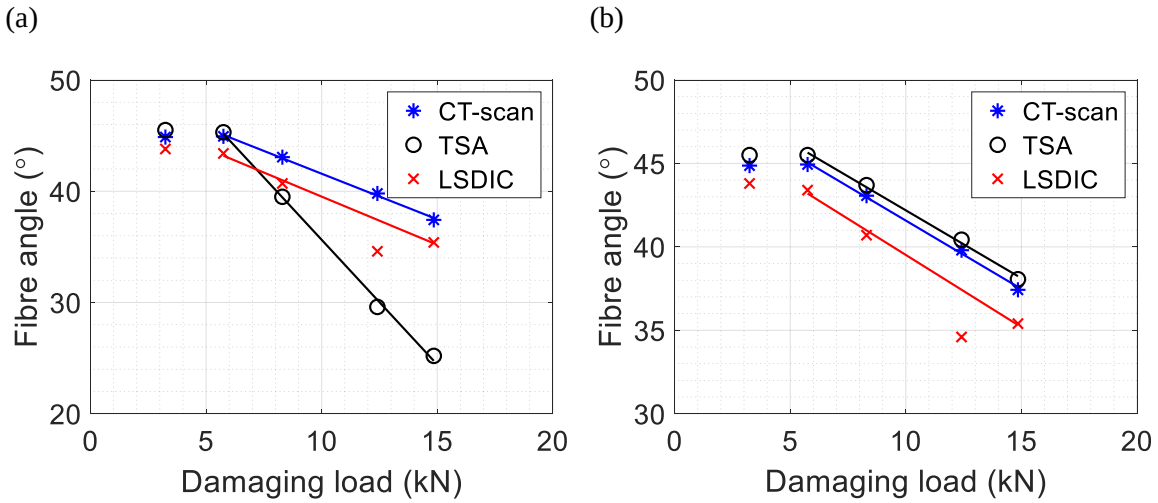

Figure 7.13 Fibre angle vs damaging load obtained with CT-scans, LSDIC and TSA (a) α_1 and α_2 constant for all stress points, (b) α_1 and α_2 adjusted for each stress point

7.2.5 Constitutive Parameter

Figure 7.14 shows the constitutive parameter as defined below against the damaging stress. The parameter depends on the load of the test, therefore, it is a state variable. The constitutive parameter is a measurement of the material state and changes of this parameter after subsequent loading would signify damage. The constitutive parameter C is defined as

$$C \sim \frac{\frac{\Delta T}{T_0}}{\Delta(\varepsilon_{xx} + \varepsilon_{yy})} \tag{7.1}$$

where $\Delta T/T_0$ is an indication of the sum of principal stresses and $\Delta(\varepsilon_{xx} + \varepsilon_{yy})$ are the strains.

Therefore, the constitutive parameter would indicate a stiffness measure, however, it is important to note that $\Delta T/T_0$ is also coupled to the coefficients of thermal expansion (α_1 and α_2), which has been shown earlier to be sensitive to fibre angle and fibre reorientation.

It can be seen in Figure 7.14 that for both cross-ply samples, $[0,90]_{3s}$ and $[90,0]_{3s}$, the constitutive parameter remains almost constant with increasing levels of applied stress. As it was discussed above, the thermoelastic response is driven by the resin-rich layer, hence, as there is no heat transfer

to the surface, the cross-ply laminates are not showing damage progression. However, the $[\pm 45]_{3s}$ sample presents a reduction of the constitutive parameter when the stress is over 83 MPa, as it suffers significant plastic deformation with increasing stress, which damages the resin-rich layer. The constitutive parameter of $[\pm 45]_{3s}$ laminate is mainly driven by the reorientation of the fibres towards 0°, which increases stiffness, and therefore reduces the strains measured with LSDIC for a given applied stress, and decreases the thermoelastic response. Additionally, TSA suffered a higher attenuation on the $\Delta T/T_0$ due to the coefficient of thermal expansion of the resin being reduced due to possible micro-cracking as suggested in the literature [31], although the microcracks were not visible in the CT-scans.

It can be concluded that GFRP is not a suitable material to study damage progression as the thermoelastic response is driven by the resin, and no heat transfer is occurring. It is clear that if similar experiments were performed using CFRP, as described in Chapter 6, depending on the loading frequency used, damage from subsurface plies might show on the surface. Hence, a key recommendation for future work is to conduct a similar campaign on the CFRP specimens.

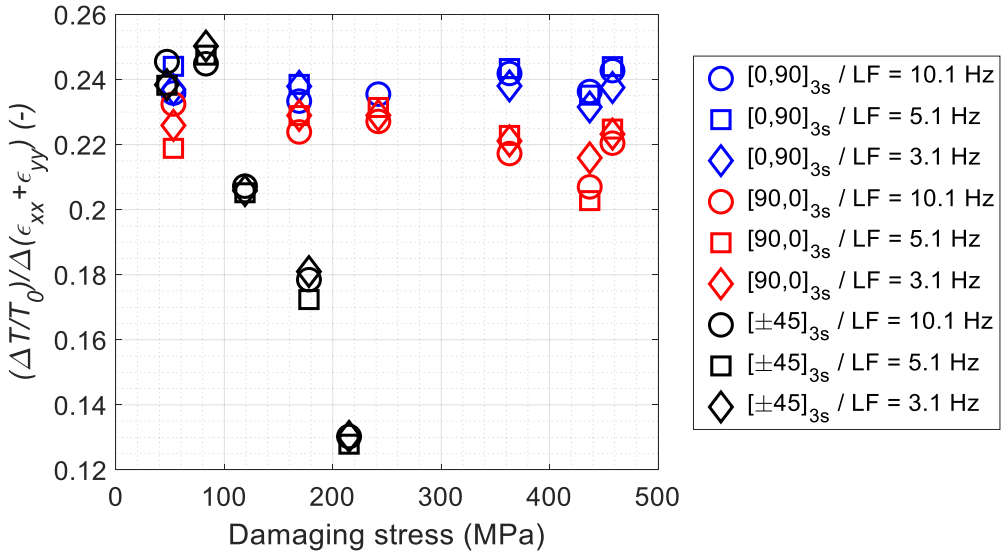

Figure 7.14 Constitutive parameter vs damaging stress for the different laminates and loading frequencies considered

7.2.6 Summary

This section has covered the investigation of a constitutive parameter inherent to the sample material to understand the possibility of extracting the sample state i.e. stiffness by means of using simultaneously LSDIC and TSA. Experiments were designed to increase the damaging stress to the specimens in load steps with TSA and LSDIC performed between each load step while the sample is within the test machine, and X-ray CT-scans, taking place after each load step out of the test

machine. This section is a follow up of the work done in Chapter 6, where it was seen that the thermoelastic response of GFRP samples was driven by the resin-rich layer.

The $\Delta T/T_0$ have shown an attenuation in the response of the $[\pm 45]_{3s}$ sample when the stress increases over 83 MPa. For the $[90,0]_{3s}$ specimen, a slight drop in $\Delta T/T_0$ was detected at the last damaging stress due to the resin-rich layer being damaged, but did not show damage progression at lower stresses. Additionally, $[0,90]_{3s}$ did not show any changes in $\Delta T/T_0$. Similarly, LSDIC results showed little change to strains on both cross-ply samples, but for the $[\pm 45]_{3s}$ sample, there was a reduction in strain over 83 MPa, which implies an increase in stiffness as the inspection load is constant. The change in stiffness is due to the change in fibre angle re-orientating towards 0° by ~ 8° that was measured directly in the CT-scans. It was also possible to calculate the fibre angle from the LSDIC measured strains as well as the TSA data to understand the effect of the change in fibre angle in both TSA and LSDIC datasets. However, to obtain the fibre angle from the TSA data, it was necessary to adjust the coefficients of thermal expansion as the rate of decline of $\Delta T/T_0$ and $\Delta(\varepsilon_{xx} + \varepsilon_{yy})$ versus the damaging stress was higher. This is due to the TSA being influenced not only by the stiffness but also by the coefficients of thermal expansion, which degrade when there is damage, and depend on the ply orientation. From the literature [31], it was seen that the coefficients of thermal expansion in composite materials degrade when the stress increases due to micro-cracking and that α_2 is significantly more affected than α_1 (80% reduction in α_2 versus 20 % reduction in α_1). Therefore, the selection of α_1 and α_2 was done following this criterion. If the degradation of α_1 and α_2 was not considered, the fibre angle extracted from TSA would not be similar to those extracted from LSDIC measured strains and CT-scans, giving much lower values at higher previous applied stresses.

Finally, the constitutive parameter obtained by dividing $\Delta T/T_0$ (indicative of stress and heat transfer) by $\Delta(\varepsilon_{xx} + \varepsilon_{yy})$ has shown that it is mainly driven by the TSA results as it combines the interaction of two different material properties (stiffness and coefficients of thermal expansion). Additionally, only significant differences between the first and last load step were seen in the $[\pm 45]_{3s}$ sample in comparison with both cross-ply specimens, so not much information could be extracted from the cross-ply laminates. Unfortunately, the CT-scans did not detect any damage between the different levels of applied stresses used to damage the test coupons, except after the last load step of the $[\pm 45]_{3s}$ specimen. Damage in the $[\pm 45]_{3s}$ specimen was present at the centre of the stacking sequence, but was not detected with TSA and LSDIC as the thermoelastic response is driven by the resin-rich layer, which demonstrated that GFRP is not suitable to study damage progression. Therefore, a key area of future work is to conduct similar tests with CFRP laminates to assess damage progression as at low loading frequencies heat transfer occurs, and evaluate if the subsurface damage can be detected; this is the object of a new PhD project.

To overcome the difficulty of the TSA response being affected by the interaction of stiffness and coefficients of thermal expansion, a procedure to decouple these two magnitudes would be the way forward to determine a constitutive parameter that would provide information of the material state i.e. stiffness. It would also be beneficial to understand the limits in terms of sample depths for TSA considering different materials.

7.3 Application to a T-joint Substructure

The work presented in this section was performed in collaboration with another PhD student, Jack S. Callaghan who is sponsored by Siemens Gamesa Renewable Energy (SGRE), and provided the T-joint demonstrator components. The T-joint provides a demonstration of a small scale substructure test that shows how TSA and LSDIC can be applied simultaneously. The output of the work described here provided an initial step in facilitating Jack S. Callaghan's research, and in particular providing the basis for validating a high-fidelity substructure FEA model. The FEA model of the T-joint was made of 20-node quadratic solid elements (ANSYS SOLID186) in material regions with defined orientations to match the ply layups. It contained 74,000 elements from 325,000 nodes, giving 976,000 Degrees of Freedom (DoF). More importantly, following the development of the microbolometer for TSA, the T-joint component provides a complex component on which to trial low-cost microbolometers.

The aim of the work is to demonstrate that microbolometer based TSA can be applied simultaneously with LSDIC to a component at a larger scale with a complex structure than the tests with the coupons presented in the preceding chapters of the thesis. The calibration parameter developed in Chapter 5 has been applied to data captured by the microbolometer with the noise reduction feature on in the T-joint demonstrator formed of different materials. In addition, a comparison between a photon detector and a microbolometer has been performed to validate the application of the microbolometer calibration to complex components. This initial work presented in this chapter assesses the feasibility of combining microbolometer based TSA with LSDIC on large structures, and identifies aspects that require further development.

7.3.1 Demonstrator T-joint Component

A schematic of how the T-joint specimens were produced from the wind turbine blade is shown in Figure 7.15. The T-joint substructure is typical of a spar section from the pressure side of a wind turbine blade from SGRE. The T-joint was manufactured using different materials, i.e. woods, resin and glass fibres, by means of a resin infusion technique. The distribution of materials on this substructure is shown in Figure 7.16. It is not possible to disclose full details of the laminate architecture, or the actual materials used as this information is commercially sensitive. However, as

a variety of materials are used, it will demonstrate that the calibration approach to correct for the low-pass filtering of the microbolometer is relevant for all the materials in the T-joint.

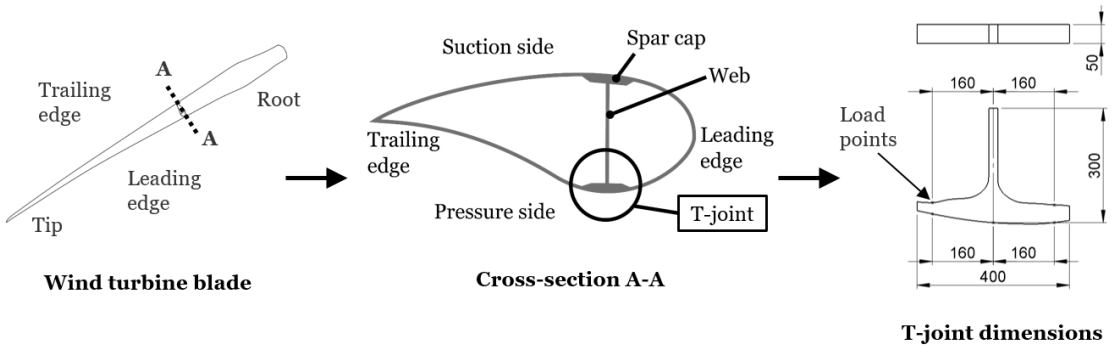

Figure 7.15 Wind turbine blade spar T-joint from the pressure side, dimensions in mm [150]

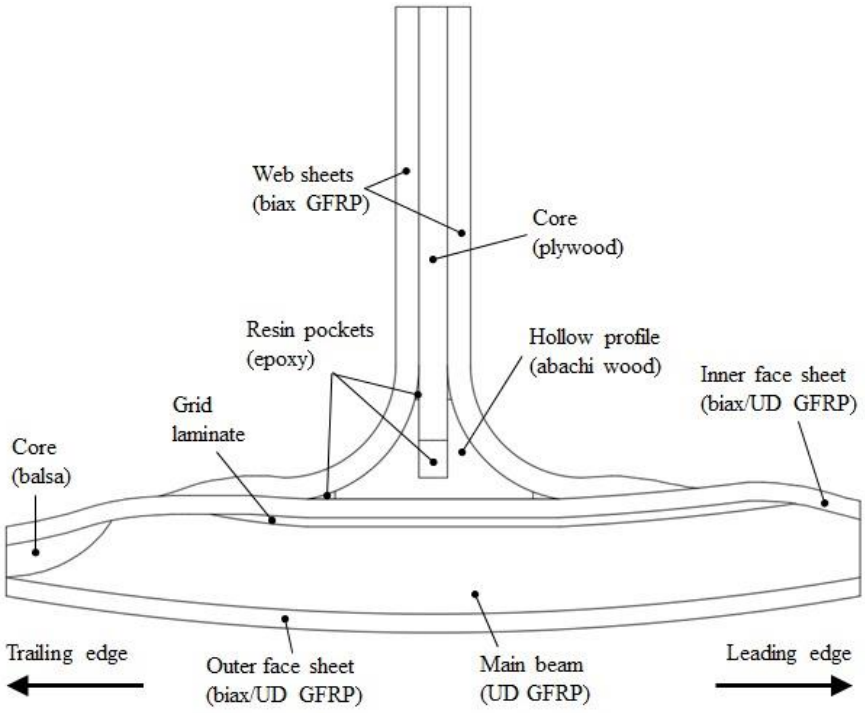

Figure 7.16 Tip side of the T-joint demonstrator, schematic of materials [150]

7.3.2 TSA comparison between photon detector vs microbolometer

7.3.2.1 Methodology

The T-joints were loaded in either tension-tension loading or compression-compression loading. A loading rig was designed and manufactured to facilitate the loading by Jack S. Callaghan and is shown in with the T-joint in Figure 7.17. The rig is mounted in a 630 kN Schenck servo-hydraulic test machine, which enables a cyclic load to be applied. TSA was conducted on the T-joint demonstrator using a photon detector (PD) camera (Telops FAST IR M2K [99] - Table 3.2), and a

microbolometer (MB) (FLIR A655sc - Table 3.3). The IR cameras were set-up with the photon detector facing the tip side and the microbolometer on the root side and then swopped, so both IR cameras captured images for the TSA from both sides. The Telops photon detector recorded 2,000 frames at 136 µs integration time and 383 Hz frame rate, while the microbolometer recorded 8,000 frames at 50 Hz frame rate.

The T-joint was loaded using the rig in the tension configuration shown in Figure 7.17 with a sinusoid load of 5 ± 4 kN at 1 Hz loading frequency. For lower frequencies < 3 Hz, it was possible to use load control. However, due to the mass of the grips and the subsequent inertia of the actuator, manual tuning was required for higher loading frequencies (3-7 Hz), which was difficult to achieve with any precision. Therefore, the experiments were performed in position control, with adjustment made to displacements to achieve the target sinusoidal load range; this procedure was applied later in subsection 7.3.3.

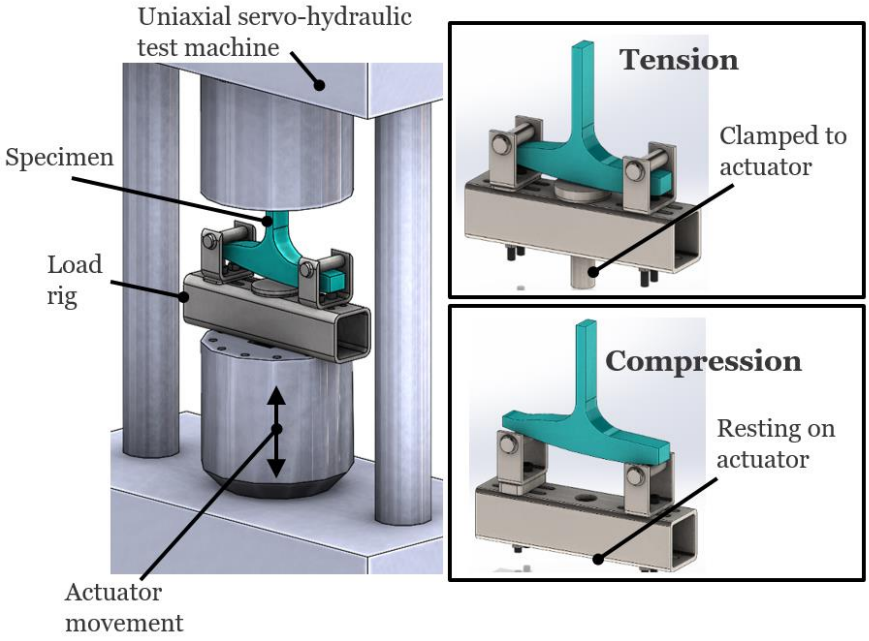

Figure 7.17 Experimental setup of the T-joint: 3 point bend test

All the tests performed with the microbolometer were done with the surface unpainted, while, for the photon detector, only the surface on the tip side was painted. Therefore, the root side was left unpainted when collecting data with both IR cameras to observe if the paint was causing any effects on the photon detector TSA data, as in Chapter 6 it was shown that if the paint was relatively thick (>18 µm), ΔT reduced when the loading frequency increases.

7.3.2.2 Experimental Results

The images from the photon detector and the microbolometer were processed to extract the images of the TSA variables from equation (3.6) using the least-squares algorithm. To compare the data at

the same spatial resolution, the ΔT image from the microbolometer was interpolated to spatially rescale the image (downsample) to the same resolution as the photon detector. A bicubic interpolation was used that considered four neighbourhood pixels using the Matlab imresize function; this is the same procedure used in section 5.4.2.1. The image from the microbolometer was corrected for the low-pass filtering effect using the factor 1.18 extracted from Figure 5.21 (a) at 1 Hz loading frequency.

The ΔT images obtained with both IR detectors facing the tip side are shown in Figure 7.18. The three ΔT images (photon detector (specimen painted), calibrated and uncalibrated microbolometer) look similar. The response is clearly different for the T-joint constituent materials, with the bending of the flange evident in the images. In the overlaminate, there is some evidence of material variation in GFRP. A detailed comparison can be seen in Figure 7.19 where ΔT along the vertical line indicated in Figure 7.18 is presented. The materials indicated in Figure 7.19 can be seen in Figure 7.16. This shows that qualitatively there is a reasonable agreement between the photon detector and the microbolometer data, as practically identical trends are followed. As the specimen was painted when the photon detector was used, it is expected that there should be a slight attenuation of the response, as is evident in the plot. This is most marked in the abachi wood region where the paint may have penetrated into the wood (similar to the peel ply imprint in Chapter 6). As expected the calibrated microbolometer shows a slightly higher temperature change than the uncalibrated data as the low-pass filtering is removed. The scatter in the calibration factor at 1 Hz loading frequency is high due to adiabatic conditions not being met. Therefore, higher loading frequencies that present less scatter in the calibration data are required. Experiments at 5 and 7 Hz loading frequencies have been conducted and shown later in Figure 7.23.

For the root side, the same procedure as described above has been followed: the ΔT images and the distribution along the T-joint vertical line are presented in Figure 7.20 and Figure 7.21, respectively. In Figure 7.20, a stress concentration is apparent at one of the corners of the resin pocket, as a result of a void on the surface of the specimen. In this case, the side of the specimen inspected with the photon detector was not painted. In the flange, the results shown in Figure 7.21 are practically identical clearly demonstrating the effect of painting. However, away from the flange, there is a marked difference between the results from the microbolometer and the photon detector. It seems that the photon detector is more sensitive to the emissivity of the surface than the microbolometer, as for wood and resin (unpainted), the thermoelastic response is lower than for matt black paint. This fact can be seen by comparing Figure 7.18 (c) - painted surface for the photon detector - and Figure 7.20 (c) - unpainted surface for the photon detector. However several other factors may be causing the different response, such as the line plot being taken from slightly different regions or that the microbolometer may be more sensitive to motion, as it has smaller sensors in the detector array.

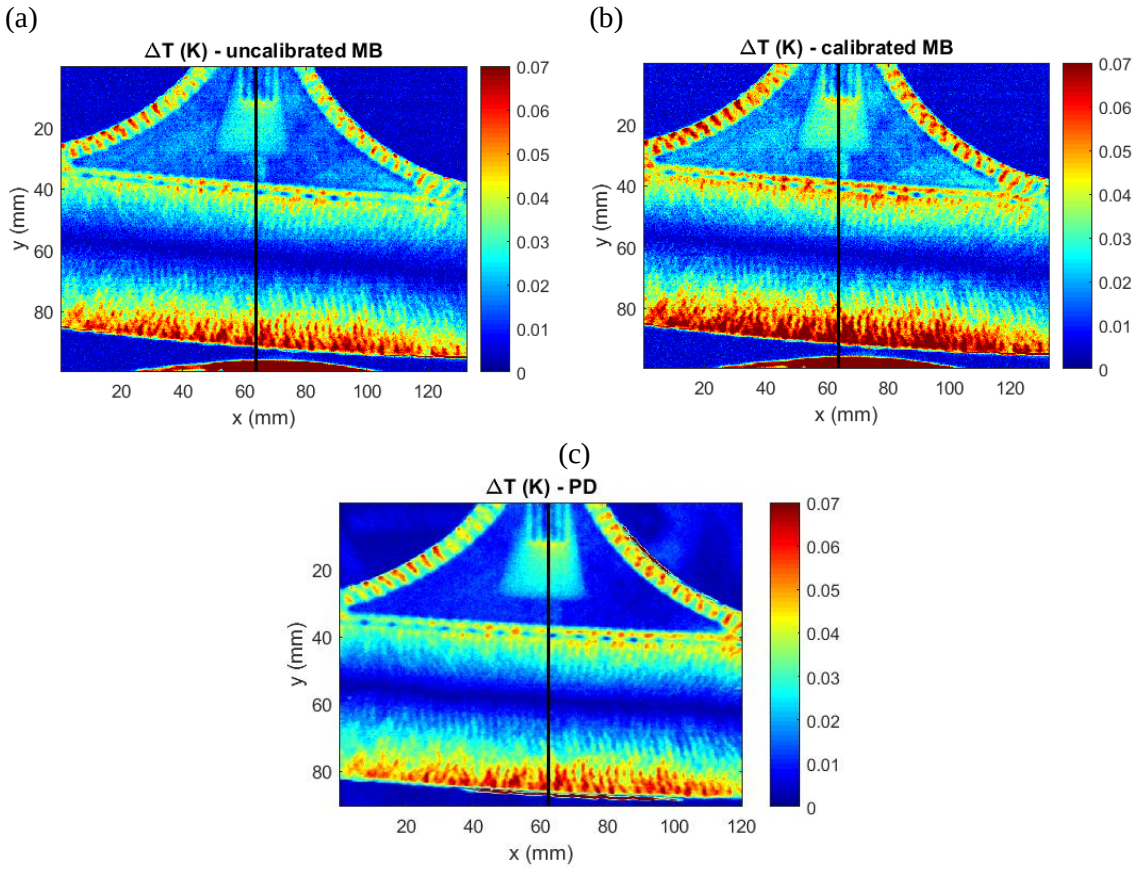

Figure 7.18 ΔT on tip side of (a) uncalibrated MB, (b) calibrated MB, (c) PD. Unpainted for MB but painted for PD.

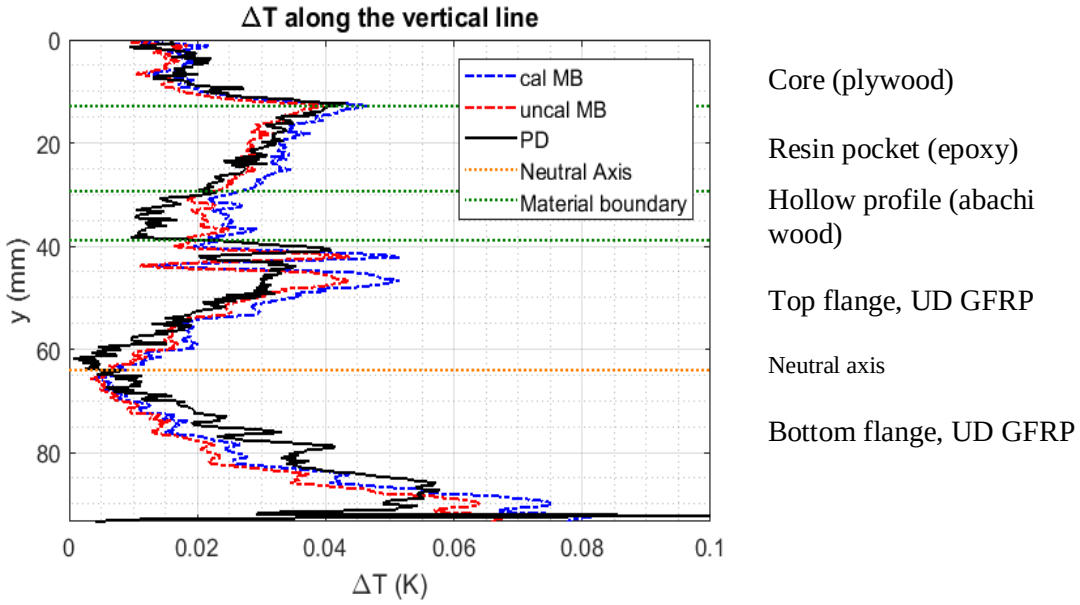

Figure 7.19 ΔT distribution along the vertical line at the tip side comparing calibrated and uncalibrated MB and PD. Painted for PD, unpainted for MB.

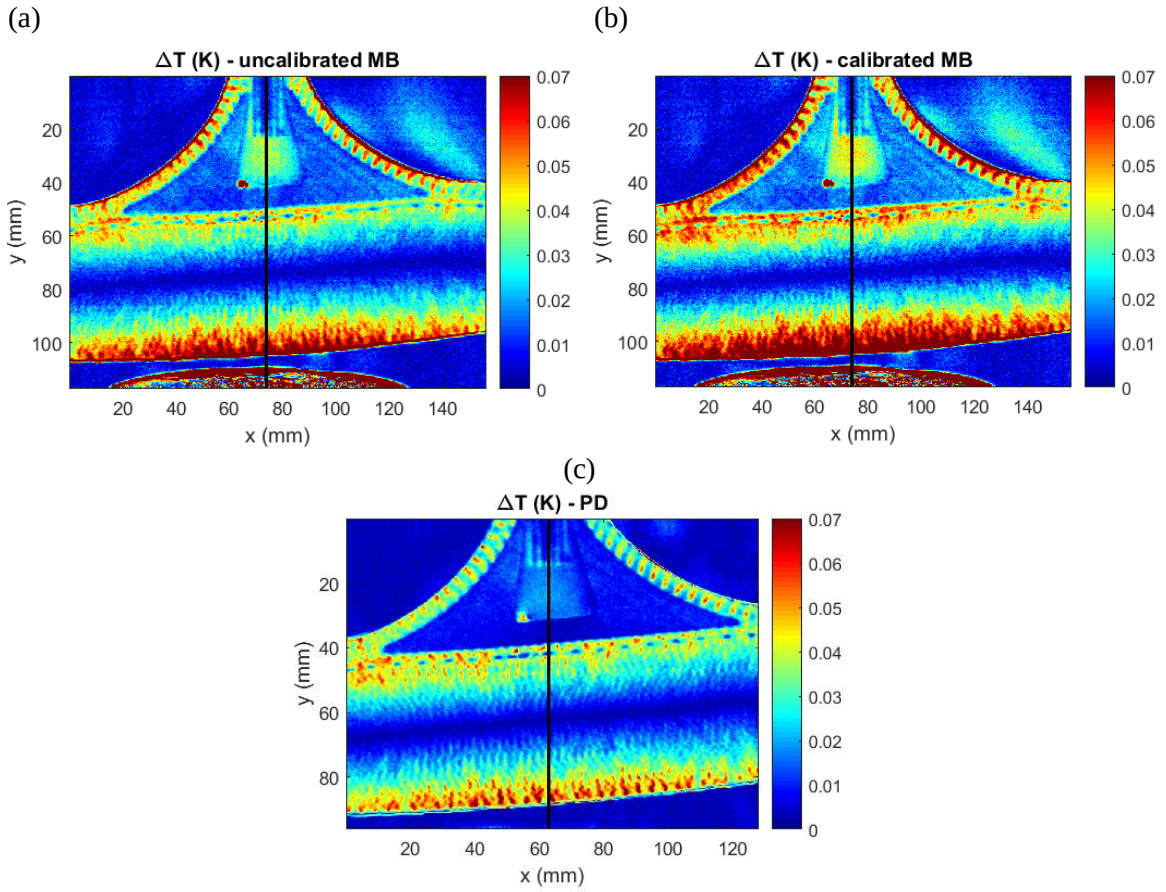

Figure 7.20 ΔT on root side of (a) uncalibrated MB, (b) calibrated MB, (c) PD. Unpainted side for both PD and MB

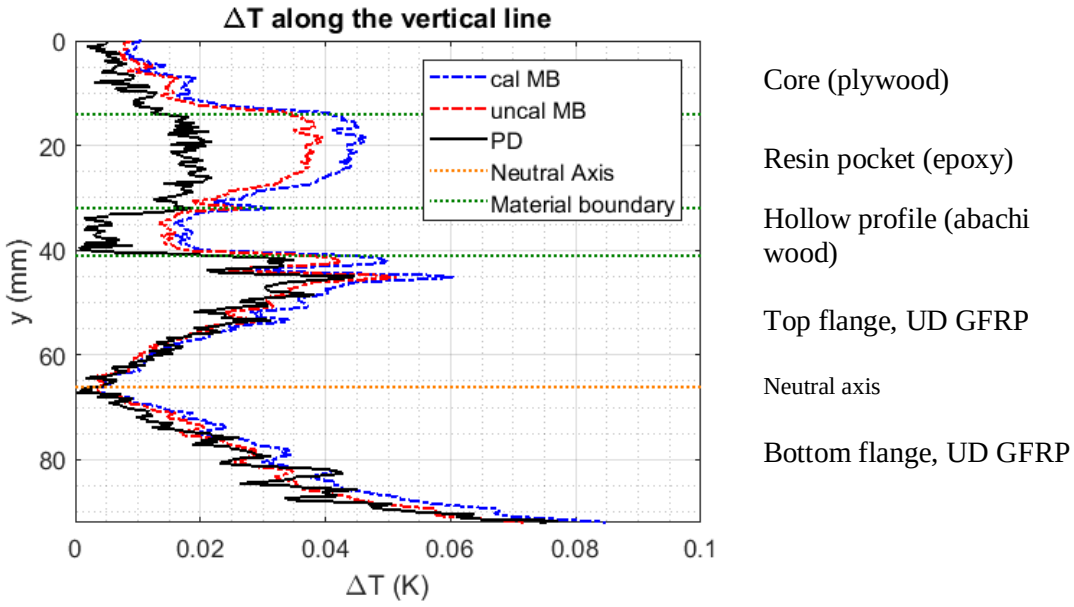

Figure 7.21 ΔT distribution along the vertical line at the root side comparing calibrated and uncalibrated MB, and PD. Unpainted side for both MB and PD.

It has been seen comparing Figure 7.19 and Figure 7.21 that the ΔT along the vertical line is different between the tip and root sides from 0 to 40 mm. To understand why that is happening, the

experimental results were compared with the sum of the principal stresses obtained with an FEA (Finite Element Analysis) model carried out by Jack S. Callaghan. As it was not possible to obtain the thermoelastic constant for the constituent materials of the T-joint, it was decided to normalise the data using the bottom point of the flange on the vertical line, at y = 90 mm, as reference point. The data comparison is presented in Figure 7.22. The calibrated and uncalibrated microbolometer data is superimposed as they were normalised at exactly the same point. It can be observed that the FEA agrees with the experimental data on the flange of the T-joint for both sides. Nevertheless, there are differences on the top 40 mm of the web and it is more significant on the tip side, as the trend of the experimental data is different than the FEA model. This difference is due to a crack that was not apparent initially that formed near the tip side during the cutting of the samples, causing a greater stress in the web and a possible gradient in the data from the web front to back. The crack was not included in the FEA model and hence explains the difference with the TSA data. The crack length increased with the number of cycles until the T-joint failed and may account for the different results in the web for the two tests.

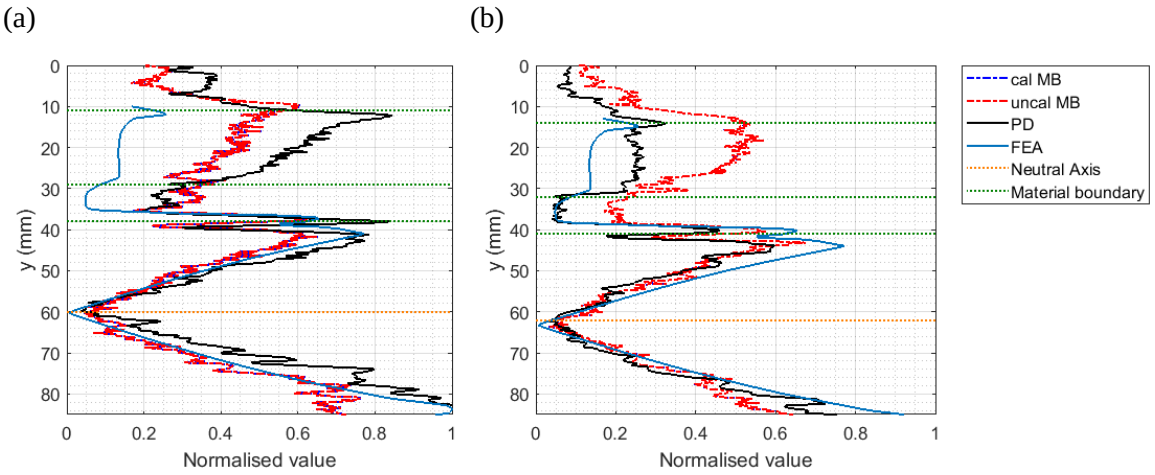

Figure 7.22 Normalised ΔT along the vertical line (a) tip side, and (b) root side of the same specimens

To mitigate for the effect of the crack, the loading rig was used in its compression configuration. In this case, to account for any differences front to back, the Telops photon detector (PD) and the microbolometer (MB) cameras both viewed the T-joint on the painted tip side with the data collected separately. The load considered was $-5 \pm 4\ kN$ and the tests were conducted at 5 and 7 Hz loading frequencies to validate the microbolometer calibration. Figure 7.23 shows the ΔT along the vertical line of the T-joint of the data taken with the photon detector and calibrated data obtained with the microbolometer. It can be seen that in the flange of the T-joint both the photon detector and the microbolometer show a good agreement, demonstrating that the calibration for the microbolometer is correct and can be applied to substructures as well. However, there are differences at the web, especially at the resin pocket, where differences could be attributed to a different sensitivity to the

surface emissivity detected by the IR camera, i.e. each camera responds slightly different to this region. Additionally, it could be related to a slight deviation of the camera positions with respect to each other.

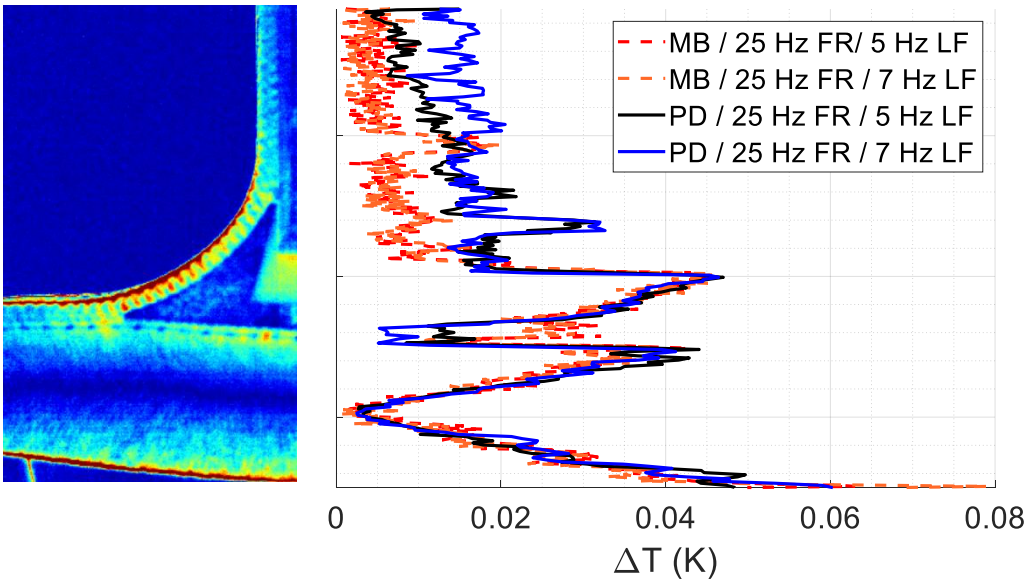

Figure 7.23 Comparison of the thermoelastic response from calibrated microbolometer (MB) and photon detector (PD) at 5 and 7 Hz loading frequencies

7.3.3 TSA and LSDIC Integration

In this subsection, TSA with a microbolometer and LSDIC are simultaneously combined to study the T-joint component. Both techniques captured the same surface region where images from both methods were aligned, registered and rescaled to match the same spatial resolution. By having both TSA and LSDIC images aligned together, a constitutive parameter was generated to inform of the stiffness state of the structure.

7.3.3.1 Experimental Setup

The setup of the experiment is similar to the experiments carried out in Chapter 6 shown in Figure 6.6. For TSA, the microbolometer was placed perpendicular to the surface of the sample at a distance of 0.6 m. 8,000 frames were collected at a 25 Hz frame rate. For the LSDIC, two Imager E-lite 5M cameras with 50 mm lenses were chosen to perform stereo LSDIC and avoid errors due to out-of-plane displacements. They were located 1.5 m from the T-joint and they were separated 0.7 m from each other. Lighting was provided by two LED lights to increase the brightness and the contrast between the black background and the white speckle patterns applied on the surface of the sample. The exposure time selected for the white light cameras was 3000 μs and the aperture of the lens was set to f.11. 312 frames were collected at a frequency of 0.975 Hz, which corresponds to the same recording time as the microbolometer at a 25 Hz frame rate.

The surface preparation was done with matt black MBP Electrolube, for the background, and matt white paint Ambersil RAL 9010, for the speckle pattern. The markers were reflective metal tape circles cut using a standard paper punch, the circle diameter was 7.14 mm. The FOV is shown in Figure 7.24 where the relevant distances are annotated.

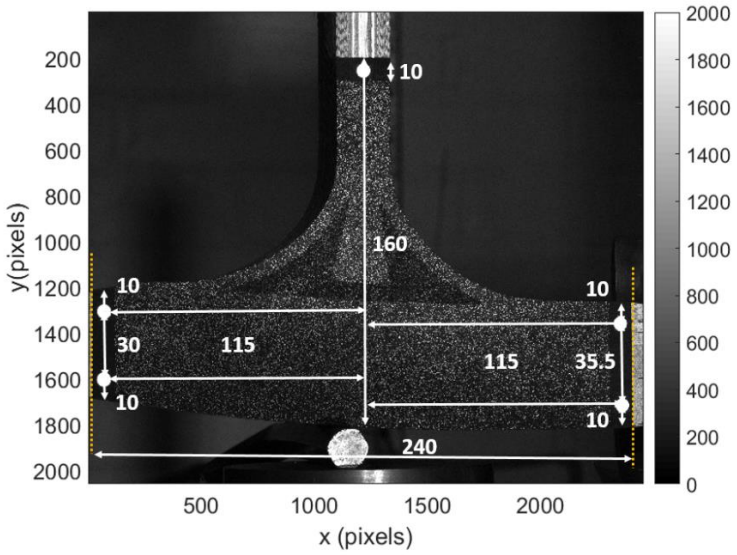

Figure 7.24 Surface preparation, distances in mm and colour bar in grey level

The DIC noise, displacement and strain resolution are reported in Table 7.7 following the analysis shown in Appendix B.

Table 7.7 Parameters considered for DIC

Technique used	**3D Digital Image Correlation**	
	Camera 1	**Camera 2**
Sensor and digitization	2448 x 2050, 12-bit	
Camera noise (% of range)	1.09%	0.85%
Lens and imaging distance	50 mm F-mount, 1.5 m	
Total number of images	2 (0.975 Hz)	
Pixel to mm conversion	1 pixel = 0.10 mm	
ROI (mm)	220 x 160 mm	
Subset, step	33, 11	
Interpolation, Shape functions, correlation criterion	Bicubic (6^{th} order spline), affine, ZNSSD	
Pre-smoothing	None	
Displacement resolution	0.0885 mm	
Strain		
Smoothing technique	Local polynomial - affine least-squares fit	
Strain window	3 data points	
VSG	55 pixels	
Resolution	0.0114 %	

7.3.3.2 Results

TSA and LSDIC systems recorded frames at 25 Hz and 0.975 Hz, respectively. The number of frames collected for each technique was 8000 for TSA and 312 for LSDIC allowing both techniques to collect data during the same time. The loading rig was configured to apply a tension load to the T-joint, it was a sinusoidal load of 5 kN mean and 4 kN amplitude, at 2 Hz loading frequency. In the experimental work presented in this subsection, the machine was manually tuned to achieve 3 Hz loading frequency in load control. However, the sample failed during the transition from 2 Hz to 3 Hz loading frequency whilst tuning the test machine due to a crack that developed during the cyclic test.

The least-squares algorithm implemented by Devivier [81] was used to extract the amplitude and phase of the strain data obtained with LSDIC as well as to obtain the TSA variables. The calibration technique developed in Chapter 5 was applied to the ΔT images obtained from the microbolometer. The markers were used to select the same region of the image for each dataset (image registration). Then, a bicubic interpolation technique (using 4 neighbourhood pixels) was applied to the TSA data (resolution: 2.54 pix/mm) to downsample it to the same resolution as the LSDIC strains (0.92 pix/mm). Therefore, the resolution of the TSA and LSDIC data is 0.92 mm/pix. The displacements were extracted and presented in Figure 7.25, which indicates that there is rigid body motion and out-of-plane displacement at the right of the beam. The crack is clearly visible in the x-direction displacement plot.

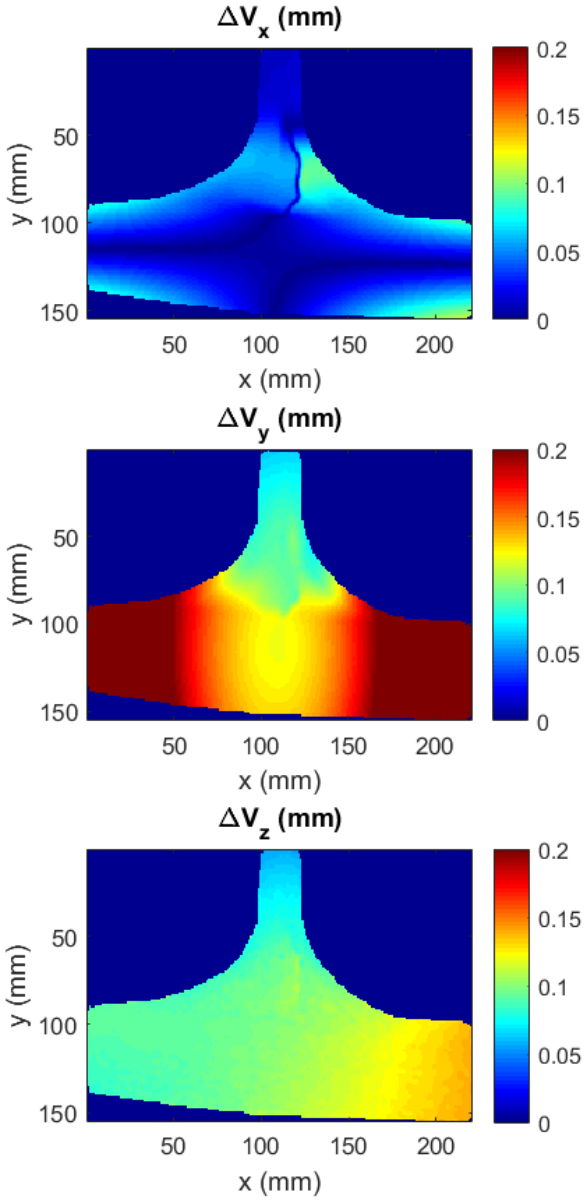

Figure 7.25 Amplitude displacements

The ΔT and the strain change at x-, y- and z-axes are shown in Figure 7.26 with numbered annotated features to highlight the defects/damage that TSA and LSDIC can detect separately. At the centre of the T-joint, within the resin pocket, there is (1) a stress concentration of ~0.07 K due to a void defect. Additionally, other stress concentration regions (ΔT data) can be seen at the lower part of the flange, at the centre of the grid laminate, at the right corner of the hollow profile and at the boundary between the abachi wood and the web sheets formed of biaxial GFRP. The $\Delta\varepsilon_{xx}$ shows the presence of a crack inside the substructure at the boundary between the abachi wood and the resin pocket (2). The crack is observed to be propagating upwards, where the stress concentration (3) was seen in the ΔT field. The $\Delta\varepsilon_{xx}$ level of the crack is >0.1% and has a length of 70 mm and is 0.7 mm wide. There are strain concentration regions at the top edge and bottom edge of the flange. The T-joint part that suffers more deformation on the y-axis is the web and the core of abachi wood at the centre of it. The $\Delta\varepsilon_{yy}$

at the wood is >0.1 % while at the web is ~0.06%. Additionally, in the bottom part of the flange $\Delta\varepsilon_{yy}$ is ~ 0.04%. The $\Delta\varepsilon_{xy}$ indicates that the shear strain change affects the abachi wood at $\Delta\varepsilon_{xy} > 0.1\%$ and the centre right of the T-joint at the web sheets, because the crack is located at this side of the T-joint. The centre left of the T-joint is experiencing a shear strain level between 0.06% to 0.08%. The neutral axis (4) of the flange, which experiences bending, can be observed on the ΔT and $\Delta\varepsilon_{xx}$ fields. A motion compensation algorithm is needed to compensate for motion blur due to the movement of the sample with respect to the IR camera and is a recommendation for future work.

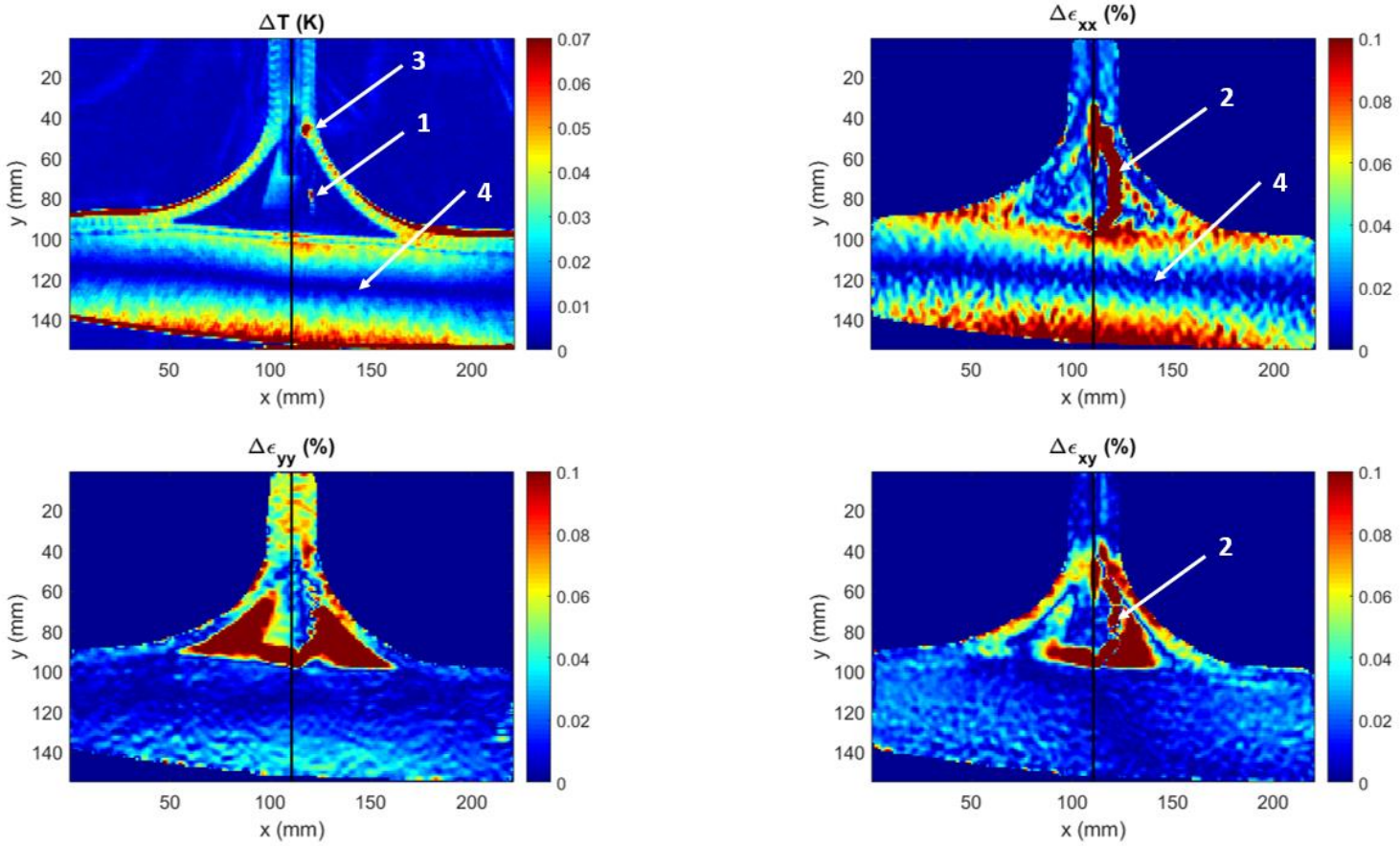

Figure 7.26 TSA and LIDIC results presented with the same resolution

The strain change $\Delta\varepsilon_{xx}$, $\Delta\varepsilon_{yy}$ and $\Delta\varepsilon_{xy}$ along the central vertical line (Figure 7.26) of the T-joint are presented in Figure 7.27 so that the maximum peaks can be compared easily. It can be seen that the highest strain $\Delta\varepsilon_{xx}$ of 0.7% takes place at $y = 45$ mm at the web in the vicinity of the crack. The location of the highest strain matches the position in other T-joint specimens, where the strain concentration is associated with the presence of a crack. The peaks of $\Delta\varepsilon_{yy}$ and $\Delta\varepsilon_{xy}$ are 0.28% and 0.24%, respectively, and occur at $y = 95$ mm, at the boundary between the abachi wood of the core and the GFRP of the flange.

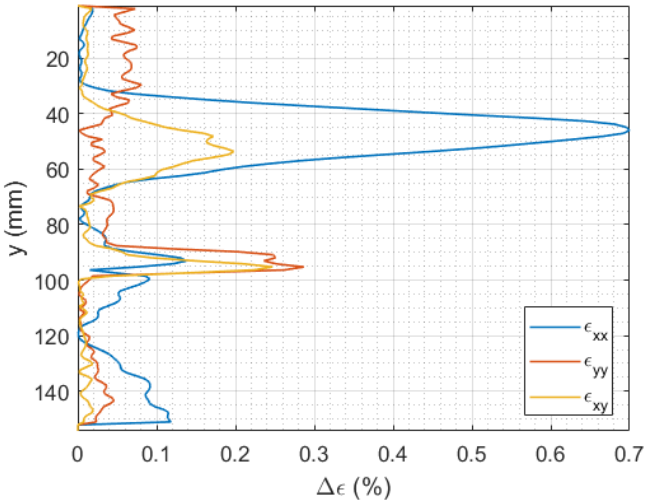

Figure 7.27 Vertical position vs change in strain

The temperature change along the vertical line is plotted in Figure 7.28. The peak in ΔT is found at the top and bottom of the flange and it is ~0.06 K. At the bottom edge of the flange, the motion present on the whole data set can be seen as an edge effect by showing $\Delta T > 0.06$ K along ~3 pixels, showing a no well-defined boundary. The other peaks correspond to changes of material boundaries.

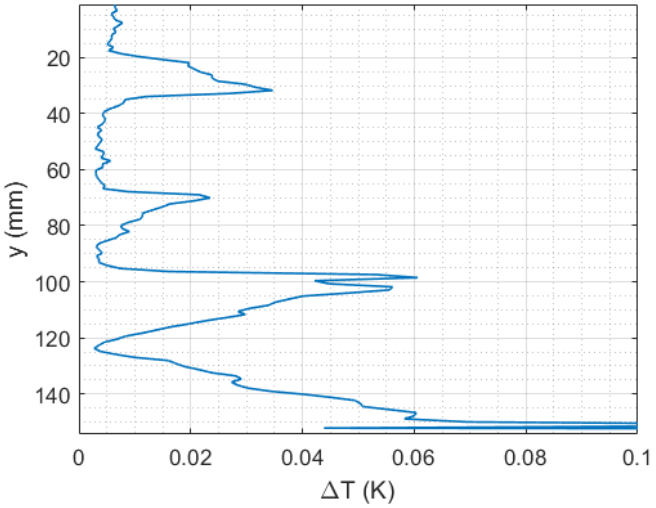

Figure 7.28 Vertical position vs change in temperature

The phases of the strain change in xx, yy and xy are shown in Figure 7.29. It represents the regions of the structure that are loaded in tension and compression with respect to the reference load (mean load). As expected, there is a phase shift of 180° between the tensile and compression sides of bending in the flange. The phase in shear presents a flip in phase between the left and right-hand sides of the flange that needs to be analysed and fully understood.

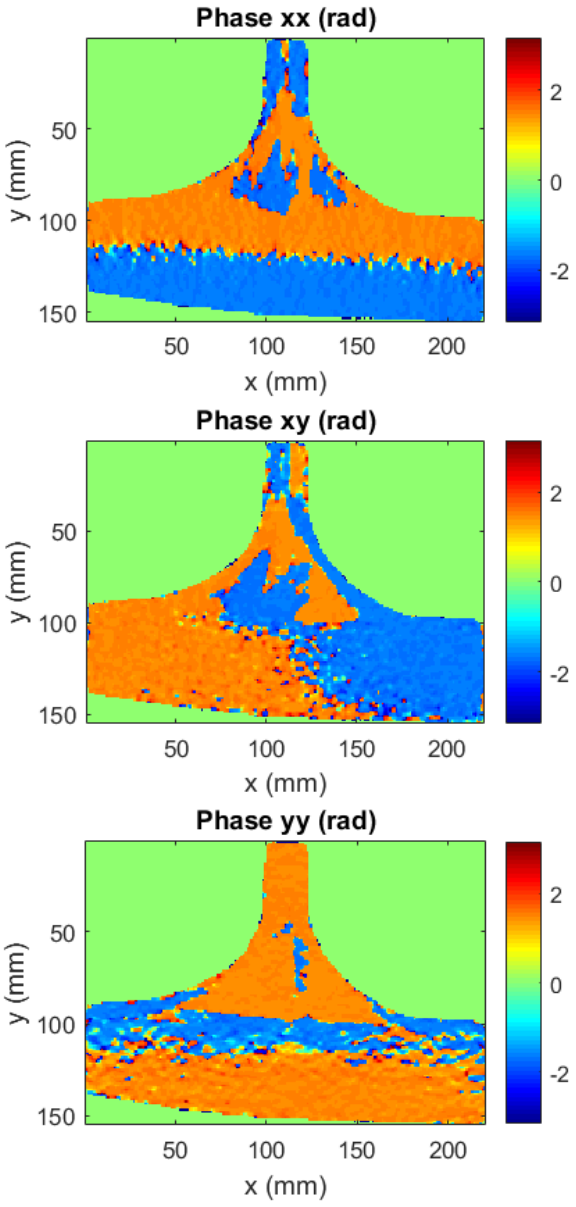

Figure 7.29 Phases of the strain in xx, xy and yy in rad

A constitutive parameter can be extracted from the TSA and LSDIC data presented in Figure 7.30. It has been calculated following equation (7.1). The phases of TSA and LSDIC are opposite due to the negative sign in the TSA equation (3.5), but they provide the same information, that is tension in the upper part of the T-joint and compression at the lower part of the flange.

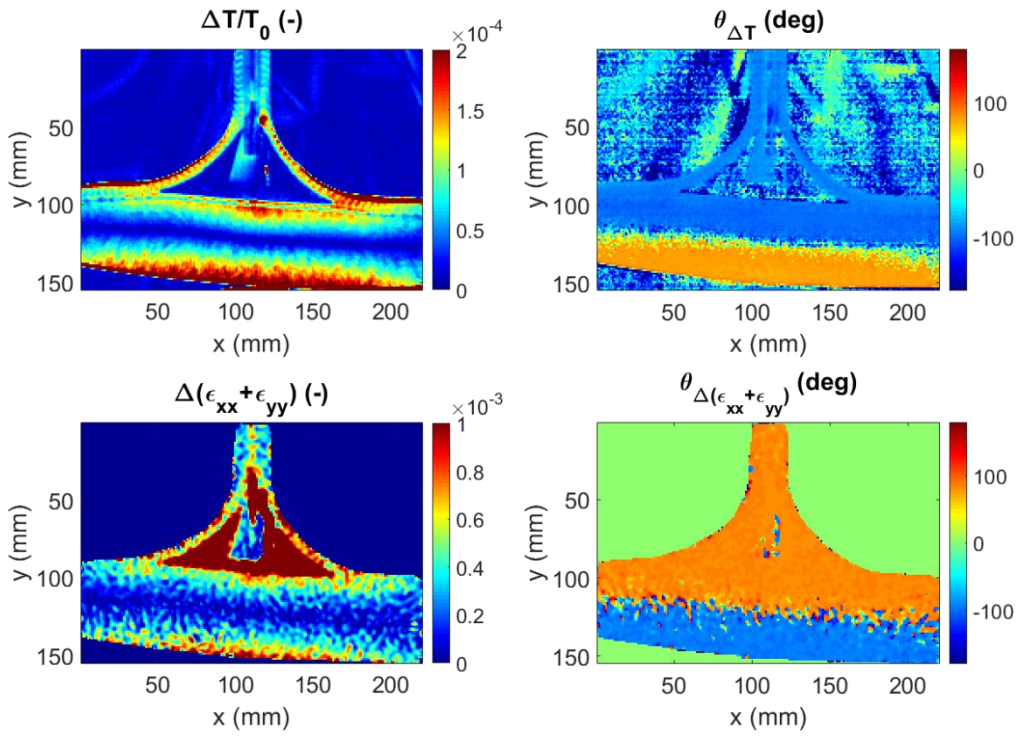

Figure 7.30 TSA and LSDIC T-joint data for constitutive parameter

The constitutive parameter is presented in Figure 7.31 by using equation (7.1). Due to features appearing at different scales, Figure 7.31 (a) and (b) are the same image represented with higher and lower scaling on the colour map respectively. In Figure 7.31 (a), the effect of different materials within the structure shows up different stiffness, however, there is noise present due to alignment issues between the TSA and LSDIC datasets that needs to be addressed in further work. However, below the noise threshold in Figure 7.31 (b) the crack is visible as its stiffness is zero. Therefore, the constitutive parameter can aid the detectability of cracks, which is demonstrated by this particular case.

(a) (b)

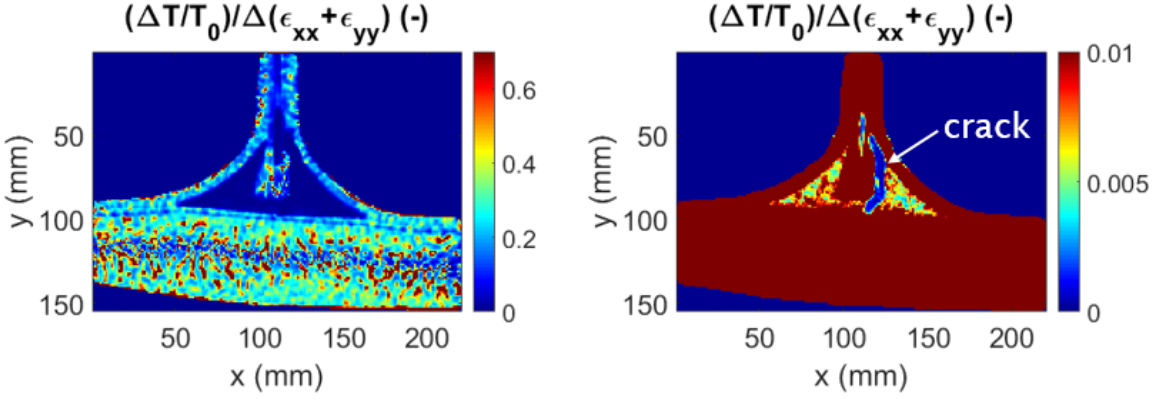

Figure 7.31 T-joint constitutive parameter

7.3.4 Summary

In this section, the application of microbolometers for TSA in complex structures has been demonstrated. The microbolometer showed good agreement with the results of the photon detector at 1 Hz loading frequency, but due to the scatter of the data on the calibration parameter at 1 Hz, the calibration was not successfully validated in this first test. Therefore, 5 and 7 Hz loading frequencies have been analysed comparing photon detector and calibrated microbolometer data showing a good agreement when comparing line profiles of both datasets.

The first attempt on integrating TSA and LSDIC was performed. The test set-up was successfully prepared to obtain test data acquired at the same start and end time. The post-processing consisted of obtaining the amplitude of strain and temperature change independently from both methods, then using image registration to select the same ROI and perform a bicubic interpolation to scale down the TSA data to have the same resolution as the LSDIC. It was seen that the LSDIC data had noise due to the size of the speckles, therefore, in future experiments, larger speckles need to be applied. The TSA data was corrupted by a significant amount of noise which requires further work in developing motion compensation algorithms.

For the first time, a constitutive parameter has been obtained by dividing the $\Delta T/T_0$ TSA data and $\Delta(\varepsilon_{xx} + \varepsilon_{yy})$ LSDIC data from two aligned datasets. As TSA produces an indication of the level of stress and LSDIC provides the measured strains, the constitutive parameter can be considered an indicator of material stiffness. It was seen that the constitutive parameter presented high level of noise due to noise sources in both TSA and LSDIC data sets. However, at lower scales, it was possible to identify different materials on the T-joint component (associated with different thermoelastic responses and stiffnesses) and to clearly identify the crack as its stiffness is zero. Therefore, the work demonstrates that the constitutive parameter could be used to detect different materials and damage, but it warrants further work to understand its significance quantitatively and its repeatability across different structures.

Chapter 8. Conclusions and Future Work

8.1 Conclusions

The main aim of the PhD was to develop a **low-cost approach for TSA** using microbolometers to be used **simultaneously with DIC as an alternative NDE technique** for composite structures. A series of objectives were set out in Chapter 1 and these have been fulfilled in the preceding chapters of the thesis with the following conclusions.

- Chapter 4 focused on the development of **microbolometer camera models** for TSA and concluded:
    - The **least-squares algorithm** is the most appropriate algorithm for TSA, as the extraction of ΔT was not influenced by non-integer number of loading cycles and the processing speed was faster than the lock-in and FFT algorithms.
    - Microbolometers behave as **low-pass filters** when viewing a transient scene such as that necessary for TSA.
    - Images captured using the very low-cost Lepton 3.5 radiometric **thermal core** can only provide **qualitative results for TSA** as the attenuation in ΔT with respect to the loading frequency was not only due to **low-pass filter** behaviour but also to possible **sampling issues** due to the upper limit imposed on the frame rate.
- Chapter 5 focused on the development of a **novel calibration for microbolometer based TSA** and concluded:
    - To assess the performance of microbolometers when applied to TSA a simple simulation approach can be adopted based on an **electrical equivalence series RC circuit**.
    - The simulation demonstrated that the least-squares imaging processing procedure developed in Chapter 4 acts as a **notch filter**, and successfully enables a signal to be extracted from a noisy input i.e. when the SNR is low, as is the case for TSA.
    - The **noise reduction feature** embedded in the FLIR A655sc IR camera system introduces a further low-pass filtering of any transient signal and has a severely detrimental effect for microbolometer based TSA by effectively introducing a tenfold **increase in the thermal time constant** with the consequent severe attenuation in ΔT, **limiting the loading frequency to a few Hz**.
    - The **simulation** showed that the **noise reduction** was achieved by taking a temporal **rolling average** from several images and confirmed that this was cause of the severe attenuation.

- The simulation showed that a major limitation of the least-squares image processing approach meant that the **waveform** had to be close to the expected waveform, in this case sinusoidal, otherwise the extracted ΔT is **over- or under- predicted**.
- To correct for the low-pass filtering of the microbolometer and resultant reduction in the ΔT, a new **unified calibration approach** was devised that is only **dependent on the loading frequency and if the noise reduction feature is utilised** that is faster than the calibration proposed in [21].
- The **calibration approach** was **validated** using a damaged CFRP sample by comparing the extracted ΔT with that from a photon detector, and by comparing experimental and analytical stresses in an aluminium Brazilian disc specimen.

- In Chapter 6 TSA and DIC were combined to provide a new means of determining the **source of the thermoelastic response of orthotropic laminated composites**, it was shown that:
  - An **independent measure of strain** is required to account for **test machine inaccuracies**, i.e. reductions in strain amplitude with the loading frequency.
  - The new technique enables the **source of the thermoelastic response** to be **determined categorically for both GFRP and CFRP laminated composites**.
  - For the **GFRP** specimens, the thermoelastic response was driven by the thick **isotropic resin-rich layer** (~17 μm).
  - Regarding the **CFRP** laminates, heat transfer at **low loading frequencies** means the source was driven by the **global laminate behaviour**. However, at **high loading** frequencies, the CFRP thermoelastic response was due to the **orthotropic surface ply**.
  - The **thickness of the resin-rich layer plays a role** as for the CFRP was thin 5.10 ± 3.69 μm in comparison to the GFRP one.
  - The **paint thickness** has a detrimental effect on TSA, if the paint thickness is >18.32 ± 2.73 μm, ΔT drops significantly when the loading frequency increases.
  - The **surface finish**, such as resin-rich layer and paint, the **fibre volume fraction** and **lay-up construction affect the thermoelastic response**.
  - The **main conclusion** from the chapter is that prior to embarking on TSA studies of composite structures, a detailed **calibration procedure** must be carried out on the manufactured material to determine the source of the thermoelastic response at the desired loading frequency for structural tests. Then, it is possible to conduct **quantitative TSA of laminated composite components**.
- In Chapter 7 initial work on the **integration of TSA and DIC as a strain based NDE technique** was described and concluded that:
  - The **GFRP cross-ply laminates** used in Chapter 6 did not represent a good choice, as they **did not damage progressively** and the surface cracking of the $[90,0]_{3s}$

laminate was hidden by the thermoelastic response of the resin-rich layer, although damage was revealed at larger stresses when the resin-rich layer cracked.

- Significant progressive damage was observed in the $[\pm\mathbf{45}]_{\boldsymbol{3s}}$ sample. However, **fibre reorientation** towards the 0° axes occurred as the applied stress increased, so $\boldsymbol{\Delta T}$ changed because the **coefficient of thermal expansion** changed, which was also affected by microcracking.
- Markers on the component surface can be used to align both the **TSA and LSDIC images** so that they can be **integrated on the same image plane**. The integration was demonstrated on a T-joint component.
- The **constitutive parameter** for the T-joint component **identified the different materials** present in the T-joint construction as well as a **crack**.
- **Microbolometer based TSA** was validated for a T-joint **substructure** at 5 and 7 Hz loading frequency against photon detector data.

8.2 Impact of the Research

The work performed during the PhD studies has resulted in different conference presentations and journal papers listed in the following subsections.

8.2.1 Conference Presentations

1. Society for Experimental Mechanics (SEM) Annual Conference (4-7 June 2018)
   Extended Abstract & Presentation:
   I. Jiménez-Fortunato, D.J. Bull, J.M. Dulieu-Barton, and O.T. Thomsen, *Towards Integrating Imaging Techniques to Assess Manufacturing Features and In-service Damage in Composite Components*
2. Institute of Physics (IOP) Conference on Modern Practice in Stress and Vibration Analysis (2-4 July 2018)
   Abstract & Presentation:
   I. Jiménez-Fortunato, D.J. Bull, J.M. Dulieu-Barton, and O.T. Thomsen, *Towards combining imaging methods to evaluate defect and damage in composite sub-structures*
3. British Society for Strain Measurement (BSSM) International Conference on Advances in Experimental Mechanics (29-31 August 2018)
   Abstract & Presentation:
   I. Jiménez-Fortunato, D.J. Bull, J.M. Dulieu-Barton, and O.T. Thomsen, *Towards developing a calibration technique to apply TSA with microbolometers*
4. Society for Advancement of Material and Process Engineering (SAMPE) Europe
   Theme: Large Structures in Composite Engineering (11-13 September 2018)
   Proceedings paper & Presentation:

I. Jiménez-Fortunato, D.J. Bull, J.M. Dulieu-Barton, and O.T. Thomsen, *Towards combining imaging techniques to characterise defects and damage in composite structures*

5. British Society for Strain Measurements International Conference - 5th Postgraduate Experimental Mechanics Conference (December 2018)
   I. Jiménez-Fortunato, D.J. Bull, J.M. Dulieu-Barton, and O.T. Thomsen, *Thermoelastic Stress Analysis and Lock-In Digital Image Correlation Techniques Applied to a T-joint Substructure*
6. Twenty-Second International Conference on Composite Materials (ICCM22) (11-16 August 2019)
   Proceedings paper & Presentation:
   I. Jiménez-Fortunato, D.J. Bull, J.M. Dulieu-Barton, and O.T. Thomsen, *Damage Characterisation of Composite Components Using Full-Field Imaging Techniques*
7. Society for Experimental Mechanics (SEM) Annual Conference (14-17 September 2020)
   Extended Abstract & Presentation (Shortlisted for Michael Sutton International Student Paper Competition):
   I. Jiménez-Fortunato, D.J. Bull, J.M. Dulieu-Barton, and O.T. Thomsen, *Quantitative Thermoelastic Stress Analysis Using Low Cost Thermal Cameras*
8. Society for Experimental Mechanics (SEM) Annual Conference (14-17 September 2020)
   Extended Abstract & Presentation:
   I. Jiménez-Fortunato, D.J. Bull, J.M. Dulieu-Barton, and O.T. Thomsen, *Quantifying the Thermoelastic Response from Laminated Fibre Reinforced Polymer Composites using Digital Image Correlation*

8.2.2 Journal Articles

1. I. Jiménez-Fortunato, D.J. Bull, O.T. Thomsen, and J.M. Dulieu-Barton, *On the source of the thermoelastic response from orthotropic fibre reinforced composite laminates*. Journal of Composites Part A: Applied Science and Manufacturing (accepted)
2. I. Jiménez-Fortunato, C. Devivier, and J.M. Dulieu-Barton, *Assessment of Infra-Red Cameras for Thermoelastic Stress Analysis* (in progress)
3. I. Jiménez-Fortunato, D.J. Bull, J.M. Dulieu-Barton, and O.T. Thomsen, *Quantitative Thermoelastic Stress Analysis using Low-Cost Microbolometers* (in progress)

8.3 Lessons Learned and Best Practice Recommendations for TSA and LSDIC

The aim of this section is to summarise the knowledge gained from performing TSA and LSDIC on the same sample. It includes the analysis of the loading frequencies used in the test, the cameras, the

surface preparation, and how these influence the application of both techniques to substructural components.

It was demonstrated that microbolometer based TSA requires a calibration to take account of the attenuation caused by the loading frequency of the test. For large structures, a low loading frequency is required as it would be difficult to perform the tests at higher loading frequencies, due to the size of the structure and inertial issues, which benefits the microbolometer based TSA technique. Additionally, LSDIC data capturing could be performed oversampling instead of undersampling i.e. loading frequency is 1 Hz, so that the LSDIC frame rate could be at least 2.1 Hz, which is possible for the E-lite cameras used, as their maximum frame rate is 10 Hz.

It was observed that the surface plays a role on the thermoelastic response and on the quality of the speckle pattern. TSA usually requires a black background paint to increase the emissivity of the surface. However, a thick paint layer produces attenuation of the thermoelastic response. Therefore, the application of paint should only be considered when necessary, such as when the surface produces reflection or the emissivity is not high enough. The emissivity of non-black surfaces should be verified using a blackbody (as described in Chapter 6) so that application of paint could be avoided. Nevertheless, if paint is needed, it requires careful application to ensure it is as thin as possible. Additionally, composite materials can have a resin-rich surface layer depending on the manufacturing method, and it can also influence the thermoelastic response obtained with TSA. Therefore, initial knowledge of the construction of the composite structure by using a micrograph close to the surface will inform on the resin-rich layer thickness. Moreover, it is clear that painting a surface with a peel ply imprint will change the thermoelastic response.

Regarding the speckle pattern, a smooth surface is an advantage, as the edges of the speckles will be well defined, the contrast will be magnified, and the size of the speckles will be constant. For surfaces with texture, e.g. the peel ply side of a laminated composite or wood in the T-joint substructure, a quality speckle pattern is difficult to achieve, the speckles appear smaller in comparison with the speckles on a smooth surface resulting in an error in the strain measurements. Hence, DIC and LSDIC should be performed preferably on a smooth surface finish to maximise the quality of the speckle pattern and, therefore, reduce the noise on LSDIC data.

8.4 Recommendations for Future Work

The work presented has drawn different paths for further work that can be summarised as follow:

- Understand the **thermal core working principles** and how the **limitation on the frame rate** can be accounted for. The low-cost and lightweight nature of the Lepton 3.5 radiometric thermal core means that the cameras can be permanently installed in locations outside the laboratory environment and used for continuous monitoring purposes in hazardous and extreme environments, i.e. space, offshore wind turbine systems and in nuclear facilities.

Hence, it would be advantageous to carry out further investigations to **develop a means of quantitative TSA with these devices**.

- Develop a customised data collection program using a low cost **Raspberry Pi system**, as it would provide a flexible implementation of **thermal core based TSA at an ultra low cost**. This TSA system would be portable and could be used anywhere.
- Develop a system to **synchronise the load data from the test machine to the microbolometer** to obtain additional information from the **phase**.
- Investigate by means of **a thermal model** the effects of different **variables**, i.e. the isotropic resin-rich layer, fibre volume fraction and ply thickness, in the **thermoelastic response**.
- Study experimentally different **thicknesses of CFRP plies** to find the limit in which **adiabatic conditions are met** at low loading frequencies.
- **Explore damage progression on CFRP laminates** as the heat transfer at low loading frequencies could provide information of **damage** occurring at **subsurface level**. Hence, it would provide information on the **depth detectability of TSA** in CFRP.
- Investigate the possibility of **decoupling the stiffness and coefficients of thermal expansion** in damaged components from **TSA** measurements.
- Devise an **automatic image registration** to position **TSA and LSDIC** to obtain accurate results when integrating both datasets into a constitutive parameter.
- Development of **motion compensation approaches** to increase the accuracy of **TSA**.
- The distribution of multiple microbolometers and white light cameras around a large structure leads a trade-off with FOV and resolution. Hence, it may be required to assess the suitability of using a **multifunctional speckle pattern**, i.e. [120], to apply **DIC at different magnifications** without the need to repaint or reapply a pattern.

Appendix A Telops IR Camera Calibration

The Telops calibration [151, 152] presents a different procedure than traditional method described previously. It is independent of the integration time of the camera and is performed in terms of flux count.

The curve required to transform counts into radiometric temperature is the normalised flux curve, which is a function of the temperature solely. To obtain this curve, the process is to collect the counts vs integration time of the camera for different blackbody temperatures and each pixel of the Focal Plane Array (FPA) following the equation below and shown in Figure A.1 (a).

$$DL^p = F^p \cdot IT + D_{off}^p \tag{A.1}$$

where DL^p is Digital Level measured in counts of each pixel (p), the slope F^p is the flux count of each pixel in $\mathrm{counts}/\mu s$, IT is the integration time of the camera in μs, and D_{off}^p is the intercept of the curve (offset) for each pixel.

D_{off}^p is the signal obtained when there are no photons impinging the sensor, so the counts are independent of the photon flux or target temperature. It occurs at zero integration time. D_{off}^p is mainly caused by the dark current in the readout circuit. Figure A.1 (b) shows the digital level vs integration time curve for a particular Telops camera. At higher temperature and integration time, the data was saturated and could not be plotted for the 100 μs integration time.

(a) (b)

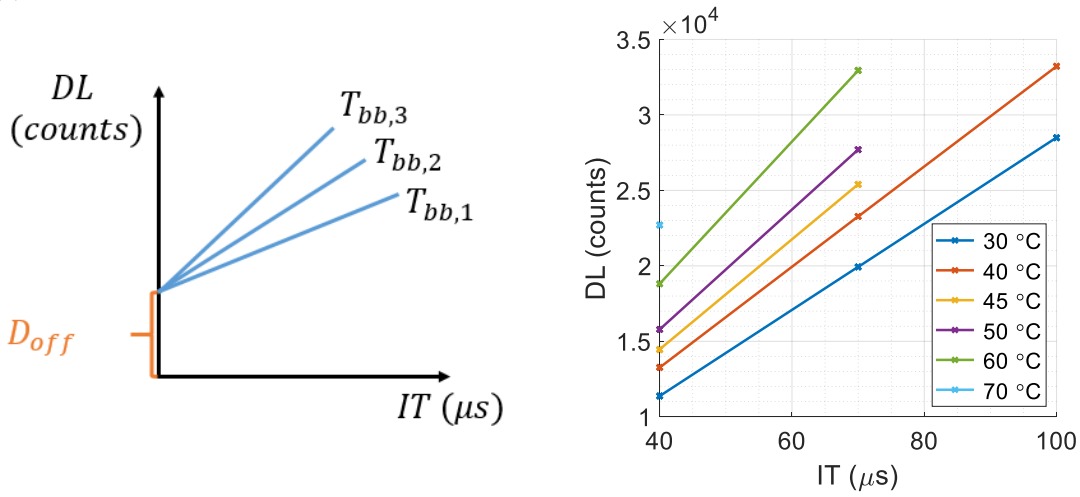

Figure A.1 Digital levels vs integration time for each pixel (a) for three blackbody temperatures being $T_{bb,3} > T_{bb,2} > T_{bb,1}$ [152] and (b) for a particular Telops camera at different blackbody temperatures specified

It is possible to obtain the offset and the slope for each blackbody temperature and pixel Figure A.1 (a), where the slope is the flux count, F_p. Therefore, another curve presenting flux count versus the

temperature (Figure A.2) can be obtained by placing the flux count obtained with the previous plot (slope of Figure A.1 (a)). This curve is again for each pixel in the FPA. The F_{offset}, dark flux, shown in Figure A.2 corresponds to the relatively small current that flows when photons are not entering the device, and, therefore, the temperature of the observed blackbody is 0 K. It must be noted that it is also affected by the optics of the camera, i.e. the radiant emission of the optics and associated electronics.

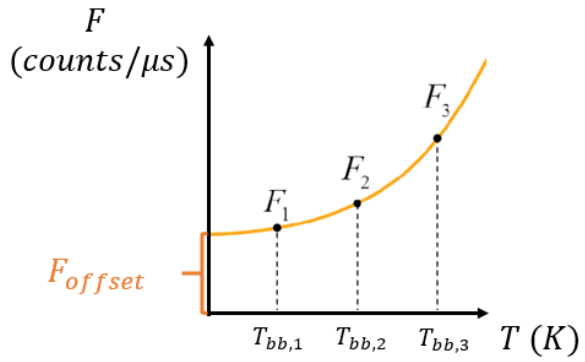

Figure A.2 Flux count vs blackbody temperature for each pixel [152]

The following step is to average the curves for each pixel and obtain a single one, called average flux count (F_{avg}), shown in a dashed green line in Figure A.3 (a). Figure A.3 (b) shows the flux vs the temperature of three different pixels for a particular Telops FAST M2K camera. The flux count vs temperature curve for each pixel is obtained from the average curve (F_{avg}) as follows:

$$F^p = \alpha^p \cdot F_{avg} + \beta^p \tag{A.2}$$

where α^p is the gain (non-dimensional) of each pixel, F_{avg} is the average flux count that is a function of the temperature and β^p is the offset of the curve of each pixel.

(a) (b)

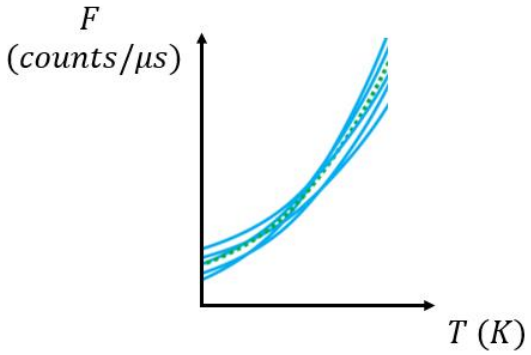

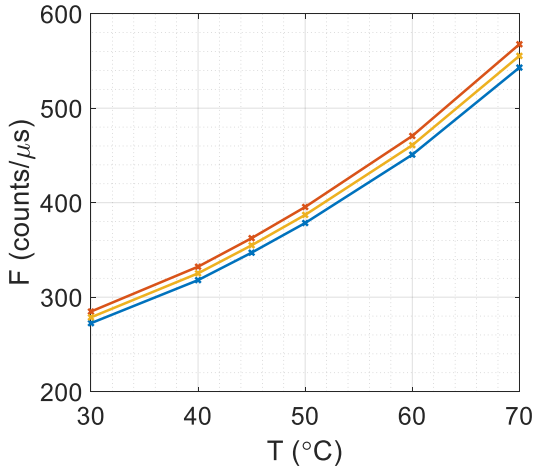

Figure A.3 Flux count vs black body temperature for different pixels [152] (a) general and (b) for a particular Telops FAST M2K camera and 3 pixels

The next step is to consider the uniform ambient flux from the internal lens (F_{amb}), as it affects the F_{offset} due to variations in the system temperature. The shape of the curve in the plots of flux count versus temperature is maintained but is shifted upwards or downwards depending on the change of the dark flux due to the ambient temperature. Therefore, an additional step on the calibration to radiometric temperature to adjust the flux count curve is needed. Telops has done this by measuring the dark flux with the system inside an environmental chamber, where the ambient temperature is controlled, and have obtained the difference between the initial dark flux and the dark flux at a certain ambient temperature. The average flux count is the sum of a nominal camera curve, F_{nom}, and the uniform ambient flux, F_{amb}:

$$F_{avg} = F_{nom} + F_{amb} \tag{A.3}$$

Hence, the nominal camera curve, F_{nom} can be obtained as:

$$F_{nom} = F_{avg} - F_{amb} \tag{A.4}$$

which is the final calibration curve that is going to be used as a look-up table (LUT).

Figure A.4 (a) shows the average and nominal flux with respect to the temperature where the difference is the ambient flux and (b) shows the nominal flux curve used as a LUT to transform counts to radiometric temperature. Figure A.4 curves are for a particular Telops FAST M2K camera; in this case, the ambient flux has been estimated, while Telops were able to measure it using an environmental chamber for the data acquisition.

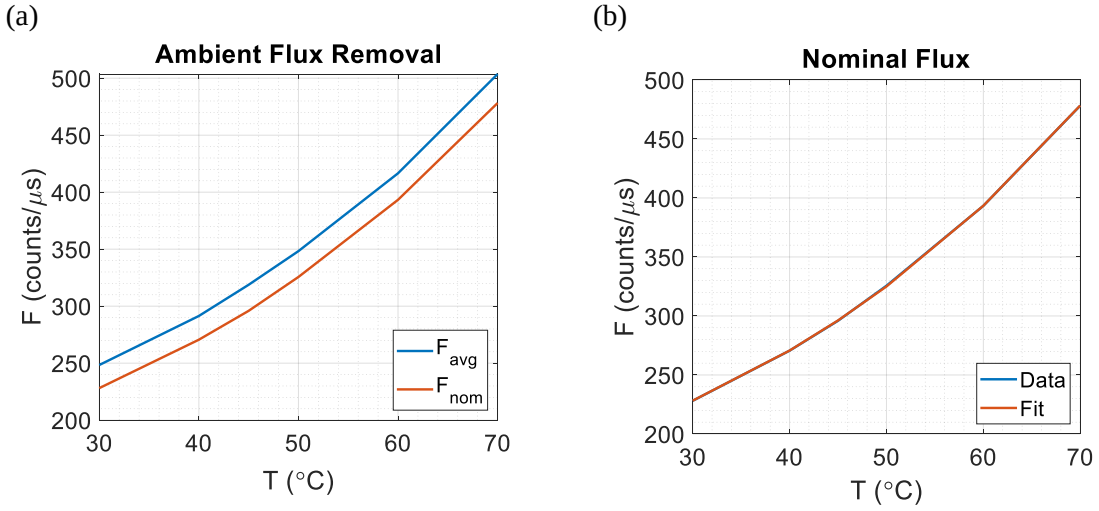

Figure A.4 Flux vs temperature (a) average flux with and without ambient flux and (b) nominal flux for a particular Telops camera

As a summary, the normalised flux curve is used as a LUT, which is independent of the integration time, FPA pixel and system temperature. Therefore, the memory used in the camera to perform a real time calibration is much lower than the traditional methodology as it is a single flux count versus temperature curve. In addition, it does not require a blackbody calibration every time the camera is

used or there is a change in ambient temperature. This simplifies the test setup allowing the camera to be used straight away once it is turned on and cooled down. The process to convert a scene from Digital Level to Radiometric temperature follows the following procedure:

1) Transform Digital Level to flux count (F^p) of the image data pixel per pixel

$$F^p = \frac{DL_p - DL_{off}^p}{IT} \tag{A.5}$$

2) Apply the gain and offset to obtain the values of the average flux count curve

$$F_{avg} = \frac{F^p - \beta^p}{\alpha^p} \tag{A.6}$$

3) Obtain the nominal curve by considering the uniform ambient flux from the internal lense

$$F_{nom} = F_{avg} - F_{amb} \tag{A.7}$$

4) Remove bad pixels by using the pixel value as the average of the pixels nearby

5) Use the LUT, i.e. nominal flux count vs temperature curve, to obtain the radiometric temperature associated with the F_{nom} obtained in equation (A.4).

Appendix B LSDIC Validation

Most of the DIC applied to cyclic testing has been done using LIDIC [22, 25, 121], therefore, it is required to validate the LSDIC process. The LSDIC validation was made using a 316L Stainless Steel strip with a strain gauge installed at the surface in the longitudinal direction and a speckle pattern applied to the opposite surface. The sample dimensions were 300 mm long, 30 mm wide and 2 mm thick. The gauge length of the sample was 138 mm. The yield strength and the Young' modulus of the 316L stainless steel are 170 MPa and 193 GPa, respectively. The sample was loaded in tension, in particular, the load considered was 4.2 ± 3.9 kN, which provides a change in stress, $\Delta\sigma$, of 130 MPa, below the yield strength. From the material properties and the sample dimensions, it is possible to estimate the theoretical strain change from

$$\Delta\sigma = E\Delta\varepsilon = E\frac{\Delta l}{L} \tag{B.1}$$

where E is the Young's modulus, $\Delta\varepsilon$ is the strain change, L is the gauge length of the sample, and Δl is the peak-to-peak displacement.

Therefore, the longitudinal strain change that should be obtained from the experiments is 0.067% and the theoretical peak-to-peak displacement, Δl, is 0.093 mm.

The white light cameras used for DIC in this PhD are the Imager E-lite 5M LaVision of 12 bit analogue to digital converter, which are high sensitivity digital cameras and have a resolution of 2448 x 2050 pixels. They can record up to 10 frames/s and the load can be input into the acquisition computer equipped with DaVis software. The experiments were performed at a combination of loading frequencies and frame rates to analyse oversampled and undersampled cases. For a frame rate of 9 Hz, the loading frequencies analysed were 1.1, 2.1, 3.1 and 4.1 Hz, in this case, the data is oversampled. To validate undersampled cases, the frame rate considered was 2 Hz, and the loading frequencies, 7.1 and 21.1 Hz. The number of frames collected was 320 to have enough data to produce a reliable strain measurement.

The data was analysed at different subset sizes to select the optimum size (Figure B.1) following the DIC good practice guide [147]. The trade off to consider is the Standard Deviation (STD) or noise with subset size. The bigger the subset size, the lower the noise, however, it tends to average down strain gradients, which is not useful for localised cracks. On the contrary, the smaller the subset size is, the higher the strain resolution is, however, it is noisier than at bigger subset size. Therefore, the subset size chosen was 71 pixels as it provides lower standard deviation compared to smaller values, but higher resolution than larger subset sizes. The resolution for the longitudinal strain and displacement is 0.0081%, which is lower than the theoretical strain that would be obtained for these experiments, and $6.43 \cdot 10^{-4}$ mm.

Appendix B

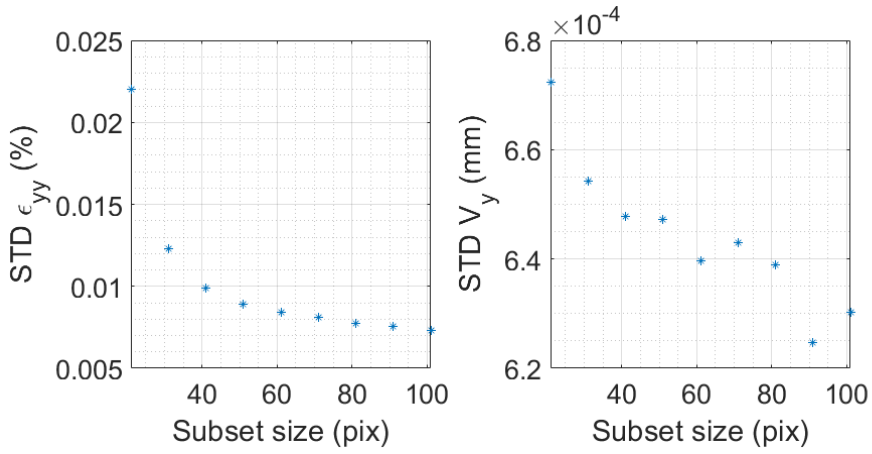

Figure B.1 Standard deviation vs subset size of the longitudinal strain and displacement

It is important for DIC to report the noise and displacement and strain resolutions. The camera noise has been calculated by subtracting two still images, calculating the standard deviation and dividing it by the number of grey levels (2^{12} grey levels for Imager E-Lite 5M LaVision cameras). The level of noise is acceptable for both cameras as it is about 1% or below. The displacement and strain resolutions were calculated by using the subset and step size of 71 and 23 pixels and post-processing the still images to obtain displacement and strains. The selection of the subset size and step size was based on a noise study on the longitudinal strain along the vertical line, where it was determined that it presented high spatial resolution (peak strain) and smaller noise, with respect to other subset size and step sizes. Then, the standard deviation of the displacement and strain is calculated for the first correlated frame, because the post-processing of LSDIC refers to the first picture that is done at the mean load. The standard deviation is the resolution for the particular parameter i.e. displacement or strain. The matching criterion applied is the zero normalised sum of squared difference (ZNSSD), which performs well on shifted and compressed contrast, however, it adds random noise but it is the only matching criterion available on DaVis. The interpolation selected is the bicubic (6^{th} order spline) method that provides the most accurate calculation compared with the bilinear. Finally, the shape function selected is the affine that takes into account translations and rotation. The parameters considered for LSDIC can be seen in Table B.1. The Virtual Strain Gauge (VSG) is calculated as follows:

$$VSG = [(\mathrm{SW} - 1)\mathrm{ST}] + \mathrm{SS} \tag{B.2}$$

where SW is the strain window, which is 3 data points, ST is the step size, 71 pixels and SS is the subset size, 23 pixels.

Table B.1 Parameters considered for LSDIC

Technique used	**3D Digital Image Correlation**	
	Camera 1	**Camera 2**
Sensor and digitization	2448 x 2050, 12-bit	
Camera noise (% of range)	1.119%	0.98%
Lens and imaging distance	50 mm F-mount, 1.1 m	
Total number of images	2 (9 Hz / 2 Hz)	
Pixel to mm conversion	1 pixel = 0.071 mm	
ROI (mm)	174 x 116 mm	
Subset, step	71, 23	
Interpolation, shape functions, correlation criterion	Bicubic (6^{th} order spline), affine, ZNSSD	
Pre-smoothing	None	
Displacement resolution	$6.43 \cdot 10^{-4}$ mm	
Strain		
Smoothing technique	Local polynomial - affine least-squares fit	
Strain window	3 data points	
VSG	165 pixels	
Resolution	0.0081 %	

Table B.2 shows the strain gauges and LSDIC results for the different loading frequencies and frame rates. The LSDIC results are averaged across the specimen area. It can be seen that there is a good agreement between the strain gauges and the LSDIC results for all combinations of frame rate and loading frequency, with relative error ranging from 0.9% to 5.1%.

Table B.2 LSDIC vs strain gauges comparison on 316L Stainless Steel sample

Frame rate (FR) LSDIC (Hz)	**Loading frequency (LF) (Hz)**	**$\Delta\varepsilon$ (%) strain gauges**	**$\Delta\varepsilon$ (%) LSDIC**	**Relative error (%)**
9	0.75	0.0576 ± 0.0029	0.0603 ± 0.0119	4.7
	1.1	0.0579 ± 0.0029	0.0605 ± 0.0120	4.5
	2.1	0.0585 ± 0.0029	0.0590 ± 0.0116	0.9 / 6.9
	3.1	0.0603 ± 0.0030	0.0614 ± 0.0122	1.8
	4.1	-	0.0586 ± 0.0117	-
2	7.1	0.0599 ± 0.0030	0.0583 ± 0.0115	2.7
	21.1	0.0554 ± 0.0028	0.0582 ± 0.0115	5.1

Appendix C First Ply Failure Analysis

In this section, the load level of inspection is determined based on the First Ply Failure (FPF) laminate stress of the GFRP and CFRP for the considered laminates in Chapter 6. The load of inspection does not add any damage to the laminate and it is always the same for the considered laminate.

Different criteria have been compared, which include maximum stress and strain, Tsai-Wu, Puck 2D and LaRC03. The analysis has been performed in ESAComp. The failure strength and strains considered are shown in Table C.1, where X and Y are the stresses to failure (strengths) in the directions parallel and transverse of the fibres, and S is the shear strength. The subscripts t and c represent tension and compression.

Table C.1 Failure strength and strains GFRP RP-528 [134, 145]

Property	Value
X_t (MPa)	1050
Y_t (MPa)	51
X_c(MPa)	790
Y_c (MPa)	134
S (MPa)	47
ε_{1t}	2.76 %
ε_{2t}	0.46 %
ε_{1c}	2.07 %
ε_{2c}	1.21 %
γ_{12}	2.44 %

The results of the FPF for a 45° and 90° plies are presented in Table C.2, Table C.3, and Table C.4. It can be seen that as expected 90° ply fails before on 90 UD samples, i.e. at a lower stress level, than the 45° ply. The failure criteria considered are Puck and LaRC03, as they are advanced failure criteria and failure-mode-based-theories. It is calculated for two basic failure modes based on 2D plane stress, in fibre failure mode and inter-fibre failure mode [37, 38]. Hence, the level of inspection considered for the coupons $[\pm 45]_{3s}$ is 36 MPa and for the cross-ply ($[0,90]_{3s}$ and $[90,0]_{3s}$) is 48 MPa. The FPF for the 90 UD is considered for the determination of the coefficient of thermal expansion transverse to the fibre, α_2.

Table C.2 FPF laminate stress 45° ply GFRP on $[\pm 45]_{3s}$

FPF criterion	Failure load (N/m)	Failure stress (MPa)
Max stress	259440.00	94.00
Max strain	259440.00	94.00
Tsai-Wu	220138.32	79.76
LaRC03	235232.91	85.23
Puck 2D	215475.05	78.07

Table C.3 FPF laminate stress 90° ply GFRP on $[90]_{10}$

FPF criterion	Failure load (N/m)	Failure stress (MPa)
Max stress	140760.36	51.00
Max strain	86645.60	31.39
Tsai-Wu	140760.36	51.00
LaRC03	140760.36	51.00
Puck 2D	140760.36	51.00

Table C.4 FPF laminate stress 90° ply GFRP on $[0,90]_{3s}$ and $[90,0]_{3s}$

FPF criterion	Failure load (N/m)	Failure stress (MPa)
Max stress	319150.69	115.63
Max strain	314754.70	114.04
Tsai-Wu	317213.07	114.93
LaRC03	319149.60	115.63
Puck 2D	319149.60	115.63

A similar study has been done to determine the FPF of CFRP IM7/8552. The failure strength are shown in Table C.5. Considering LaRC03 failure criterion, the failure load and stress for the 90° ply on both cross-ply samples are 982536.45 N/m and 625.02 MP, respectively, for the 45° ply on $[\pm 45]_{3s}$ laminate are 276348.62 N/m and 175.79 MPa, respectively, and for the 90° ply on a UD $[90]_{10}$ laminate are 81613.31 N/m and 62.30 MPa, respectively. Therefore, the $[\pm 45]_{3s}$ and both cross-ply samples, $[0,90]_{3s}$ and $[90,0]_{3s}$, will be loaded at 46 MPa and 173 MPa respectively, which are stress levels below FPF but high enough to measure the thermoelastic response with an IR camera. To obtain the coefficient of thermal expansion transverse to the fibre, α_2, a 90 UD, $[90]_{10}$ sample will be loaded at a stress level of 15 MPa.

Table C.5 Failure strength CFRP IM7/8552 [146]

Property	Value
X_t (MPa)	2326.2
Y_t (MPa)	62.3
X_c (MPa)	1200.1
Y_c (MPa)	199.8
S (MPa)	92.3
ε_{1t}	1.56%
ε_{2t}	0.68%
ε_{1c}	0.81%
ε_{2c}	2.17%
γ_{12}	3.64%

Appendix D Mechanical Properties

To determine the mechanical properties of the RP-528 GFRP and IM7/8552 CFRP prepregs UD i.e. $[0]_{10}$ - 0UD - and $[90]_{10}$ - 90UD - as well as $[\pm 45]_{3s}$ samples have been tested. The testing procedure followed for the UD samples is described in ASTM D3039 (Standard Test Method for Tensile Properties of Polymer Matrix Composite Materials). ASTM D 3518 (Standard Test Method for In-Plane Shear Response of Polymer Matrix Composite Materials by Tensile Test of a $\pm 45°$ Laminate) has been followed to determine the shear modulus. The sample dimensions can be seen in Table 6.1.

The methodology used to obtain the mechanical properties is stereo-DIC on one side of the sample and Tee Rosette strain gauges (CEA-13-125UT-350) on the opposite side to compare both experimental techniques and obtain reliable results. The coupons were loaded over the elastic range. The 0UD, 90UD and $[\pm 45]_{3s}$ GFRP coupons were loaded up to 10.5 kN, 1.9 kN and 4 kN respectively. The 0UD, 90UD and $[\pm 45]_{3s}$ CFRP coupons were loaded up to 4 kN, 300 N and 2 kN respectively. The tests were done in displacement control and the actuator was moving at a rate of 2 mm/min as recommended in ASTM D3039.

The Young's modulus along the fibre direction, $E_1$is calculated from the 0UD sample as follows

$$E_1 = \frac{F/A}{\varepsilon_1} \tag{D.1}$$

where F is the tensile load applied, A the cross-sectional area of the coupon and ε_1 is the strain along the fibre direction.

The Poisson's ratio, ν_{12}, is obtained by dividing the strain perpendicular to the load and fibre direction, ε_2, over the strain along the fibre direction, ε_1, from the 0UD sample as follows

$$\nu_{12} = -\frac{\varepsilon_2}{\varepsilon_1} \tag{D.2}$$

Similarly to the Young's modulus along the fibre direction, the Young's modulus perpendicular to the fibres, E_2, is obtained by testing a 90UD sample and calculated as

$$E_2 = \frac{F/A}{\varepsilon_2} \tag{D.3}$$

Finally, the shear modulus, G_{12}, is obtained by testing the $[\pm 45]_{3s}$ coupon and is calculated as

$$G_{12} = \frac{\tau_{12}}{\gamma_{12}} = \frac{F/(2A)}{\varepsilon_x - \varepsilon_y} \tag{D.4}$$

where τ_{12} is the shear stress, γ_{12} is the shear strain, which is calculated by subtracting the strain parallel and perpendicular to the load, ε_x and ε_y, respectively.

The axes systems for the different coupons can be seen in Figure 3.1. The results of the GFRP mechanical properties are presented in Table D.1, Table D.2, and Table D.3 for each test. Additionally, the same results have been presented for the CFRP and shown in Table D.5, Table D.6, and Table D.7. A summary of the final GFRP and CFRP results is shown in Table D.4 and Table D.8, respectively.

Table D.1 GFRP Young's modulus E_1 and Poisson's ratio ν_{12}

Type	Sample	Test number	Strain gauges		DIC	
			E_1 (GPa)	ν_{12}	E_1 (GPa)	ν_{12}
0UD	1	1	37.42 ± 0.0015	$0.273 \pm 9.0 \cdot 10^{-6}$	38.74 ± 0.029	0.309 ± 0.0017
	1	2	37.29 ± 0.0014	$0.271 \pm 7.9 \cdot 10^{-6}$	38.94 ± 0.042	0.314 ± 0.0039
	1	3	37.28 ± 0.0014	$0.272 \pm 7.0 \cdot 10^{-6}$	38.92 ± 0.030	0.309 ± 0.0030
	1	4	37.28 ± 0.0015	$0.271 \pm 4.4 \cdot 10^{-6}$	38.89 ± 0.031	0.312 ± 0.0029

Table D.2 GFRP Young's modulus E_2

Type	Sample	Test number	Strain gauges	DIC
			E_2 (GPa)	E_2 (GPa)
90UD	1	1	11.55 ± 0.0038	10.74 ± 0.053
	1	2	11.44 ± 0.0039	10.75 ± 0.077
	2	1	11.42 ± 0.0043	10.71 ± 0.056
	2	2	11.30 ± 0.0038	10.74 ± 0.081

Table D.3 GFRP shear modulus G_{12}

Type	Sample	Test number	Strain gauges	DIC
			G_{12} (GPa)	G_{12} (GPa)
$[\pm 45]_{3s}$	1	1	3.59 ± 0.0041	3.77 ± 0.068
	1	2	3.91 ± 0.0033	3.88 ± 0.054
	2	1	3.96 ± 0.0042	3.90 ± 0.062
	2	2	3.98 ± 0.0031	3.91 ± 0.048

Table D.4 GFRP summary of the obtained mechanical properties

Property	Experiments	Literature [145]
E_1(GPa)	38.10 ± 0.83	41.33 ± 0.41
ν_{12}	0.291 ± 0.021	0.317 ± 0.008
E_2 (GPa)	11.08 ± 0.38	10.94 ± 0.34
G_{12} (GPa)	3.86 ± 0.13	3.6 ± 0.1
ρ (kg/m^3)	1861.6 ± 3.4	1900

Table D.5 CFRP Young's modulus E_1 and Poisson's ratio ν_{12}

Type	Test number	Strain gauges		DIC	
		E_1 (GPa)	ν_{12}	E_1 (GPa)	ν_{12}
0UD	1	146.87 ± 0.17	$0.34 \pm 9.5 \cdot 10^{-7}$	151.1 ± 3.1	$0.34 \pm 3.8 \cdot 10^{-6}$
	2	146.84 ± 0.17	$0.33 \pm 9.6 \cdot 10^{-7}$	150.4 ± 0.7	$0.35 \pm 8.2 \cdot 10^{-6}$

Table D.6 CFRP Young's modulus E_2

Type	Test number	Strain gauges	DIC
		E_2 (GPa)	E_2 (GPa)
90UD	1	9.27 ± 0.02	9.08 ± 0.13
	2	9.27 ± 0.03	9.14 ± 0.06

Table D.7 CFRP shear modulus G_{12}

Type	Test number	Strain gauges	DIC
		G_{12} (GPa)	G_{12} (GPa)
$[\pm 45]_{3s}$	1	5.01 ± 0.12	5.12 ± 0.20
	2	5.00 ± 0.10	5.12 ± 0.15

Table D.8 CFRP summary of the obtained mechanical properties

Property	Experiments	Literature [141, 146]	Literature [142]
E_1(GPa)	148.80 ± 2.27	171.42 ± 2.38	161
ν_{12}	0.34 ± 0.01	0.32 ± 0.02	0.32
E_2 (GPa)	9.19 ± 0.10	9.08 ± 0.09	11.38
G_{12} (GPa)	5.06 ± 0.07	5.29 ± 0.13	5.17
ρ (kg/m^3)	1556.75 ± 72.5	1570	1570

List of References

[1] T. Reyno, C. Marsden, and D. Wowk, "Surface damage evaluation of honeycomb sandwich aircraft panels using 3D scanning technology", *NDT and E International*, vol. 97, pp. 11-19, 2018, doi: https://doi.org/10.1016/j.ndteint.2018.03.007.

[2] L. S. Sutherland, "A review of impact testing on marine composite materials: Part IV - Scaling, strain rate and marine-type laminates", *Composite Structures*, vol. 200, pp. 929-938, 2018, doi: https://doi.org/10.1016/j.compstruct.2018.06.052.

[3] M. Escobar, D. Cadena, and L. F. Castañeda, "Electric public transport vehicle with composite material body diagnostic - User safety", in *17th International Conference Diagnostics of Machines and Vehicles*, 2018, vol. 182: EDP Sciences, doi: https://doi.org/10.1051/matecconf/201818201001.

[4] B. F. Sørensen, "Materials and Structures for Wind Turbine Rotor Blades - An Overview", in "Improved design of large wind turbine blades of fibre composites (phase 2) - summary report", Denmark, 2005. [Online]. Available: http://www.iccm-central.org/Proceedings/ICCM17proceedings/Themes/Plenaries/P1.3%20Sorensen%20full.pdf

[5] S. Stoycheva, D. Marchese, C. Paul, S. Padoan, A.-S. Juhmani, and I. Linkov, "Multi-criteria decision analysis framework for sustainable manufacturing in automotive industry", *JOURNAL OF CLEANER PRODUCTION*, vol. 187, pp. 257-272, 2018, doi: https://doi.org/10.1016/j.jclepro.2018.03.133.

[6] A. Juengert and C. U. Grosse, "Inspection techniques for wind turbine blades using ultrasound and sound waves", presented at the Nondestructive Testing in Civil Engineering, Nantes, France, 2009. [Online]. Available: http://citeseerx.ist.psu.edu/viewdoc/download?doi=10.1.1.216.6267&rep=rep1&type=pdf.

[7] R. Yang, Y. He, and H. Zhang, "Progress and trends in nondestructive testing and evaluation for wind turbine composite blade", *Renewable and Sustainable Energy Reviews*, Review Article vol. 60, pp. 1225-1250, 2016, doi: https://doi.org/10.1016/j.rser.2016.02.026.

[8] A. Ampatzoglou and V. Kostopoulos, "Design, Analysis, Optimization, Manufacturing, and Testing of a 2U Cubesat", *International Journal of Aerospace Engineering*, Article pp. 1-15, 2018, doi: https://doi.org/10.1155/2018/9724263.

[9] R. S. Pierce and B. G. Falzon, "Simulating Resin Infusion through Textile Reinforcement Materials for the Manufacture of Complex Composite Structures", *Engineering*, vol. 3, pp. 596-607, 2017, doi: https://doi.org/10.1016/J.ENG.2017.04.006.

[10] K. B. Katnam, A. J. Comer, D. Roy, L. F. M. Da Silva, and T. M. Young, "Composite Repair in Wind Turbine Blades: An Overview", *Journal of Adhesion*, vol. 91, pp. 113-139, 2015, doi: https://doi.org/10.1080/00218464.2014.900449.

[11] A. Dobyns, C. Q. Rousseau, and P. Minguet, "6.12: Helicopter Applications and Design," in *Comprehensive Composite Materials*, vol. 6: Design and Applications, A. Kelly and C. Zweben Eds., 2000.

[12] D. W. Radford, "3.14 Development of Composite Chassis for Motorsports," in *Comprehensive Composite Materials II*, vol. 3: Polymer Matrix Composites: Applications, P. W. R. Beaumont and C. H. Zweben Eds., 2018.

[13] J. M. Dulieu-Barton, "Thermoelastic Stress Analysis," in *Optical methods for solid mechanics*, P. Rastogi and E. Hack Eds. Weinheim: Wiley-VCH, 2012, ch. 8.

[14] F. Hild and S. Roux, "Digital Image Correlation," in *Optical methods for solid mechanics*, P. Rastogi and E. Hack Eds. Weinheim: Wiley-VCH, 2012, ch. 5.

[15] P. A. Bonnet and A. G. Dutton, "Finite element modelling of blade thermoelastic stress analysis results", presented at the Proceedings of the European wind energy conference and exhibition, Brussels.

[16] N. Rajic and S. Galea, "Thermoelastic stress analysis and structural health monitoring: An emerging nexus", *STRUCTURAL HEALTH MONITORING-AN INTERNATIONAL JOURNAL*, vol. 14, no. 1, pp. 57-72, 2015, doi: https://doi.org/10.1177/1475921714548936.

[17] R. Gade and T. B. Moeslund, "Thermal cameras and applications: a survey", *Machine Vision and Applications*, vol. 25, pp. 245-262, 2014, doi: https://doi.org/10.1007/s00138-013-0570-5.

[18] D. Chen, S. Sun, J. M. Dulieu-Barton, Q. Li, and W. Wang, "Crack growth analysis in welded and non-welded T-joints based on lock-in digital image correlation and thermoelastic stress analysis", *International Journal of Fatigue*, vol. 110, pp. 172-185, 2018.

[19] R. K. Fruehmann, J. M. Dulieu-Barton, and S. Quinn, "Thermoelastic Stress and Damage Analysis Using Transient Loading", *Experimental Mechanics*, Article vol. 50, no. 7, pp. 1075-1086, 2010, doi: https://doi.org/10.1007/s11340-009-9295-9.

[20] A. K. Wong, N. Rajic, and Q. Nguyen, "50th Anniversary Article: Seeing Stresses through the Thermoelastic Lens-A Retrospective and Prospective from an Australian Viewpoint", *Strain*, vol. 51, no. 1, pp. 1-15, 2015, doi: https://doi.org/10.1111/str.12116.

[21] N. Rajic and D. Rowlands, "Thermoelastic stress analysis with a compact low-cost microbolometer system", *Quantitative infrared thermography journal*, vol. 10, no. 2, pp. 135-158, 2013, doi: https://doi.org/10.1080/17686733.2013.800688.

[22] R. K. Fruehmann, J. M. Dulieu-Barton, S. Quinn, and J. P. Tyler, "The use of a lock-in amplifier to apply digital image correlation to cyclically loaded components", *Optics and Lasers in Engineering*, Article vol. 68, pp. 149-159, 2015, doi: https://doi.org/10.1016/j.optlaseng.2014.12.021.

[23] G. Crammond, S. W. Boyd, and J. M. Dulieu-Barton, "A Point-wise Approach to the Analysis of Complex Composite Structures Using Digital Image Correlation and Thermoelastic Stress Analysis", *Strain*, vol. 51, no. 4, pp. 311-323, 2015, doi: https://doi.org/10.1111/str.12142.

[24] W. Wang, R. K. Fruehmann, and J. M. Dulieu-Barton, "Application of digital image correlation to address complex motions in thermoelastic stress analysis", *Strain*, vol. 51, no. 5, pp. 405-418, 2015, doi: https://doi.org/10.1111/str.12151.

[25] D. J. Bull *et al.*, "Reshaping the testing pyramid: Utilisation of data-rich NDT techniques as a means to develop a 'high fidelity' component and sub-structure testing methodology for composites", in *21st International Conference on Composite Materials*, Xi'an, China, 2017, pp. 20-25.

[26] N. Rajic and N. Street, "A performance comparison between cooled and uncooled infrared detectors for thermoelastic stress analysis", *Quantitative Infrared Thermography Journal*, vol. 11, no. 2, pp. 207-221, 2014, doi: https://doi.org/10.1080/17686733.2014.962835.

[27] G. Pitarresi, "Evaluation of lock-in signal data processing procedures for Thermoelastic Stress Analysis", presented at the BSSM's 14th International Conference on Advances in Experimental Mechanics, Belfast, UK, 2019.

[28] S. Timoshenko and J. N. Goodier, *Theory of Elasticity*, 3rd ed. McGraw Hill Asia, 2010.

[29] T. R. Emery, J. M. Dulieu-Barton, J. S. Earl, and P. R. Cunningham, "A generalised approach to the calibration of orthotropic materials for thermoelastic stress analysis", *Composites Science and Technology*, vol. 68, pp. 743-752, 2008, doi: https://doi.org/10.1016/j.compscitech.2007.09.002.

[30] S. Sambasivam, S. Quinn, and J. M. Dulieu-Barton, "Identification of the source of the thermoelastic response from orthotropic laminated composites", in *17th International Conference on Composite Materials*, Edinburgh, United Kingdom, 2009: IOM Communications Ltd.

[31] E. J. Barbero, F. A. Cosso, and F. A. Campo, "Benchmark solution for degradation of elastic properties due to transverse matrix cracking in laminated composites", *Composite Structures*, vol. 98, pp. 242-252, 2013, doi: https://doi.org/10.1016/j.compstruct.2012.11.009.

[32] J. N. Reddy, *Mechanics of Laminated Composite Plates and Shells*. Florida: CRC Press LLC, 2004.

[33] R. M. Jones, *Mechanics of Composite Materials*, 2nd ed. Taylor & Francis, 1999.

[34] I. M. Daniel and O. Ishai, *Engineering Mechanics of Composite Materials*, Second Edition ed. 2006.

[35] S. U. Khan, R. C. Alderliesten, and R. Benedictus, "Post-stretching induced stress redistribution in Fibre Metal Laminates for increased fatigue crack growth resistance", *Composite Science and Technology*, vol. 69, pp. 396-405, 2009, doi: https://doi.org/10.1016/j.compscitech.2008.11.006.

[36] R. Ponginan. "ESAComp Theoretical Background - Analyses - Part 3 - Laminates". https://altairuniversity.com/learning-library/esacomp-theoretical-background-analyses-part-3-laminates/ (accessed 2020).

[37] H. M. Deuschle and A. Puck, "Application of the Puck failure theory for fibre-reinforced composites under three-dimensional stress: Comparison with experimental results", *Journal of Composite Materials*, vol. 47, pp. 827-846, 2012, doi: https://doi.org/10.1177/0021998312462158.

[38] C. G. Dávila and P. P. Camanho, "Failure Criteria for FRP Laminates in Plane Stress", NASA Scientific and Technical Information (STI) Program Office, 2003.

[39] *Altair ESAComp*. [Online]. Available: https://altairhyperworks.com/product/esacomp

[40] R. Talreja, *Damage and failure of composite materials*, Cambridge: Dawson Books, 2012. [Online]. Available: https://www.dawsonera.com/readonline/9781139417457/startPage/48/1.

[41] R. B. Heslehurst, *Defects and Damage in Composite Materials and Structures*. Boca Raton: CRC Press, 2014.

[42] N. Rajic and J. Moran, "Remote line scan thermography for the rapid inspection of composite impact damage", *Composite Structures*, vol. 208, pp. 442-453, 2019, doi: https://doi.org/10.1016/j.compstruct.2018.10.038.

[43] N. Xie, R. A. Smith, S. Mukhopadhyay, and S. R. Hallett, "A numerical study on the influence of composite wrinkle defect geometry on compressive strength", *Materials and Design*, vol. 140, pp. 7-20, 2018, doi: https://doi.org/10.1016/j.matdes.2017.11.034.

[44] B. F. Sørensen, J. W. Holmes, P. Brøndsted , and K. Branner, "Blade materials, testing methods and structural design", *vol. 44, Wind Power Generation and Wind Turbine Design*: WIT Press, 2010, pp. 417-460.

[45] S. S. Kumar, J. Krishnamoorthi, B. Ravisankar, and V. Balusamy, "Assessing quality of diffusion bonded joints with interlayer using ultrasonic/ultrasound", *Journal of Materials Processing Tech.*, vol. 242, pp. 139-146, 2017, doi: https://doi.org/10.1016/j.jmatprotec.2016.11.036.

[46] M. Amura and M. Meo, "Prediction of residual fatigue life using nonlinear ultrasound", *Smart Materials and Structures*, vol. 21, 2010, doi: https://doi.org/10.1088/0964-1726/21/4/045001.

[47] C. Hornfeck, C. Geiss, M. Rücker, and C. Grosse, "Comparative Study of State of the Art Nondestructive Testing Methods with the Local Acoustic Resonance Spectroscopy to Detect Damages in GFRP", *Journal of Nondestructive Evaluation*, vol. 34, 2015, doi: https://doi.org/10.1007/s10921-015-0283-y.

[48] R. Raišutis, R. Kažys, E. Žukauskas, and L. Mažeika, "Ultrasonic air-coupled testing of square-shape CFRP composite rods by means of guided waves", *NDT and E International*, Article vol. 44, no. 7, pp. 645-654, 2011, doi: https://doi.org/10.1016/j.ndteint.2011.07.001.

[49] M. Kalms, O. Focke, and C. V. Kopylow, "Applications of laser ultrasound NDT methods on composite structures in aerospace industry", in *Ninth International Symposium on Laser Metrology*, Singapore, 2008, vol. 7155, doi: https://doi.org/10.1117/12.814512.

[50] A. D. Abetew, T. C. Truong, S. C. Hong, J. R. Lee, and J. B. Ihn, "Parametric optimization of pulse-echo laser ultrasonic system for inspection of thick polymer matrix composites", *STRUCTURAL HEALTH MONITORING-AN INTERNATIONAL JOURNAL*, vol. 19, pp. 443-453, 2020, doi: https://doi.org/10.1177/1475921719852891.

[51] N. Toyama, T. Yamamoto, K. Urabe, and H. Tsuda, "Ultrasonic inspection of adhesively bonded CFRP/aluminum joints using pulsed laser scanning", *Advanced Composite Materials*, vol. 28, pp. 27-35, 2019, doi: https://doi.org/10.1080/09243046.2017.1416517.

[52] S. J. Kim, "Damage detection in composite under in-plane load using tap test", *Journal of Mechanical Science and Technology*, Article vol. 29, no. 1, pp. 199-207, 2015, doi: https://doi.org/10.1007/s12206-014-1103-5.

[53] S. Esola, I. Bartoli, S. E. Horner, J. Q. Zheng, and A. Kontsos, "Defect detection via instrumented impact in thick-sectioned laminate composite", *Journal of Nondestructuve Evaluation*, vol. 47, pp. 46-47, 2017, doi: https://doi.org/10.1007/s10921-017-0422-8.

[54] Dantec Dynamics. "Non-Destructive Testing (NDT) - Laser Shearography". https://www.dantecdynamics.com/shearography-non-destructive-testing (accessed 2018).

[55] G. De Angelis, E. Dati, M. Bernabei, and F. Leccese, "Development on aerospace composite structures investigation using thermography and shearography in comparison to traditional NDT methods", in *IEEE Metrology for Aerospace (MetroAeroSpace)*, 2015 / 08 / 05 / 2015: Institute of Electrical and Electronics Engineers Inc., pp. 49-55, doi: https://doi.org/10.1109/MetroAeroSpace.2015.7180625.

[56] M. Doroshtnasir, T. Worzewski, R. Krankenhagen, and M. Röllig, "On-site inspection of potential defects in wind turbine rotor blades with thermography", *Wind Energy*, vol. 19, no. 8, p. 1407, 2016, doi: https://doi.org/10.1002/we.1927.

[57] R. G. He, D. J. Kong, Z. Zheng, N. Tao, and C. L. Zhang, "Bonding quality evaluation of wind turbine blades by pulsed thermography", in *International Symposium on Photoelectronic Detection and Imaging*, Beijing, China, S. 8193, Ed., 2011, vol. 8193, no. 1, doi: https://doi.org/10.1117/12.900770.

[58] P. H. Shin, S. C. Webb, and K. J. Peters, "Pulsed phase thermography imaging of fatigue-loaded composite adhesively bonded joints", *NDT and E International*, Article vol. 79, pp. 7-16, 2016, doi: https://doi.org/10.1016/j.ndteint.2015.11.008.

[59] A. Ellison and H. Kim, "Computed tomography informed composite damage state model generation", *Journal of Composite Materials,* vol. 52, no. 25, pp. 3523-3538, 2018, doi: https://doi.org/10.1177/0021998318773464.

[60] Z. Hu, H. Luo, H. Lu, S. G. Bardenhagen, C. R. Siviour, and R. W. Armstrong, "Internal Deformation Measurement of Polymer Bonded Sugar in Compression by Digital Volume Correlation of In-situ Tomography", *Experimental Mechanics,* Article vol. 55, no. 1, pp. 289-300, 2015, doi: https://doi.org/10.1007/s11340-014-9856-4.

[61] F. Wan, R. Liu, Y. Wang, Y. Cao, C. Zhang, and T. J. Marrow, "Damage development during flexural loading of a 5-directional braided C/C-SiC composite, characterized by X-ray tomography and digital volume correlation", *Ceramics International,* Article vol. 45, pp. 5601-5612, 2019, doi: https://doi.org/10.1016/j.ceramint.2018.12.020.

[62] G. Pitarresi, L. D'Acquisto, and A. M. Siddiolo, "Thermoelastic stress analysis by means of an infrared scanner and a two-dimensional fast Fourier transform-based lock-in technique", *Journal of Strain Analysis for Engineering Design,* Article vol. 43, no. 6, pp. 493-506, 2008, doi: https://doi.org/10.1243/03093247JSA348.

[63] Laser Technology Inc., "Rapid Sensitive Inspection of Marine Composites using Laser Shearography". [Online]. Available: www.LaserNDT.com

[64] S. S. Pawar and K. Peters, "Through-the-thickness identification of impact damage in composite laminates through pulsed phase thermography", *Measurement Science and Technology* vol. 24, no. 11, 2013, doi: https://doi.org/10.1088/0957-0233/24/11/115601.

[65] R. T. Potter, "Stress analysis in laminated fibre composites by thermoelastic emission", *Proceedings of SPIE - The International Society for Optical Engineering,* Article vol. 731, pp. 110-121, 1987, doi: https://doi.org/10.1117/12.937892.

[66] E. Patterson and G. Pitarresi, "A review of the general theory of thermoelastic stress analysis", *Journal of Strain Analysis for Engineering Design,* vol. 38, no. 5, pp. 405-417, 2003, doi: https://doi.org/10.1243%2F03093240360713469.

[67] J. M. Dulieu-Barton and P. Stanley, "Development and applications of thermoelastic stress analysis", *Journal of Strain Analysis for Engineering Design,* Article vol. 33, no. 2, pp. 93-104, 1998, doi: https://doi.org/10.1243%2F0309324981512841.

[68] T. R. Emery and J. M. Dulieu-Barton, "Thermoelastic Stress Analysis of damage mechanisms in composite materials", *Composites Part A: Applied Science and Manufacturing,* vol. 41, no. 12, pp. 1729-1742, 2010, doi: https://doi.org/10.1016/j.compositesa.2009.08.015.

[69] A. Alshaya, X. Shual, and R. Rowlands, "Thermoelastic Stress Analysis of a Finite Orthotropic Composite Containing an Elliptical Hole", *Experimental Mechanics,* vol. 56, no. 8, pp. 1373–1384, 2016, doi: https://doi.org/10.1007/s11340-016-0174-x.

[70] T. R. Emery, J. M. Dulieu-Barton, J. S. Earl, and P. R. Cunningham, *A generalised approach to the calibration of orthotropic materials for thermoelastic stress analysis*. 2008.

[71] P. Stanley and W. K. Chan, "The application of thermoelastic stress analysis techniques to composite materials", *The Journal of Strain Analysis for Engineering Design,* Article vol. 23, no. 3, pp. 137-143, 1988, doi: https://doi.org/10.1243%2F03093247V233137.

[72] A. K. Wong, "A Non-Adiabatic Thermoelastic Theory for Composite Laminates", *Journal of Physics and Chemistry of Solids,* vol. 52, no. 3, pp. 483-494, 1991, doi: https://doi.org/10.1016/0022-3697(91)90180-8.

[73] D. Zhang, N. F. Enke, and B. I. Sandor, "Thermographic Stress Analysis of Composite Materials", *Experimental Mechanics*, vol. 30, no. 1, pp. 68-73, 1990, doi: https://doi.org/10.1007/BF02322705.

[74] P. R. Cunningham, J. M. Dulieu-Barton, A. G. Dutton, and R. A. Shenoi, "The effect of ply lay-up upon the thermoelastic response of laminated composites", *Key Engineering Materials*, Conference Paper vol. 221-222, pp. 325-336, 2002, doi: https://doi.org/10.4028/www.scientific.net/KEM.221-222.325.

[75] G. Pitarresi, M. S. Found, and E. A. Patterson, "An investigation of the influence of macroscopic heterogeneity on the thermoelastic response of fibre reinforced plastics", *Composites Science and Technology*, vol. 65, no. 2, pp. 269-280, 2005, doi: https://doi.org/10.1016/j.compscitech.2004.07.008.

[76] G. Pitarresi, A. Conti, and U. Galietti, "Investigation on the Influence of the Surface Resin Rich Layer on the Thermoelastic Signal from Different Composite Laminate Lay-Ups", *Applied Mechanics and Materials*, vol. 3-4, pp. 167-172, 2006, doi: https://doi.org/10.4028/www.scientific.net/AMM.3-4.167.

[77] R. K. Fruehmann, J. M. Dulieu-Barton, and S. Quinn, "On the thermoelastic response of woven composite materials", *The Journal of Strain Analysis for Engineering Design*, vol. 43, no. 6, pp. 435-450, 2008, doi: https://doi.org/10.1243%2F03093247JSA381.

[78] R. K. Frühmann, S. Sambasivam, J. M. Dulieu-Barton, and S. Quinn, "Material Properties for Quantitative Thermoelastic Stress Analysis of Composite Structures", *Applied Mechanics and Materials*, vol. 13-14, pp. 99-104, 2008, doi: https://doi.org/10.4028/www.scientific.net/AMM.13-14.99.

[79] S. Quinn and J. M. Dulieu-Barton, "Identification of the sources of non-adiabatic behaviour for practical thermoelastic stress analysis", *Journal of Strain Analysis*, Article vol. 37, pp. 59-72, 2002, doi: https://doi.org/10.1243/0309324021514835.

[80] D. A. Crump and J. M. Dulieu-Barton, "Assessment of non-adiabatic behaviour in thermoelastic stress analysis of composite sandwich panels", *Experimental Mechanics*, vol. 52, pp. 829-842, 2012, doi: https://doi.org/10.1007/s11340-012-9601-9.

[81] *Matlab code to post-process Lock-in DIC and TSA experiments*. (2017). University of Southampton.

[82] J. Q. Zhang, Z. Xinmin, H. Xiao, and S. Jinwei, "Sinewave Fit Algorithm Based on Total Least-Squares Method with Application to ADC Effective Bits Measurement", *IEEE Transactions on Intrumentation and Measurement*, vol. 46, no. 4, pp. 1026 - 1030, 1997, doi: https://doi.org/10.1109/19.650821.

[83] R. C. Tighe, G. P. Howell, J. P. Tyler, S. Lormor, and J. M. Dulieu-Barton, "Stress based non-destructive evaluation using thermographic approaches: From laboratory trials to on-site assessment", *NDT and E International*, Article vol. 84, pp. 76-88, 2016, doi: https://doi.org/10.1016/j.ndteint.2016.08.005.

[84] T. Sakagami, Y. Izumi, N. Mori, and S. Kubo, "Development of self-reference lock-in thermography and its application to remote nondestructive inspection of fatigue cracks in steel bridges", *Quantitative InfraRed Thermography Journal*, vol. 7, no. 1, pp. 73-84, 2010, doi: https://doi.org/10.3166/qirt.7.73-84.

[85] G. Gaussorgues, *Infrared Thermography* (Microwave Technology Series 5). London: Chapman & Hall, 1994.

[86] D. S. Mountain and J. M. B. Webber, "Stress Pattern Analysis By Thermal Emission (SPATE)", in *4th European Electro-Optics Conference*, Utrecht, Netherlands, 1979, pp. 189-196, doi: https://doi.org/10.1117/12.965516.

[87] T. G. Ryall and A. K. Wong, "Design of a Focal-plane Array Thermographic System for Stress Analysis", *Experimental Mechanics*, vol. 35, pp. 144-147, 1995, doi: https://doi.org/10.1007/BF02326472.

[88] R. A. Wood, "Chapter 3 Monolithic Silicon Microbolometer Arrays", *vol. 47*, *Uncooled Infrared Imaging Array and Systems*, P. W. Kruse and D. D. Skatrud, Eds., San Diego, 1997.

[89] H. Budzier, V. Karause, S. Böhmer, G. Gerlach, and U. Hoffmann, "Fast microbolometer-based infrared camera system", presented at the 9th International Conference on Infrared Sensors & Systems, Nürnberg, Germany, 2006. [Online]. Available: http://www.dias-infrared.de/pdf/p020.pdf.

[90] I. Jiménez Fortunato, D. J. Bull, J. M. Dulieu-Barton, and O. T. Thomsen, "Towards developing a calibration technique to apply TSA with micro-bolometers", presented at the BSSM Conference, Southampton, 2018.

[91] FLIR, "IR Detectors for Thermographic Imaging". [Online]. Available: http://www.techni-tool.com/site/ARTICLE_LIBRARY/FLIR%20-%20IR%20Detectors%20For%20Thermographic%20Imaging.pdf

[92] Chemistry Glosary. "Blackbody Radiation". https://glossary.periodni.com/download_image.php?name=blackbody_radiation.png&source=blackbody+radiation (accessed 2017).

[93] R. Paschotta. "Photoconductive detectors". https://www.rp-photonics.com/photoconductive_detectors.html (accessed 2019).

[94] MoviTHERM. "Thermal Infrared Imaging explained!". https://movitherm.com/knowledgebase/thermal-infrared-imaging-explained/#:~:text=The%20majority%20of%20all%20thermal,resistance%20in%20their%20detector%20elements. (accessed 2020).

[95] L. J. Kozlowski and W. F. Kosonocky, "Infrared Detector Arrays," in *Handbook of Optics volume 2: Devices, Measurements and Properties*, 1995, ch. 33.

[96] A. Rogalski, "Infrared detectors: an overview", *Infrared Physics and Technology*, Article vol. 43, pp. 187-210, 1/1/2002 2002, doi: https://doi.org/10.1016/S1350-4495(02)00140-8.

[97] X. Sui, Q. Chen, and G. Gu, "Nonuniformity correction of infrared images based on infrared radiation and working time of thermal imager", *Optik*, vol. 124, pp. 352-356, 2011, doi: https://doi.org/10.1016/j.ijleo.2011.12.055.

[98] DISTEK Measuring Instruments. "FLIR SC5200 SC5500 SC5600 SC5650 High Sensitivity and Accuracy Infrared Camera for Industrial/Educational Therography". http://www.distek.ro/en/Product/Flir-SC5200-SC5500-SC5600-SC5650-High-Sensitivity-and-Accuracy-Infrared-Camera-for-Industrial-Educational-Therography--2063 (accessed 2017).

[99] Telops. "High-Speed IR Cameras: MWIR". https://www.telops.com/products/high-speed-cameras/mwir-cameras (accessed 2018).

[100] H. Budzier and G. Gerlach, *Thermal Infrared Sensors: Theory, Optimisation and Practice*, Chichester: Wiley, 2011. [Online]. Available: https://ebookcentral.proquest.com/lib/soton-ebooks/reader.action?docID=699437&query.

[101] A. Teich. "FLIR Lepton: One Million Produced and More to Come". https://www.flir.com/news-center/camera-cores--components/flir-lepton-one-million-produced-and-more-to-come/ (accessed 2020).

[102] T. McDowd. "FLIR Systems Launches Next Generation High-Performance Uncooled Thermal Camera Core". https://flir.gcs-web.com/news-releases/news-release-details/flir-systems-launches-next-generation-high-performance-uncooled#:~:text=Press%20Release&text=WILSONVILLE%2C%20OR%20%2D%2D(Marketwired%20%2D%20April,original%20equipment%20manufacturers%20(OEMs). (accessed 2020).

[103] FLIR Systems Inc. "Tau Camera User's Manual". http://www.ads-tec.co.jp/wordpress/wp-content/uploads/2012/09/Tau_320_Users_GuideRev120.pdf (accessed 2020).

[104] FLIR Systems Inc. "Want a Higher Resolution Lepton? Check Out Lepton 3". https://www.flir.com/news-center/camera-cores--components/httpwww.flir.comcoresblogdetailsid84075/ (accessed 2020).

[105] FLIR Systems Inc. "FLIR Lepton 3.5 Now Available to Manufacturers and Makers". https://www.flir.com/news-center/camera-cores--components/flir-lepton-3.5-now-available-to-manufacturers-and-makers/ (accessed 2020).

[106] FLIR. "FLIR A655sc Infrared Camera". http://www.flir.com/science/display/?id=46802 (accessed 2018).

[107] FLIR Lepton. "Documentation". https://lepton.flir.com/documentation/ (accessed 2020).

[108] Y. R. Choi and N. Rajic, "In-situ thermoelastic stress analysis for airframe full scale fatigue testing: An overview of lessons learnt", presented at the 17th Australian International Aerospace Congress: AIAC 2017, Melbourne, Australia, 2017, 2017, Conference Paper.

[109] R. B. Vieira, G. L. G. Gonzáles, and J. L. F. Freire, "Thermography Applied to the Study of Fatigue Crack Propagation in Polycarbonate", *Experimental Mechanics*, Article vol. 58, no. 2, pp. 269–282, 2018, doi: https://doi.org/10.1007/s11340-017-0341-8.

[110] N. Rajic, D. Rowlands, and S. Galea, "Probing the limits - New opportunities in thermoelastic stress analysis", in *28th International Congress of the Aeronautical Sciences*, Brisbane, Australia, 2012, vol. 6, pp. 5117-5126.

[111] Department of defence science and technology - Australian Government. "Microbolometer thermoelastic evaluation (MiTE)". https://www.dst.defence.gov.au/opportunity/mite (accessed 2018).

[112] J. M. Dulieu-Smith, "Alternative calibration techniques for quantitative thermoelastic stress analysis", *Strain*, Article vol. 31, no. 1, pp. 9-16, 1995, doi: https://doi.org/10.1111/j.1475-1305.1995.tb00949.x.

[113] G. Crammond, S. W. Boyd, and J. M. Dulieu-Barton, "Speckle pattern quality assessment for digital image correlation", 2013, doi: https://doi.org/10.1016/j.optlaseng.2013.03.014.

[114] B. Pan, A. Asundi, K. Qian, and H. Xie, "Two-dimensional digital image correlation for in-plane displacement and strain measurement: A review", *Measurement Science and Technology*, Article vol. 20, no. 6, 2009, doi: https://doi.org/10.1088/0957-0233/20/6/062001.

[115] LaVision. "2D/3D Digital Image Correlation". http://lavision.de/en/products/strainmaster/2d-stereo-dic/index.php (accessed 2018).

[116] LaVision. "3D Calibration Plates". https://www.smart-piv.com/en/products/strainmaster/system-components/calibration-plates/ (accessed 2018).

[117] F. Bernachy-Barbe, L. Gélébart, M. Bornert, J. Crépin, and C. Sauder, "Characterization of SiC/SiC composites damage mechanisms using Digital Image Correlation at the tow scale",

Composites Part A: Applied Science and Manufacturing, vol. 68, pp. 101-109, 2015, doi: https://doi.org/10.1016/j.compositesa.2014.09.021.

[118] E. del Rey Castillo, T. Allen, R. Henry, M. Griffith, and J. Ingham, "Digital image correlation (DIC) for measurement of strains and displacements in coarse, low volume-fraction FRP composites used in civil infrastructure", *Composite Structures*, vol. 212, pp. 43-57, 2019, doi: https://doi.org/10.1016/j.compstruct.2019.01.024.

[119] P. McKinley, A. Sinha, and F. A. Kamke, "Understanding the effect of weathering on adhesive bonds for wood composites using digital image correlation (DIC)", *Wood Research and Technology*, vol. 73, no. 2, pp. 155-164, 2019, doi: https://doi.org/10.1515/hf-2018-0024.

[120] G. F. Bomarito, J. D. Hochhalter, and T. J. Ruggles, "Development of Optimal Multiscale Patterns for Digital Image Correlation via Local Grayscale Variation", *Experimental Mechanics*, vol. 58, no. 7, pp. 1169-1180, 2017, doi: https://doi.org/10.1007/s11340-017-0348-1.

[121] G. P. Battams and J. M. Dulieu-Barton, "Data-rich characterisation of damage propagation in composite materials", *Composites: Part A*, Article vol. 91, no. 2, pp. 420-435, 2016, doi: https://doi.org/10.1016/j.compositesa.2016.08.007.

[122] N. Cholewa, P. T. Summers, S. Feih, A. P. Mouritz, B. Y. Lattimer, and S. W. Case, "A Technique for Coupled Thermomechanical Response Measurement Using Infrared Thermography and Digital Image Correlation (TDIC)", *Experimental Mechanics*, vol. 56, no. 2, pp. 145-164, 2015, doi: https://doi.org/10.1007/s11340-015-0086-1.

[123] G. Crammond, S. W. Boyd, and J. M. Dulieu-Barton, "Evaluating the localised through-thickness load transfer and damage initiation in a composite joint using digital image correlation", *Composites Part A: Applied Science and Manufacturing*, vol. 61, pp. 224-234, 2014, doi: https://doi.org/10.1016/j.compositesa.2014.03.002.

[124] J. E. Thatcher, D. A. Crump, C. Devivier, P. B. S. Bailey, and J. M. Dulieu-Barton, "Low cost infrared thermography for automated crack monitoring in fatigue testing", *Optics and Lasers in Engineering*, vol. 126, 2020, doi: https://doi.org/10.1016/j.optlaseng.2019.105914.

[125] A. Agarwal and J. H. Lang, *First-Order Transient in Lineal Electrical Networks* (Foundations of Analog and Digital Electronic Circuits). San Francisco: Morgan Kaufmann, 2005.

[126] A. F. Robinson, J. M. Dulieu-Barton, S. Quinn, and R. L. Burguete, "Paint coating characterization for thermoelastic stress analysis of metallic materials", *Measurement Science and Technology*, vol. 21, no. 8, p. 085502, 2010, doi: https://doi.org/10.1088/0957-0233/21/8/085502.

[127] G. P. Howell, "Identification of Plastic Strain using Thermoelastic Stress Analysis", Doctor of Philosophy, Engineering Materials, University of Southampton, 2017.

[128] MakeItFrom. "Material Properties Database". https://www.makeitfrom.com/material-properties/6081-6081-T6-AlSi0.9MgMn-Aluminum (accessed 2018).

[129] United performance metals. "316 and 316L Stainless Steel Sheet, Coil & Bar - AMS 5524, 5507, UNS S31600, S31603". https://www.upmet.com/products/stainless-steel/316316l (accessed 2018).

[130] Infrared Systems Development Corporation. IR-2106/301 Blackbody System [Online] Available: https://www.infraredsystems.com/Products/blackbody2106.html

[131] Thorlabs Inc. "MC2000B". https://www.thorlabs.com/thorproduct.cfm?partnumber=MC2000B (accessed 2020).

[132] G. Pitarresi, R. Cappello, and G. Catalanotti, "Quantitative thermoelastic stress analysis by means of low-cost setups", *Optics and Lasers in Engineering*, vol. 134, 2020, doi: https://doi.org/10.1016/j.optlaseng.2020.106158.

[133] P. J. Seelan, "Revealing the Heterogeneity in Weld Microstructures Using the Thermomechanical Dissipative Heat Source", Doctor of Philosophy, Engineering Materials, University of Southampton, 2018.

[134] *Toughened Epoxy Prepreg System RP-528*, Dorset, England, UK, 2016.

[135] Hexcel. Product Data Sheet HexPly 8552 [Online] Available: https://www.hexcel.com/Resources/DataSheets/Prepreg

[136] Hexcel. Product Data Sheet HexTow IM7 [Online] Available: https://www.hexcel.com/Resources/DataSheets/Carbon-Fiber

[137] MatWeb. E-Glass Fiber, Generic [Online] Available: http://www.matweb.com/search/DataSheet.aspx?MatGUID=d9c18047c49147a2a7c0b0bb1743e812&ckck=1

[138] Substances & Technologies. "Thermoset Epoxy (EP)". http://www.substech.com/dokuwiki/doku.php?id=thermoset_epoxy_ep (accessed 2020).

[139] J. Thomason, L. Yang, and F. Gentles, "Characterisation of the Anisotropic Thermoelastic Properties of Natural Fibres for Composite Reinforcement", *Fibers*, vol. 5, no. 4, 2017, doi: https://doi.org/10.3390/fib5040036.

[140] M. T. Saad, S. G. Miller, and T. Marunda, "Thermal Characterisation of IM7/8552-1 Carbon-Epoxy Composites", in *ASME 2014 International Mechanical Engineering Congress and Exposition (IMECE2014)*, Montreal, Quebec, Canada, 2014, doi: https://doi.org/10.1115/IMECE2014-40030.

[141] P. P. Camanho, P. Maimí, and C. G. Dávila, "Prediction of size effects in notched laminates using continuum damage mechanics", *Composites Science and Technology*, vol. 67, no. 13, pp. 2715-2727, 2007, doi: https://doi.org/10.1016/j.compscitech.2007.02.005.

[142] J. P. Stacey, M. O'Donnell, and M. Schenk, "Thermal Prestress in Composite Compliant Shell Mechanisms", in *ASME 2018 International Design Engineering Technical Conferences & Computers and Information in Engineering Conference*, Quebec, Canada, 2018, doi: https://doi.org/10.1115/DETC2018-85826.

[143] Everest Intersicence Inc. "Everest Interscience Emissivity of Total Radiation for Various Metals". http://everestinterscience.com/info/emissivitytable.htm (accessed 2020).

[144] Electrolube. "MBP400 Matt Black Paint". https://electrolube.com/product/mbpmatt-black-paint/#:~:text=Product%20Description,oils%20and%20other%20environmental%20elements. (accessed 2020.

[145] T. Laux, K. W. Gan, J. M. Dulieu-Barton, and O. T. Thomsen, "A simple nonlinear constitutive model based on non-associative plasticity for UD composites: Development and calibration using a Modified Arcan Fixture", *International Journal of Solids and Structures*, vol. 162, pp. 135-147, 2019, doi: https://doi.org/10.1016/j.ijsolstr.2018.12.004.

[146] P. P. Camanho and M. Lambert, "A design methodology for mechanically fastened joints in laminated composite materials", *Composites Science and Technology*, vol. 66, pp. 3004-3020, 2006, doi: https://doi.org/10.1016/j.compscitech.2006.02.017.

[147] iDICs, E. M. C. Jones, and M. A. Iadicola, "A good practices guide for digital image correlation", 2018, doi: https://doi.org/10.32720/idics/gpg.ed1/print.format.

[148] R. K. Fruehmann, D. A. Crump, and J. M. Dulieu-Barton, "Characterization of an infrared detector for high frame rate thermography", *Measurement Science and Technology*, vol. 24, no. 10, p. 105403, 2013, doi: https://doi.org/10.1088/0957-0233/24/10/105403.

[149] J. A. Nairn, "The Strain Energy Release Rate of Composite Microcracking: A Variational Approach", *Journal of Composite Materials*, vol. 23, no. 11, pp. 1106-1129, 1989, doi: https://doi.org/10.1177/002199838902301102.

[150] J. S. Callaghan, J. M. Dulieu-Barton, O. T. Thomsen, and S. Laustsen, "Full-field evaluation of the load response of a wind turbine blade substructure", presented at the 13th International Conference on Advances in Experimental Mechanics, Southampton, 2018.

[151] P. Tremblay *et al.*, "Pixel-wise real-time advanced calibration method for thermal infrared cameras", in *SPIE Defence, Security and Sensing*, Orlando, Florida, United States, 2010, doi: https://doi.org/10.1117/12.850560.

[152] A. Huot, "Telops Permanent Infrared Camera Calibration Webinar: Basics and Benefits," Photonics Online, Ed., ed, 2018.